Universitat de Barcelona

Growth and characterisation of Bi-based multiferroic thin films

Eric Langenberg Pérez

Growth and characterisation of Bi-based multiferroic thin films

Eric Langenberg Pérez

PhD thesis

Memòria presentada per a l'obtenció del grau de Doctor per la Universitat de Barcelona en el marc del programa de **Doctorat en Física**

Directors:

Dr. **Manuel Varela Fernández**

Dr. **Josep Fontcuberta i Griñó**

Departament de Física Aplicada i Òptica, Facultat de Física

Universitat de Barcelona

Juny 2013

UNIVERSITAT DE BARCELONA

ICMAB CSIC

Abstract

Multiferroic materials, in which both ferroelectric and (anti)ferromagnetic orders coexist in the same phase, have received much interest in the last few years. The possibility of these two ferroic orders being coupled allows new functionalities in these materials as controlling the magnetisation by an electric field or, conversely, controlling the polarisation by a magnetic field. The fulfilment of this magnetoelectric coupling is not only interesting in terms of fundamental research but it would also pave the way for designing novel magnetoelectric applications, especially in the field of spintronics, like spin filters or magnetic tunnel junctions controlled by electric fields instead of using magnetic fields, and thus promoting a new generation of high-density and low-power-consumption storage devices. For this latter purpose, ferromagnetic multiferroics would have greater advantages over the antiferromagnetic ones because of the net magnetisation, which would allow an easier control of the magnetic state. However, it is the antiferromagnetic order which prevails in multiferroic materials; hence, research focused on identification of new ferromagnetic ferroelectrics is needed.

Bi-based perovskite and double-perovskite oxides, $BiBO_3$ and $Bi_2BB'O_6$, respectively, where B and B' are magnetic transition metal ions (*i.e.* with a partially occupied outer electron *d* shell), present an excellent starting point to investigate new ferromagnetic ferroelectric materials. In these compounds ferroelectricity arises from the stereochemical activity of Bi^{3+} cations. The outer electrons of the 6*s* orbitals of Bi^{3+}, called *lone pairs*, do not participate in chemical bonds. When surrounded by the oxygen anions they off-centre from the centrosymmetric position due to the Coulombian electrostatic repulsion, forming an electric dipole and breaking the spatial inversion symmetry (the required condition, though not sufficient, for ferroelectric order to occur). Conversely, magnetism is driven by the superexchange interaction between the magnetic ions, *i.e.* B-cations, through the adjacent oxygen ions (B – O – B). Whether superexchange interaction is ferromagnetic or antiferromagnetic depends, to a large extent, on the electronic configuration of the *d* orbitals of B cations, which in perovskites splits into high-energy e_g orbitals and low-energy t_{2g} orbitals. In an ideal perovskite in which B – O – B bond angle is 180º, either B (empty e_g orbitals) – O – B (empty e_g orbitals) or B (half-filled e_g orbitals) – O – B (half-filled e_g orbitals)

configurations give rise to antiferromagnetic interactions, whereas B (half-filled e_g orbitals) – O – B (empty e_g orbitals) configuration gives rise to ferromagnetic interactions. As the B-site is occupied by only one kind of ion in perovskite oxides and, in general, with the same oxidation state, *i.e.* having the same e_g orbital filling, antiferromagnetic interactions are much more common than the ferromagnetic ones. Instead, by appropriately choosing the B – B' cations in double-perovskite oxides, ferromagnetic superexchange interactions can be designed. Hence, Bi-based double-perovskite oxides provide the possibility of engineering long-range ferromagnetism (as long as B – B' – B – B' – ... long-range B-site order is accomplished) and consequently overcoming the scarcity of ferromagnetic multiferroics.

In particular, to date, $BiMnO_3$ and Bi_2NiMnO_6 systems are the only reported ferromagnetic Bi-based perovskite oxides, possessing a magnetic Curie temperature around 105 K and 140 K, respectively, in bulk form. Additionally, they are promising candidates to display ferroelectricity driven by the aforementioned stereochemical activity of Bi cations and, hence, both systems are investigated in the work of this thesis in thin films.

First of all, this thesis addresses the synthesis of these compounds. In this process, three main hindrances were met. Firstly, these Bi-based compounds are highly metastable, which implies that they are only possible to be synthesised in bulk under extreme conditions, *i.e.* under high temperatures and high pressures (around 5 GPa). The strategy used to circumvent the required high pressures consisted of replacing the mechanical pressure by the epitaxial stress in thin films, *i.e.* using substrates whose crystal lattice parameters show a low mismatch with those of the compound that is to be formed. For this purpose these Bi-based compounds were grown by pulsed laser deposition (PLD) onto single-crystal (001)-oriented $SrTiO_3$ substrates. Secondly, Bi is a highly volatile element and consequently the synthesis temperature was not a free deposition parameter, forcing the use of low synthesis temperatures in order to prevent non-stoichiometric films or even the no-formation of the compound when the Bi-deficiency was too large. Yet the general metastable character of these compounds demands the use of high temperatures to the synthesis process. These two antagonistic requirements were tried to be balanced by using 10% Bi-rich PLD targets in the case of $BiMnO_3$ system and by partial replacement of Bi^{3+} cations by La^{3+} cations (by 10%) in the case of Bi_2NiMnO_6 system. In the latter approach, La-doping gives rise to a slightly

reduced unit cell volume, exerting the so-called chemical pressure (equivalently to a hydrostatic pressure) which contributes to prevent Bi^{3+} cations from desorption during the growth process. Thirdly, both in the ternary Bi – Mn – O and quaternary Bi – Ni – Mn – O systems a strong multiphase formation tendency was found, especially in the former, in which apart from the desired $BiMnO_3$ and Bi_2NiMnO_6 compounds, different parasitic oxide phases like Mn_3O_4, Bi_2O_3 and MnO_2 for the former system and NiO for the latter system appeared in the grown films. As a consequence of all these facts the single-phase stabilisation of either $BiMnO_3$ or $(Bi_{0.9}La_{0.1})_2NiMnO_6$ was greatly hampered and only possible to be achieved under a narrow window of deposition conditions. Especially critical was the temperature deposition window, which was required to be as narrow as 10ºC around 630ºC and 620ºC for $BiMnO_3$ and $(Bi_{0.9}La_{0.1})_2NiMnO_6$ synthesis, respectively.

Once the deposition conditions for single-phase stabilisation of the Bi-based compounds are controlled, structural characterisation proves that both $BiMnO_3$ and $(Bi_{0.9}La_{0.1})_2NiMnO_6$ grow fully coherent (compressive and tensile strained, respectively) on $SrTiO_3$ substrates, thus adopting as the in-plane lattice parameter that of the cubic substrate and subsequently a tetragonal-like structure. Importantly enough for the magnetic properties, $(Bi_{0.9}La_{0.1})_2NiMnO_6$ thin films are found to display long-range B-site order and the Ni^{2+}/Mn^{4+} electronic configuration, which is the required condition for a long-range ferromagnetism. Indeed, ferromagnetic behaviour is recorded but with a reduced Curie temperature probably due to the epitaxial strain of the substrate. Instead, $BiMnO_3$ thin films are found to exhibit similar Curie temperature to that of bulk specimens, but with a reduced saturated magnetisation which is ascribed to slightly off-stoichiometric samples driven by the presence of Bi vacancies and the subsequent formation of small amounts of Mn^{4+} replacing Mn^{3+} cations. Remarkably enough for the implementation of these films in future multilayer structures devices in which flat surfaces is a requirement, two-dimensional growth mode is obtained for $(Bi_{0.9}La_{0.1})_2NiMnO_6$ thin films, attaining very low rough surface (between one and two unit cells), whereas $BiMnO_3$ thin films were in all cases displaying a clear three-dimensional growth mode, yielding rougher surface morphology.

Finally, in order to study the dielectric/resistive, magnetoelectric and ferroelectric properties parallel-plate capacitors were fabricated using single-crystal (001)-oriented

Nb doped $SrTiO_3$ substrates as bottom electrode and sputtered Pt as top electrodes. First part of the electric measurements is devoted to the ferroelectric properties. In $(Bi_{0.9}La_{0.1})_2NiMnO_6$ thin films ferroelectric domains switching current is measured, which allows conclusively stating that $(Bi,La)_2NiMnO_6$ compounds are indeed ferroelectric up to at least 10% La content. By structural characterisation the ferroelectric transition temperature is inferred to be around 450 K, well above room temperature. Instead, $BiMnO_3$ thin films were not able to be proved its possible ferroelectric character (which is still on debate in the scientific community), probably due to the fact that leakage was too large with regard to the ferroelectric domain switching current that may masked any footprint of ferroelectricity by conventional macroscopic measurements. The second part of this bloc is devoted to study the dielectric properties and the possible magnetoelectric coupling of these compounds. It is worth remarking that in this work both the dielectric response and the magnetoelectric response was assessed by impedance spectroscopy, the latter using magnetic fields while recording the impedance response, with the final aim of observing any deviation of the dielectric permittivity of these compounds either in the vicinity of the ferromagnetic transition temperature or when applying a magnetic field. Either phenomenon would indicate that the ferroelectric and ferromagnetic orders display a certain degree of coupling. Nonetheless, special attention is given to the conventional artefacts these measurements often produce when performed on dielectric thin films, causing misleading interpretations, like apparent colossal dielectric constants and/or apparent large magnetoelectric couplings. For this aim a thorough study is devoted, in which simulations of real dielectric materials are carried out covering the different sources of artefacts in order to better understand the dielectric and magnetoelectric data. Following these precautions the intrinsic dielectric and magnetoelectric response of $BiMnO_3$ and $(Bi_{0.9}La_{0.1})_2NiMnO_6$ thin films are extracted. Despite the fact that $BiMnO_3$ dielectric data shows clear magnetoelectric signs, results points to a weak magnetoelectric coupling, which is especially emphasised in $(Bi_{0.9}La_{0.1})_2NiMnO_6$ thin films, probably driven by the fact that magnetism and ferroelectricity arise by two independent mechanisms in these Bi-based compounds.

Resumen

Los materiales multiferroicos, en los cuales coexisten en la misma fase un ordenamiento ferroeléctrico y magnético, han recibido mucho interés en los últimos años. La posibilidad de que estén acoplados los dos órdenes ferroicos permite nuevas funcionalidades en estos materiales como el control eléctrico de la magnetización o, por el contrario, el control magnético de la polarización. La realización de dicho acoplamiento magnetoeléctrico no solo sería interesante en términos de investigación básica, sino que abriría camino para el diseño de nuevas aplicaciones magnetoeléctricas, especialmente en el campo de la spintrónica, como filtros de spin o uniones túneles magnéticas controladas mediante campos eléctricos en lugar de campos magnéticos y por lo tanto promoviendo una nueva generación de dispositivos de almacenamiento de alta densidad y bajo consumo. Para este último propósito, los multiferroicos que poseen un ordenamiento ferromagnético tendrían mayores ventajas que aquellos antiferromagnéticos debido a que los primeros mostrarían magnetización neta y por lo tanto permitirían un control más fácil del estado magnético. No obstante, es el orden antiferromagnético el que prevalece en estos materiales. Por eso es necesario la búsqueda de nuevos materiales que sean ferromagnéticos y ferroeléctricos.

Los óxidos en estructura perovskita y doble perovskita basados en Bi, $BiBO_3$ y $Bi_2BB'O_6$, respectivamente, donde B y B' son iones magnéticos de metales de transición (es decir, con la capa electrónica externa *d* parcialmente ocupada), presentan un excelente punto de partida para investigar nuevos materiales ferromagnéticos y ferroeléctricos. En estos compuestos la ferroelectricidad se origina debido a la actividad estereoquímica de los cationes Bi^{3+}. La capa externa electrónica de los orbitales 6*s* de dichos iones, llamados *lone pairs*, no participan en los enlaces químicos, por lo que rodeados por los aniones oxígeno en la perovskita se desplazan del centro de simetría formando un dipolo eléctrico y rompiendo la simetría de inversión espacial (condición necesaria, aunque no suficiente, para que se produzca el ordenamiento ferroeléctrico). Por el contrario, el magnetismo en estos compuestos se produce como consecuencia de la interacción de supercanje entre los iones magnéticos, es decir, los cationes B, por medio de los iones de oxígenos adyacentes (B – O – B). Dependiendo en gran medida de la configuración electrónica de los orbitales *d* de los cationes B, los cuales en

perovskitas se dividen en orbitales de alta energía e_g y baja energía t_{2g}, dicha interacción de supercanje es ferromagnética o antiferromagnética. En perovskitas ideales en las cuales el ángulo de enlace químico B – O – B es 180º, tanto la configuración B (orbitales e_g vacíos) – O – B (orbitales e_g vacíos) como B (orbitales e_g semillenos) – O – B (orbitales e_g semillenos) dan lugar a interacciones antiferromagnéticas, mientras que B (orbitales e_g semillenos) – O – B (orbitales e_g vacíos) dan lugar a interacciones ferromagnéticas. Debido a que el sitio B es ocupado por un solo tipo de ion en perovskitas y, en general, con el mismo estado de oxidación, lo que implica el mismo llenado de los orbitales e_g, las interacciones antiferromagnéticas son mucho más comunes que las ferromagnéticas. En cambio, eligiendo apropiadamente los cationes B y B' en doble perovskitas, se puede diseñar que las interacciones de supercanje sean ferromagnéticas. Es por eso que los óxidos en estructura de doble-perovskita basados en Bi pueden proporcionar la posibilidad de ingeniar ferromagnetismo de largo alcance (siempre que se produzca un ordenamiento cationico B de largo alcance siguiendo cadenas de B – B' – B – B' – …) y por consiguiente superar la escasez de multiferroicos ferromagnéticos.

En concreto, los sistemas $BiMnO_3$ y Bi_2NiMnO_6 son los únicos de la familia de óxidos en estructura perovskita basados en Bi que hasta la fecha han manifestado un ordenamiento ferromagnético en su forma masiva, con temperaturas de Curie alrededor de 105 K y 140 K, respectivamente. Por otro lado, son candidatos prometedores de manifestar ordenamiento ferroeléctrico debido a la mencionada actividad estereoquímica de los cationes de Bi^{3+}, por lo que ambos sistemas son investigados, en láminas delgadas, en el trabajo de esta tesis.

En primer lugar, esta tesis aborda el problema de sintetizar estos compuestos. En este proceso se topó con tres principales obstáculos. Primero, estos compuestos basados en Bi son altamente metaestables, lo que implica que en su forma masiva sólo se pueden sintetizar bajo condiciones extremas: altas temperaturas y altas presiones (del orden de los GPa). La estrategia que se usó para eludir las altas presiones consistió en reemplazar la presión mecánica por el estrés epitaxial, es decir, usando sustratos cuyos parámetros de red cristalinos fueran semejantes a los del compuesto que se tiene que formar. Para este propósito, estos compuestos basados en Bi se crecieron sobre sustratos monocristalinos de $SrTiO_3$ orientados (001) por ablación de láser pulsado (PLD).

Segundo, Bi es un elemento altamente volátil y por consiguiente la temperatura de síntesis de estos compuestos no fue un parámetro de crecimiento libre. Esto llevó al uso de bajas temperaturas de crecimiento con el objeto de impedir el crecimiento de láminas delgadas no estequiométricas o incluso la no formación del compuesto cuando la deficiencia en Bi fuera demasiado grande. No obstante, el carácter metaestable de estos compuestos demandaba el uso de altas temperaturas en el proceso de síntesis. Para equilibrar estos dos requerimientos antagónicos se usó blancos de PLD enriquecidos en Bi en el caso de $BiMnO_3$ y una sustitución parcial (10 %) de Bi^{3+} por cationes La^{3+} en el caso de Bi_2NiMnO_6. El dopaje con La da lugar a un volumen ligeramente reducido de la celda unidad, ejerciendo la presión química (equivalente a una presión hidrostática) que contribuye a prevenir la desabsorción de Bi durante el proceso de crecimiento. Tercero, tanto en el sistema ternario Bi – Mn – O como cuaternario Bi – Ni – Mn – O se encontró una fuerte tendencia multifásica, especialmente en el primero, en los cuales, aparte de los compuestos deseados $BiMnO_3$ y Bi_2NiMnO_6, se forman diferentes fases parásitas de óxidos como Mn_3O_4, Bi_2O_3 y MnO_2 en el primer caso y NiO en el segundo. Como consecuencia de todos estos factores la estabilización monofásica de tanto $BiMnO_3$ como $(Bi_{0.9}La_{0.1})_2NiMnO_6$ fue dificultada en gran medida y solo se pudo conseguir bajo una ventana estrecha de condiciones de crecimiento. Especialmente crítico fue la temperatura de depósito, la cual sólo permitía una ventana de 10ºC alrededor de 630ºC y 620ºC para la síntesis de $BiMnO_3$ y $(Bi_{0.9}La_{0.1})_2NiMnO_6$, respectivamente.

Una vez controladas las condiciones de crecimiento para la estabilización monofásica de los compuestos de Bi, la caracterización estructural evidenció que tanto $BiMnO_3$ como $(Bi_{0.9}La_{0.1})_2NiMnO_6$ crecen completamente coherentes (tensionadas por compresión y por tracción, respectivamente) sobre los sustratos $SrTiO_3$, por lo tanto adaptando el parámetro de red en el plano al del sustrato cúbico y por consiguiente adoptando una estructura tetragonal. Suficientemente importante para las propiedades magnéticas, las láminas delgadas de $(Bi_{0.9}La_{0.1})_2NiMnO_6$ manifiestan ordenamiento catiónico de largo alcance en el sitio B y la configuración electrónica Ni^{2+}/Mn^{4+}. De hecho, su comportamiento ferromagnético es corroborado, aunque con una temperatura de Curie reducida con respecto a su forma masiva probablemente debida al estrés epitaxial del sustrato. En cambio, en las láminas delgadas de $BiMnO_3$ se encontró que exhibían temperaturas de Curie similares a las halladas en especímenes en forma

masiva, aunque con una reducida magnetización de saturación la cual se atribuye a una ligera desviación estequimétrica de las muestras por la presencia de vacantes de Bi y la subsiguiente formación de pequeñas cantidades de Mn^{4+} remplazando los cationes Mn^{3+}. Un aspecto importante a la hora de implementar estas láminas delgadas en dispositivos de estructura multicapa es el requerimiento de superficies planas. En el caso de las láminas delgadas de $(Bi_{0.9}La_{0.1})_2NiMnO_6$ se obtuvo un crecimiento bidimensional, logrando superficies con muy baja rugosidad (entre una y dos celdas unidades). Sin embargo, las láminas delgadas de BiMnO3 mostraron un crecimiento tridimensional en todos los casos, dando lugar a una morfología superficial más rugosa.

Finalmente, con el objeto de estudiar las propiedades dieléctricas/resistivas, magnetoeléctricas y ferroeléctricas condensadores con geometría de electrodos plano-paralelos fueron fabricados, usando sustratos monocristalinos de $SrTiO_3$ dopados con Nb como electrodo inferior y Pt depositado por pulverización catódica como electrodos superiores. La primera parte de las medidas eléctricas se centra en las propiedades ferroeléctricas. En las láminas delgadas de $(Bi_{0.9}La_{0.1})_2NiMnO_6$ se consiguió medir corriente eléctrica que era debida únicamente al cambio de orientación de los dominios ferroeléctricos, lo cual permitió afirmar de forma concluyente que los compuestos $(Bi,La)_2NiMnO_6$ son ferroeléctricos, al menos hasta un 10% de contenido de La. Por medio de caracterización estructural, se deduce que la temperatura de transición ferroeléctrica es aproximadamente sobre los 450 K, por encima de temperatura ambiente. En cambio, no fue posible revelar el posible carácter ferroeléctrico de $BiMnO_3$ (el cual es todavía materia de debate en la comunidad científica), probablemente debido a que las pérdidas eléctricas eran demasiado grandes enmascarando cualquier posible huella de ferroelectricidad por medio de medidas convencionales macroscópicas. La segunda parte de este bloque se centra en el estudio de las propiedades dieléctricas y el posible acoplamiento magnetoeléctrico de dichos compuestos. Vale la pena remarcar que en este trabajo tanto la respuesta dieléctrica como magnetoeléctrica se ha evaluado por medio de la técnica de espectroscopia de impedancias, usando además campos magnéticos en el último caso, con el objeto final de observar cualquier variación de la permitividad dieléctrica de estos compuestos tanto en las cercanías de la temperatura de transición magnética como debido a la aplicación de campo magnético. Ambos fenómenos indicarían un acoplamiento entre los órdenes ferroeléctrico y ferromagnético. Se da una especial atención a los artefactos

convencionales que producenc frecuentemente este tipo de medidas eléctricas, llevando a interpretación errónea de los resultados como constantes dieléctricas aparentemente colosales o acoplamientos magnetoeléctricos aparentemente fuertes. Con este propósito un exhaustivo estudio es presentado en la tesis, en el cual se llevan a cabo simulaciones del comportamiento de materiales dieléctricos reales cubriendo las diferentes fuentes de artefactos con el objeto de entender mejor los datos medidos sobre la respuesta dieléctrica y magnetoeléctrica. Siguiendo estas precauciones, se extraen las propiedades dieléctricas y magnetoeléctricas intrínsecas de $BiMnO_3$ y $(Bi_{0.9}La_{0.1})_2NiMnO_6$. A pesar de que los resultados de las medidas dieléctricas de $BiMnO_3$ muestran claros signos de acoplamiento magnetoeléctrico, dicho acoplamiento es débil, especialmente enfatizado en $(Bi_{0.9}La_{0.1})_2NiMnO_6$, probablemente debido al hecho de que en los compuestos basados en Bi el magnetismo y la ferroelectricidad se originan por medio de dos mecanismos independientes.

Contents

Chapter 1

Introduction

1.1 Multiferroics

1.1.1 Ferroic properties

Multiferroics are materials where at least two ferroic orders coexist in the same phase. The definition of the term ferroic aimed to characterise materials in which domains are formed, having a corresponding net macroscopic magnitude that can be hysteretically switched by applying an external field, *i.e.* ferroelectric, ferromagnetic, ferroelastic and ferrotoroidic orders (primary ferroics) [1, 2], see table 1.1. Nonetheless, antiferroic orders, which basically consist of antiferromagnetism –*i.e.* also ferrimagnetism– and antiferroelectricity, are widely accepted to be also included in the extended definition of the term multiferroic, as listed in Table 1.1.

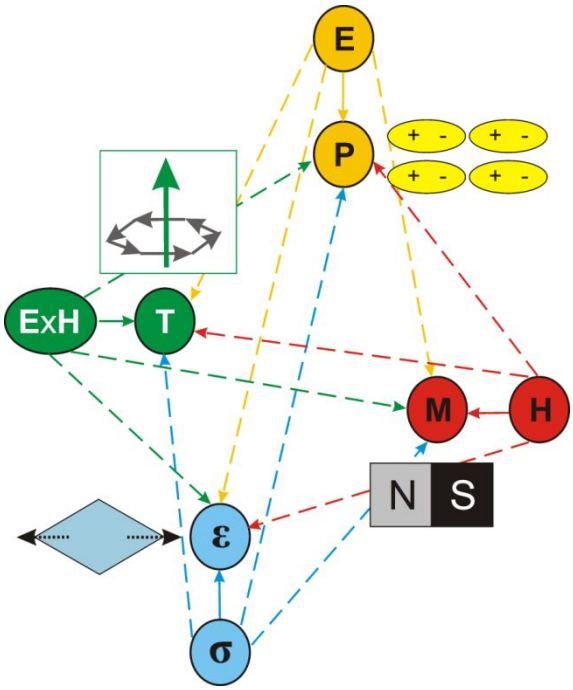

Fig. 1.1 – *Illustrative sketch of the primary (solid lines) and cross-coupling (dashed lines) interactions allowed in multiferroic materials. P, M, ε and T denote the primary ferroic orders, namely polarisation, magnetisation, strain and ferrotoroidic order, respectively; whereas E, H, σ and E x H denote their conjugate fields, namely electric field, magnetic field, stress and cross electric-magnetic field, respectively. Adapted from Ref. [3].*

Ferroic property	Description
Ferroelectric order	Materials that below a certain temperature undergo a phase transition in which an ordering of dielectric dipole moments is present, leading to spontaneous polarization (***P***) that can be hysterically switched by applying an external electric field (***E***).
Antiferroelectric order	Materials that below a certain temperature undergo a phase transition in which an antiparallel ordering of dielectric dipole moments is present, leading to zero overall polarisation.
Ferromagnetic order	Materials that below a certain temperature undergo a phase transition in which an ordering of magnetic moments is present, leading to spontaneous magnetisation (***M***) that can be hysterically switched by applying an external magnetic field (***H***).
Antiferromagnetic order	Materials that below a certain temperature undergo a phase transition in which an antiparallel ordering of magnetic moments is present, leading to zero overall magnetisation.
Ferrimagnetic order	Materials that below a certain temperature undergo a phase transition in which an antiparallel ordering of magnetic moments is present, but the opposing magnetic moments are unequal, leading to a remaining net magnetisation (***M***) that can be switched hysterically by applying a magnetic field (***H***).
Ferroelasticity	Materials that below a certain temperature possess spontaneous strain ($\boldsymbol{\varepsilon}$), which can be hysterically switched by applying an external stress ($\boldsymbol{\sigma}$).
Ferrotoroidic order	Materials that below a certain temperature an ordering of the so-called toroidal moments, $T \propto \sum_n \mathbf{r}_n \times \mathbf{S}_n$, is present, where $\mathbf{r}_n$ denotes the radius vector (from an origin of coordinates) and $\mathbf{S}_n$ the spin of the *n* magnetic ion. These toroidal moment should be hysterically switched by crossed electric and magnetic field.

Table 1.1 – *Description of the ferroic orders*

The coexistence of different ferroic orders leads to additional interactions in multiferroic materials, as illustrated in Fig. 1.1. Whereas in conventional ferroic materials, its ferroic order is modified by its conjugate field (*i.e.* the magnetic field modifies the magnetisation, the electric field the polarisation, etc), in multiferroic

materials exists the possibility that two or more ferroic orders are coupled, which would allow cross-interactions between the ferroic properties and their conjugated fields, *i.e.* tuning the magnetisation by an electric field, tuning the strain by a magnetic field and so on (Fig. 1.1).

Among all kinds of multiferroics, those showing both ferroelectric and magnetic order draw special attention in terms of magnetoelectric properties, as will discussed later on, on which this work is focused. Thus, for the sake of simplicity, on the following the term multiferroicity will be used to refer, exclusively, to those materials being ferroelectric and magnetic (either ferromagnetic or antiferromagnetic).

1.1.2 Motivation

In terms of fundamental research, multiferroic materials are very appealing just by the mere fact of combining ferroelectric and magnetic order. Whereas electricity and magnetism were demonstrated to be unified in the common discipline of electromagnetism during 19^{th} century, culminated by Maxwell's equations which specify how magnetic and electric fields relate to each other, ferroelectricity and magnetism in matter tend to be independent disciplines and rarely found together. Indeed, microscopically both ferroic orders arise from different origin: electric dipole ordering versus spin ordering. Thus, the research on new multiferroic materials will contribute to make advances in the comprehension of the mechanism which enable multiferroicity to exist and how both orders may relate to each other.

From the technological point of view, magnetic and ferroelectric materials are widely used in many devices. The former have played an important role in the stored data devices (hard disks, magnetic RAM's, ...) as well as sensors, read heads, ... The latter are used in sensors and transducers because of their large piezoelectric response, in capacitors because of their high dielectric permittivity and also in storage data devices (ferroelectric RAM's). Thus, multiferroics are especially interesting not only because they have the same properties, and therefore the same applications, as their 'parents' (ferroelectrics and magnetics) have, but also because of the interplay between magnetism and ferroelectricity, which gives an extra degree of freedom and hence additional funcionalities.

Some of these additional applications could be the four-state memories, in which the ferroelectric and ferromagnetic character of the multiferroic is used to encode the information in either four resistive states [4 – 6] (also proposed eight resistive states [7]), or the electric control of magnetic RAM's [6, 8]—if the magnetoelectric coupling is large enough (see Sect. 1.1.3)—, which would reduce, to a large extent, the inherent problem of the crosstalk (as the electric field can be applied very localized) and energy consumption (as sustaining and producing magnetic fields are much more energetically inefficient than electric fields), allowing, thus, high density and low-energy consuming magnetic RAM's.

Moreover, electrically controlled magnetic sensors, electrically tuneable microwave applications, such as filters, oscillators and phase shifters, and other kinds of applications in magnetoelectronics and spintronics have also been proposed for multiferroic materials [6, 8 – 12], and, possibly, new ones are expected to be suggested in future.

1.1.3 Magnetoelectric coupling

The magnetoelectric coupling or magnetoelectric effect describes any effect on the polarisation by applying a magnetic field, *H,* or, conversely, any effect on the magnetisation by applying an electric field, *E*. By the Neumann principle [13], which states that the symmetry elements of all the physic properties of a material should be contained in the symmetry elements of its crystalline structure, magnetoelectric coupling is enabled in multiferroic materials.

This magnetoelectric coupling can be described thermodynamically. In terms of the expansion of the free energy, *F*, of a magnetoelectric media, *i.e.* $F = F(\vec{H}, \vec{E})$, it follows [14]:

$$F(\vec{H},\vec{E}) = F_0 - P_i^s E_i - M_i^s H_i - \frac{1}{2}\varepsilon_0 \chi_{ij}^e E_i E_j - \frac{1}{2}\chi_{ij}^m H_i H_j - \alpha_{ij} E_i H_j - \ \ldots \qquad (1.1)$$

where, as listed in table 1.2, P_i^s and M_i^s denote the spontaneous polarisation and magnetisation, respectively; χ_{ij}^e and χ_{ij}^m are the electric and magnetic susceptibility, respectively ; and α_{ij} is the linear magnetoelectric coupling, which entails the induction of polarisation and magnetisation by a magnetic and electric field, respectively, what is called the linear magnetoelectric effect. Note that the expansion 1.1 has been cut in the first order magnetoelectric term. There are also quadratic magnetoelectric terms, and so on, but in general they are much weaker than the linear magnetoelectric effect [14].

Corresponding mechanism	Contribution to polarisation	Contribution to magnetisation
Spontaneous moment	P_i^s	M_i^s
Induced moment	$\frac{1}{2}\varepsilon_0\chi_{ij}^e E_i$	$\frac{1}{2}\chi_{ij}^m H_i$
linear magnetoelectric coupling	$\alpha_{ij}H_j$	$\alpha_{ij}E_i$

Table 1.2 – *Significance of the expansion terms of the free energy*

Hence, the polarisation and the magnetisation can be expressed as [14]:

$$\begin{aligned} P_i(\vec{H},\vec{E}) &= -\frac{\partial F}{\partial E_i} = P_i^s + \varepsilon_0\chi_{ij}^e E_j + \alpha_{ij}H_j + \ \ldots \\ M_i(\vec{H},\vec{E}) &= -\frac{\partial F}{\partial H_i} = M_i^s + \chi_{ij}^m H_j + \alpha_{ij}E_j + \ \ldots \end{aligned} \tag{1.2}$$

The magnetoelectric coefficient is, though, subjected to the magnetic and electric susceptibilities, which determine the upper bound on the magnitude of the magnetoelectric effect [15]:

$$\alpha_{ij}^2 < \chi_{ii}^e\chi_{jj}^m \tag{1.3}$$

Therefore, as ferromagnetic and ferroelectric materials show large magnetic and electric susceptibilities, respectively, multiferroic materials are enabled to show large magnetoelectric coupling. On the other hand, as the magnetic (and electric) susceptibility tend to diverge around the transition temperatures, the magnetoelectric coupling is expected to be larger around the Curie temperatures. Yet it is worth

mentioning that the sole coexistence of the two ferroic orders is not a sufficient condition for magnetoelectric coupling to occur, which is a more restrictive property.

On the other hand, when the magnetic and ferroelectric parameter are coupled to each other, the magnetic order is coupled to the polarisation and consequently to the dielectric permittivity. The origin of which can also be understood in the framework of the Ginzburg-Landau theory [16]. In the simplest scenario, the Taylor expansion of the free energy, *F*, now as a function of the magnetisation, *M*, and polarisation, *P*, in a magnetoelectric media, follows:

$$F(M,P) = F_0 + \frac{a}{2}M^2 + \frac{b}{4}M^4 + \ ... \ + \frac{a'}{2}P^2 + \frac{b'}{4}P^4 + \ ... \ + \gamma M^2P^2 + \ ... \qquad (1.4)$$

where no odd terms appear following the symmetry restrictions *F(M) = F(-M)* and *F(P) = F(-P)* as both states are energetically equivalent. The coefficients *a, a', b, b'* and γ are in general temperature dependent. The γM^2P^2 is hence the first order term allowed in the Taylor expansion related to the magnetoelectric coupling.

When applying an external electric, *E*, and magnetic, *H*, field, which couples linearly with the polarisation and magnetisation, respectively, expression 1.4 should be rewritten:

$$F(M,P) = F_0 - HM + \frac{a}{2}M^2 + \frac{b}{4}M^4 + \ ... \ - EP + \frac{a'}{2}P^2 + \frac{b'}{4}P^4 + \ ... \ + \gamma M^2P^2 + \ ... \qquad (1.5)$$

The electric susceptibility can be computed by $(\chi^e)^{-1} \sim \frac{\partial f^2}{\partial P^2} \sim a' + 3b'P^2 + \gamma M^2$ [16]. Hence, in a magnetoelectric material the dielectric permittivity is not only modified by the polarisation but also by the square of magnetisation (as long as $\gamma \neq 0$) [16].

Therefore, a useful, and widely extended [16 – 19], indirect way to bear out the occurrence of the coupling of the two ferroic orders consists of looking for deviations of the dielectric permittivity either in the vicinity of the magnetic transition temperature

and/or when applied a magnetic field, the so-called magnetocapacitance or magnetodielectric effect.

1.1.4 Pathways to the coexistence of magnetism and ferroelectricity

Despite the large number of ferroelectric or magnetic materials existing in nature, the combination of both ferroic orders in one intrinsic material seems to be quite elusive to be encountered. The reasons for this scarcity of multiferroic materials can be summarised in the following [10, 11, 20]:

1) Whereas magnetic materials can be either insulating or conductive, ferroelectric materials can solely be insulating, otherwise an applied electric field would induce an electric current rather than switching ferroelectric domains. This restricts the search for multiferroic materials to those magnetic materials that are insulators.

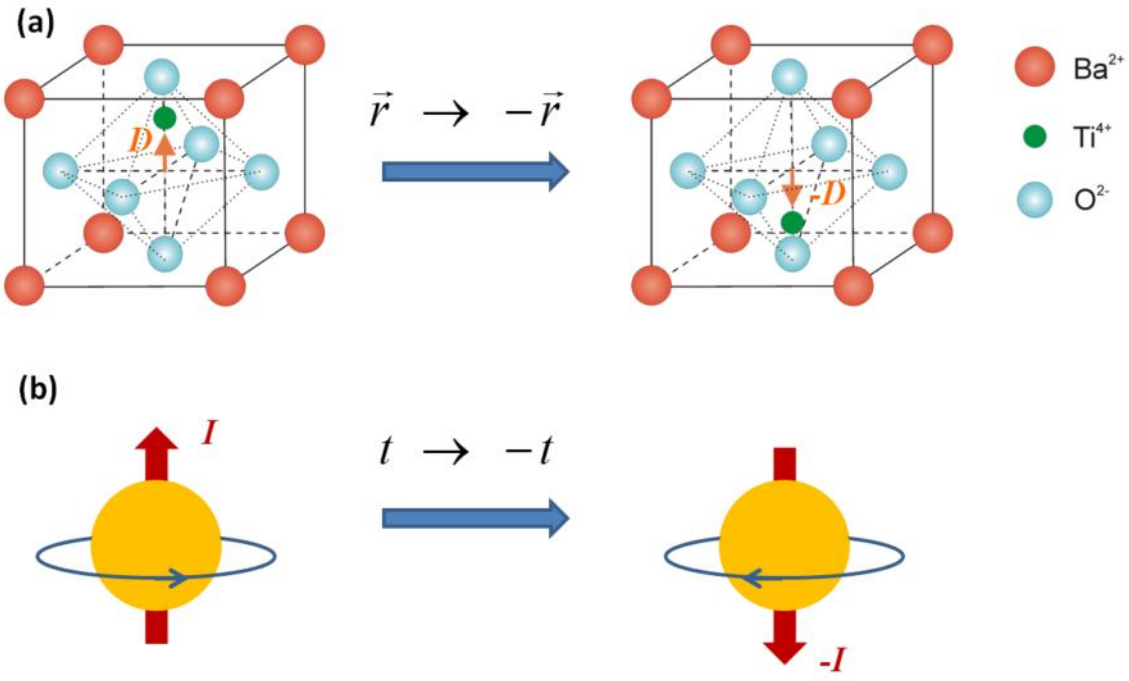

Fig. 1.2 – (a) *Ferroelectric material ($BaTiO_3$) under spatial inversion symmetry: changes orientation of electric dipole moment, D.* **(b)** *Classical representation of a particle with spin angular momentum I under time reversal operation.*

2) Second, from crystal symmetry considerations (see Fig. 1.2) ferroelectricity breaks the spatial inversion symmetry, which requires non-centrosymmetric crystal structures for ferroelectric order to occur [2]. Moreover, it should accomplish additional criteria: ferroelectric order can only be enabled in polar point groups. This leaves 10 out of the 32 possible point groups (or crystal classes) that can sustain spontaneous polarisation [13, 21]. Conversely, magnetism breaks time-reversal symmetry [2] (see Fig. 1.2). When time reversal operation is included in the set of the customary symmetry operations (rotations and reflexions) contained in the 32 point groups, 90 additional point groups should be included, in total leading to 122 magnetic point groups (or Shubnikov point groups) [13, 21]. Combination of the two symmetry restrictions which multiferroics must fulfil leaves only 21 magnetic point groups (out of 122) that enable ferroelectric and magnetic orders to coexist in the same phase [10, 11, 20, 21]. Moreover, if we restrict the magnetic materials to those allowed displaying spontaneous magnetisation (*i.e.* excluding antiferromagnetics) the list of possible multiferroic candidates is then reduced to 13 magnetic point groups [10, 11, 20, 21].

3) Since most of ferroelectric and a large number of magnetic materials are transition metal oxides with the ABO_3 perovskite structure, see Sect. 1.2.1, (*e.g.* $BaTiO_3$ and $(La,Sr)MnO_3$), much of the attention was reasonably drawn to this structure for the search for multiferroic materials. Both, in the ferroelectric and magnetic perovskites it is usually the *B* cation which drives the ferroelectric displacement and the magnetic order, respectively. In the case of ferroelectrics, the *B* cation displaces from the centre of the surrounding oxygen octaheadra, breaking the centrosymmetry and creating an electric dipole [Fig. 1.2 (a)]. Yet this condition requires the *B* cation to have a d^0 electron configuration, *i.e.* empty *d* orbitals like Ti^{4+}, to minimize the Coulombian electrostatic repulsion of the surrounding oxygen anions [20]. Magnetism in transition metal perovskites arises from magnetic superexchange interactions, see Sect. 1.2.3, (or double exchange for conductive magnetic oxides) of the *B* cations mediated by the adjacent oxygen ions [20, 22]. Yet this condition requires *B* cation to possess a magnetic moment, which is only possible when the *d* orbitals of the *B* cation are

partially occupied. Thus, there is an inherent mutual exclusion between ferroelectricity and magnetism in perovskites oxides [19].

To date, most of the attempts to design multiferroic materials have been based on looking for new mechanisms of ferroelectricity, while maintaining the same recipes for magnetism. Depending on these mechanisms, multiferroics have been classified into two types, as described by Khomskii [23]: In Type-I multiferroics ferroelectricity and magnetism rely on two independent mechanisms, whereas in Type-II ferroelectricity arises from the magnetic order, *i.e.* ferroelectricity exists only in a magnetically ordered state. The latter is expected to produce large magnetoelectric coupling as one order is intrinsically related to the other, but such ferroic orders tend to appear only at rather low temperatures. The most studied example of Type-II multiferroics is the Rare-Earth manganites, in which ferroelectricity appears because of the particular spiral or cycloid arrangement of the spins of Mn cations [24]. Contrarily, Type-I multiferroics tend to show much higher ferroic transition temperatures at the expense of small magnetoelectric coupling. To this group belong the multiferroics in which the ferroelectric order might be achieved (though not demonstrated in all cases) as a consequence of (*i*) a particular *charge ordering*, like (Pr,Ca)MnO_3 [25], (*ii*) tilting of the BO_6 octahedron, the so-called *geometrical ferroelectrics*, like $YMnO_3$ [26], and (*iii*) of the stereochemical activity of the *lone pairs* of Bi^{3+} and Pb^{2+} cations, located at the A-site in the perovskite, like $BiFeO_3$ [27]. This latter approach applies to the systems studied here.

1.2 Bi-based multiferroic perovskites

The simplest scenario where both ferroic orders are to be independently achieved in transition metal perovskite oxides would naturally lead to use one of the cations for inducing the ferroelectric order, while using the other one for the magnetism. One possibility is the exploitation of a d^0 transition metal cation located on the *B*-site and a magnetic cation on the *A*-site, for example in $EuTiO_3$ [28]. The second possibility is the use of stereochemical active cations like Bi^{3+} or Pb^{2+} at the perovskite *A*-site inducing

ferroelectricity due to lone-pair electrons, and a magnetic cation located on the B-site, as described in this section.

1.2.1 Perovskite structure

The perovskite structure, whose chemical formula is given by ABO_3 (where A and B are cations), is formed by the alternation of BO_2 and AO atomic planes along any of the orthogonal directions $\hat{i}, \hat{j}, \hat{k}$, as shown in Fig. 1.3, in its ideal cubic configuration. As a result of these staggered atomic planes, B cations are surrounded by 6 first-neighbour oxygen anions, forming the characteristic BO_6 octahedron, whereas A cations are surrounded by 12 oxygen anions (Fig. 1.3).

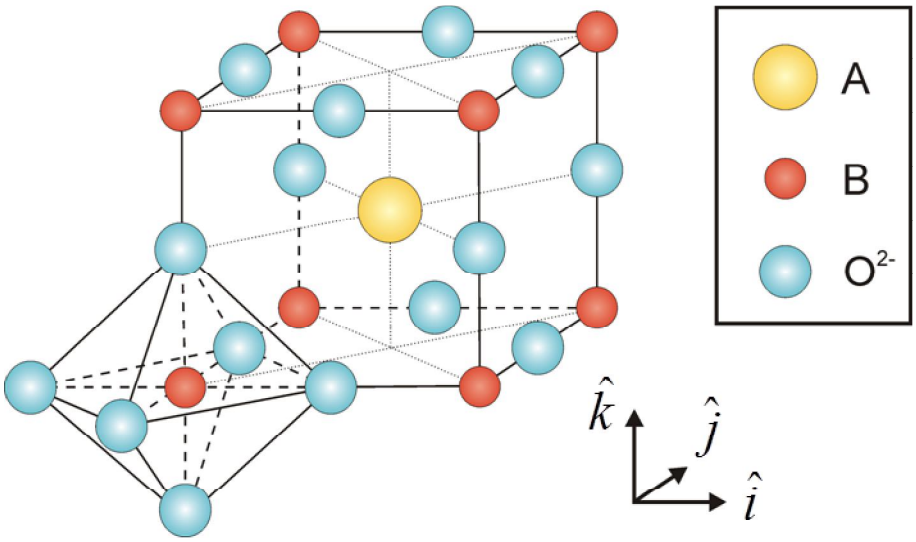

Fig. 1.3 – *Ideal perovskite structure, ABO_3.*

The stability of this structure is determined by the Goldschmidt tolerance factor, which is defined as follows:

$$t = \frac{r_A + r_O}{\sqrt{2} \cdot (r_B + r_O)} \tag{1.6}$$

where r_A, r_B and r_O denote the ionic radii of A, B cations and oxygen anion, respectively. The ideal cubic perovskite, such as the one shown in Fig. 1.3, is found when t = 1. Lower values of t means that the ionic radius of the A cation is smaller than that of the B

cation, so that, in order to achieve a close packaging of the ions, BO_6 octahedrons tilt (Fig. 1.4), forming, typically, orthorhombic or rhombohedral structures. Instead, when $t > 1$ the size of the *A* cation is too large to be accommodated in the cubic perovskite and different hexagonal polymorphs become stable (Fig. 1.4).

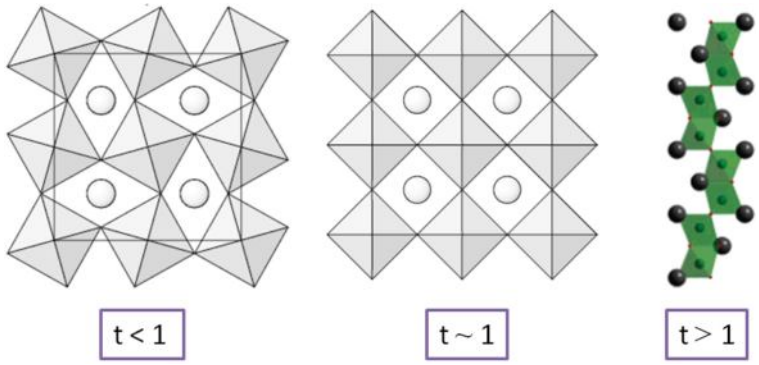

Fig. 1.4 – *Stability of the perovskite structures as a function of the tolerance factor, t.*

1.2.2 Ferroelectricity of Bi-containing perovskite oxides: the role of the *lone pair* electrons

An alternative route to the d^0 transition metal ion, located at the B-site, as the mechanism for the ferroelectric instability, is the use of stereochemical active ions like Bi^{3+} or Pb^{2+}, which always locate at the A-site. The electronic configuration of Bi^{3+} (and also Pb^{2+}), $[Xe]4f^{14}5d^{10}6s^26p^0$, signals empty *p*-states as the lowest unoccupied state, which form a covalent bond with the surrounding oxygen. Instead, the two outer electrons of the 6*s* orbitals, called *lone pairs*, do not participate in chemical bonds. In absence of interactions the *lone pairs* are nearly spherically distributed, but when surrounded by the oxygen anions they shift away from the centrosymmetric position due to the Coulombian electrostatic repulsion, forming a localized lobe-like distribution (very much alike the ammonia molecule [Fig. 1.5]) [29]. Thus, the *lone pairs*, which form an electric dipole, break the spatial inversion symmetry and become the driving force for the ferroelectric distortion in all Bi-based multiferroics.

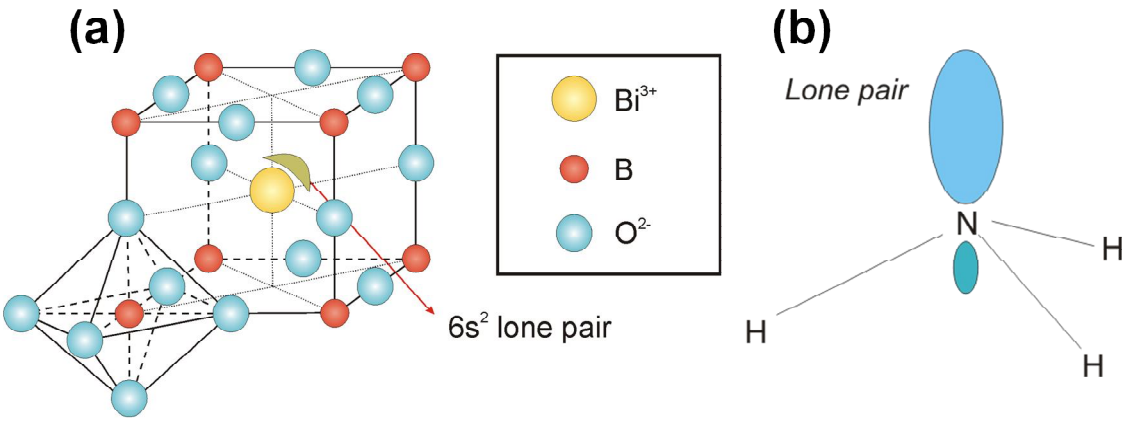

Fig. 1.5 – (a) *Schematic representation of the lobe-like distribution of the $6s^2$ lone-pair electrons in Bi-based perovskite structures, $BiBO_3$, breaking the spatial inversion symmetry.* **(b)** *Lone-pair $2s^2$ in the ammonia molecule.*

Still, it is worth mentioning that the non-centrosymmetric structure is a requirement for ferroelectricity to be enabled, but not a sufficient condition, as cooperative behaviour between the electric dipoles and hysteretically electric-field switching of the polarisation of the formed ferroelectric domains is to be additionally accomplished.

In an ideal perovskite the electrostatic repulsion of the oxygen anions over the lone pair electrons of Bi^{3+} cations is softened along the [111] pseudocubic direction, which, thus, tend to be the polar axis in Bi-multiferroic perovskites. Yet the common distortion of the ideal cubic perovskite in these compounds and/or the epitaxial strain in thin films (as will discussed in Sect. 1.3) may severely modify this polar orientation.

1.2.3 Magnetic order in Bi-containing perovskite oxides

Bi^{3+} is always situated at the perovskite A-site, thus allowing the location of a magnetic transition metal cation at the B-site, *i.e.* with a partially occupied outer electron *d* shell. The electronic configuration of the B-cations, in particular the occupancy of their *d*-orbitals, is highly related to the magnetic properties, as will be described later on. Note that as *d*-states correspond to the orbital angular quantum number $l = 2$, they consist of 5 orbitals, $2l + 1$. In absence of interactions all *d*-states are energetically degenerated. However, in perovskite oxides the surrounding oxygen

octahedron of the B-site splits them into two energy states: high-energetic two e_g orbitals (z^2 and x^2-y^2) and the low-energy three t_{2g} orbitals (xy, xz and yz) [30]. This splitting comes as a consequence of the electrostatic repulsion (note that e_g orbitals point directly toward the oxygen anions, whereas t_{2g} do not), as shown in Fig. 1.6. This effect is known as *crystal field*.

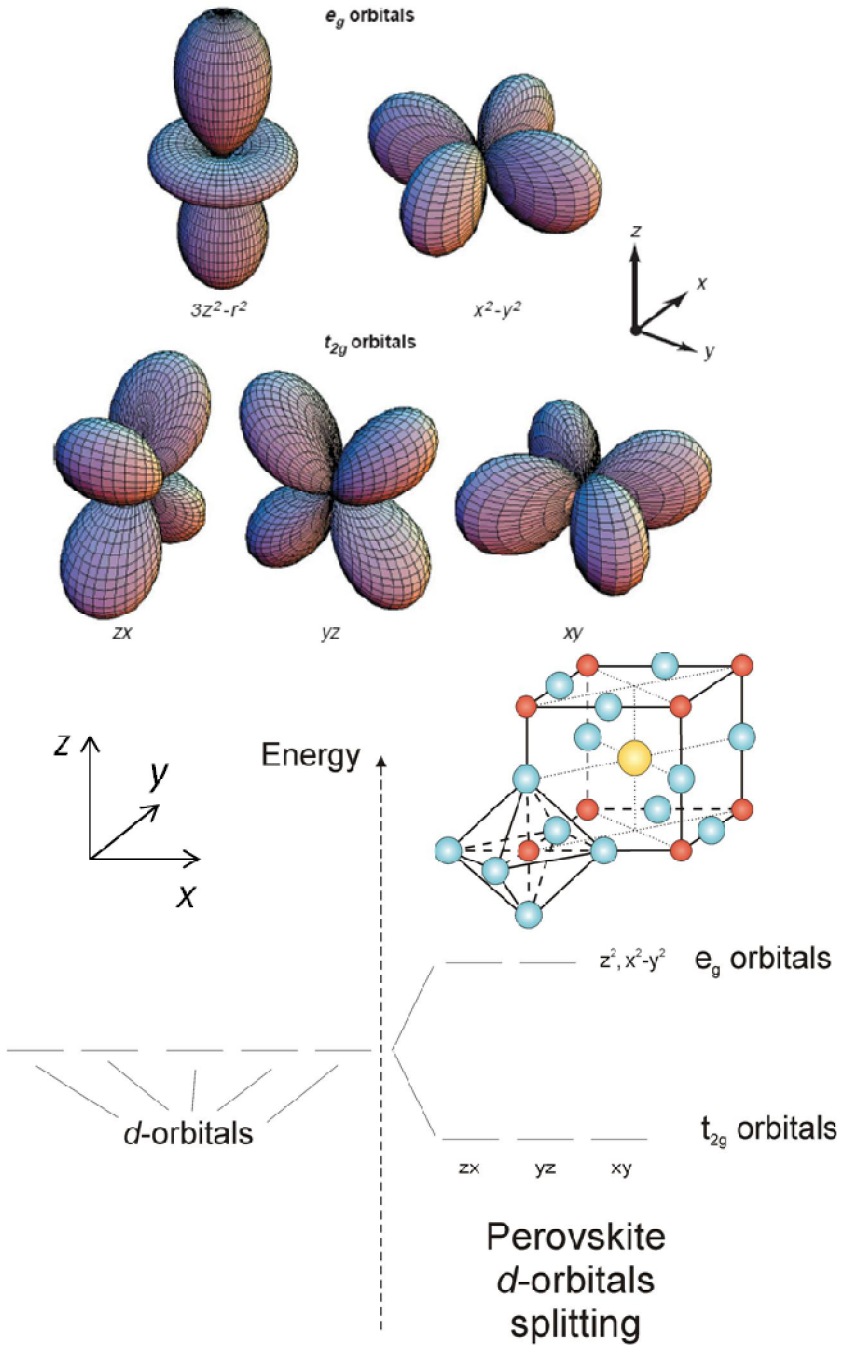

Fig. 1.6 – *Energy splitting of the d-orbitals of a transition metal cation, B, in BO_6 octahedron of ABO_3 perovskite oxide. The d orbital images are reproduced from Ref. [30].*

Unless the crystal field is too strong, electrons in *d*-orbitals are placed as further apart as possible, *i.e.* occupying different *d*-orbitals, so as to minimise their electrostatic repulsion. Moreover, the first *Hund*'s rule states that electrons in *d* orbitals minimize their energy in a parallel spin alignment, *i.e.* the ground state of the magnetic ion has the maximum possible spin *S*.

The magnetic moment of an ion is given by $\vec{m} \sim g_J \mu_B \vec{J}$, where μ_B is the Bohr magneton, g_J is the *Landé g-factor* and $\vec{J}$ is the total angular momentum $\vec{J} = \vec{L} + \vec{S}$ ($\vec{L}$ and $\vec{S}$ are the orbital angular and spin angular momentum, respectively). Yet in transition metal ions, due to the non-degeneration of the *d* states, the orbital angular momentum barely contribute to the magnetic moment of the ion, $\vec{L}$ is said to be 'quenched'. Consequently, the magnetic moment comes almost entirely from the spin angular momentum of the ion, *i.e.* $\vec{m} \sim g_e \mu_B \vec{S}$, where g_e is the dimensionless electron spin g-factor, which is close to 2.

The magnetic interaction between localised spins, $\boldsymbol{S}_i$ (the bold notation denotes vector character), is given by the exchange interaction of Heisenberg model, the Hamiltonian of which is given by $H = -\frac{1}{2}\sum_{ij, i \neq j} J_{ij} \boldsymbol{S}_i \cdot \boldsymbol{S}_j$. Since B-site cation chains in perovskites are interrupted by oxygen anions, direct magnetic exchange is weakened. Magnetic interactions are mediated by the adjacent oxygen ions by the so-called superexchange interaction, involving B – O – B bonds. Whether superexchange interaction is ferromagnetic or antiferromagnetic depends, to a large extent, on the filling of the e_g orbitals according to the Goodenough-Kanamori's (GK) rules [22]. Bearing in mind *(i)* the Pauli's exclusion principle stating that two electrons in the same orbital must possess antiparallel spins, and *(ii)* the Hund's rule stating that electrons in *d* orbitals minimize their energy in a parallel spin alignment, Goodenough-Kanamori's rules can be deduced as following:

a) Either B (empty e_g orbitals) – O – B (empty e_g orbitals) or B (half-filled e_g orbitals) – O – B (half-filled e_g orbitals) give rise to weak and strong antiferromagnetic interactions, respectively [Fig. 1.7(a,b)].

b) B (empty e_g orbitals) – O – B (half-filled e_g orbitals) give rise to ferromagnetic interaction [Fig. 1.7(c)]

Note that these GK rules are deduced in the simplest scenario, *i.e.* in an ideal perovskite where B – O – B bond angle is 180º. Distorted perovskites, rotation of the oxygen octahedral, different B – O – B bond angles, etc, may give rise to different magnetic interactions [22].

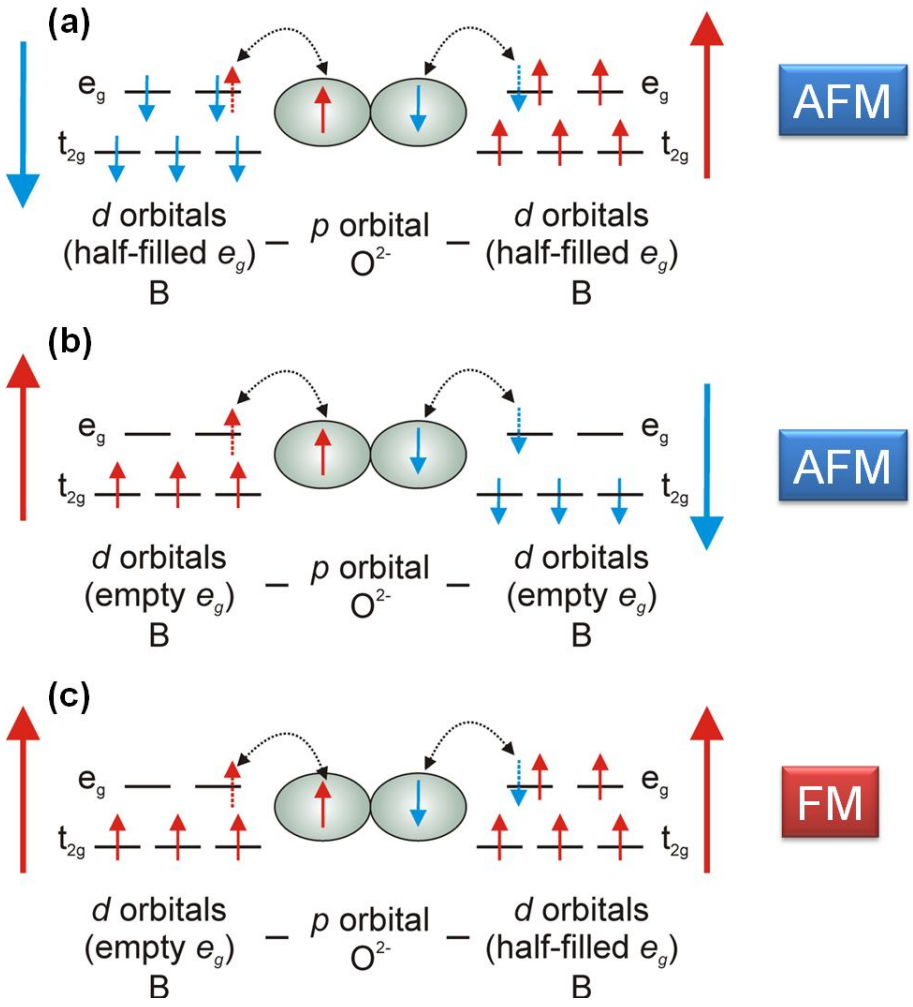

Fig. 1.7 – *Schematic representation of 180º-bond-angle B – O – B superxchange interaction in ABO_3 perovskite. Depending on the occupation of the e_g orbitals, the sign of the magnetic interaction can be antiferromagnetic* **(a, b)** *or ferromagnetic* **(c)**.

As the B-site is occupied by only one kind of ion in perovskite oxides and, in general, with the same oxidation state, *i.e.* having the same e_g orbital filling, antiferromagnetic interactions are much more common than the ferromagnetic ones. For

this reason, most multiferroic $BiBO_3$ are antiferromagnetic. Instead, by combining two different transition metal cations at the B-site, *i.e.* the so-called double perovskites oxides $Bi_2BB'O_6$, ferromagnetic paths can be engineered by choosing appropriately the B, B' magnetic ions, *i.e.* accomplishing B (empty e_g orbitals) – O – B' (half-filled e_g orbitals). But even if it is the antiferromagnetic interactions that dominate in a specific double-perovskite, ferrimagnetism is likely to occur due to the fact that each transition metal ion possesses different magnetic moment (different spin *S*), thus producing net magnetisation because of the non compensation of the magnetic moments. For this reason, Bi-based double perovskite oxides tend to be either ferromagnetic or ferrimagnetic, displaying net magnetization.

1.2.4 The $BiMnO_3$ system

$BiMnO_3$ is a metastable compound, which requires high pressures (ranging from ~3 GPa to ~6 GPa) and relatively high temperatures (~600ºC to 700ºC) to be synthesize as bulk polycrystalline samples [16, 31 – 34]. $BiMnO_3$ was also synthesised in thin film [35 – 39], where the high-pressure requirement for the metastable phase stabilization is replaced by the epitaxial stress imposed by the substrate (see Sect. 1.3).

Temperature	Phase information
> ~770 K	*Pbnm* orthorhombic structure (centrosymmetric)
< ~770 K	Non-centrosymmetric structure, monoclinic *C2* [a_m ~ 9.58 Å, b_m ~ 5.58 Å, c_m ~ 9.75 Å and β ~ 108]
< ~450 K	Non-centrosymmetric structure, monoclinic *C2* [a_m = 9.532 Å, b_m = 5.605 Å, c_m = 9.854 Å and β = 110.7º]
< ~105 K	Spins of Mn^{3+} ions order ferromagnetically

Table 1.3 – *$BiMnO_3$ phases and phase transition temperatures from Ref. [16]*

$BiMnO_3$ would be expected to crystallize in an orthorhombic structure, similar to $LaMnO_3$, as La^{3+} and Bi^{3+} have very similar ionic radii [40]. In contrast, at low temperatures, it crystallizes in a highly distorted non-centrosymmetric monoclinic *C2* structure [31] due to the stereochemical activity of Bi cations [29], with cell parameters: a_m = 9.532 Å, b_m = 5.605 Å, c_m = 9.854 Å and β = 110.7º [31]. 8 formula units, $BiMnO_3$, are contained in the monoclinic unit cell. $BiMnO_3$ can equivalently be described as a triclinic lattice ($a_t \approx c_t \approx 3.935$ Å, $b_t \approx 3.989$ Å, $\alpha \approx \gamma \approx 91.46º$, $\beta \approx 90.96º$)

[34], containing one formula unit. This pseudocubic representation (note that the angles are close to 90º) is usually used regarding $BiMnO_3$ thin films, as will be discussed in chapter 4.

At high temperatures, $BiMnO_3$ undergoes two phase transitions at ~450 K and ~770 K, respectively [16], as listed in table 1.3. The first structural change (~450 K) undergoes from a low temperature non-centrosymmetric monoclinic *C2* structure to a high temperature non-centrosymmetric monoclinic *C2* structure, *i.e.* still allowing ferroelectric order. Instead, the phase transition occurring at ~770 K leads to a centrosymmetric structure (at higher temperatures), corresponding to a *Pbnm* orthorhombic structure, which no longer allows spontaneous polarization.

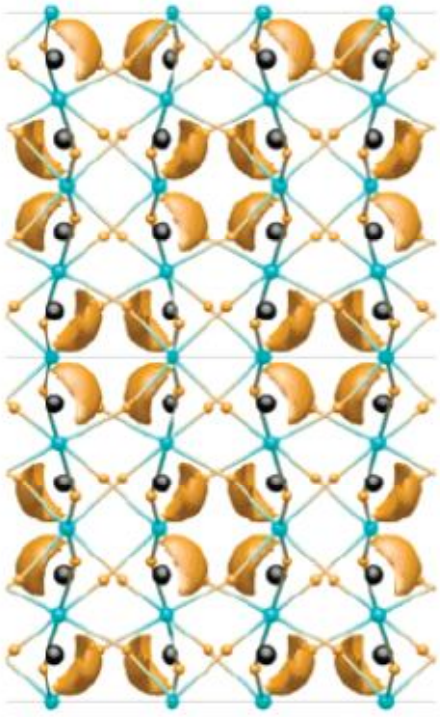

Fig. 1.8 – *Calculated electron localization of the theoretical C2/c structure, where the yellow lobes indicate the lone pair electrons on the Bi cations (indicated as solid black round symbols), reproduced from Ref. [41]. Note that the lone pair dipoles cancel each other.*

Thus, ferroelectricity in $BiMnO_3$ might exist well above room temperature, up to ~770 K, which is usually considered the ferroelectric Curie temperature. Polarization hysteresis loop as a function of the applied electric field were reported for polycrystalline sample, though producing very small remanent polarisation values (of the order of nC/cm^2) [32]. However, some revised analysis of the crystal structure [42, 43] and first principles calculations [41] have questioned the non-centrosymmetric structure of $BiMnO_3$, indicating that the crystal structure is centrosymmetric monoclinic *C2/c* and pointing to an antiparallel arrangement of the electric dipoles of the lone-pair

electrons of Bi^{3+} (Fig. 1.8) [41]. On the other hand, the four-resistive states reported for La-doped $BiMnO_3$ multiferroic tunnel junctions [4] can only be understood in the frame of a ferromagnetic and ferroelectric material, strongly indicating a ferroelectric behaviour of $BiMnO_3$, at least in thin film form. Note that the epitaxial stress (see Sect. 1.3) may modify the structural characteristics and consequently the functional properties. Additionally, nonlinear optical measurements on $BiMnO_3$ thin films have revealed changes in the polar symmetry of second harmonic generation signal by applying electric fields, consistent with changes in the ferroelectric domain structure [44].

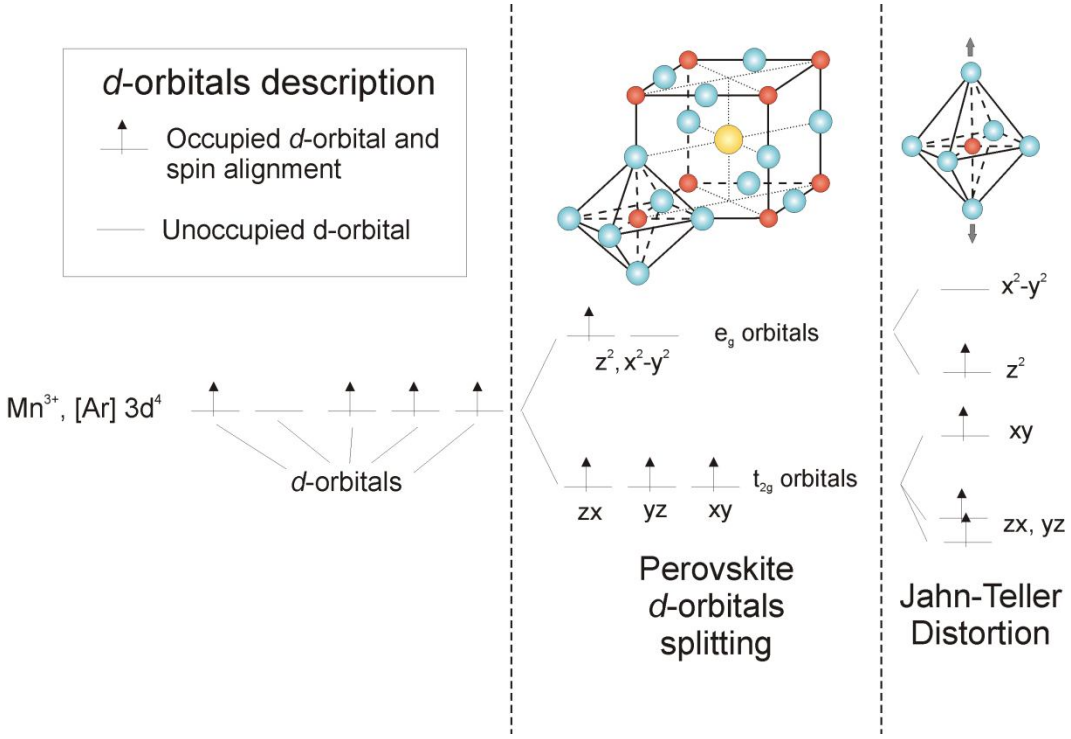

Fig. 1.9 – *Splitting in energy of the d-orbitals of Mn^{3+} due to the MnO_6 octahedron and the further Jahn-Teller distortion.*

The magnetic behaviour of $BiMnO_3$ arises from the magnetic superexchange interaction Mn^{3+} – O – Mn^{3+}. Note that Mn^{3+} is a d^4 transition metal ion. Following the Hund's rule, the four electrons occupy the *d*-orbitals maximising the total spin, as shown in Fig. 1.9, *i.e.* Mn^{3+} *d*-orbital configuration is (t_{2g}^3, e_g^1). The system reduces its energy by slightly elongating the BO_6 octahedron, the so-called Jahn-Teller distortion, as it reduces the Coulomb electrostatic repulsion of the surrounding oxygen anions over the occupied e_g orbital (Fig. 1.9). This distortion is usually found for d^4 and d^9 transition

metal ions in octahedral coordination, which results in the energy splitting of the e_g orbitals: z^2 and x^2-y^2 (it also splits t_{2g} states, which are no longer degenerated).

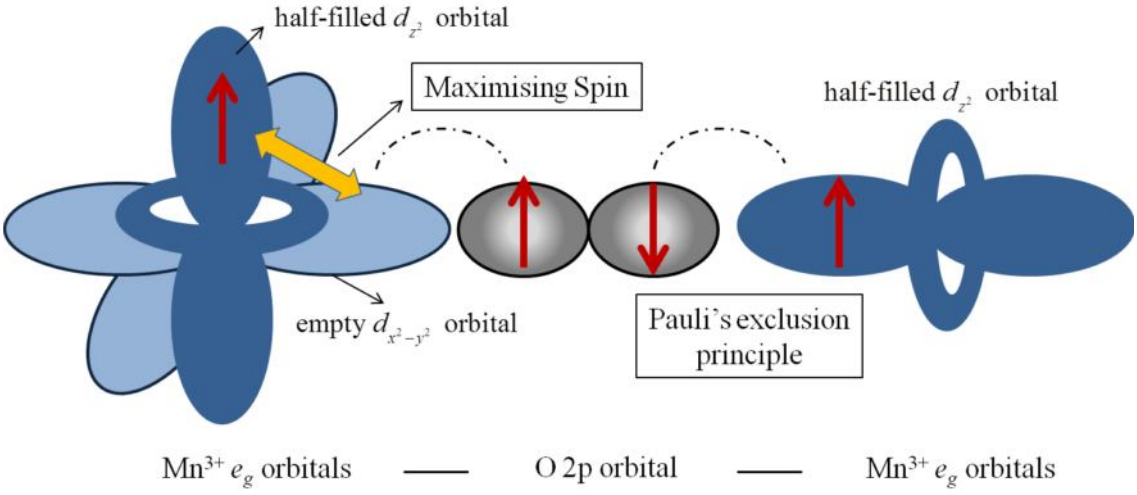

Fig. 1.10 – *Ferromagnetic coupling in $BiMnO_3$*

According to the GK rules (see Fig. 1.7), for an ideal perovskite, Mn^{3+} – O – Mn^{3+} superexchange interaction can be either ferromagnetic or antiferromagnetic, the latter having much higher probability. Indeed, similar compound $LaMnO_3$, being Mn ion also trivalent, is antiferromagnetic. Despite this fact, in $BiMnO_3$ is found that two out of three Mn – O – Mn orbital configuration favour the ferromagnetic interactions (Fig. 1.10), which results in an overall long-range ferromagnetism, overcoming the antiferromagnetic interactions [31]. This orbital ordering has been proposed to be due to the highly distorted monoclinic structure because of the stereochemical active Bi^{3+}. In fact, Mn – O – Mn bond angles are significantly smaller than ideal 180º (between 140º and 160º) [31]. Ferromagnetism in $BiMnO_3$, which orders below 105 K [32], is quite exceptional among insulator single perovskite oxides.

The theoretic magnetic moment of Mn^{3+} (spin S = 2) is 4 μ_B, thus $BiMnO_3$ is expected to show a saturated magnetisation of 4 μ_B/f.u., where f.u. denotes formula unit. Yet the recorded for $BiMnO_3$ bulk samples were slightly smaller, ~3.6 μ_B/f.u. [16], but even lower for thin films [36].

The *p* orbitals of oxygen couple with *d* orbitals of magnetic ions, at the same time form a covalent bond with *p* orbitals of Bi^{3+}. On the other hand, oxygen anions are responsible for the lobe-like distribution of the *lone pair* electrons of Bi^{3+}. Hence, the magnetoelectric coupling between the two ferroic properties in $BiMnO_3$, if it is

produced, is to be produced indirectly. The magnetoelectric properties will be discussed in chapter 4.

1.2.5 The Bi_2NiMnO_6 system

Bi_2NiMnO_6 is double-perovskite oxide, *i.e.* it combines two cations at the B-site in a 3D rock-salt ordered pattern (as described later on). It is a metastable compound, like $BiMnO_3$, and high pressures (6 GPa) as well as relatively high temperatures (~800ºC) were required to synthesize bulk polycrystalline samples [44]. Bi_2NiMnO_6 was also synthesised in thin film [46, 47], where the high-pressure requirement for the metastable phase stabilization is replaced by the epitaxial stress imposed by the substrate (see Sect. 1.3).

Temperature	Phase information
> ~485 K	Centrosymmetric structure, monoclinic $P2_1/c$ [a_m = 5.4041 Å, b_m = 5.5669 Å, c_m = 7.7338 Å and β = 90.184]
< ~485 K	Non-centrosymmetric structure, monoclinic $C2$ [a_m = 9.4646 Å, b_m = 5.4230 Å, c_m = 9.5431 Å and β = 107.8º]
< ~140 K	Spins of Ni^{2+} and Mn^{4+} ions order ferromagnetically

Table 1.4 – *Bi_2NiMnO_6 phases and phase transition temperatures deduced from Ref. [45]*

Similar to $BiMnO_3$, Bi_2NiMnO_6 crystallizes in monoclinic *C2* structure (the lattice parameters are listed in table 1.4), which is non-centrosymmetric and hence allowing spontaneous polarisation. In fact, lattice parameters of Bi_2NiMnO_6 are found to be close to those of $BiMnO_3$. Bi_2NiMnO_6 undergoes a phase transition at ~485 K, above which the structure is indexed as centrosymmetric monoclinic $P2_1/c$ [45]. The occurrence of this phase transition with a dielectric anomaly suggested the ferroelectric transition temperature be placed at that temperature [45] [Fig. 1.11(a)]. It was predicted that a remanent polarisation between ~20 and ~30 μC/cm^2 is to be attained in this compound [45, 48, 49]. However, neither conclusive ferroelectric hysteresis loops nor ferroelectric domain switching current measurements have been reported, probably due to high leakage (more details are found in chapter 5).

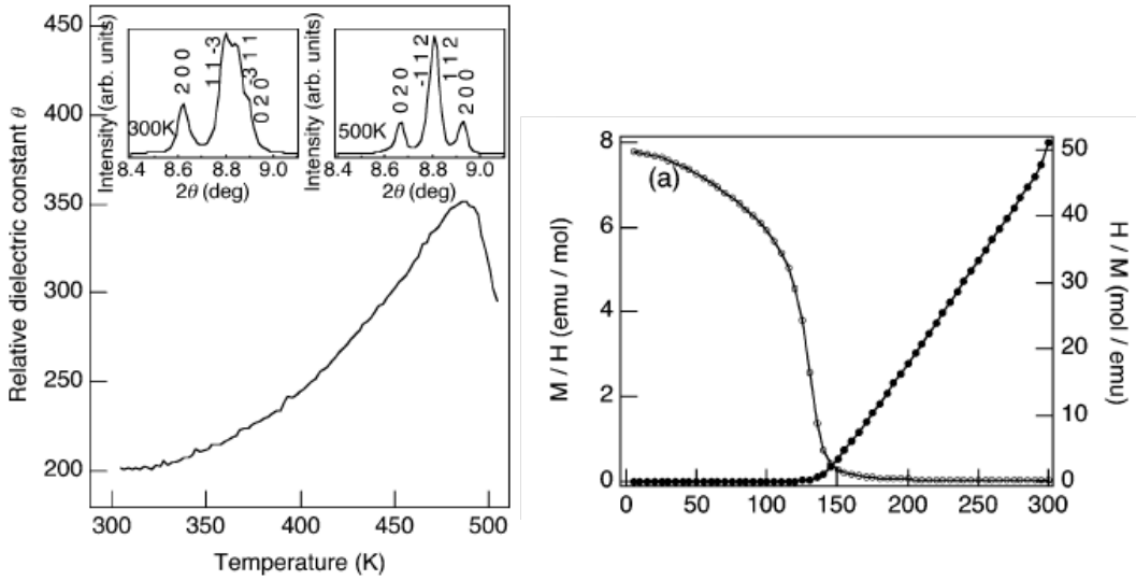

Fig. 1.11 – *Temperature dependence of the dielectric permittivity* **(a)** *and magnetization* **(b)** *of bulk Bi_2NiMnO_6. Reproduced from Ref. [45]*

According to GK rules (Fig. 1.7), for an ideal ferromagnetic coupling, the electronic configuration of Ni and Mn cations should be divalent and tetravalent, respectively, *i.e.* Ni^{2+} (t_{2g}^6, e_g^2) having half-filled e_g orbitals whereas Mn^{4+} (t_{2g}^3, e_g^0) empty e_g orbitals (Fig. 1.12). However, this is a required condition, but not sufficient, for a long-range ferromagnetism in the compound. It is additionally necessary that the first B-cation neighbours of Mn^{4+} should be Ni^{2+} and conversely, *i.e.* it is necessary the alternation of Ni^{2+} and Mn^{4+} cations along the pseudocubic directions of the fundamental perovskite structure, [100], [010] and [001] forming B – O – B' – O – B – O – B' – .... chains of ferromagnetic superexchange interactions (Fig. 1.13). Note that either Ni^{2+} – O – Ni^{2+} or Mn^{4+} – O – Mn^{4+} result in antiferromagnetic superexchange interactions (Fig. 1.7). This specific long-range B-site order is usually called rock-salt configuration of the B-cations, evoking the configuration of Na^{1+} and Cl^{-1} in the rock-salt mineral. For the sake of simplicity, on the following, the term B-site order will refer, exclusively, to this type of ordering.

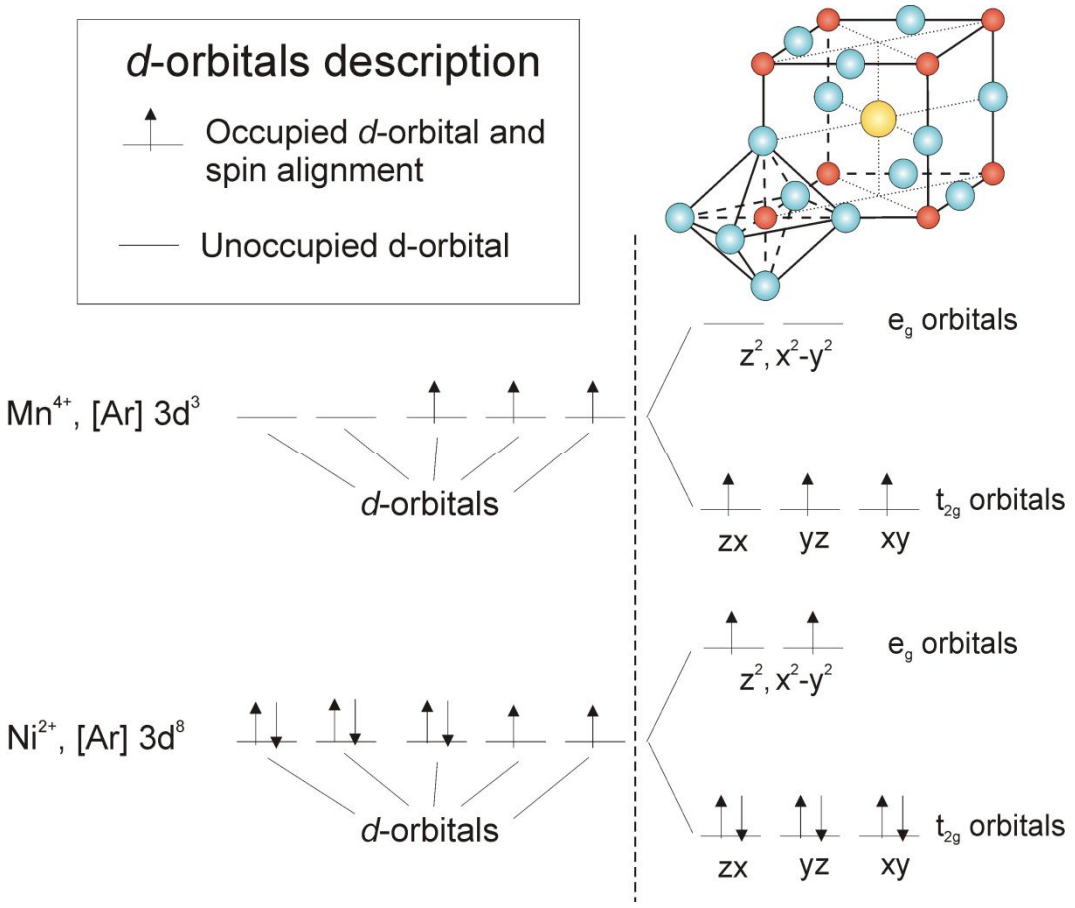

Fig. 1.12 – *Splitting in energy of the d-orbitals of Mn^{4+} and Ni^{2+} in BO_6 octahedron of perovskite oxides.*

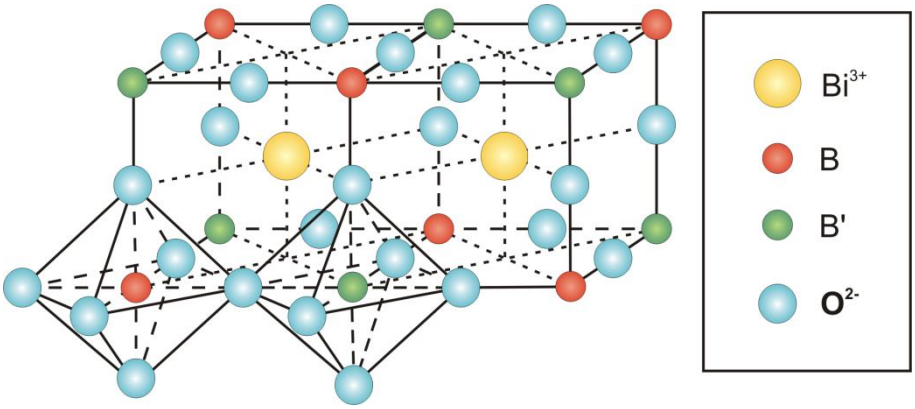

Fig. 1.13 – *Scheme of the double-perovskite structure with long range B-site order in a rock-salt configuration.*

The stability of the B-site order is given, mainly, by two factors:

i) The oxidation state of the B, B' cations. The different oxidation state favours long-range B-site ordering in order to avoid instable regions in the compound of electric disequilibrium. The larger the valence difference, the more stable the B-site order.

ii) The size of the B, B' cations. The larger the difference in the ionic radii of the B cations, the more stable is the B-site order in order to achieve a stable crystal structure.

In Bi_2NiMnO_6, two configurations of the B/B' cations are possible: Ni^{2+}/Mn^{4+} and Ni^{3+}/Mn^{3+}. The former promotes the B-site order, due to both the difference in oxidation state and the difference in ionic radii (0.690 Å and 0.530 Å, respectively, in octahedral coordination [40]). Instead, the latter is hardly expected to be ordered at the B-site on having the same valence and more similar ionic radii: 0.56 Å (or 0.60 Å in the high-spin configuration of Ni^{3+}) and 0.645 Å, respectively, in octahedral coordination [40]).

On the other hand, it is worth noting that even if Ni^{3+}/Mn^{3+} ordering was to occur B-site order, the fact that at least one of the e_g orbitals in both cations is half-filled (in the high-spin configuration of Ni^{3+} two e_g orbitals are half-filled), antiferromagnetic interactions would be much more likely. Additionally, the d^4 electron character of Mn3+ should promote a Jahn-Teller distortion, as described for $BiMnO_3$ (Sect. 1.2.4).

The theoretic magnetic moments of Ni^{2+} (spin S = 1) and Mn^{4+} (spin S = 3/2) are 2 μ_B and 3 μ_B, respectively. Thus, for a configuration Ni^{2+}/Mn^{4+} and long-range B-site order, Bi_2NiMnO_6 is expected to show a saturated magnetisation of 5 μ_B/f.u. According to the reported data [45], Bi_2NiMnO_6 shows a very large saturated magnetization (~4 μ_B/f.u), close to the theoretical value, indicating that it is the Ni^{2+}/Mn^{4+} configuration that prevails and that B-site order is achieved. The Curie temperature was found to be around 140 K (Fig. 1.11 (b)] [45].

The magnetoelectric coupling, if produced, in Bi_2NiMnO_6 should be originated in a similar way to $BiMnO_3$. The magnetoelectric properties will be discussed in chapter 5.

1.2.6 La-doping in Bi_2NiMnO_6 system

In terms of experimental procedures, one of the main drawbacks one find when it comes to synthesising Bi-based multiferroic oxides is the high volatility of Bi element, which entails the use of relatively low temperatures in the synthesis process. Yet the general metastable character of these compounds demands the use of high temperatures to the synthesis process. These two antagonistic requirements greatly hamper the synthesis of Bi-based multiferroic materials [50, 51].

One strategy to diminish the effect of the Bi volatility consists of partial replacement of Bi^{3+} cations by La^{3+} cations at the A-site [51]. La^{3+} and Bi^{3+} cations have very similar ionic radii (0.130 nm and 0.131 nm, respectively [40]), but the former is slightly smaller. Thus, small La-doping gives rise to a slightly reduced unit cell volume, exerting the so-called chemical pressure (equivalently to a negative hydrostatic pressure) which contributes to prevent Bi^{3+} cations from desorption during the growth process in thin films (see Sect. 1.3). Indeed, partial substitution of Bi^{3+} cations by La^{3+} cations has been proved to facilitate single-phase stabilisation in $BiMnO_3$ thin films [51].

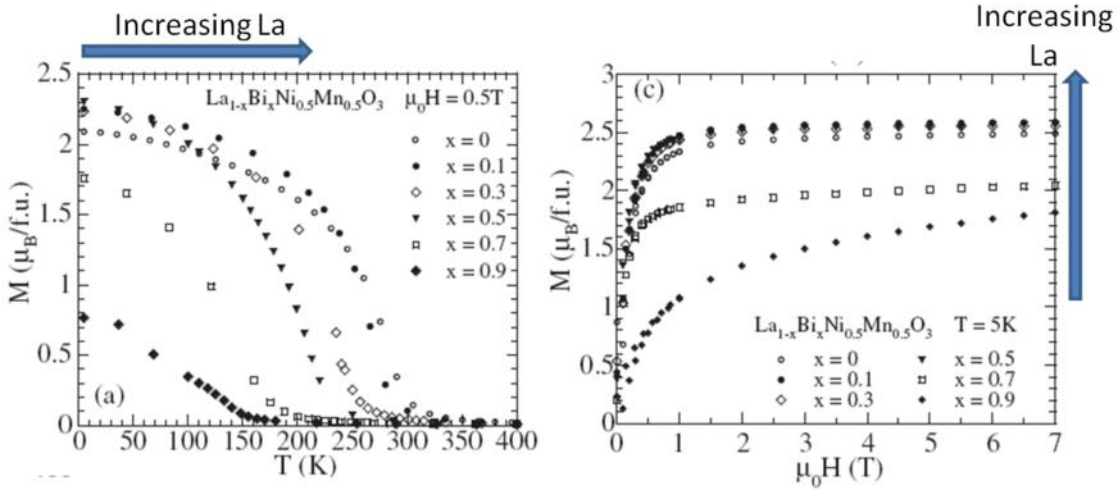

Fig. 1.14 – *Temperature (left) and magnetic field (right) dependence of bulk $(La_{1-x}Bi_x)Ni_{0.5}Mn_{0.5}O_3$ samples reproduced from Ref. [52]).*

On the other hand, the solid solution $(Bi_{1-x}La_x)_2NiMnO_6$ is interesting in itself. Both Bi_2NiMnO_6 and La_2NiMnO_6 compounds display B-site order, giving rise to long range ferromagnetism [45, 53]. Yet the latter show more robust ferromagnetic properties as

the spins order at ~300 K. By increasing La content in $(Bi_{1-x}La_x)_2NiMnO_6$ it is proved to significantly increase the ferromagnetic Curie temperature [52] (Fig. 1.14). Thus, one way to improve the ferromagnetic properties of Bi_2NiMnO_6 might consist of doping it by La.

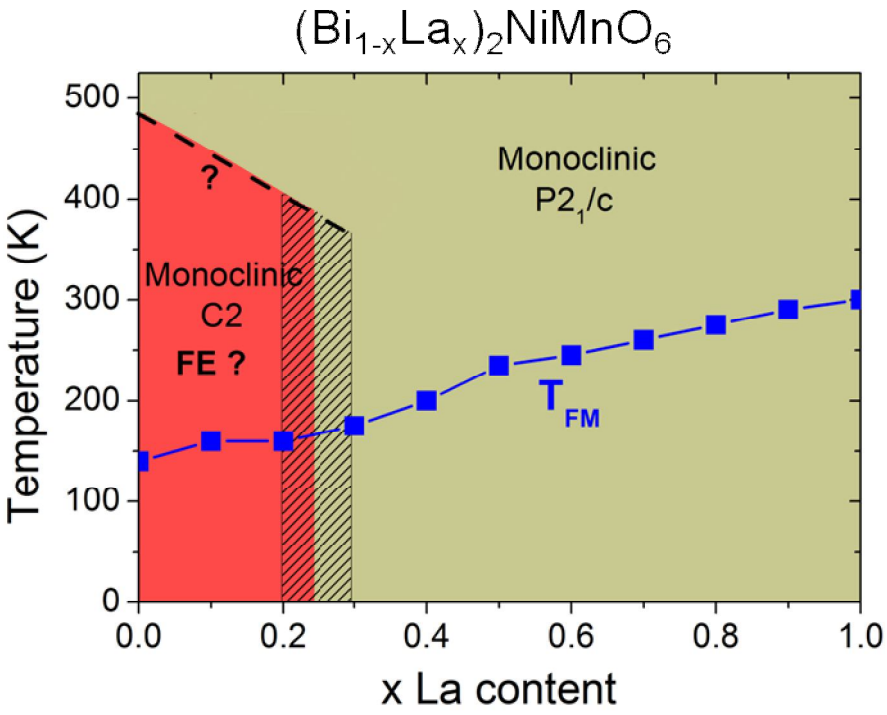

Fig. 1.15 – *Possible phase diagram of solid solution $(Bi_{1-x}La_x)_2NiMnO_6$ deduced from reported data of La_2NiMnO_6, Bi_2NiMnO_6 and $(Bi_{1-x}La_x)_2NiMnO_6$ [45, 52, 53]. Square blue symbols indicate the magnetic Curie temperature as a function of La-content. The dashed region indicates the possible morphotropic phase boundary. The dashed line indicates the possible phase transition temperature.*

The crystal structure of the solid solution $(Bi_{1-x}La_x)_2NiMnO_6$ remains non-centrosymmetric (monoclinic *C*2) for $x \leq 0.2$ [52]. For $x \geq 0.3$ $(Bi_{1-x}La_x)_2NiMnO_6$ can be indexed as centrosymmetric monoclinic $P2_1/c$ [52], which coincides with the crystal structure of the high-temperature paraelectric phase of Bi_2NiMnO_6 (see Sect. 1.2.5). Thus, ferroelectric order can only be enabled for 20% of La substitution, limiting the possibilities of obtaining multiferroicity. In Fig. 1.15 a possible phase diagram of $(Bi_{1-x}La_x)_2NiMnO_6$ is shown. It is to be noted, though, that the ferroelectric character of monoclinic *C*2 phase of Bi_2NiMnO_6 is to be conclusively proved.

Interesting enough, La^{3+} is not a stereochemical active ion, thus not involved in the ferroelectric distortion. Hence, increasingly La-content (up to x ~ 0.2) may monotonously diminish the ferroelectric response of $(Bi_{1-x}La_x)_2NiMnO_6$ and might eventually reduce the ferroelectric Curie temperature. Conversely, La-doping increases the magnetic transition temperature, as seen in Fig. 1.14. Therefore, La-content may also be used to approach both transition temperatures, which, according to expression 1.3, may enable larger magnetoelectric coupling.

1.2.7 State-of-the-art of multiferroic Bi-based perovskite oxides

1.2.7.1 Bi-based perovskite, $BiBO_3$

Almost all $BiBO_3$ perovskite multiferroics are antiferromagnetic, with the unique exception of $BiMnO_3$. Therefore, $BiMnO_3$ may be one of the most prominent multiferroics, together with $BiFeO_3$, which is the only known single phase compound which display multiferroicity at room temperature.

No other multiferroic material has been as more extensively studied than $BiFeO_3$, because its multiferroic properties are robustly maintained well above room temperature. The crystal structure of $BiFeO_3$ is rhombohedral $R3c$ [54], which is a polar group and thus permitting the establishment of ferroelectric order. Indeed, the ferroelectric transition temperature was proved to be very high, T_{FE} = 1103 K, above which a centrosymmetric paraelectric phase with space group $R\bar{3}c$ can be indexed [55]. The polar axis is found along the [111] direction and a large saturated polarization, ~80 – 100 μC/cm^2, is reported as expected for a high-Curie temperature ferroelectric [56]. On the other hand, $BiFeO_3$ has a complicated magnetic behaviour, which is still on debate. It is antiferromagnetic with G-type antiferromagnetic arrangement and a Néel temperature of ≈ 620 K [57]. Additionally, superimposed on the antiferromagnetic order, an incommensurate cycloidal spiral arrangement of the spins with a long period of 620 Å was reported [58]. Moreover, the symmetry of the $BiFeO_3$ structure allows small canting of the spins, which gives rise to a net magnetization in terms of weak

ferromagnetism of the Dzyaloshinski-Moriya type [59]. This weak ferromagnetism was confirmed experimentally, recorded a magnetisation value of around ~0.1 μ_B/f.u [60].

Other Bi-based perovskites have been proposed and proved to be multiferroic, but all of them are antiferromagnetic with only weak ferromagnetism at most. First principles calculations predicted $BiCrO_3$ to be antiferroelectric and antiferromagnetic [61]. Experimental results show weak ferromagnetism (~0.05 μ_B/f.u. saturated magnetization) ordered below ~120 K in bulk [62] and thin film samples [63], but contradictory conclusions were made about whether $BiCrO_3$ is antiferroelectric [64] or ferroelectric [63]. Another potential multiferroic is $BiCoO_3$, which was predicted to crystallize in tetragonal structure with large tetragonality c/a giving rise to huge polarization (~180 $\mu C/cm^2$) [65]. The structure was confirmed by neutron diffraction [66], though the ferroelectric character has not been experimentally confirmed yet. Furthermore, $BiNiO_3$ has been considered, in which, despite being antiferromagnetic, a weak ferromagnetism ordered below 300 K due to the spin canting, which is a consequence of the small Ni – O – Ni bond angles [67]. Due to the preferred Ni^{2+} valence state, $BiNiO_3$ displays an unusual charge disproportionation at the *A*-site of Bi^{3+} – Bi^{5+}. This is quite rare for Bi cations and, in $BiNiO_3$, affects the magnetic symmetry of the compound [67]. Still, there is no experimental evidence of its ferroelectric character and indeed structural analysis reveals $BiNiO_3$ to be centrosymmetric [68].

1.2.7.2 Bi-based double-perovskite, $Bi_2BB'O_6$

Bi-based double-perovskites have been much less studied than their counterpart perovskites. As aforementioned, according to the Goodenough-Kanamori's rules, these oxides have the advantage to allow engineering ferromagnetic paths nearly à la carte, mainly corresponding to B – B' cations being either $d^3 - d^5$ or $d^3 - d^8$, respectively, as long as B – O – B' bond angle is close to 180º [22]. Still, due to the different oxidation states transition metal ions may take, obtaining the desired electronic configuration of B and B' cations has been in general difficult. Moreover, as stated in Sect. 1.2.5, long-range ferromagnetism requires B, B' cations to be ordered alternatively along the fundamental perovskite directions (Fig. 1.13). This has also been proved to be an important challenge. Indeed, among all Bi-based double-perovskites, Bi_2NiMnO_6 is the one confirmed to display rock-salt B-site order.

Bi_2FeMnO_6 is predicted to crystallize in monoclinic *C2* structure [69], but bulk samples are usually indexed as orthorhombic [70]. Both Fe and Mn are found to be mainly in a 3+ valence state, which hinders long-range B-site order [69 – 71]. A hypothetical rock salt configuration would entail either ferromagnetic or more likely antiferromagnetic exchange with a net magnetization of 1 μ_B/f.u. in a ferrimagnetic compound (the magnetic moments of Fe^{3+} and Mn^{3+} are 5 μ_B and 4μ_B, respectively). Yet the recorded magnetization values are much lower, thus confirming the lack of B-site order in this compound [69 – 71]. On the other hand, Bi_2FeMnO_6 was proved to be ferroelectric, displaying a quite large saturated polarization (~30 $\mu C/cm^2$ at 150 K) [72].

Ab initio calculation predicted Bi_2FeCrO_6 to show a large saturated polarization (≈ 80 $\mu C/cm^2$) and a saturated magnetization of 2 μ_B/f.u. for a rock salt configuration of Cr^{3+} and Fe^{3+} [73]. Note that although ferromagnetic superexchange interaction is expected for transition metals in d^3 and d^5 orbital configuration, Fe^{3+} – O – Cr^{3+} was predicted to couple antiferromagnetically [73]. With no compensated magnetic moments (5 μ_B and 3 μ_B for Fe^{3+} and Cr^{3+}, respectively) a net magnetization would be recorded (2 μ_B/f.u.). However, long-range B-site order in Bi_2FeCrO_6 is not likely to occur due to the same charge of Fe^{3+} and Cr^{3+} and the similar ionic radii (0.645 Å and 0.615 Å, respectively [40]). Indeed Bi_2FeCrO_6 is found to exhibit low magnetization (< 0.2 μ_B/f.u.) in both bulk samples [74] and thin films [75]. Nonetheless, some recent experimental results show a certain thickness dependence of the B-site order, pointing out that partially ordering of Fe^{3+} and Cr^{3+} can be improved by decreasing the thickness of Bi_2FeCrO_6 films [76]. The ferroelectric properties were confirmed experimentally, showing the predicted large polarization of ≈60 $\mu C/cm^2$ along [001] direction at ≈ 77 K), which would result in ~100 $\mu C/cm^2$ along the polar axis [111] [75].

To date all Bi containing multiferroic double perovskite oxides consist of 3*d* transition metals occupying the B-site, like Ni, Mn, Fe, ... Recently it was predicted, though, that combining 3*d* and 5*d* transition metals at the B-site in Bi-based double perovskites could allow robust room temperature ferrimagnetism to be attained [77] (which is still a big challenge in multiferroics). In particular, Bi_2NiReO_6 and Bi_2MnReO_6 are expected to order ferrimagnetically below 360 K and 330 K, respectively. Although they would not be ferroelectric in the ground state, the ferroelectric phase is likely to be stabilized in thin films by small percentages of strain

[77]. Still, these materials have not been synthesized so far, hence their predicted multiferroic properties remain to be confirmed experimentally.

A summary of the ferroic properties of reported Bi-based multiferroic perovskite oxides is given in table 1.4

Bi-based magnetic perovskite oxide	Magnetic order	Ferroelectric order	M (T_{FM})	M* ($T_{Néel}$)	P (T_{FE})
$BiMnO_3$	FM	FE	3.6 μ_B/f.u. (105 K)		0.13 $\mu C/cm^2$ (770 K ?)
$BiFeO_3$	AFM	FE		0.1 μ_B/f.u (620 K)	100 $\mu C/cm^2$ (1103 K)
$BiCrO_3$	AFM	?		0.05 μ_B/f.u (120 K)	?
$BiCoO_3$	AFM	[c]FE		? μ_B/f.u (470 K)	[c]180 $\mu C/cm^2$ (? K)
$BiNiO_3$	AFM	×		? μ_B/f.u (300 K)	×
Bi_2NiMnO_6	FM	FE	4.5 μ_B/f.u. (140 K)		[c]20 $\mu C/cm^2$ (485 K)
Bi_2FeMnO_6	AFM[b]	FE		0.7 μ_B/f.u (600 K)	30 $\mu C/cm^2$ (250 K ?)
Bi_2FeCrO_6	AFM[b]	FE		0.2 μ_B/f.u (130 K)	60 $\mu C/cm^2$ (250 K ?)
[a]Bi_2NiReO_6	FiM	×		1 μ_B/f.u (360 K)	×
[a]Bi_2MnReO_6	FiM	×		2 μ_B/f.u (330 K)	×

Table 1.5 – *Summary of the ferroic properties of Bi-based multiferroic perovskite oxides. FM, AFM, FiM, FE stand for ferromagnetic, antiferromagnetic, ferrimagnetic and ferroelectric order. M, M* and P denote the highest recorded value (either in thin film or in bulk) for the magnetisation; magnetisation in AFM compound due to ferrimagnetism, spin canting or other unconventional mechanisms; and polarisation, respectively. T_{FM}, $T_{Néel}$, T_{FE} are the ferromagnetic Curie temperature, the Néel temperature and the ferroelectric Curie temperature. [a]Predicted multiferroic material (not synthesised yet). [b]No B-site order is found. [c]Predicted remanent polarisation or predicted ferroelectric order.*

1.3 Epitaxial engineering

In terms of device fabrication and applications, it is obvious that synthesising nanometric-thick films of functional materials (such as multiferroics) shows greater advantages than macroscopic bulk specimens, as many devices, like tunnel junctions, spin valves, thin film transistors, etc, are based on multilayer structures. Moreover, their functional properties are generally enabled (or enhanced) when films behave like single crystal. Hence, thin films are in general grown on a single crystal substrate with the aim of forming the so-called epitaxial film (Fig. 1.16), *i.e.* they grow crystalline with a preferred out-of-plane (perpendicular to the interface substrate-film) crystal orientation of the film unit cells (out-of-plane textured) and by maintaining the same relationship of the in-plain (contained at the interface) crystal orientations of the film unit cells with regard to the crystal orientations of the underlying substrate (in-plane textured). Note that Fig. 1.16 depicts one specific case of epitaxy as, in the aforementioned definition, the in-plane lattice parameter of the film and that of the substrate do not have to be identical, nor do the crystal directions of the film unit cells be following those of the substrate, but they should keep the same relationship with regard to those of the substrate.

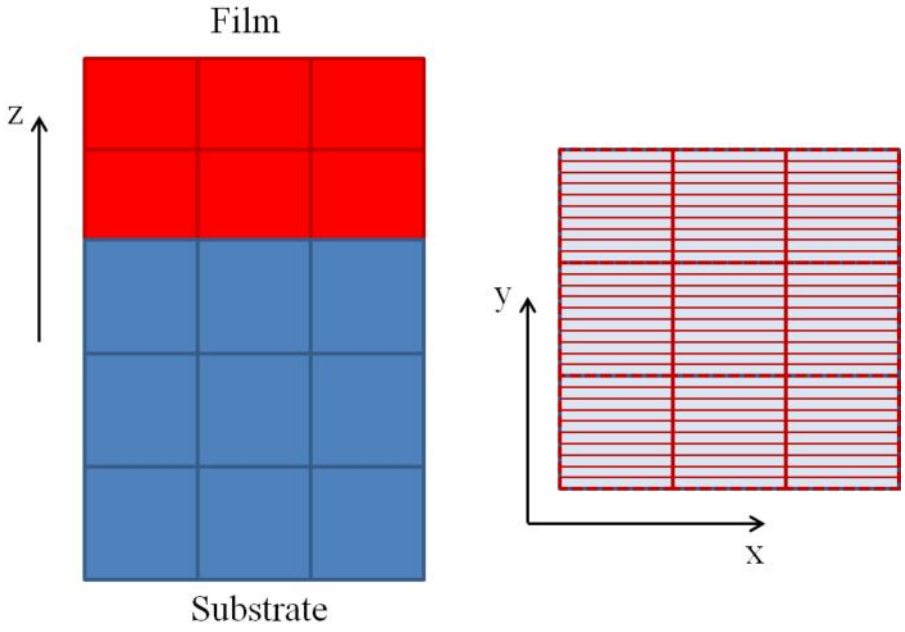

Fig. 1.16 – *Cross section (left) and top view (right) of an epitaxial thin film.*

This section aims to describe the possibilities that growing thin films offer regarding the bulk specimens in terms of physical properties and crystal structure stabilisation.

1.3.1 Stabilisation of metastable compounds

The work shown in this thesis is focused on $BiMnO_3$ and $(Bi_{0.9}La_{0.1})_2NiMnO_6$ thin films, as will be commented in Sect. 1.4. In ternary Bi – Mn – O or the quaternary Bi – Mn – Ni – O system, the different Bi, Mn and Ni oxides (such as Bi_2O_3, Mn_2O_3 or NiO), individually, are much more stable than the complex compound either $BiMnO_3$ or Bi_2NiMnO_6, thus requiring high pressures (~3 GPa – ~6 Gpa) to be synthesised.

However, preparing these compounds in thin film on a single crystal used as a substrate can ease this process, circumventing the high-pressure requirement, what is called epitaxial stabilisation or stabilisation by epitaxial stress. Two main factors favour the stabilisation of metastable compounds in thin films: (*i*) the use of lattice-matched substrates, *i.e.* with similar lattice parameters to those of the compound that is to be formed; (*ii*) the use of substrates with similar structure, *i.e.* with similar arrangement of the ions to that of the compound to be formed, *e.g.* perovskite structure. Accomplishing both criterions epitaxial thin films tend to be formed (Fig. 1.16).

To date, bulk specimens of $BiMnO_3$, $(Bi_{0.9}La_{0.1})_2NiMnO_6$ and Bi_2NiMnO_6 were all polycrystalline structures. Thus, similar to a single crystal behaviour might be obtained just by growing epitaxial thin films.

1.3.2 Epitaxial tuning

Epitaxial thin films might be grown strained on the substrate, which means that the in-plane lattice parameter of film adopts the lattice parameter of the substrate (Fig. 1.17), the so-called coherent growth. The strain of the film is usually defined as:

$$\varepsilon = \frac{a_{film} - a_{bulk}}{a_{bulk}} \tag{1.7}$$

where a_{bulk} is the free-standing lattice parameter of bulk material, whereas a_{film} is the in-plane lattice parameter of the film. Unit cell volume tends to be maintained in crystalline materials, which entails an enlargement or a contraction of the out-of-plane lattice parameter when the in-plane lattice parameter is compressive or tensile strained, respectively (Fig. 1.17).

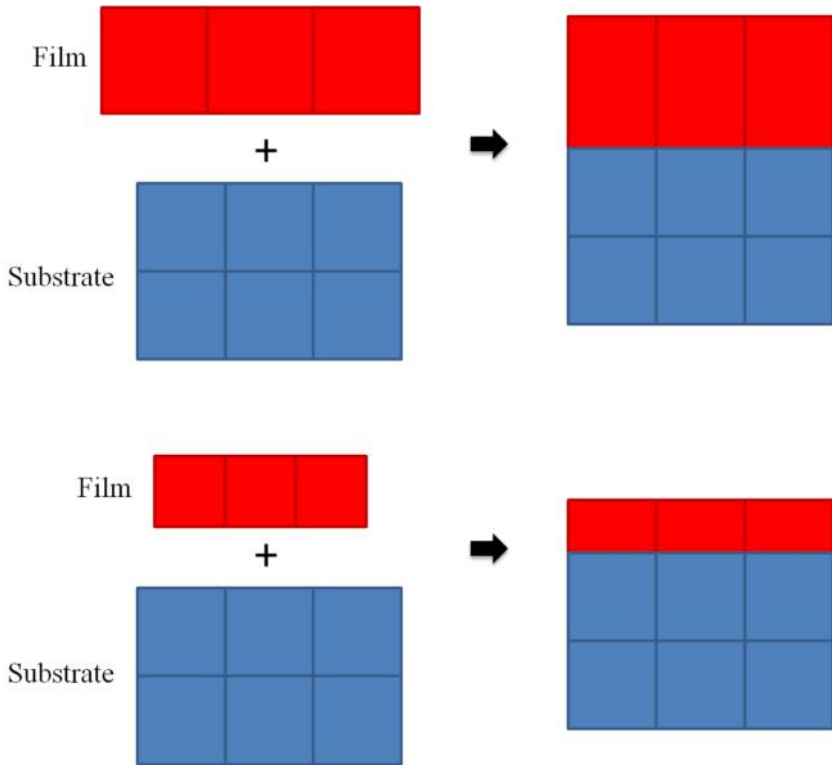

Fig. 1.17 – *Growth of strained thin films*

Strain, though, leads to stress in the material, with an energy cost. This energy cost increases on increasing thickness, up to the point where it becomes energetically more favourable to release the strain (by means of the formation of dislocations [78], crystallographic domains [79] or even changing sample stoichiometry [80 - 82]). This results in a relaxation of the film, *i.e.* recovering the bulk lattice parameter. A film is said to be fully relaxed when its structure is identical to that of the bulk.

The constraints imposed by the substrate forces in-plane lattice parameters to be fixed, apart from modifying it. Note that a cubic crystal structure of the substrate may induce a tetragonal-like structure of the film in materials that not necessarily are tetragonal. As a result the crystal structure and the crystal symmetry of the film may severely change with regard to bulk specimens, and consequently the physical properties.

Interesting enough is the effect epitaxial stress may produce on magnetic and ferroelectric properties of Bi-based multiferroic thin films. Indeed, the phase diagram of ferroelectric epitaxial thin films is noticeable modified as a function of strain [83 – 87]. In particular, $BaTiO_3$ thin films show a strongly strain-dependent Curie temperature [85]. But magnetic properties have also been reported to be altered, such as the reduced Curie temperature of strained Bi_2NiMnO_6 thin films grown on $SrTiO_3$ (~100 K) [46].

1.4 Outline of the thesis

This thesis aims to characterise the structural and functional properties of the ferromagnetic Bi-based multiferroics, which, up to now reported, consist of $BiMnO_3$ and Bi_2NiMnO_6 (see table 1.5). Specifically, this work is focused on the growth and characterisation of $BiMnO_3$ and $(Bi_{0.9}La_{0.1})_2NiMnO_6$ thin films. The use of La-doping is motivated by the reasons exposed in Sect. 1.2.6.

The films were grown by pulsed laser deposition (Sect. 2.1) onto single-crystal substrates $SrTiO_3$, (001)-oriented (*i.e.* with the [001] crystallographic direction lying along the out-of-plane direction).

Chapter 2 describes the physical mechanisms of both the thin film growth process and the experimental techniques and tools used to characterise the films.

Chapter 3 is focused on the ferroelectric measurements, dielectric/resistive and magnetoelectric measurements. For these electric measurements parallel-plate capacitors are fabricated, using Nb doped $SrTiO_3$ as a bottom electrode and Pt as a top electrode. Special attention is given to the conventional artefacts these measurements

often produce when performed on thin films. In particular, different simulations are carried out considering the different source of these artefacts.

In **Chapter 4** results of $BiMnO_3$ thin films are shown. In particular, it is determined the deposition conditions which enable stabilising single-phase formation. This has turned out an elusive task due to the multi-phase tendency of these compounds and the high volatility of Bi. A compositional study is carried out which enable to relate the multiphase tendency with the Bi-deficiency. Structural study proves single-phase $BiMnO_3$ thin films grow fully coherent on $SrTiO_3$ substrates, adopting a tetragonal-like structure. The growth mode, though, is found, at any event, three-dimensional (3D). Finally the ferromagnetic character is borne out and the electric/magnetoelectric properties extracted following the precautions stated in chapter 3, demonstrating a weak magnetoelectric coupling of these materials.

In **Chapter 5** results of $(Bi_{0.9}La_{0.1})_2NiMnO_6$ thin films are shown. Similar to $BiMnO_3$, these double-perovskite films show a multiphase tendency, although in a lesser extent probably due to the La-doping. Fully coherent growth on $SrTiO_3$ substrates is also found, adopting a tetragonal-like structure. Unlike $BiMnO_3$, $(Bi_{0.9}La_{0.1})_2NiMnO_6$ thin films grow in 2D mode, up to a critical thickness, which enable very flat surfaces. Importantly enough for the magnetic properties, $(Bi_{0.9}La_{0.1})_2NiMnO_6$ thin films are found to display long-range B-site order and the Ni^{2+}/Mn^{4+} electronic configuration, which gives as a result long-range ferromagnetism, but with a reduced Curie temperature compared to bulk data. The ferroelectric domains switching current is measured, which allows conclusively stating that $(Bi,La)_2NiMnO_6$ compounds are indeed ferroelectric up to at least 10% La content. Nonetheless, the coupling of the ferromagnetic and ferroelectric order was also proved to be weak.

References

[1] W. Eerenstein, N. D. Mathur and J. F. Scott, Nature **442** 759 (2006)

[2] B. B. Van Aken, J. Rivera, H. Schmid and M. Fiebig, Nature **449** 702 (2007)

[3] N. A. Spaldin and M. Fiebig, Science **309** 391 (2005)

[4] M. Gajek, M. Bibes, S. Fusil, K. Bouzehouane, J. Fontcuberta, A. Barthélémy and A. Fert, Nat. Mater. **6** 296 (2007)

[5] S. Ju, T. Cai, G. Guo and Z. Li, Phys. Rev. B **75** 064419 (2007)

[6] J. F. Scott, Nat. Mater. **6** 256 (2007)

[7] F. Yang, M. H. Tang, Z. Ye, Y. C. Zhou, X. J. Zheng, J. X. Tang, J. J. Zhang and J. He, J. Appl. Phys. **102** 044504 (2007)

[8] H. Béa, M. Gajek, M. Bibes and A. Barthélémy, J. Phys.: Condens. Matter. **20** 434221 (2008).

[9] G. A. Prinz, J. Mag. Mag. Mat. **200** 57 (1999)

[10] K. F. Wang, J. –M. Liu and Z. F. Ren, Adv. Phys. **58** 321 (2009)

[11] L. W. Martin, Y. –H. Chu and R. Ramesh, Mat. Sci. Eng. R **68** 89 (2010)

[12] N. A. Sapldin, S.-W. Cheong and R. Ramesh, PHYSICS TODAY, october 2010, page 38

[13] R.E. Newnham, *Properties of Materials. Anisotropy, Symmetry, Structure* (Oxford University Press, 2005)

[14] M. Fiebig, J. Phys. D: Appl. Phys. **38** R123 (2005)

[15] W. F. Brown, R. M. Hornreich, S. Shtrikman, Phys. Rev. **168** 574 (1968)

[16] T. Kimura, S. Kawamoto, I. Yamada, M. Azuma, M. Takano and Y. Tokura, Phys. Rev. B **67** 180401 (2003)

[17] J. Hemberger, P. Lunkenheimer, R. Ficht, H.-A. Krug von Nidda, V. Tsurkan, and A. Loidl, Nature **434**, 364 (2005)

[18] M. P. Singh, W. Prellier, Ch. Simon, and B. Raveau, Appl. Phys. Lett. **87**, 22505 (2005)

[19] P. Padhan, P. LeClair, A. Gupta and G. Srinivasan, J. Phys.: Cond. Mat. **20**, 355003 (2008).

[20] N. A. Hill, J. Phys. Chem. B **104** 6694 (2000)

[21] H. Schmid, J. Phys.: Condens. Matter **20** 434201 (2008)

[22] J. B. Goodenough, *Magnetism and the Chemical Bond* (R. E. Krieger Pub. Co., Huntington, NY, 1976).

[23] D. Khomskii, Physics, **2** 20 (2009)

[24] T. Kimura, G. Lawes, T. Goto, Y. Tokura, A. P. Ramirez, Phys. Rev. B **71** 224425 (2005)

[25] J. van den Brink, D. I. Khomskii, J. Phys.: Cond. Matter **20** 434217 (2008)

[26] B. B. van Aken, T. T. M. Palstra, A. Filippetti, N. A. Spaldin, Nat. Mater. **3** 164 (2004)

[27] J. Wang *et al.*, Science **299** 1719 (2003).

[28] J. H. Lee, L. Fang, E. Vlahos, X. Ke, Y. W. Jung, L. F. Kourkoutis, J.-W. Kim, P. J. Ryan, T. Heeg, M. Roeckerath, *et al.*, Nature **466** 954 (2010).

[29] R. Seshadri and N. A. Hill, Chem. Mater. **13** 2892 (2001)

[30] Y. Tokura and N. Nagaosa, Science **288** 462 (2000)

[31] T. Atou, H. Chiba, K. Ohoyama, Y. Yamaguchi and Y. Syono, J. Sol. State Chem. **145** 639 (1999)

[32] A. Moreira dos Santos, S. Parashar, A. R. Raju, Y. S. Zhao, A. K. Cheetham and C. N. R. Rao, Sol. State. Comm. **122** 49 (2002)

[33] Z. H. Chi, C. J. Xiao, S. M. Feng, F. Y. Li and C. Q. Jin, J. Appl. Phys. **98** 103519 (2005)

[34] E. Montanari, L. Righi, G. Calestani, A. Migliore, E. Gilioli and F. Bolzon, Chem. Mater. **17** 1765 (2005).

[35] A. Moreira dos Santos, A. K. Cheetham, W. Tian. X. Pan, Y. Jia, N. J. Murphy, J. Lettieri and D. G. Scholm, Appl. Phys. Lett. **84** 91 (2004)

[36] M. Gajek, M. Bibes, A. Barthélémy, K. Bouzehouane, S. Fusil, M. Varela, J. Fontcuberta and A. Fert, Phys. Rev. B **72** 020406 (2005)

[37] W. Eerenstein, F. D. Morrison, J. F. Scott and N. D. Mathur, Appl. Phys. Lett. **87** 101906 (2005)

[38] C. H. Yang, T. Y. Koo, S. H. Lee, C. Song, K. B. Lee and Y. H. Jeong, Europhys. Lett. **74** 348 (2006).

[39] S. Fujino, M. Murakami, S. –H. Lim, L. G. Salamanca-Riba, M. Wuttig and I. Takeuchi, J. Appl. Phys. **101** 013903 (2007)

[40] R. D. Shannon, Acta Cryst. **A32** 751 (1976)

[41] P. Baettig, R. Seshadri and N. A. Spaldin, J. Am. Chem. Soc. **129** 9854 (2007)

[42] A. A. Belik *et al.*, J. Am. Chem. Soc. **128** 706 (2006)

[43] T. Yokosawa, A. A. Belik, T. Asaka, K. Kimoto, E. Takayama-Muromachi and Y. Matsui, Phys. Rev. B **77** 024111 (2008)

[44] A. Sharan, J. Lettieri, Y. Jia, W. Tian, X. Pan, D. G. Scholm and V. Gopalan, Phys. Rev. B **69** 214109 (2004)

[45] M. Azuma, K. Takata, T. Saito, S. Ishiwata, Y. Shimikawa and M. Takano, J. Am. Chem. Soc. **127** 8889 (2005)

[46] M. Sakai, A. Masuno, D. Kan, M. Hashisaka, K. Takata, M. Azuma, M. Takano and Y. Shimikawa, Appl. Phys. Lett. **90** 072903 (2007)

[47] P. Padhan, P. LeClair, A. Gupta and G. Srinivasan, J. Phys.: Cond. Matter **20** 355003 (2008)

[48] Y. Uratani, T. Shishidou, F. Ishii and T. Oguchi, Physica B **383** 9 (2006)

[49] A. Ciucivara, B. Sahu and L. Kleinman, Phys. Rev. B **76** 064412 (2007)

[50] S. Fujino, M. Murakami, S. –H. Lim, L. G. Salamanca-Riba, M. Wuttig and I. Takeuchi, J. Appl. Phys. **101** 013903 (2007)

[51] M. Gajek, M. Bibes, F. Wyczisk, M. Varela, J. Fontcuberta, A. Barthélémy, Phys. Rev. B **75** 174417 (2007)

[52] Y. Kobayashi, M. Shiozawa, K. Sato, K. Abe and K. Asai, J. Phys. Soc. Jpn **77** 084701 (2008)

[53] N. S. Rogado, J. Li, A. W. Sleight, and M. A. Subramanian, Adv. Mater. **17** 2225 (2005).

[54] F. Kubel and H. Schmid, Acta Cryst. **B46** 698 (1990)

[55] S. M. Selbach, T. Tybell, M. Einarsrud and T. Grande, Adv. Mater. **20** 3692 (2008)

[56] J. Wang *et al.*, Science **299** 1719 (2003)

[57] P. Fischer, M. Polomska, I. Sosnowaska and M. Szymánski, J. Phys. C: Solid State Phys. **13** 1931 (1980)

[58] I. Sosnowska, T. Peterlin-Neumaier and E. Steichele, J. Phys. C: Solid State Phys. **15** 4835 (1982)

[59] C. Ederer and N. A. Spaldin, Phys. Rev. B **71** 060401(R) (2005)

[60] W. Eerenstein, F. D. Morrison, J. Dho, M. G. Blamire, J. F. Scott, N. D. Mathur, Science **307** 1203a (2005)

[61] N. A. Hill, P. Baettig and C. Daul, J. Phys. Chem. B **106** 3383 (2002)

[62] S. Niitaka, M. Azuma, M. Takano, E. Nishibori, M. Takata and M. Sakata, Solid State Ionics **172** 557 (2004)

[63] M. Murakami, S. Fujino, S. –H. Lim, C. J. Long, L. G. Salamanca-Riba, M. Wuttig, I. Takeuchi, V. Nagarajan and A. Varatharajan, Appl. Phys. Lett. **88** 152902 (2006)

[64] D. H. Kim, H. N. Lee, M. Varela and H. M. Christen, Appl. Phys. Lett. **89** 162904 (2006)

[65] Y. Urantani, T. Shishidou, F. Ishii and T. Oguchi, Jpn. J. Appl. Phys. **44** 7130 (2005)

[66] A. A. Belik *et al.*, Chem. Mater. **18** 798 (2006)

[67] S. Ishiwata, M. Azuma, M. Takano, E. Nishibori, M. Takata, M. Sakata and K. Kato, J. Mater. Chem. **12** 3733 (2002)

[68] S. J. E. Carlsson, M. Azuma, Y. Shimikawa, M. Takano, A. Hewat, J. P. Attfield, J. Sol. State Chem. **181** 611 (2008)

[69] L. Bi, A. R. Taussig, H. Kim, L. Wang, G. F. Dionne, D. Bono, K. Persson, G. Ceder and C. A. Ross, Phys. Rev. B **78** 104106 (2008)

[70] P. Mandal *et al.*, Phys. Rev. B **82** 100416(R) (2010)

[71] E. –M. Choi, S. Patnaik, E. Weal, S. –L. Sahonta, H. Wang, Z. Bi, J. Xiong, M. G. Blamire, Q. X. Jia and J. L. MacManus-Driscoll, Appl. Phys. Lett. **98** 01250 (2011)

[72] J. Miao, X. Zhang, Q. Zhan, Y. Jiang and K. –H. Chew, Appl. Phys. Lett. **99** 062905 (2011)

[73] P. Baettig and N. A. Spaldin, Appl. Phys. Lett. **86** 012505 (2005)

[74] M. R. Suchomel, C. I. Thomas, M. Allix, M. J. Rosseinsky, A. M. Fogg, M. F. Thomas, Appl. Phys. Lett. **90** 112909 (2007)

[75] D. H. Kim, H. N. Lee, M. D. Biegalski, H. M. Christen, Appl. Phys. Lett. **91** 042906 (2007)

[76] R. Nechache, C. Harnagea, A. Pignolet, J. Phys.: Condens. Matter **24** 096001 (2012)

[77] M. Lezaic and N. A. Spaldin, Phys. Rev. B **83** 024410 (2011)

[78] J. W. Matthews and A. E. Blakeslee, J. Cryst. Growth **27** 118 (1974).

[79] W. Pompe, X. Gong, Z. Suo, and J. S. Speck, J. Appl. Phys. **74** 6012 (1993).

[80] S. Estradé, J. Arbiol, F. Peiró, Ll. Abad, V. Laukhin, Ll. Balcells and B. Martínez, Appl. Phys. Lett. **91** 252503 (2007).

[81] S. Estradé, J. Arbiol, F. Peiró, I. C. Infante, F. Sánchez, J. Fontcuberta, F. de la Peña, M. Walls, C. Colliex, Appl. Phys. Lett. **93** 112505 (2008).

[82] S. Estradé, J. M. Rebled, J. Arbiol, F. Peiró, I. C. Infante, G. Herranz, F. Sánchez, J. Fontcuberta, R. Córdoba, B. G. Mendis and A. L. Bleloch, Appl. Phys. Lett. **95** 072507 (2009).

[83] N. A. Perstev and B. Dkhil, Appl. Phys. Lett. **93** 122903 (2008).

[84] Z. Chen, Z. Luo, C. Huang, Y. Qi, P. Yang, L. You, C. Hu, T. Wu, J.Wang, C. Gao et al., Adv. Funct. Mater. **21** 133 (2011).

[85] K. J. Choi, M. Biegalski, Y. L. Li, A. Sharan, J. Schubert, R. Uecker, P.Reiche, Y. B. Chen, X. Q. Pan, V. Gopalan et al., Science **306** 1005 (2004).

[86] I. C. Infante, S. Lisenkov, B. Dupé, M. Bibes, S. Fusil, E. Jacquet, G. Geneste,S. Petit, A. Courtial, J. Juraszeck et al., Phys. Rev. Lett. **105** 057601 (2010).

[87] A. Sambri, S. Gariglio, A. T. Pardo, J.-M. Triscone, O. Stéphan, J. W.Reiner, and C. H. Ahn, Appl. Phys. Lett. **98** 012903 (2011).

Chapter 2

Experimental Techniques and Data Analysis

2.1 Growth Techniques

2.1.1 Pulsed Laser Deposition

$BiMnO_3$ and $(Bi,La)_2NiMnO_6$ thin films were grown by Pulsed Laser Deposition (PLD). The system equipment is placed in the *Departament de Física Aplicada i Òptica (Facultat de Física, University of Barcelona)* in the research group of *Grup d'Estructures en Capa Fina per a l'Espintrònica (GECFE)*.

PLD, the process of which is schematically depicted in Fig. 2.1, belongs to the set of Physical Vapour Deposition techniques [1 - 3]. An intense ultraviolet laser pulse is focused by means of external lens onto a bulk piece –called the target–, placed inside a high vacuum chamber, which contains the oxide mixture with the desired composition of the compound to be studied (see target fabrication 2.1.3). The relatively high energy of the laser pulse concentrated on a small area (typically 1 – 3 J/cm^2) in a short period of time (around a few tens of nanoseconds) leads the material of the target to be ejected, forming a high-energetic plasma (called 'plume'). In the near-vacuum the ablated material expands to the substrate which is located in front of the target, at a few centimetres away. The film is formed pulse after pulse as the ejected material is condensed on the relatively cold substrate. The plume of the ejected material is very directional, as $\cos^n\varphi$ ($8 < n < 12$) [1 - 3], which prevents large areas from being uniformly covered.

High energy photons are used, in the ultraviolet range, as the absorption coefficients of most non-metallic materials tend to increase the shorter the wavelength of the photon is. That makes the ablation process take place only in the very near surface of the target, avoiding heating large volumes of the target by the laser pulses and promoting a high energy transfer. There is a threshold in the so-called fluency, *i.e.* the energy per area of the coming laser pulses onto the target, from which the absorbed energy is higher than that needed for material emission. Thus, above the ablation threshold, the emission process is not controlled by the vapour pressure of the target species and, consequently, the ejected material preserves the stoichiometry of the target. For this reason PLD has been widely used to grow complex multi-cation oxide compounds such as

superconducting materials like $YBa_2Cu_3O_7$ [4], ferroelectric materials like $BaTiO_3$ [5] and magnetic materials like $(La,Sr)MnO_3$ [6]. Very often O_2 is introduced for oxides growth in order to compensate for oxygen desorption from the growing film during the deposition process and hence achieve the right oxidation state of the cations.

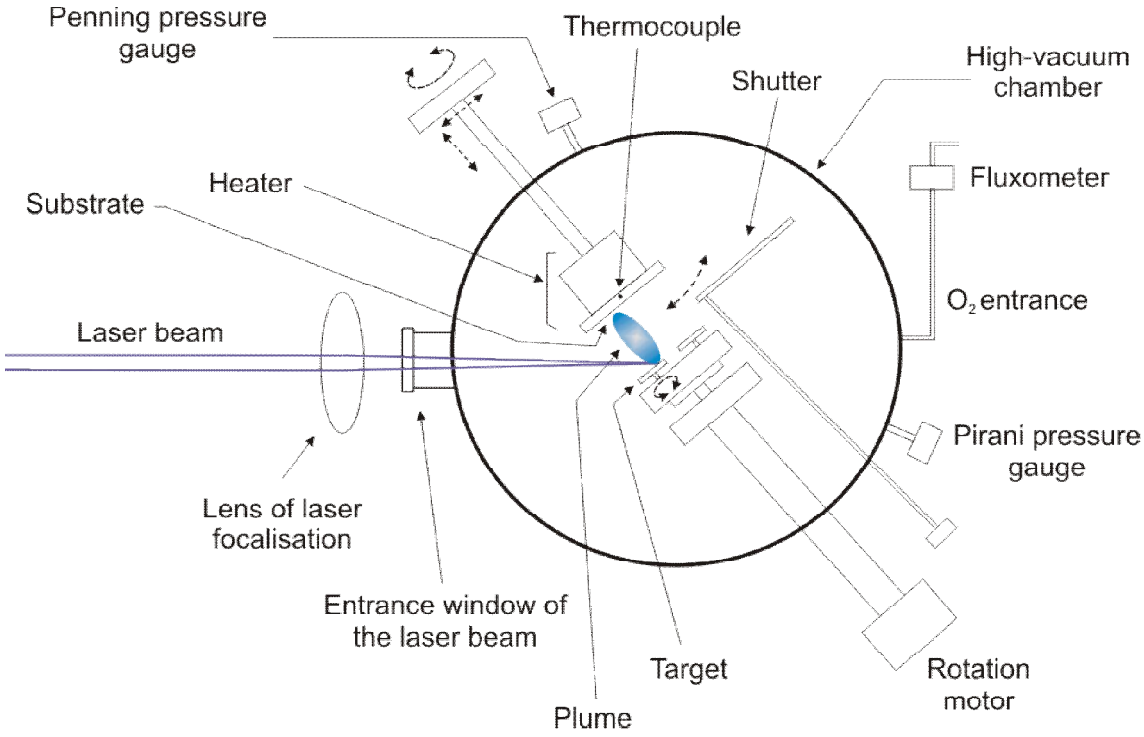

Fig. 2.1 – *Schematic representation of the PLD system.*

2.1.2 Thin film growth process

Our pulsed laser deposition system, described in Fig. 2.2, consists of a KrF excimer laser source (Lambda Physik LPX-210), emitting light pulses of 34 ns with a wavelength of 248 nm. The laser beam is focused on the target with an incident angle of 45º. The deposition process takes place in a high vacuum chamber in which a pressure lower than 10^{-5} mbar can be attained by using a mechanical and a turbomolecular pumps. The gas management system enables O_2 to be controllably introduced into the chamber. The pressure is measured by means of two separate vacuum gauges depending on the pressure range: one of thermal conductivity type (*pirani*) for high pressures (from room pressure to 10^{-1} mbar) and the other one of cold cathode type (*penning*) for lower pressures than 10^{-1} mbar. The target is mounted on a target-holder which can rotate assisted by an electric motor. The substrate is heated by contact to an oxygen

compatible holder –called the heater–, which is heated by Joule effect. Thermal conducting silver paste is used to stick the substrate onto the heater in order to ensure good thermal transfer. The temperature is measured by a thermocouple placed inside the heater. Electronic PID (Proportional-Integral-Derivative controller) system is used to monitor the supplied electric power to the heater, aimed at achieving a stable temperature for the growth process.

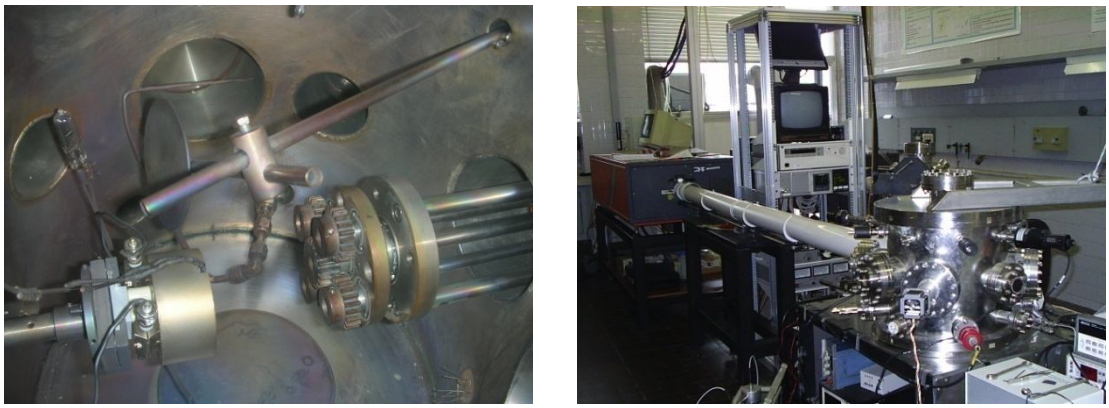

Fig. 2.2 – *PLD system and laboratory where samples have been grown*

The growth process consists of several stages. First, high vacuum is reached in the deposition chamber in order to ensure no impurity coming from the atmosphere. The substrate is heated, afterwards, up to the deposition temperature, whereas the desired O_2 pressure is reached by controlling the O_2 flow. When substrate temperature is stabilised, the rotating target is hit by around 150 pre-ablation laser pulses in order to eliminate impurities that may be present on the surface. A shutter in front of the target inhibits the material ablated in the 'cleaning' process from arriving to the substrate. After the pre-ablation process, the shutter is removed and the deposition starts, keeping the target rotating. The number of laser pulses is set before the deposition process takes place. The rotation of the target is essential to achieve a homogeneous plume of the ablated material and to ensure uniform erosion of the target. Otherwise, stoichiometry as well as density of the target surface may be quicker altered when hitting the laser pulses on the same spot [1 – 3]. When deposition finishes, the sample is immediately cooled down (except when annealing is applied) under full O_2 pressure (~1 bar). The purpose is, apart from minimising bismuth desorption from the film during the cooling process, oxygenating the sample in order to reach the appropriate oxidation state of the transition metal cations. The PLD deposition parameters are summarised in table 2.1.

Deposition Parameter	Setting
Laser fluence	1.5 J/cm^2 – 2.5 J/cm^2
Pulses frequency	1 Hz – 10 Hz
Substrate temperature	590ºC – 700ºC
O_2 deposition pressure	0.05 mbar – 0.60 mbar
Target-to-substrate distance	5.0 cm
O_2 cooling	1.0 bar
Annealing	0 hour – 2 hour @ 450ºC, 1 bar O_2

Table 2.1 – *Overview of the deposition parameters*

After every deposition process the target should be polished in order to ensure that the irregularities in the surface morphology caused by the hit of the laser pulses are eliminated and the original stoichiometry and morphology recovered.

2.1.3 Target fabrication

The targets used for the growth of $BiMnO_3$ and $(Bi,La)_2NiMnO_6$ were made in *Institut de Ciència de Materials de Barcelona* (ICMAB, CSIC) and the *Departament de Ciència de Materials i Enginyeria Metal·lúrgica (Facultat de Química, University of Barcelona)*.

The pellets were produced from mixing the primary oxide powders, *i.e.* Bi_2O_3 (99.99 % pure) and MnO_2 (99.90 % pure) for $BiMnO_3$; Bi_2O_3 (99.99 % pure), La_2O_3 (99.90 % pure), MnO_2 (99.90 % pure) and NiO (99.0 % pure) for $(Bi,La)_2NiMnO_6$. The oxide powders were obtained from the commercial company *Alfa Aesar* .The process consists of several steps:

1) The powders are weighted according to the stoichiometry needed for $BiMnO_3$ and $(Bi,La)_2NiMnO_6$, except for Bi_2O_3, in which an excess around 10 % is used in order to compensate for the high Bi volatility. In the case of La_2O_3, which is high hydrophilic, it is heated for 12 hours at 1000ºC before weighting in order to

evaporate the water content and preventing stoichiometry deviations in $(Bi,La)_2NiMnO_6$ targets.

2) The powders are mixed for one hour in an agatha mortar aimed to homogenise the oxides and reduce the volume of the powder particles so as to maximise the surface of them. This will increase the homogenisation of the different oxides in the posterior thermal treatment.
3) The mixture is hydraulically pressed in a slow continuous process up to attaining $10 \cdot 10^3$ kg/cm^2.
4) The pressed pellet is temperature treated, *i.e.* it is heated inside an alumina crucible up to 500ºC for 15 hours (with a 5ºC/min increasing and decreasing ramps).
5) The pellet is again homogenised and step 2) and 3) are repeated. Then the thermal treatment is applied as in step 4) but up to 600ºC for 15 hours.
6) Finally, the process 2), 3) and 4) is repeated for a third time, but with a thermal annealing of 700ºC for 15 hours. The repetition of the process ensures to achieve as homogeneous and dense target as possible.

The low temperature used in the thermal treatments, compared to the fabrication of common oxide targets, aims to minimise Bi evaporation and hence preserving the desired target stoichiometry. But, as a consequence, the target does not contain the compound itself, *i.e.* $BiMnO_3$ or $(Bi,La)_2NiMnO_6$, but the mixture of the primary oxides. The compound is formed in the PLD process by the epitaxial pressure induced by the substrate onto the coming ablated stoichiometric material (see section 1.3.1).

2.2 Structural characterisation techniques

2.2.1 X-ray diffraction

X-ray diffraction (XRD) is a powerful and thorough technique to study the structure of materials. Lattice parameters, crystal symmetry, compounds and phases identification, texture of the film, epitaxial relation with the substrate, etc, are some of

the structural aspects of the samples that can be assessed by XRD. This technique is based on the interference pattern produced by a monochromatic incident beam light when interacts with a periodic structure, *i.e.* the periodic arrangement of the ions in a crystalline material forming atomic planes (Fig. 2.3).

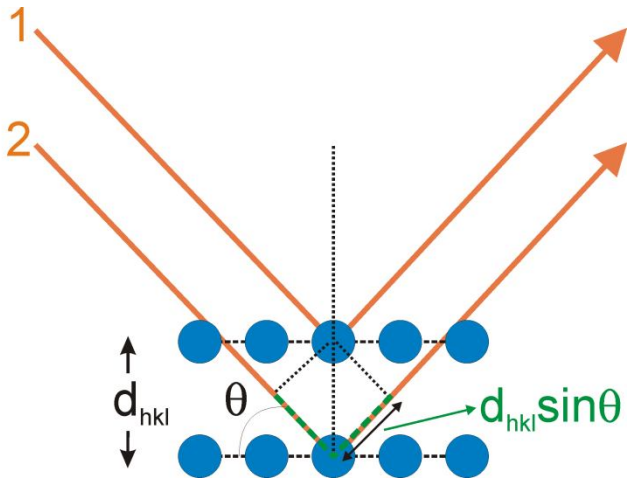

Fig. 2.3 – *Schematic representation of the Bragg's law.*

For a given family of planes (*hkl*), interplanar distance d_{hkl}, constructive interference occurs when incident angle, θ, is such that accomplishes that the path difference of two waves equals a multiple of the wavelength of the incoming radiation (see Fig. 2.3), the so-called diffraction condition of the Bragg's law:

$$2d_{hkl}\sin\theta = n\lambda \qquad (2.1)$$

where n is the order of diffraction and λ is the wavelength of the incoming X-ray radiation, in our case the $K_{\alpha 1}$ line of copper: $\lambda = 1.5406\,\text{Å}$.

The XRD experiments were performed on a four-circle diffractometer MRD PANalytical placed at the *Centres Científics i Tecnològics de la Universitat de Barcelona* (*CCiTUB*). It is to be noted that the X-ray beam reaching the sample in this diffractometer is not full monochromatic as it also contains $K_{\alpha 2}$ and, in much lesser extent, K_β (K_β is almost completely filtered) lines of Cu.

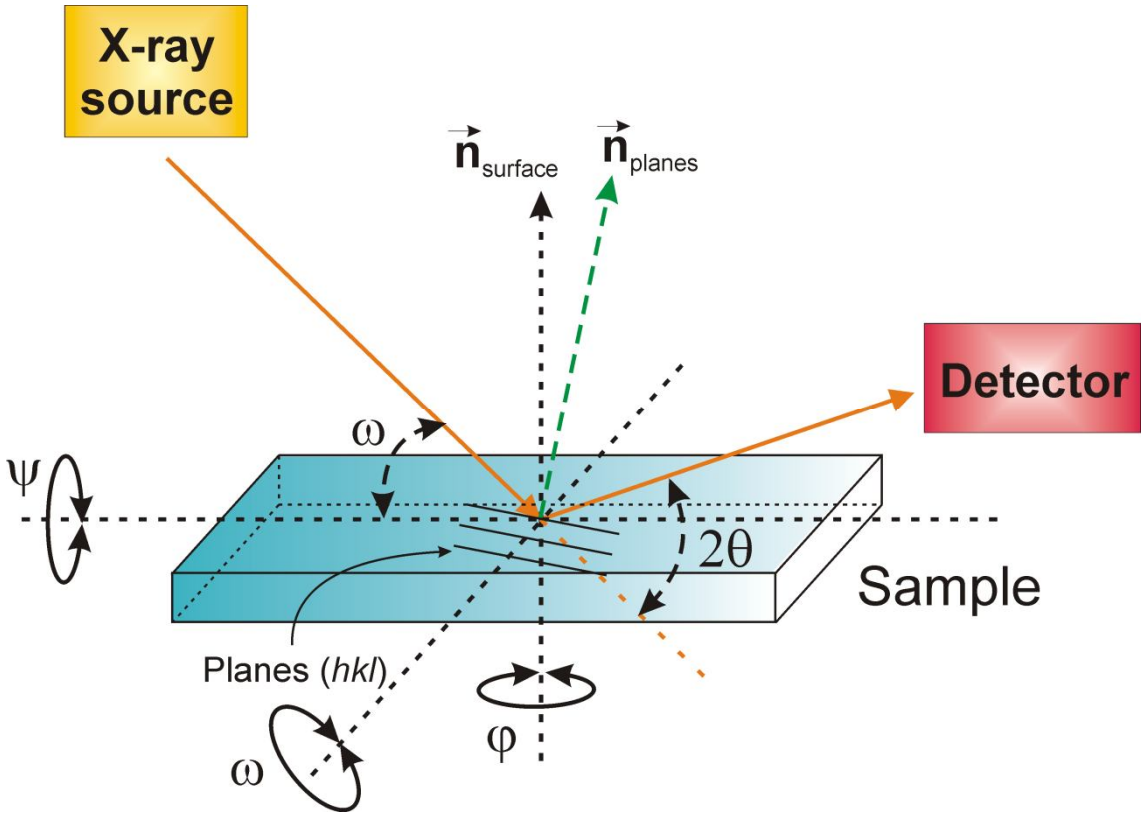

Fig. 2.4 – *Schematic representation of a four-circle diffractometer.* $\vec{n}_{surface}$ *is the vector normal to the surface of the sample and* $\vec{n}_{planes}$ *is the vector normal to the diffracting (hkl) planes.*

The four-circle geometry, depicted in Fig. 2.4, is very appropriate in the structural characterisation of thin films, as it will be discussed later on. The four angles are defined as follows:

- ω is the angle between the incident beam and the plane of the sample surface. It is modified by rotating the sample-holder around the axis which is parallel to the sample surface and perpendicular to the diffraction plane (the plane containing the incident and diffracted beam).
- 2θ is the angle between the incident beam and the diffracted beam. It is modified by changing the position of the detector.
- φ is the angle related to the rotation of the sample-holder around the axis normal to the sample.
- ψ is the angle between the diffraction plane and the axis normal to the sample surface.

Diffraction reflections in symmetric and asymmetric configuration

When the XRD experiment is carried out under the restriction of $\theta = \omega, \psi = 0$, the configuration is said to be symmetric. In this configuration only the planes which are parallel to the surface of the sample contribute to the diffraction scan, as it is depicted in Fig. 2.5 (a). The so-called *2θ-ω scan* (also known by *θ/2θ scan*) is the most typical symmetric scan, in which the sample angle, *ω*, and the detector position, *2θ*, are simultaneously rotated such us ω = (2*θ*)/2, *i.e.* coupled in such a way that the restriction $\theta = \omega$ is fulfilled. This kind of scan allows verifying weather the film has grown with a preferred orientation, *i.e.* all the crystallites of the film grow with the same (*hkl*) planes parallel to the surface or is polycrystalline (random distribution of (*hkl*) planes). Additionally, *2θ-ω scans* allows determining the interplanar distance, d_{hkl}, of the atomic planes parallel to the surface by using Bragg law (2.1), *i.e.* the out-of-plane lattice parameter of the film (see Appendix A). On the other hand, *2θ-ω scans* are also used to to detect any diffraction reflection of any phase formed in the film growth and therefore to assess whether the film has grown single-phase or not. Phases were identified using Ref. [7].

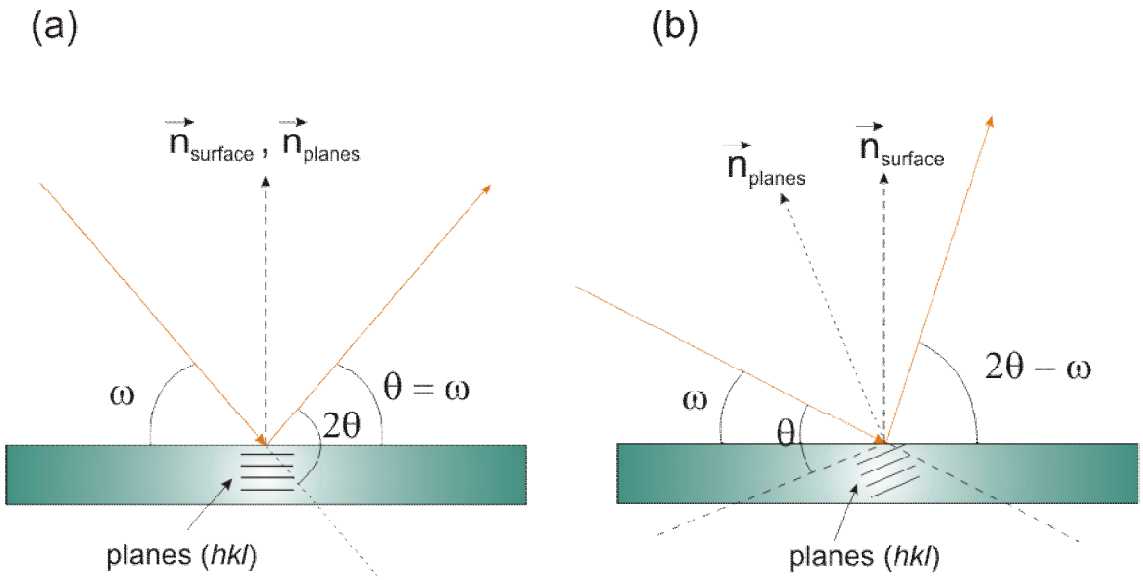

Fig. 2.5 – *XRD scan in* **(a)** *symmetric configuration (2θ-ω scan) and* **(b)** *in asymmetric configuration*

The asymmetric configurations, in which $\omega \neq \theta$ and/or $\psi \neq 0$, enables the planes that are not parallel to the surface of the sample to diffract and to be analysed, as it is depicted in Fig. 2.5 (b). These XRD scans are widely used to characterise the in-plane crystal structure of the film, *e.g.* the in-plane lattice parameter.

Texture of the films characterisation

A) Out-of-plane texture of the film

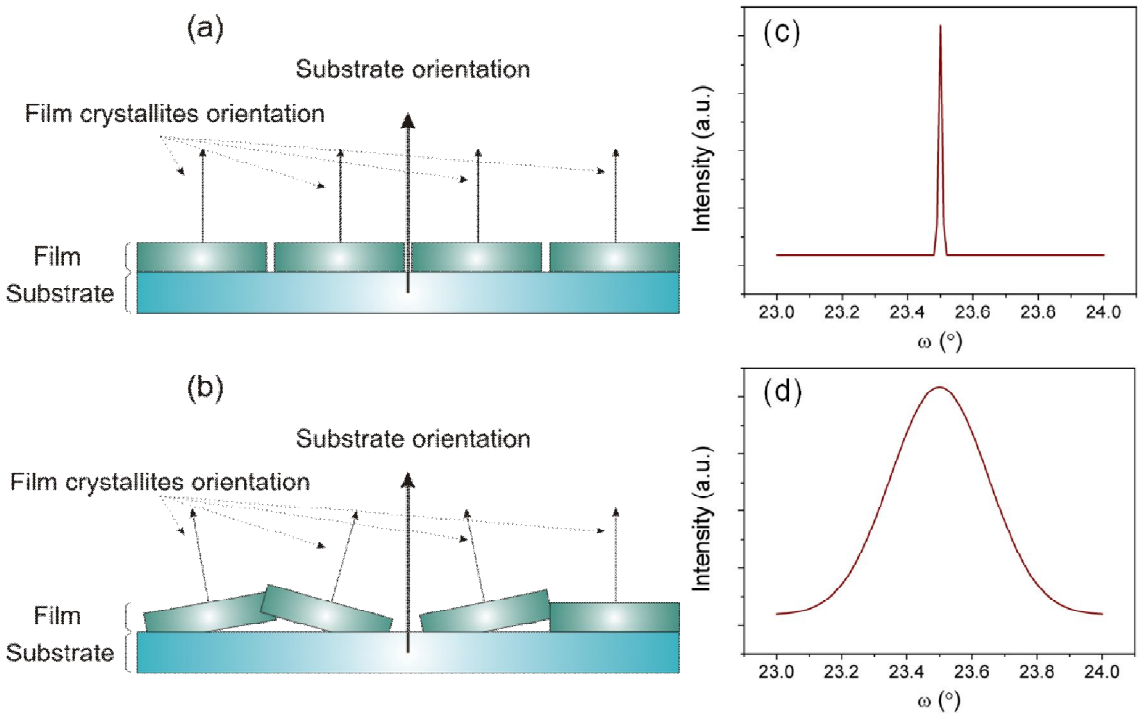

Fig. 2.6 – *Schematic representation of* **(a)** *fully textured film and* **(b)** *mosaic texture film and the corresponding rocking curves:* **(c)** *and* **(d)**, *respectively*

Although the film may grow with an out-of-plane preferred orientation, a certain dispersion of the crystallites of the film occurs. The less dispersion the more texture quality of the film (Fig. 2.6). A way to quantify this crystalline quality is by means of the so-called *Rocking curves* (also known by ω *scan*), Fig. 2.6 (c and d). In this scan the 2θ angle of a given reflection peak is maintained fixed while the ω angle is swept around $\omega = \theta$ within a short range. Thus, narrow *Rocking curve* peaks, characterised by full width at half maximum (FWHM), become a figure of merit of the crystal quality of the films.

B) In-plane texture of the film and cube-on-cube growth

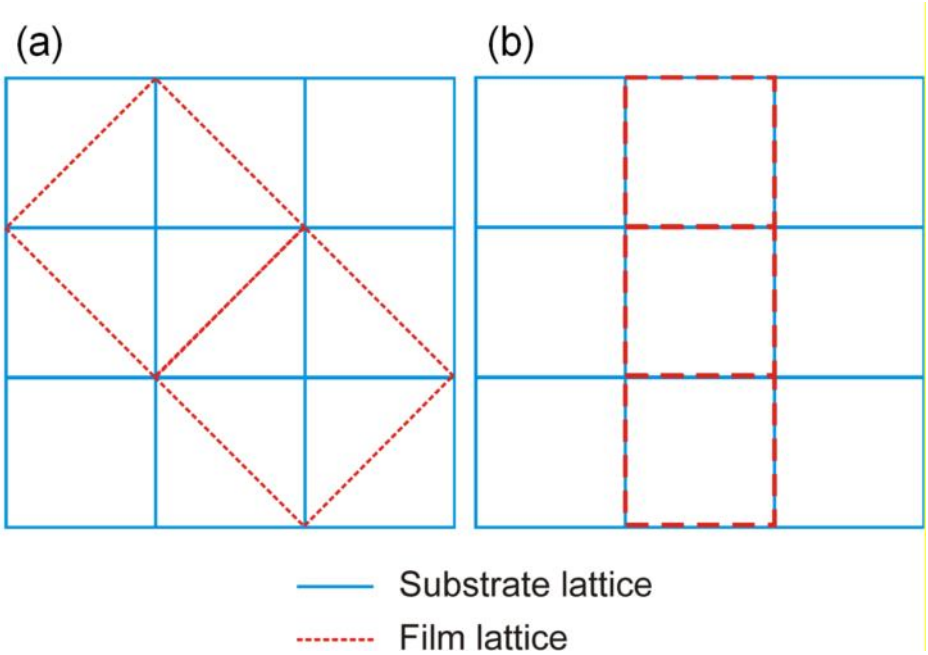

Fig. 2.7 – (a) *and* **(b)** *top planar view for in-plane textured films (red dashed line) on substrate lattice (blue solid line). In picture* **(b)** *a particular case of in-plane textured film is depicted:* c*ube-on-cube growth.*

The in-plane texture of the film that is the relative orientation of the unit cell of the film compared to that of the substrate can be assessed by asymmetric configuration [Fig. 2.5 (b)] by the so-called *φ scans* and *pole figures* as described in the following.

- *φ scans* consists of rotating 360º the φ angle (Fig. 2.4) for a an asymmetric reflexion, in which 2θ and ω angles are fixed fulfilling the Bragg's diffraction condition for the given asymmetric reflexion. As $\omega = \theta$ is accomplished, ψ is tilted in order to enable the asymmetric planes to be in the diffraction plane. When the film is in-plane textured, the φ scan will produce as many diffraction peaks as the in-plane symmetry of the film, *e.g.* a cubic or tetragonal symmetry with the *a* axis perpendicular to the axis normal to the sample must reproduce 4 diffraction peaks on φ being rotating 360º. Additionally, when the angular position of the film diffraction peaks are coincident with the angular position of the substrate diffraction peaks, the growth mode is said to be cube-on-cube (Fig. 2.7 (b)).

- *Pole figures* is an extension of the *φ scans*, in which for each *ψ* value a *φ scan* is performed, giving rise to a 2D in-plane diffraction map.

The film is called to grow epitaxial when grows in-plane and out-of-plane textured.

Reciprocal space maps

Reciprocal space maps are used to determine the epitaxial relationship and the lattice parameters of the film, as will be described in the following.

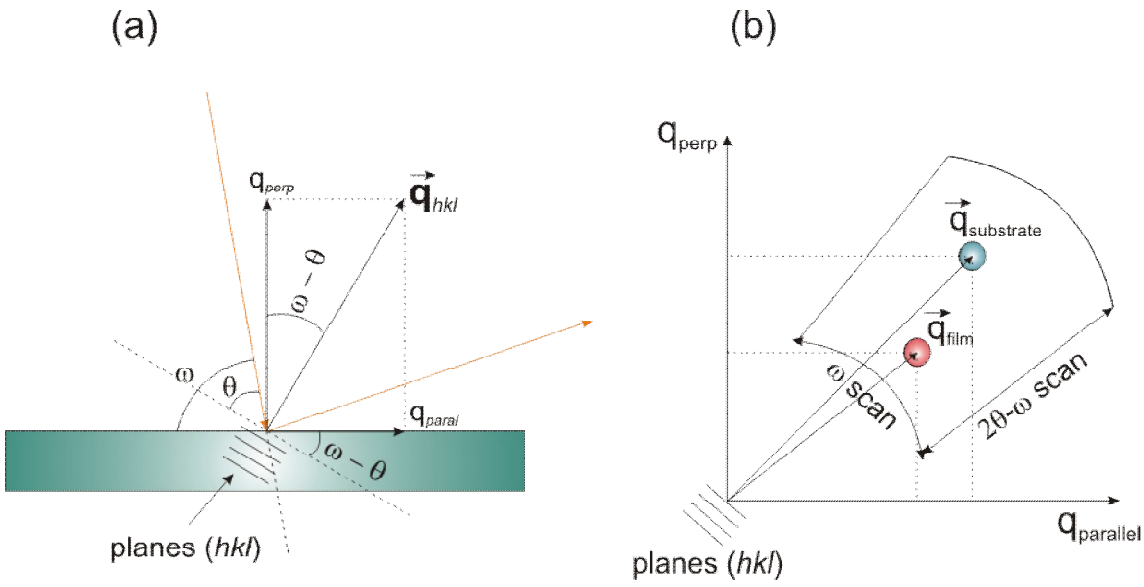

Fig. 2.8 – (a) *Reciprocal space vector* $\vec{q}_{hkl}$ *and the relationship with the angles (θ, ω);* **(b)** *Schematic description of a q-plot scan.*

Let's define the vector $\vec{q}_{hkl}$ as the reciprocal space vector of the family of planes (*hkl*). A condition of reciprocal space vector is to be perpendicular to the planes (*hkl*), as depicted in Fig. 2.8 (a). Moreover, next expression is also satisfied:

$$\left|\vec{q}_{hkl}\right| = \frac{1}{d_{hkl}} \tag{2.2}$$

where d_{hkl} is the distance between the planes (*hkl*). Thus, $|\vec{q}_{hkl}|$ units are [m^{-1}].

Being *a*, *b*, *c* the lattice parameters of a crystal structure, one can describe a vector base of the real space $\vec{a}$, $\vec{b}$, $\vec{c}$, from which the vector base of the reciprocal space, $\vec{a}^*$, $\vec{b}^*$, $\vec{c}^*$, can be defined as follows:

$$\vec{a}^* = \frac{\vec{b}\times\vec{c}}{\vec{a}\cdot(\vec{b}\times\vec{c})};\quad \vec{b}^* = \frac{\vec{c}\times\vec{a}}{\vec{a}\cdot(\vec{b}\times\vec{c})};\quad \vec{c}^* = \frac{\vec{a}\times\vec{b}}{\vec{a}\cdot(\vec{b}\times\vec{c})} \tag{2.3}$$

Once defined the reciprocal space base, the reciprocal space vector $\vec{q}_{hkl}$ can be written as $\vec{q}_{hkl} = h\vec{a}^* + k\vec{b}^* + l\vec{c}^*$. When $\vec{a}$, $\vec{b}$, $\vec{c}$ vectors are orthogonal, that is for cubic, tetragonal and orthorhombic crystalline structure, then next expressions are fulfilled:

$$\vec{a}^* \parallel \vec{a};\quad \vec{b}^* \parallel \vec{b};\quad \vec{c}^* \parallel \vec{c} \qquad \left|\vec{a}^*\right| = \frac{1}{a};\quad \left|\vec{b}^*\right| = \frac{1}{b};\quad \left|\vec{c}^*\right| = \frac{1}{c} \tag{2.4}$$

and it is satisfied: $\left|\vec{q}_{hkl}\right| = \sqrt{\frac{h^2}{a^2}+\frac{k^2}{b^2}+\frac{l^2}{c^2}}$

A general expression of $\left|\vec{q}_{hkl}\right|$ for the different crystal structures is found in the Appendix A.

In order to determine the in-plane parameter and the out-of-plane parameter is useful to define $q_{parallel}$ and q_{perp} as the parallel and perpendicular component of $\vec{q}_{hkl}$ to the surface of the sample, respectively. If we consider *a* and *b* the in-plane parameters and *c* the out-of-plane parameter in an orthogonal base, then next expressions are fulfilled:

$$q_{parallel} = \sqrt{\frac{h^2}{a^2}+\frac{k^2}{b^2}} \qquad q_{perp} = \frac{l}{c} \tag{2.5}$$

A reflexion of the type (*h0l*) tends to be used. Then, the expressions are simplified:

$$q_{parallel} = \frac{h}{a} \qquad q_{perp} = \frac{l}{c} \tag{2.6}$$

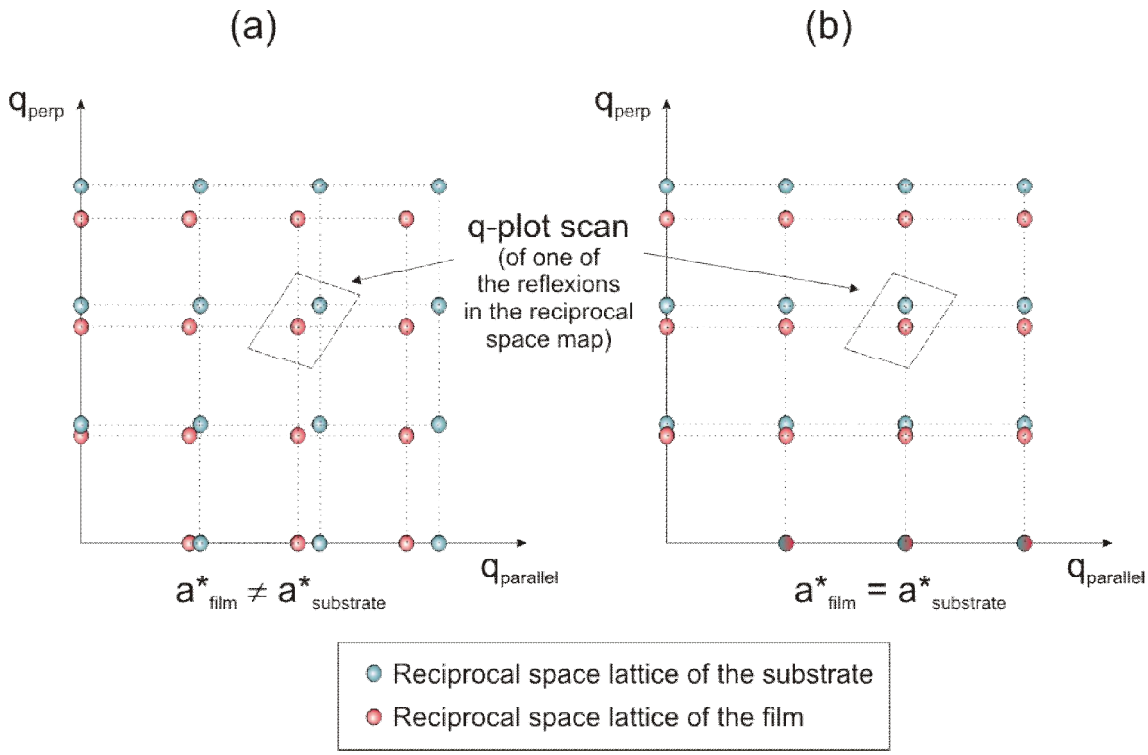

Fig. 2.9 *– Reciprocal space map of film and substrate when* **(a)** *the film has grown relaxed (bulk lattice parameters) and* **(b)** *the film has grown completely, adapting the in-plane parameter to the substrate.*

The determination of q_{hkl} is carried out by the so-called *q-plot scan* (or *reciprocal space maps*), which consists of doing a 2θ-ω scan for different values of ω of a given asymmetric reflexion (otherwise only q_{perp} could be determined), as depicted in Fig. 2.8 (b). It is necessary to relate the angles (θ, ω) to q_{paral} and q_{perp}. From the Bragg law, $2d_{hkl}\sin\theta = \lambda$, and from Fig. 2.8 (a), next expressions can easily be deduced:

$$q_{parallel} = \frac{2}{\lambda}\sin\theta\sin(\theta-\omega)$$
$$q_{perp} = \frac{2}{\lambda}\sin\theta\cos(\theta-\omega) \qquad (2.8)$$

The reciprocal space maps allow determination of $q_{parallel}$ and q_{perp} of the Bragg spots and thus to determine in-plane and out-of-plane cell parameters of the film and the substrate. Consequently the epitaxial strain exerted by the substrate can be determined. If the measured $q_{parallel}$ of the substrate and the film are coincident, as depicted in Fig. 2.9 (b), then the in-plane lattice parameter of film has adopted the substrate lattice

parameter. In this case the film is said to grow coherently (fully strained) on the substrate. On the other hand, when the measured $q_{parallel}$ of the film corresponds to the bulk lattice parameter, then the film is said to grow fully relaxed, as depicted in Fig. 2.9 (a).

2.2.2 X-ray reflectivity

X-ray reflectivity (XRR) is a non-destructive and non-contact technique for accurately determining the thickness of films in the range of 2 – 200 nm, with a precision of about a few Å. In addition, this technique allows determining the roughness and the density of the film or even multilayers. The XRR experiments were performed on a Siemens D-500 diffractometer with grazing incident angle optics, placed at the *CCiTUB*.

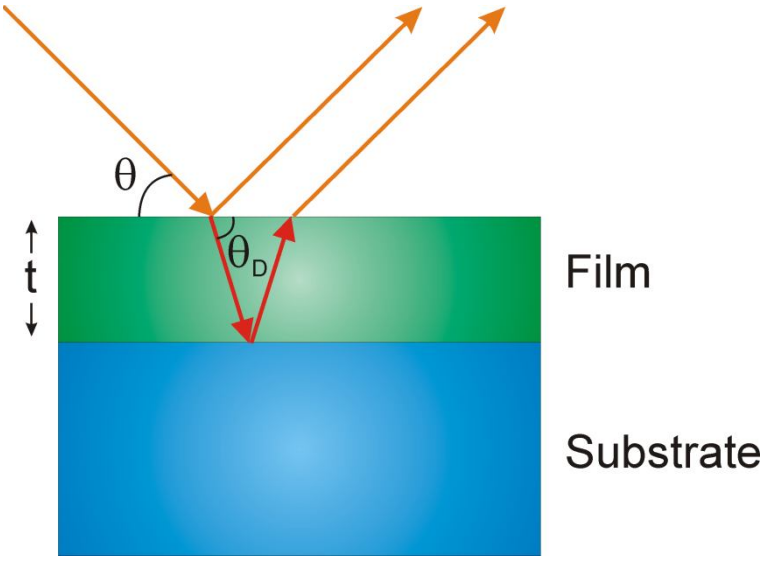

***Fig. 2.10** – Sketch of the XRR experiment, where t is the thickness of the film, θ the incident angle, and θ_D the diffracted angle.*

XRR consists of irradiating the sample with an incident X-ray beam (λ of $K_{\alpha 1}$ of Cu in our case) at grazing angles (small ω angle, Fig. 2.4) and collecting the reflected beam in a detector (placed at 2θ angle, Fig. 2.4), very much alike to Fig. 2.4, accomplishing the condition $\omega = \theta$ and $\psi = 0$. As incident grazing angles are used much of the intensity of the X-ray beam is reflected, being θ_c the critical incident angle, below which total external reflexion occurs. θ_c depends on the electronic density of the material, with

typical values below 0.5º. Above θ_c part of the incident radiation penetrates the film (see Fig. 2.10), with a diffracted angle, θ_D, that is given by the Snell's law, $\cos\theta/\cos\theta_D = n = \cos\theta_c$, where n is the refraction index of the film. Due to the different electronic density of film and substrate, reflection of the diffracted beam occurs at the interface. Thus, the incident beam is reflected from both the top of the film (surface) and the bottom of the film (interface), giving rise to constructive and destructive interference pattern depending on the difference in the optical path (Fig. 2.10). Using trigonometry and the Snell's law, the interference condition, in which the optical path difference equals a multiple of the wavelength, is given by [8]:

$$2 \cdot t \cdot \sqrt{\sin^2 \theta_m - \sin^2 \theta_c} = m \cdot \lambda \qquad (2.9)$$

where t is the thickness of the film, θ_m is the incident angle at which constructive (destructive) interference is produced and m is the order of the constructive (destructive) interference.

In contrast to XRD, the refractive effects are significant at low incident angle solely, becoming negligible for high θ. Thus, XRR experiments are normally performed as a coupled $\theta/2\theta$ scan up to $2\theta < 6º$, in which a pattern of interference fringes are recorded above θ_c (Fig. 2.11). Eq. 2.9 can be rewritten as:

$$\sin^2 \theta_m = \sin^2 \theta_c + \left(\frac{\lambda}{2 \cdot t} \right)^2 \cdot m^2 \qquad (2.10)$$

Extracting the position of the minima, θ_m, (or, equivalently, the maxima) of the oscillations of interference (Fig. 2.11) and computing $\sin^2\theta_m$, a linear dependence is expected with the square of the order of the minima (or maxima), m^2, Eq. 2.10. The linear fit (Inset: Fig. 2.11) should give us both the thickness of the film (from the slope of the fit) and the critical angle, θ_c.

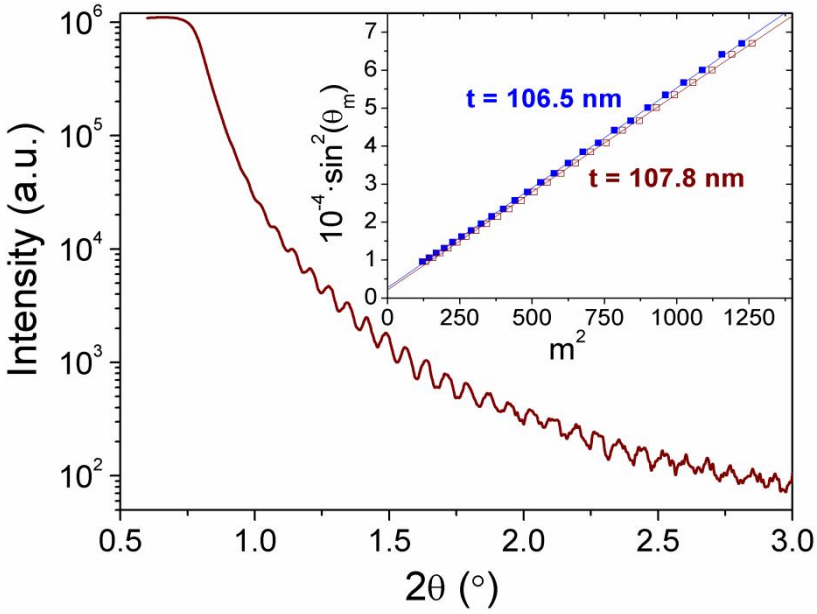

Fig. 2.11 – *XRR spectrum of a 107 nm-thick* $(Bi_{0.9}La_{0.1})_2NiMnO_6$ *film on* $SrTiO_3$ *substrate.* **Inset:** *Fitting (solid line) of* $\sin^2\theta_m$ *vs* m^2 *data (blue solid square symbols) and* $\sin^2\theta_{m'}$ *vs* $(m')^2$ *data (red open square symbols), where m and m' are integer and semiinteger numbers, respectively.*

It is worth adding that if the refraction index of the substrate is larger than that of the film, the X-ray beam reflected at the interface is inverted, *i.e.* is π-phase shifted. In order to correct this shift, integer m in expression 2.10 is replaced by a semiinteger number ($m' = m + 1/2$), being $\Delta m' = \Delta m = 1$ [8]. This small correction is shown in the inset of Fig. 2.11 (open symbols) where $\sin^2\theta_{m'}$ is plotted versus m'. As observed the difference in thickness is small (around 1 nm over ~100 nm of thickness), of the order of 1.2 %.

2.2.3 Transmission electron microscopy

Transmission electron microscopy (TEM) uses the wave-like character of the electron to obtain images of the explored materials, alike its optical counterparts but in a nanometric scale due to the small electronic wavelength (~ 10^{-12} m) that follows the energy range at which electrons are accelerated (typically 100 – 400 kV). Using different operating modes TEM allows not only image formation (image mode) but also registering diffraction patterns of selected areas of the sample (diffraction mode). Additionally, TEMs are usually equipped by compositional analysis components (such

as electron energy loss spectroscopy or energy dispersive spectroscopy), as it will be discussed in section 2.4, which makes this technique very versatile.

However, samples need prior preparation for TEM analysis, *i.e.* they need to be thinned down in order to enable electrons to pass through. The so-called TEM lamellas of our samples were prepared by J. M. Rebled, Dr. S. Estradé and Dr. F. Peiró by focused ion beam (FIB) in a FEI Strata dual beam system located at the *CCiTUB*. Lamellas were prepared in cross section geometry, *i.e.* allowing characterising both substrate and film.

The TEM process is schematically depicted in Fig. 2.12 (a). Electrons are produced either thermoionically, by heating W or LaB_6 cathode, or by field emission electron gun, which generates electrons when exposed to an intense electric field. The latter has the advantage of a more monochromatic electron source and a finer probe which gives rise to a better resolution. The electron beam is accelerated and confined onto the specimen by a condenser magnetic lens system. The transmitted electron-wave is gathered by the objective lens, after which some intermediate lens allows choosing between two basic operating modes:

- Image mode. In this mode the transmitted electrons are gathered by the objective lens and collected in the image plane [Fig. 2.12 (b)], where a preliminary image is formed. The subsequent intermediate lens is focused on the image plane. Finally the image is formed on the screen (or CCD camera) after further magnification and the projector lens [Fig. 2.12 (a)].

- Diffraction mode. In this mode, instead, the intermediate lens is focused on the back focal plane of the objective lens [Fig. 2.12 (b)], where the diffraction pattern of the sample is recorded. Thus, by changing the strength of the intermediate lens, the operating mode can be switched from image mode to diffraction mode and vice versa. The selected area diaphragm is usually used to select specific regions of the TEM specimen, *e.g.* only a small region of the substrate or substrate + film. This mode is called *Selected Area Electron Diffraction* (SAED) and it is the one used in this work. Depending on the crystallographic axis along which the cross section is prepared, different

crystallographic planes are enabled to diffract. SAED patterns allow obtaining information about the unit cell, the epitaxial relationship, etc.

Within image mode, obtaining higher contrast images is possible by introducing an objective diaphragm in the back focal plane [Fig. 2.12 (a)], which permits selecting only the transmitted beam [Fig. 2.12 (c)], so-called bright field images, or by tilting the beam (or moving the aperture) only the diffracted beam [Fig. 2.12 (d)], so-called dark field images. Usually dark field images have higher contrast, although the intensity is greatly reduced.

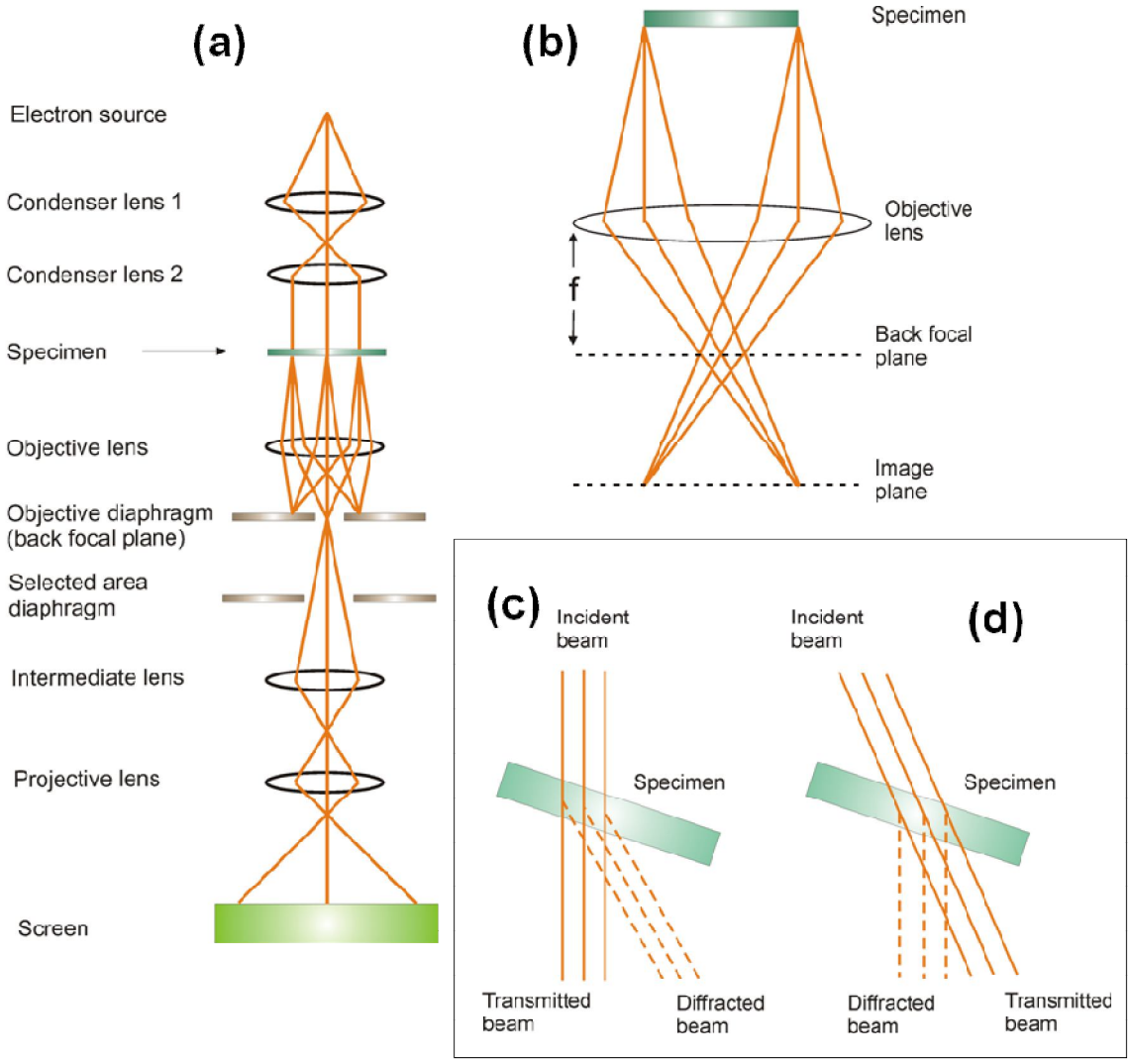

Fig. 2.12 – (a) *Scheme of TEM process.* **(b)** *Image plane vs back focal plane. Bright field* **(c)** *and Dark field* **(d)** *mode for imaging.*

Finally, special TEM techniques can also be performed as described in the following. First, *Scanning Transmission Electron Microscopy* (STEM), which no longer

consists of a static electron beam but, instead, the condenser lenses concentrate the beam on a small spot size that can be scanned on the sample by means of scan coils. STEM images have better contrast than conventional TEM images and they can also be obtained either in dark field or in bright field mode. Second, *High Resolution Transmission Electron Microscopy* (HRTEM), in which TEM images are formed by a process called phase contrast. The contrast is formed by constructive and destructive interference from the electron waves passing through a material showing a certain periodicity (crystalline material). This phase-contrast technique allows obtaining much information about the crystal structure of the material.

Both TEM and HRTEM images, as well as SAED patterns of film and substrate, were obtained by J. M. Rebled, Dr. S. Estradé and Dr. F. Peiró in a Jeol 2010F field emission gun TEM operating at 200 keVs located at the *CCiTUB*.

2.2.4 X-ray diffraction using synchrotron radiation

Synchrotron facilities at HASYlab, DESY (*Deutsches Electronen-Syncrotron*) in Hamburg (Germany) were used during a three-months stay in Zernike Institute for Advanced Materials (University of Groningen, the Netherlands) in the group *Solid-State of Materials for Electronics* headed by Dr. B. Noheda and Dr. T. T. M. Palstra. XRD experiments with synchrotron radiation were assisted and supervised by Dr. C. J. M. Daumont.

Synchrotron radiation was used with the aim of determining the B-site ordering in $(Bi,La)_2NiMnO_6$. As explained in Sect. 1.2.5, long-range ferromagnetism is achieved, solely, when Ni^{2+} and Mn^{4+} are ordered alternatively along [100], [010] and [001] crystallographic perovskite directions. This B-site order produces the alternation of Ni-planes and Mn-planes along [111] direction (Fig. 2.13), as a consequence of which diffraction signal of these crystallographic planes, $\left(\frac{1}{2}\frac{1}{2}\frac{1}{2}\right)$ superstructure double-perovskite reflexion, should be recorded. Yet the structure factor of Ni and Mn are very similar which gives rise to a very small signal, so that high intensity synchrotron radiation was needed.

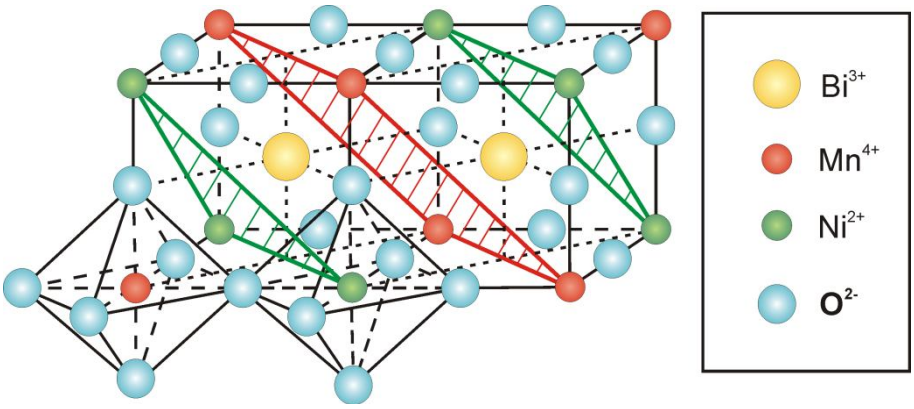

Fig. 2.13 – *B-site ordered double perovskite entails the alternation of Ni-planes and Mn-planes along [111] crystallographic direction.*

Coupled θ/2θ XRD scans around the (111) and $\left(\frac{1}{2}\frac{1}{2}\frac{1}{2}\right)$ asymmetric reflexions (see Sect. 2.2.1) using synchrotron radiation were performed, so that ψ and φ were set to 54.56º and 135º, respectively, in order to enable the asymmetric crystallographic planes to diffract by keeping the condition $\omega = \theta$ (see Sect. 2.2.1). The energy of synchrotron radiation corresponded to a wavelength of 1.2651 Å.

2.3 Surface morphology characterisation techniques

2.3.1 Field emission scanning electron microscopy

Field emission scanning electron microscopy (FESEM) is an electronic microscope that permits taking high resolution three-dimensional-appearance images of the surface of samples. Alike TEM microscopes, the difference between a FESEM and a conventional SEM is the way the electrons are produced. In FESEM a field emission electron gun is used, whereas in conventional SEM the electrons are produced thermoionically by heating a W or LaB_6 cathode. FESEM has the advantage of producing much smaller-diameter electron beam (< 100 Å), which leads to obtain much higher resolution images (it can be attained spatial resolutions down to 2 nm, between 3

and 6 times better than the resolution of a conventional SEM). In addition, since the electron beam has a smaller diameter, the affected area of the sample is reduced. As a consequence, samples are less electrostatically charged and the need of covering insulating materials with conducting coatings is reduced to a large extent or even eliminated.

The FESEM images were performed on a Hitachi S-4100-FE microscope situated in the *CCiTUB*. The images were collected by using the software Quartz PCI 5.1 (Quartz Imaging Corporation).

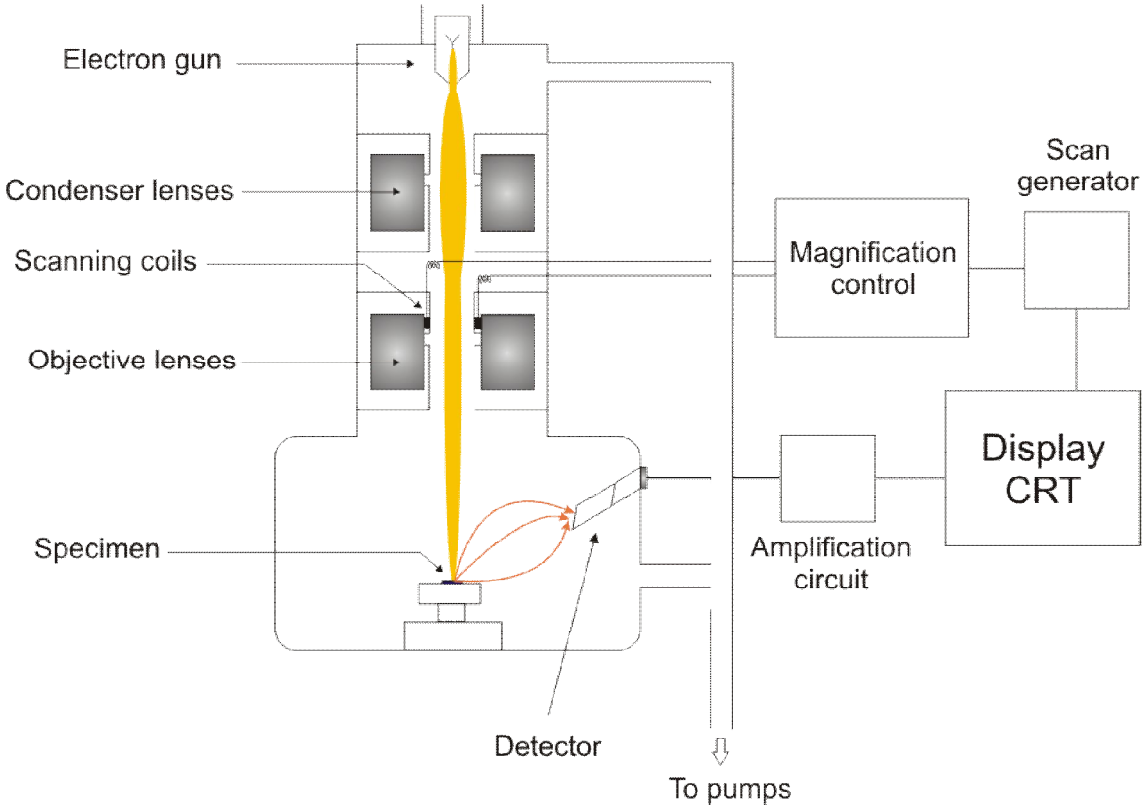

Figure 2.14 – *Basic scheme of a typical SEM.*

The SEM process is schematically depicted in Fig. 2.14. The electron beam follows a vertical path through the column of the microscope in ultra-high vacuum, where electromagnetic lenses focalises the beam onto the sample. The scanning coils are used to move the electron beam on the sample. When the electron beam hits the sample, then an interaction between the primary electrons (electron beam) and the matter takes place. From the sample both electron and photon signals are emitted. Not all the signals are detected and used for information. The signals most commonly used are the so-called

secondary electrons, backscattered electrons and X-rays. The secondary electrons are the electrons coming from atoms of the sample that have been ionised by the impact of the primary electrons; the backscattered electrons are primary electrons that have been elastically backscattered; and the production of X-ray is due to electron transitions of the atoms of the sample as they have been excited on being hit by the primary electrons. Both the secondary and the backscattered electrons are used to form the image. They are collected and turned into a signal that is represented by a two-dimensional distribution of intensities and it is viewed as an image by means of a cathode-ray-screen. The X-rays give compositional information and therefore they are not used to characterise the topography.

There are two basic modes for taking the image: by collecting the secondary electrons or by collecting the backscattered electrons. The first ones have the advantage of giving higher resolution images since they tend to have energies around 50 eV and they are therefore ejected from a region very close to the surface. It is necessary to apply a low voltage in order to collect them. The second ones might come from deeper regions as they have higher energy. Because of this they lose surface resolution; however, they give a better contrast as they follow rectilinear trajectories. In this work it has been collected the secondary electrons in order to attain higher spatial resolutions.

2.3.2 Atomic force microscopy

Atomic force microscopy (AFM) is a very high-resolution type of scanning probe microscope, with demonstrated resolutions of fractions of a nanometre. AFM provides a true three-dimensional surface profile, which permits determining the roughness of the sample. It works in room pressure and the samples do not need to be covered with a conducting coating.

The AFM consists of a microscale cantilever with a sharp tip at its end that is used to scan the sample surface. When the tip is moved close to the surface of the sample, short-range forces (as Van der Waals) between the tip and the sample surface appear which leads to bend the cantilever. The deflection is measured by using a laser beam focused on the top of cantilever and reflected into an array of photodiodes, as it is shown in Fig. 2.15. The measures within this work have been done in tapping mode, in

which there is no contact between the tip and the sample, but the tip oscillates with a resonance frequency. The oscillation amplitude, phase and resonance frequency are modified because of the tip-sample interactions forces. These changes respect to an external reference oscillation give information about the surface morphology of the sample. A feedback mechanism is used to adjust the tip-to-sample distance in order to maintain a constant force between them.

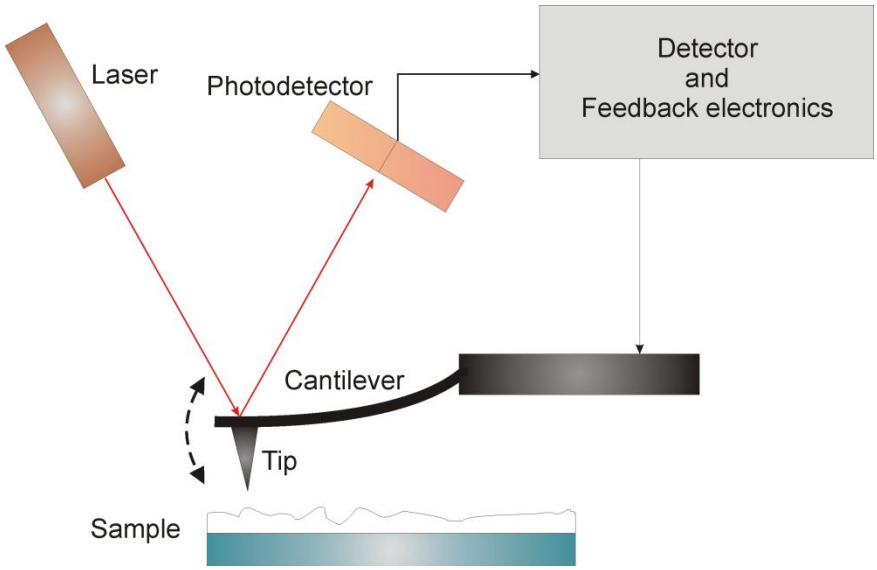

Figure 2.15 – *Basic scheme of an AFM*

AFM images were taken in a multimode force microscopy (Veeco model), which is placed in the *CCiTUB*. The images were analysed with the software Nanoscope IV (Digital Instruments). For roughness measurements of our films the *root mean square* (rms) standard has been used.

2.4 Compositional characterisation techniques

2.4.1 X-ray photoelectron spectroscopy

X-ray photoelectron spectroscopy (XPS), also known as electron spectroscopy for chemical analysis (ESCA), is based on the photoelectron effect. It consists of irradiating the surface of the sample by monochromatic photons (X-ray beam), producing

excitation of the electrons of the material toward higher energy levels, or, eventually, they may leave the solid provided that the energy of the incoming photon is sufficiently large. The escaped electrons are detected and collected by an electron energy analyser, which determines the kinetic energy of them. Thus, the energy of the photon, hv, is invested: first, in extracting the electron from its binding site of the atom, E_B; second, in sending it to the vacuum, *i.e.* to leave the solid (work function, ϕ); and third, in providing the electron kinetic energy. Hence, the kinetic energy, E_K, is given by

$$E_K = hv - E_B - \phi \tag{2.11}$$

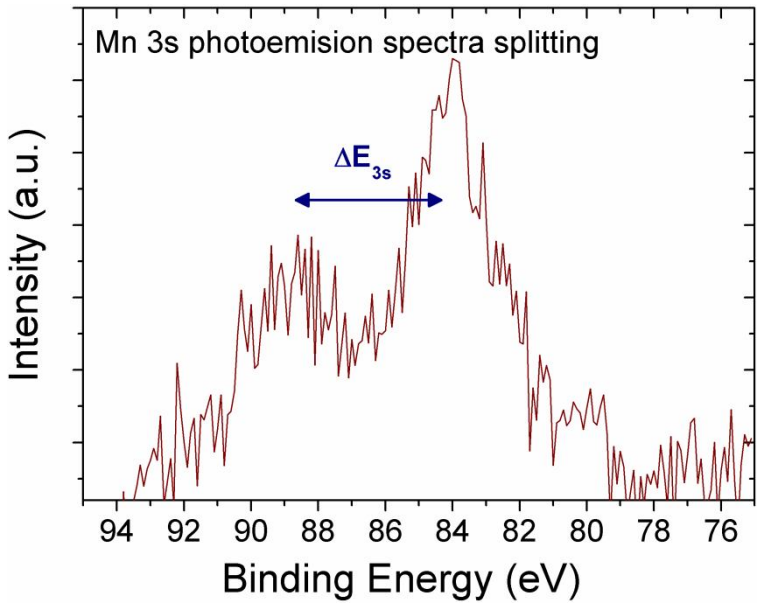

Fig. 2.16 – *Mn 3s photoemission spectra of* $(Bi_{0.9}La_{0.1})_2NiMnO_6$ *thin film.*

As E_B is unique for each element, this technique allows determining the elements present in the sample. Moreover, as the energy detector quantifies the number of arriving electrons, this technique is also quantitative. However, as the mean path of the electron through the solid is of the order of a few nm (< 10 nm), XPS is a very sensitive surface technique.

On the other hand, the exact binding energy of an electron does not only depend on the level from which photoemission is occurring, but the formal oxidation state of the atom and/or the local chemical and physical environment. This can be used to determine the valence of the elements in the sample. In particular, in the case of Mn, which was

studied in this work, its valence state is strongly related to the Mn 3*s* photoelectron spectra [9]. The spectral splitting of the 3*s* core-level X-ray photoemission (see Fig. 2.16) originates from the exchange coupling between the 3*s* holes and 3*d* electrons in the transition metals. The magnitude of the splitting ($\equiv\Delta E_{3s}$) is proportional to ($2S+1$), where S is the local spin of the 3*d* electrons in the ground state. Thus, a roughly linear behaviour is found between ΔE_{3s} and the formal valence of Mn (Fig. 1.17).

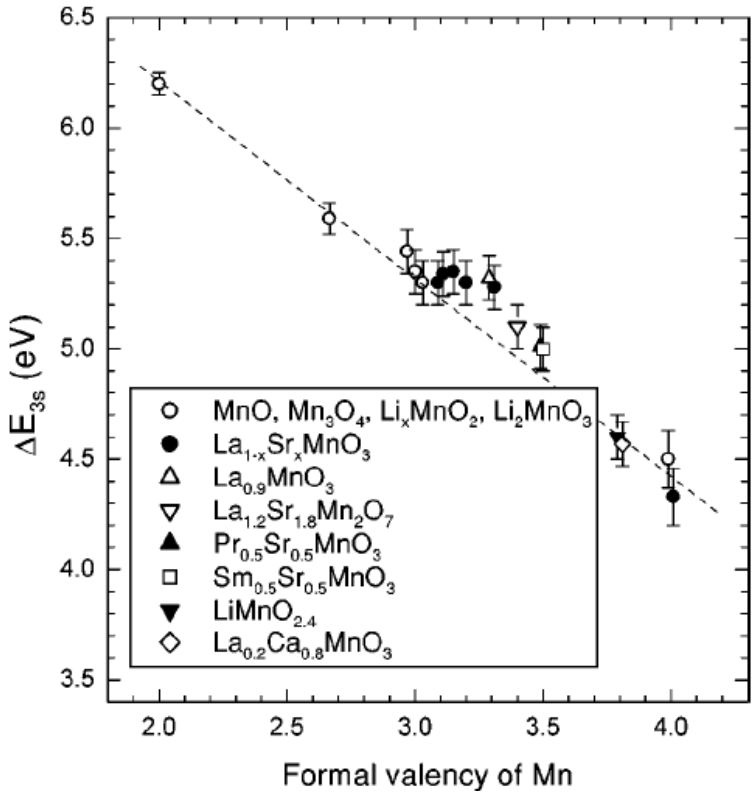

Fig. 2.17 – *Mn 3s splitting as a function of the formal valence of Mn (from Ref. [9]).*

XPS experiments were performed in a PHI 5500 Multitechnique System (Physical Electronics) located at the *CCiTUB*. The system has a monochromatic X-ray source (Al-K_α). Multipak v6.0 (Physical Electronics) package was used as a software analysis.

2.4.2 Variable-voltage electron microprobe analysis

As it was explained in SEM (Sect. 2.3.1) the impact of electrons on matter produced the emission of X-rays. This phenomenon is used in electron microprobe analysis to

characterise the composition of materials. In fact, the electron microprobe is usually placed in a SEM equipment.

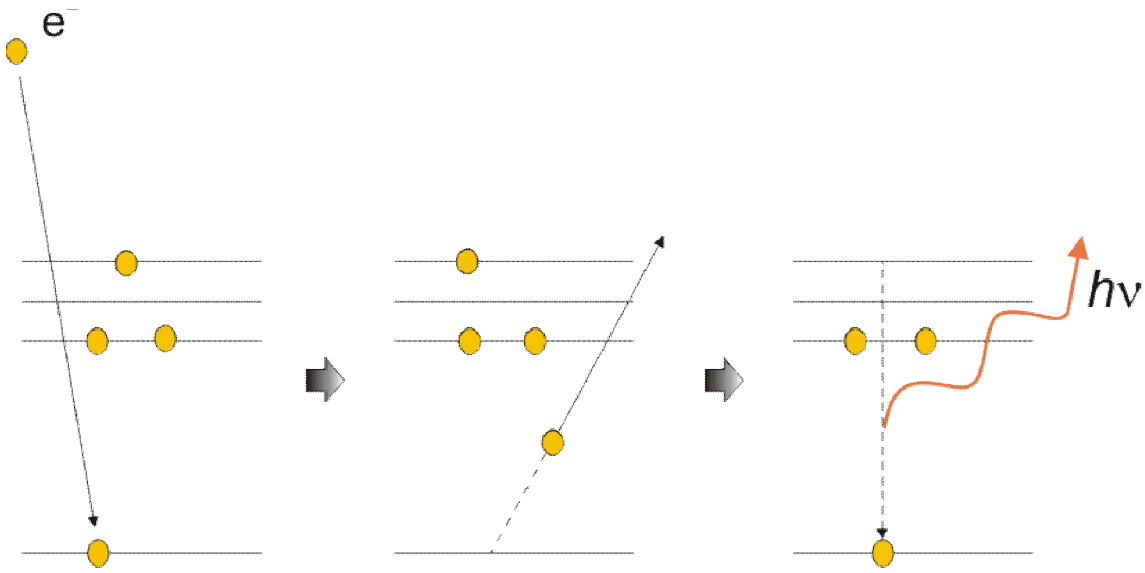

Fig. 2.18 – *Scheme of the X-ray photon generation by the hit of an incoming electron.*

The basic principle is shown in Fig. 2.18. The hit of the electrons on the matter cause vacancies in the internal electronic levels of the atoms of the sample. The electron transition between an external electronic level and this internal level generates an X-ray photon, whose wavelength (or frequency) is characteristic and unique for each element. In principle, all elements from beryllium in the periodic table can be detected by this technique.

The X-ray photons can be determined in energy or in wavelength depending on the detector. The technique is designated in function of the detection system: energy dispersive spectroscopy (EDS) and wavelength dispersive spectroscopy (WDS), respectively. Within this work it has been used a WDS detection system, which is based on the diffraction of the X-rays through a crystal. The WDS has the advantage of having a better resolution than the EDS.

The problem of using the electron microprobe to the compositional analysis of thin films is the fact that the interaction volume is larger than the thickness of the film and there is a contribution of the substrate. In order to subtract this contribution, different electron beam energies are used so that from the different interaction volumes the substrate contribution can be estimated and then corrected.

WDS experiments were performed on Electron Microprobe Cameca SX50 placed at the *CCiTUB*. STRATAGem (SAMx Co.) is the software that monitors the process.

2.4.3. Electron energy loss spectroscopy

Electron energy loss spectroscopy (EELS) involves measuring the energy distribution of electrons that have crossed the sample (TEM lamella, see Sect. 2.2.3) that have interacted with a specimen and loss energy due to inelastic scattering. The energy loss is related to some characteristic atomic transition or solid state effect, which is used to obtain chemical information about the sample.

A typical EELS spectrum consists of three main parts, as a function of the energy loss. First, the zero-loss peak which represents the electrons that have not undergone inelastic scattering, and hence they have not loosen energy. Second, the low-loss region (from ~40 eV to ~400 eV) which consists of inelastic scattering by conduction/valence electrons and by some inner-shell electrons. Third, the core-loss region (from ~400 eV to ~900 eV), which consists of inelastic scattering by core electrons, typically the L-edges (2s, $2p^{1/2}$ and $2p^{3/2}$ electrons).

Whereas both the low-loss and the core-loss region are used to extract compositional information, the latter can also be used to determine the fine structure and the valence of the transition metals, like Mn and Ni in our case.

EELS profiles were obtained by J. M. Rebled, Dr. S. Estradé and Dr. F. Peiró in cross section lamellas of our samples (see Sect. 2.2.3) using a Gatan GIF spectrometer in a Jeol 2010F field emission gun TEM placed at *CCiTUB*.

2.5 Functional properties characterisation

2.5.1 Magnetic characterisation

Magnetic properties were assessed by a superconducting quantum interference device (SQUID), which is a very sensitive magnetometer based on superconducting loops containing Josephson junctions (insulating barrier between two superconductor materials). The magnetic measurement is carried out by displacing the sample along the vertical axis between two coils connected to a Josephson junction, which turns the magnetic flux variation into voltage and transmitted as an electric signal. The Josephson junctions permit attaining high precision, in principle, a magnetic quantum flux ($\Phi_0 = e/(2h) \sim 2.07 \cdot 10^{-15}$ T·m^2). In practise, in terms of the recorded magnetic moment of the sample, the maximum resolution is around 10^{-7} emu.

Magnetic measurements were performed in a SQUID magnetometer of Quantum Design, placed at the *Institut de Ciència de Materials de Barcelona (ICMAB, CSIC)*. The equipment is designed to work with magnetic fields up to 9 T and a range of temperatures between 5 K and 300 K. Typical measurements in this work were the so-called field cool and hysteresis magnetisation. The former consists of recording the magnetic moment response of the sample when cooling it down from room temperature to 5 K under fix applied magnetic field (typically 1000 Oe), which enables determining the magnetic transition temperature of the sample. The later consists of applying a cycling magnetic field at a given temperature and recorded the magnetic moment response, which allows obtaining the saturated magnetisation and the hysteresis loop of the sample. It is worth mentioning that the main contribution to the measured magnetic hysteresis loop is the diamagnetism of the substrate, which is subtracted (see Appendix B).

2.5.2 Electric characterisation

Dielectric measurements (see chapter 3) were mainly performed during a three-months stay in Zernike Institute for Advanced Materials (University of Groningen, the Netherlands) in the group *Solid-State of Materials for Electronics* headed by Dr. B. Noheda and Dr. T. T. M. Palstra. Impedance analyser Agilent 4284 was used, applying, from top to top electrode, an oscillating voltage of 50 mV of amplitude and ranging from 40 Hz to 1 MHz. Contact with top electrodes (see chapter 3, sect. 3.1) were carried out in a cryogenic micropositioning probe station (Janis Research Co.), see Fig. 2.19. The probe station consist of 4 micro-manipulating dc/low-frequency (up to 40 MHz) probe arms (Fig. 2.19), with tungsten tips (used to contact the top electrodes) that can be moved in x, y z spatial-directions with a resolution of 5 μm inside a vacuum chamber. Sample is mounted on a cryogenic stage (inside the vacuum chamber) that can cooled down the sample up to ~4.5 K using a closed-cycled liquid helium system, with a vibration level inferior to 1 micron. An electrical resistance in the sample stage is used to warm up the sample up to ~420 K. On top of the probe station an optical system consisted of a zoom lens system connected with a camera allows visualising the displacements of the micropositioning probes on the sample in order to contact the tips onto the electrodes. In order to avoid parasitic capacitances, coaxial cables were used from the impedance analyser to the probe arms.

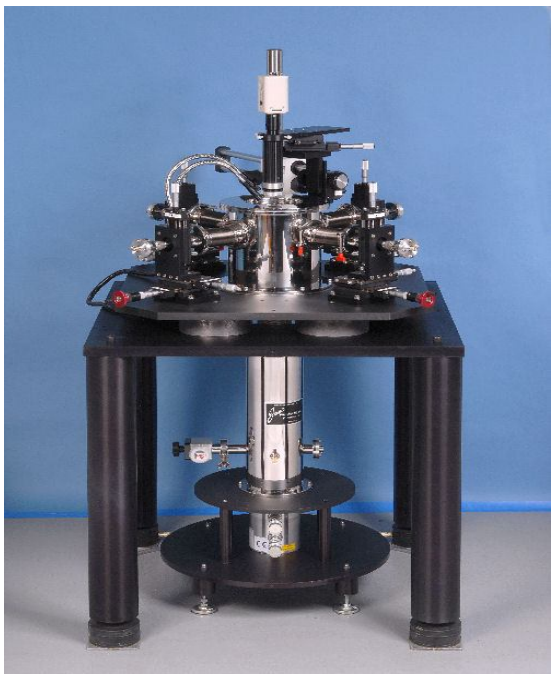

Fig. 2.19 – *Cryogenic micropositioning probe station (Janis Research Co.).*

On the other hand, magnetodielectric measurements, *i.e.* dielectric measurements carried out under applied magnetic field, were performed in a Physical Properties Measurement System (PPMS) of Quantum Design Co. placed at the *Institut de Ciència de Materials de Barcelona (ICMAB, CSIC)* by Dr. I. Fina. This equipment allows a temperature range of 4 K – 400 K and applying magnetic fields up to 9 T, while an electric field is applied to the sample by means of the impedance analyser, in our case LF4182 of Agilent Co. The sample is set in a sample tray with electric pins that are connected by coaxial cables to the impedance analyser. Top electrodes connexion with the electric pins is made by pasting tungsten wires.

Additionally, an external collaboration was established with the *Dpto. Física Aplicada III (University Complutense de Madrid)*, in which Dr. R. Schmidt performed magnetodielectric measurements of our Pt/$BiMnO_3$/Nb:$SrTiO_3$ capacitors (see Chapter 3), using a PPMS (Quantum Design Co.) and Quadtech Impedance Analyser.

The simulation and fitting of impedance data was carried out by the commercial software ZView.

2.5.3 Ferroelectric characterisation

A) Electric characterisation of the ferroelectric properties

Electric measurements for ferroelectric characterisation (see chapter 3) were performed by Dr. I. Fina in a PPMS (Quantum Design Co.) placed at *Institut de Ciència de Materials de Barcelona (ICMAB, CSIC)* using the commercial ferroelectric tester TF Analyzer 2000 (AixACCT Co.) as pulse generator and current detector. Triangular voltage pulses of typically 25 μs of rise time were used.

B) Structural characterisation of the ferroelectric properties

The ferroelectric phase transition of $(Bi,La)_2NiMnO_6$ films was studied in collaboration with the group headed by Dr. B. Dkhil in the *Laboratoire Structures, Propriétés et Modélisation des Solides, UMR CNRS-Ecole Centrale Paris* (France). The transition temperature was investigated by means of structural changes using

temperature-dependent X-ray diffraction (XRD) and Raman Spectroscopy. The experiments were performed by P. Gemeiner and Dr. B. Dkhil.

Temperature-dependent XRD

Temperature-dependent XRD measurements consist of the same procedures explained in Sect. 2.2.1, but equipped with a sample stage which allows modifying and stabilising the sample temperature (range 200 K to 460 K was used). A high accuracy, two-axis diffractometer in Bragg-Brentano geometry using Cu- K_α wavelength was used, with resolution in 2θ angle below 0.002º.

Raman Spectroscopy

Raman Spectroscopy is based on inelastic scattering of monochromatic light (usually from a laser) when interacts with the matter. The monochromatic photons are absorbed by the sample and then reemitted with a frequency shifted due to the interaction with the phonons of the crystal structure. This technique is, therefore, very sensitive to structural changes, in particular to ferroelectric phase to paraelectric phase transitions.

Raman spectra were recorded between 80 K and 620 K with a temperature step of 20K using a T64000 triple Raman spectrometer (Jobin-Yvon-Horiba).

References

[1] D. B. Chrisey and G. K. Hubler, *Pulsed Laser Deposition of Thin Films*, John Wiley & Sons, Inc, New York, NY, 1994.

[2] R. Eason, *Pulsed Laser Deposition of Thin Films*, John Wiley & Sons, Inc, New York, NY, 2007.

[3] M. Ohring, *Materials Science of Thin Films: Deposition and Structure*, Academic Press, San Francisco, 2002.

[4] B. Roas, L. Schultz and G. Endres, Appl. Phys. Lett. **53** 1557 (1988).

[5] D. H. Kim and H. S. Kwok, Appl. Phys. Lett. **67** 1803 (1995).

[6] J. –H. Park, E. Vescovo, H. –J. Kim, C. Kwon, R. Ramesh and T. Venkatesan, Nature **392** 794 (1998).

[7] "Powder Diffraction File, version 2; Joint Comitee of Powder Diffraction Standards" (2002), International Centre for Diffraction Data, 12, Campus Blvd, Newton Square, Pennsylvania 19073-3273, USA.

[8] J. Als-Nielsen, D. McMorrow, *Elements of Modern X-Ray Physics*, John Wiley & Sons Ltd, Chichester UK, 2011.

[9] V. R. Galakhov, M. Demeter, S. Bartkowski, M. Neumann, N. A. Ovechkina, E. Z. Kurmaev, N. I. Lobachevskaya, Ya. M. Mukovskii, J. Mitchell, D. L. Ederer, Phys. Rev. B **65** 113102 (2002).

Chapter 3

Electric measurements

3.1 Parallel-plate capacitors fabrication

In order to assess the dielectric and resistive properties of the multiferroic material, *i.e.* in order to apply an electric field and measuring the electric response, electrodes should be used. The easiest configuration is the so-called parallel-plate capacitors, in which the insulating multiferroic film is inserted between two electrodes (Fig. 3.1).

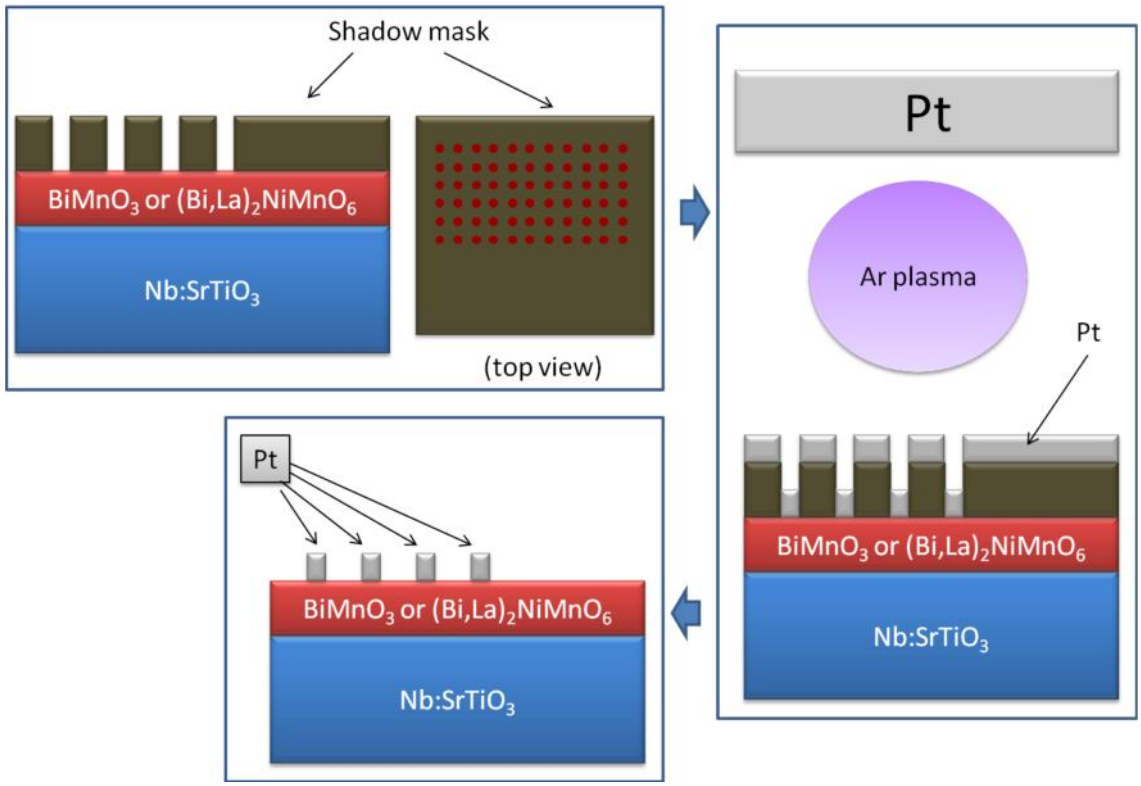

Fig. 3.1 – *Scheme of the process of parallel-plate capacitors fabrication.*

The process of fabricating the parallel-plate capacitors in this work is explained in the following and depicted in Fig. 3.1. Commercial conductive substrate was used as a bottom electrode: 0.5 % Nb doped $SrTiO_3$ (Nb:$SrTiO_3$) as it has practically identical structural features of non-doped insulating $SrTiO_3$. Next the multiferroic film is grown by PLD as described in Sect. 2.1.2. Top electrode, instead, is made ex-situ of the PLD process chamber. A shadow mask is used, in which lines of different-diameter round-shaped holes are patterned. The mask is put into contact with the film by mechanical pressure inside a radio frequency (RF) sputtering chamber. This deposition technique is

based on the bombardment of a target by ions of a plasma, in our case Ar plasma. Platinum is sputtered using, typically, $3 \cdot 10^{-3}$ mbar of pressure of Ar plasma with a typical value of 20 W of power, attaining a usual thickness of 200 nm on the film. Thus, several top electrodes are obtained on the film when the masked is removed. Typical area of the top electrodes used in this thesis was 0.25 mm of radius (round-shaped area).

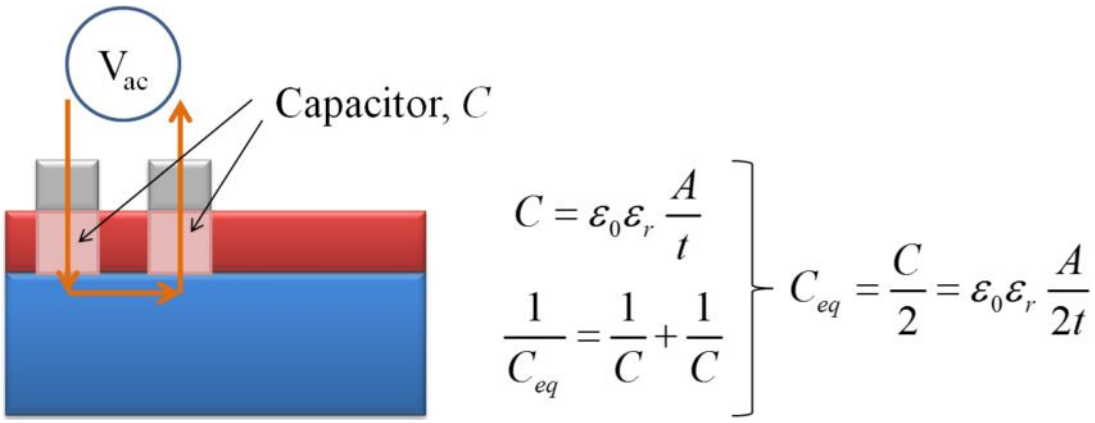

Fig. 3.2 – *Scheme of electric measurements from top to top electrode in the parallel-plate capacitor configuration. C_{eq}, A, t, ε_0 and ε_r stand for equivalent capacitance, area of the top electrodes, thickness, vacuum dielectric permittivity and relative permittivity of the film, respectively.*

In this geometry, the electric field is applied perpendicular to the film from top to top electrode (Fig. 3.2), which entails measuring two identical capacitors connected in series, each with a distance *t* between electrodes (which is the multiferroic film thickness). Equivalently, it can be considered measuring one unique capacitor of distance between electrodes of *2·t* (Fig. 3.2).

Top electrodes were deposited in a RF sputtering chamber placed at the *Institut de Ciència de Materials de Barcelona (ICMAB, CSIC)* by Dr. I. Fina and in a home-made RF sputtering chamber placed at the *Departament de Física Aplicada i Òptica (University of Barcelona)* in the research group *Energia Solar* under the supervision of Dr. A. Antony.

3.2 Dielectric and resistive measurements of dielectric thin films

3.2.1 Impedance spectroscopy

When measuring the dielectric response (*i.e.* the capacitance) of a dielectric material an ac voltage is required to be applied. An impedance analyser (Sect. 2.5.2) was used as ac voltage generation and analysis of the impedance response of the dielectric. The impedance is generally given by the modulus, $|Z|$, and the phase, θ, in the complex representation: $Z^* = |Z|e^{i\theta} = Z' + i\,Z''$, where $Z' = |Z|\cos\theta$ and $Z'' = |Z|\sin\theta$ are the real and the imaginary part, respectively. When perfect insulator, the multiferroic film should behave as an ideal capacitor:

$$Z_C^* = \frac{-i}{\omega C} = \frac{1}{\omega C} e^{i\cdot\left(-\frac{\pi}{2}\right)} \tag{3.1}$$

where C and ω stand for the capacitance of the dielectric and the angular frequency ($2\pi\nu$) of the applied alternating voltage, respectively. Thus, the phase, θ, should be -90º.

Nonetheless, perfect insulators do not exist in nature, let alone multiferroics, which tend to show poor insulating features. Hence, when an electric field is applied to the sample, part of voltage is used to charge the capacitor, regarded as displacement current, I_{DE}, but some small part produces an electric current to flow through, which is called leakage, $I_{leakage}$, as depicted in Fig. 3.3. Therefore, the impedance response of a leaky capacitor (*i.e.* a multiferroic film in our case) can be modelled by a resistor, R, and a capacitance, C, connected in parallel, in which the former accounts for the leakage, whereas the latter accounts for the dielectric character (Fig. 3.3) [1 - 6].

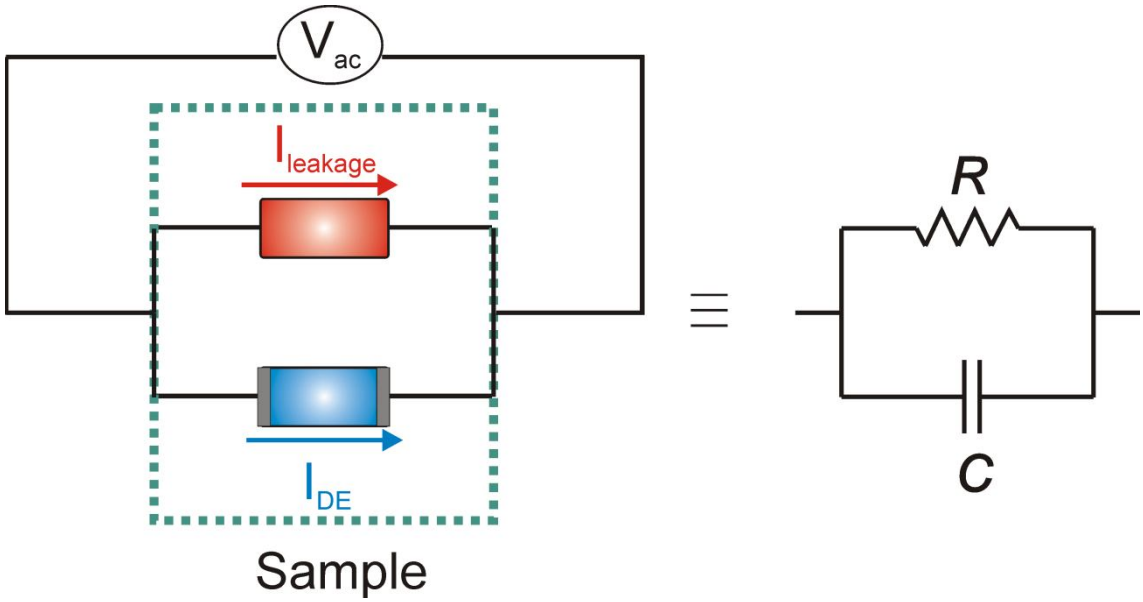

Fig. 3.3 – *Equivalent circuit of a leaky dielectric.*

The impedance of the so-called *RC*-element is given by:

$$\left.\begin{array}{l} Z_R^* = R \\ Z_C^* = \dfrac{1}{i\cdot\omega C} \end{array}\right\} \Rightarrow Z_{RC}^* = \frac{1}{\dfrac{1}{R}+i\cdot\omega C} = \frac{R}{1+i\cdot\omega RC} = \frac{R}{1+\omega^2C^2R^2} - i\cdot\frac{\omega R^2C}{1+\omega^2C^2R^2} \qquad (3.2)$$

Note that for $R \rightarrow \infty$, *i.e.* a quite insulating film, we recover expresion 3.1, *i.e.* $Z^*_{RC} \rightarrow Z^*_C$ and thus θ being close to -90º.

However, for typical values of the resistivity found in multiferroic materials, 10^6 Ω·cm, and considering a moderate/relatively large dielectric permittivity according to a ferroelectric material, ε_r =125, [7 - 11], the phase, θ, of the impedance response of a 100 nm film displays a dependency on the frequency of the applied ac voltage, *i.e.* θ is no longer close to –90º in the whole frequency range, as shown in the simulation of Fig. 3.4. Actually, the leaky dielectric film (*RC*-element) behaves as a capacitor for high frequencies ($\theta \sim$ –90º), whereas for low frequencies it behaves as a resistor ($\theta \sim$ 0º). This is also corroborated by the modulus of the impedance, $|Z|$, which acquires a constant value at low frequencies (indicating the resistance value, R), whereas at high frequencies it decreases at a constant logarithmic rate: $\Delta\log|Z| \sim -\Delta\log|\omega|$, characteristic of a capacitor. This impedance response can be demonstrated by computing the limit of

Eq. 3.2 when $\omega \rightarrow \infty$, in which expression 3.1 is obtained, and when $\omega \rightarrow 0$, in which we obtain $Z^*_{RC} \rightarrow R$. Hence, the impedance measured of a leaky dielectric at low frequencies is dominated by the leakage current, $I_{leakage}$, whilst at high frequencies it is the displacement current, I_{DE}.

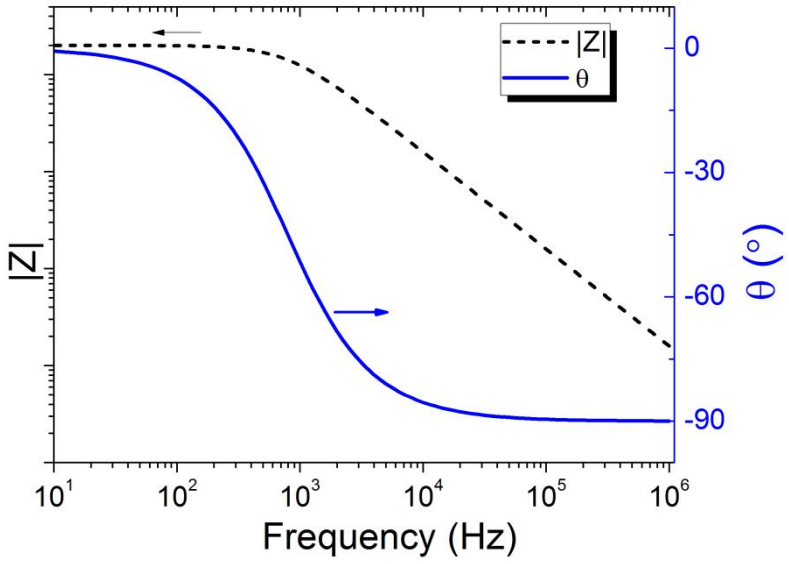

Fig. 3.4 – *Simulation of the impedance response of an RC-element. The dashed line shows the frequency dependence of |Z| (left axis), whereas the solid line shows the frequency dependence of θ (right axis).*

On the other hand, the resistivity, ρ, of insulating dielectrics shows a semiconductor-like temperature dependence, $\rho(T)$, thus following an Arrhenius law [8, 12, 13]:

$$\rho = \rho_0 \exp\left(\frac{E_a}{k_B T}\right) \tag{3.3}$$

where E_a and k_B are the activation energy (related to the energy gap) and the Boltzman constant, respectively. Using typical values of E_a of multiferroic materials, 0.2 eV [5, 8, 13], and applying Eq. 3.3 to the example of Fig. 3.4, a temperature evolution of the impedance response is found as shown in the simulation plotted in Fig. 3.5. Accordingly, the resistive character of the dielectric film (*i.e.* $\theta \sim 0^o$) is present on higher frequencies of the spectra on increasing temperature just due to the reducing resistivity of the *RC*-element upon temperature (Eq. 3.3). Note that the capacitance was

considered temperature independent in this simulation. Thus, the frequency transition, ω_{max}, between the dielectric and resistive region of the frequency spectra is shifted to higher frequencies on decreasing the resistivity of the material, accomplishing the relation $\omega_{max}(T) = 1/\tau(T) = [R(T)\cdot C]^{-1}$, where τ is the time constant of the equivalent circuit representing the leaky dielectric.

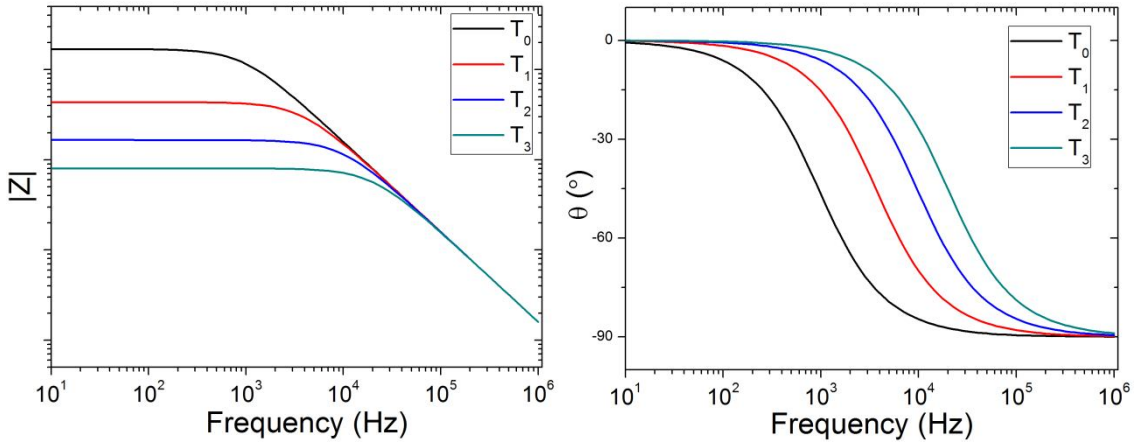

Fig. 3.5 – *Simulation of the frequency dependence of the impedance modulus (left) and phase (right) of a leaky dielectric at different temperatures, $T_0 < T_1 < T_2 < T_3$, where $\Delta T = 20$ K.*

It is worth mentioning, though, that few real dielectric systems can be represented by a pure *RC*-element [1, 8, 14 – 18]. Most dielectrics deviate from the ideal behaviour, including the ones studied in this thesis, showing slightly larger values than –90º of the phase of the impedance response in the frequency spectra region where the dielectric character contribution dominates over the resistive one. In order to account for this non-ideality, the capacitance, *C*, is usually replaced by the so-called phenomenological Constant Phase Element, *CPE* [1, 8, 15, 17, 18], whose impedance response is given by

$$Z^*_{CPE} = \frac{1}{Q\cdot(i\cdot\omega)^{\alpha}} \tag{3.4}$$

where Q and α ($\alpha \leq 1$, being $\alpha = 1$ the ideal capacitor) denote the amplitude and the phase of the *CPE*, respectively. Thus, leaky non-ideal dielectrics can be modelled by a *R-CPE* element (*R* and *CPE* connected in parallel), giving the following impedance response:

$$Z^*_{R-CPE} = \frac{R}{1 + RQ(i \cdot \omega)^{\alpha}} \tag{3.5}$$

Yet Q does not have the dimension of capacitance, *i.e.* [F], but its units are given by [$F \cdot s^{(\alpha-1)}$]. Such CPE 'capacitance' can be converted to real capacitance, C, which is the real dielectric response, according to the relationship $C = (Q \cdot R)^{(1/\alpha)}/R$ [8, 19 – 21] (deduced in Appendix C).

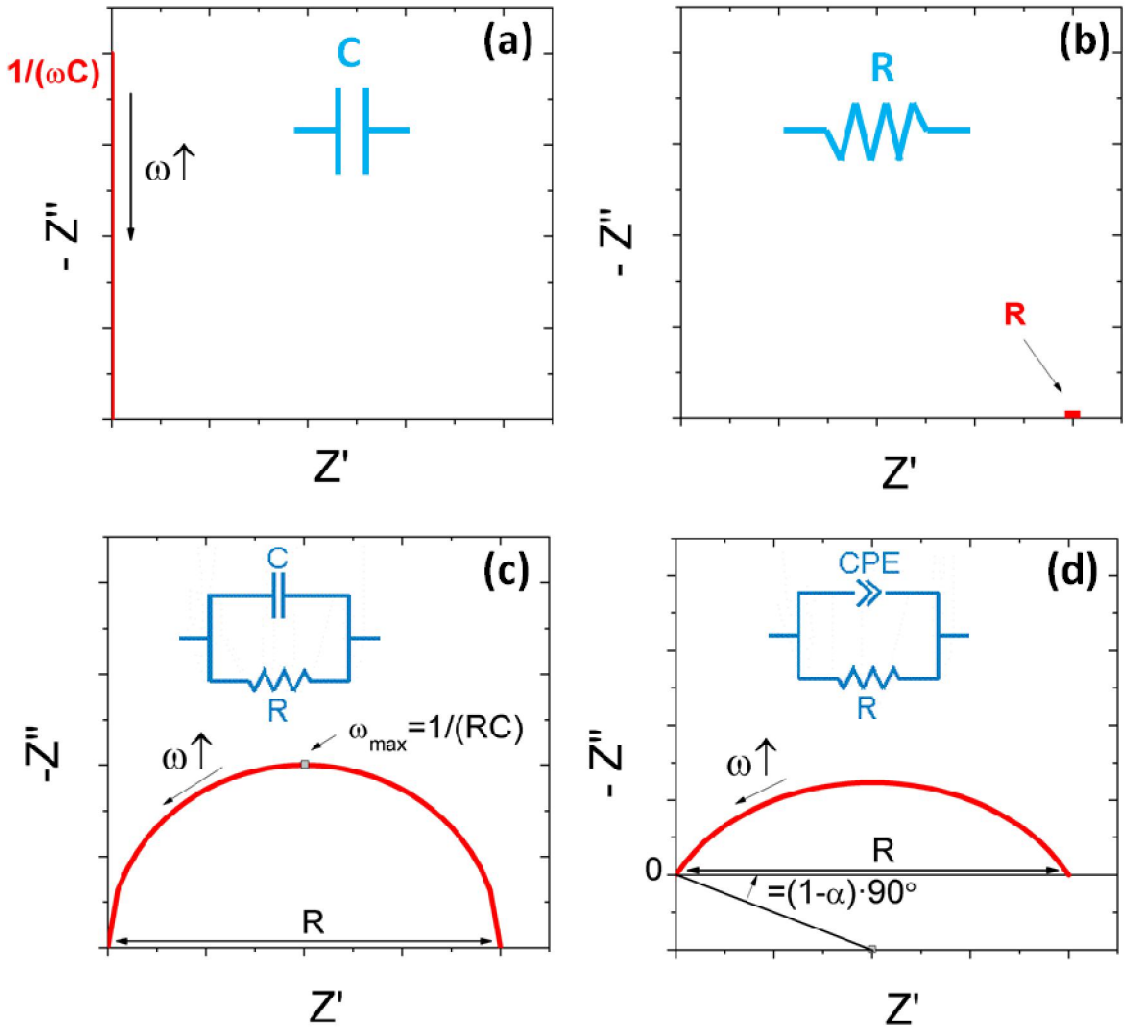

Fig. 3.6 – *Nyquist plots (–Z" vs Z' plots) of a* **(a)** *capacitor,* **(b)** *resistor,* **(c)** *RC-element and* **(d)** *R-CPE element.*

A useful representation of the recorded impedance data consists of plotting the negative of the imaginary part *–Z"* as a function of the real part *Z'*. In these impedance complex planes, also known as Nyquist plots [1], a perfect insulator should depict a

vertical straight line on the *–Z"* axis (*i.e. Z'* = 0), in which, on increasing frequency ω, Z^*_C approaches to zero following Eq. 3.1 [Fig. 3.5 (a)]. Instead, a resistor should depict a point in the *Z'* axis [Fig. 3.5 (b)], which indicates the value of the resistance. Thus, using Eq. 3.2, a dielectric material modelled by a *RC*-element should depict a semicircle [Fig. 3.5 (c)], centred in the *Z'* axis and of radius R/2, in which on increasing frequency, Z^*_{RC} approaches to origin of coordinates [1 – 3, 5, 6, 8]. The angular frequency of the applied voltage at which the semicircles shows the maximum accomplishes $\omega_{max} = 1/RC = 1/\tau$ [1 – 3, 5, 6, 8]. The semicircle in the Nyquist plots of a *R-CPE* element is slightly depressed, *i.e.* no longer centred in the *Z'* axis, but slightly below [Fig. 3.5 (d)], forming an angle of $(1-\alpha)\cdot 90^o$ with the *Z'* axis [1, 8]. Note that for $\alpha = 1$, the ideal case, the *RC* semicircle is obtained.

3.2.2 Complex dielectric constant and ac conductivity

In order to assess the frequency response of the dielectric properties, sometimes it is useful to express the dielectric data in terms of the complex dielectric constant, $\varepsilon^* = \varepsilon' - i\cdot\varepsilon''$, which relates to the complex impedance by $Z^*=1/[i\cdot\omega\varepsilon_0\cdot(A/2\cdot t)\cdot\varepsilon^*]$ [1, 2, 8], where $A/(2\cdot t) \equiv G$ is the geometrical factor of the measurement (Fig. 3.2). Thus, using expression 3.2, the complex dielectric response of a leaky dielectric (modelled by a *RC*-element) is given by:

$$\varepsilon^*_{RC} = \frac{1}{i\cdot\omega\varepsilon_0 G Z^*_{RC}} = \frac{-i\cdot(1+i\cdot\omega RC)}{\omega\varepsilon_0 GR} = \frac{C}{\varepsilon_0 G} - i\frac{1}{\omega\varepsilon_0 GR} \tag{3.6}$$

Therefore, unlike the impedance response shown in Eq. 3.2, in the complex dielectric constant notation, the real part, ε', denotes, only, the dielectric character of the material, which can be identified as the relative dielectric permittivity [$C = \varepsilon_0\varepsilon_r A/(2\cdot t)$], whereas the imaginary part, ε'', only shows the resistive character. Note that this is valid for frequency spectra regions where no dielectric relaxation occurs [12, 14, 22, 23]. For the frequency range use in this thesis (up to 1 – 2 MHz), this statement is fulfilled as electric dipole relaxations occur at microwaves frequencies (above 300 MHz) [12, 14, 22, 23] and even at higher frequencies is the occurrence of the dielectric relaxations related to the electronic nature of the ions [12, 14, 22, 23].

Using the same example as that shown in Fig. 3.5, thus with the same temperature dependence of the resistivity, the simulation of the complex notation of the dielectric constant is shown in Fig. 3.7. As a result of Eq. 3.6, ε' remains frequency and temperature independent (note that we have assumed the dielectric permittivity of the material, $\varepsilon = 125$, temperature independent) around the associated capacitance value, $C = \varepsilon'\varepsilon_0 A/(2 \cdot t)$. However, ε'', being almost negligible in the frequency spectra region where the dielectric contribution dominates (high frequencies), notably increases in the frequency spectra region dominating by the resistive contribution (low frequencies). Moreover, on increasing temperature larger values of ε'' are obtained as a result of the decreased resistivity upon temperature [ε'' scales over $1/R$, Eq. 3.6].

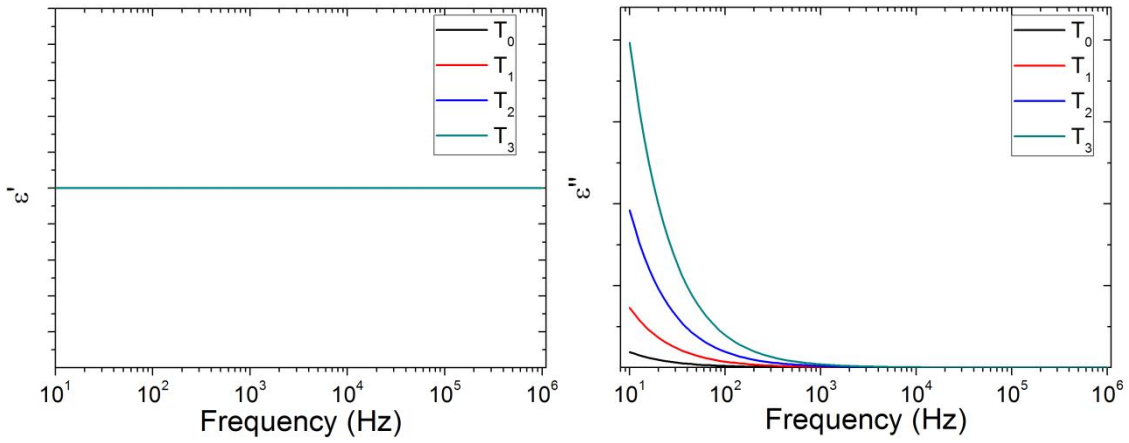

Fig. 3.7 – *Simulation of the frequency dependence of the real part (left) and imaginary part (right) of the complex dielectric constant of the leaky dielectric shown in Fig. 3.5 at different temperatures, $T_0 < T_1 < T_2 < T_3$, where $\Delta T = 20$ K.*

For a non-ideal leaky dielectric (modelled by an *R-CPE* element), ε' shows a small frequency dependence (Fig. 3.8, in which $\alpha = 0.9$ was considered), which follows a $-\omega^{\alpha-1}$ dependence as a result of introducing the *CPE* element contribution in expression 3.6:

$$\varepsilon^*_{R-CPE} = \frac{1}{i \cdot \omega \varepsilon_0 G Z^*_{R-CPE}} = \frac{-i\left[1 + RQ(i\omega)^\alpha\right]}{\omega \varepsilon_0 GR} = -\omega^{\alpha-1}\frac{Qi^{\alpha+1}}{\varepsilon_0 G} - i\frac{1}{\omega \varepsilon_0 GR} \qquad (3.7)$$

Note that for $\alpha = 1$, expression 3.6 is obtained signalling the ideal character.

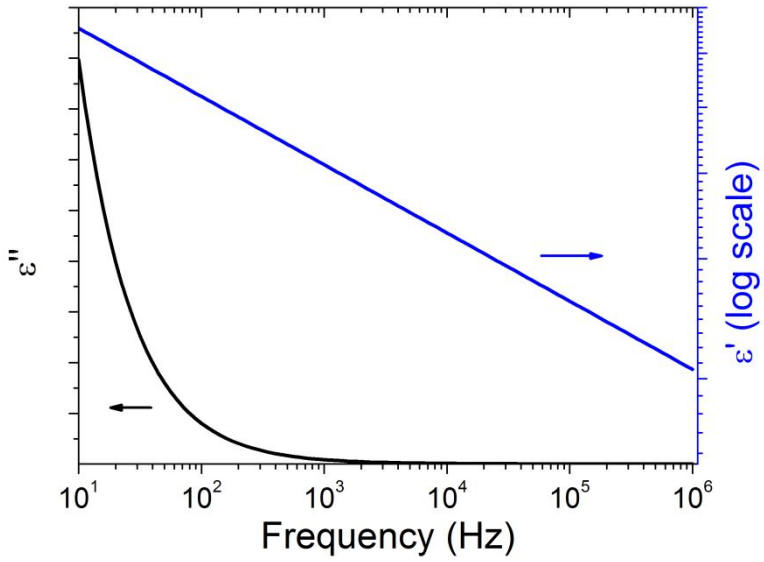

Fig. 3.8 – *Simulation of the complex dielectric constant of non-ideal leaky dielectric (modelled by an R-CPE element). Blue solid line shows the real part in log scale (right axis) and the black solid line the imaginary part (left axis).*

Equivalently, $\varepsilon^* = \varepsilon' - i\cdot\varepsilon''$ is usually replaced by the two figures of merit: the effective capacitance [$C = \varepsilon'\varepsilon_0 A/(2\cdot t)$], and the loss tangent or dissipation factor ($\tan\delta = \varepsilon''/\varepsilon'$) [14].

On the other hand, when an alternating current (ac) voltage is applied, data can also be analysed by the complex conductivity, $\sigma^* = i\cdot\omega\varepsilon_0\varepsilon^*$ [8, 14, 16, 18], from the real part of which, σ', much information about the dielectric can be deduced. In an ideal dielectric (characterised by an *RC*-element), the complex conductivity follows [14, 16, 18]:

$$\sigma^* = \sigma_{dc} + i\cdot\omega\varepsilon_0\varepsilon' \tag{3.8}$$

where the real part, $\sigma' = \sigma_{dc}$, corresponds to the frequency-independent direct current (dc) conductivity, which is always present due to the leakage (related to the *R* of the equivalent circuit, Fig. 3.3). Thus, the resistivity of the dielectric can be extracted by computing $\rho = 1/\sigma_{dc}$. However, when nonideality is taking into account, *i.e.* replacing

ideal capacitor *C* by a *CPE*, σ' is no longer frequency independent [14, 16, 18] but follows:

$$\sigma' = \sigma_{dc} + \sigma_0 \cdot \omega^{\alpha} \tag{3.9}$$

where the frequency-dependent term, $\sigma_{ac} = \sigma_0 \cdot \omega^{\alpha}$, showing the typical power-law dependence on frequency, corresponds to the Jonscher's universal dielectric response [14, 16, 18].

Thus, by extrapolating σ' data values toward zero frequency the resistivity of the material can be computed ($\rho = 1/\sigma_{dc}$).

3.2.3 Extrinsic contributions to the dielectric measurements

When performing dielectric measurements onto a sample, *i.e.* when applying an ac voltage to a dielectric material, it is widely known that extrinsic electric contributions can contribute to the total dielectric response [2 – 6, 8, 13, 16, 24 – 27]. In ceramic and polycrystalline samples parasitic capacitance are formed at the grain boundaries as a consequence of the different resistivity compared to that of the core of the grains. Additionally, at the interface between the electrode and the dielectric material, a capacitive layer, with high resistivity, tend to be formed as a consequence of the difference between the work function of the metal and the electronic affinity of the dielectric, causing a charge depletion/accumulation region which electrically behaves different from the core of the material. Irrespective of the origin, due to the different electric performance, each of these electric contributions to the total dielectric response of the system can be considered as though they were different dielectric materials and, hence, be modelled by an *RC*-element (*R-CPE* in non-ideal cases) [2 – 6, 8, 13, 16, 24 – 27]. For the sake of comprehension, only ideal cases will be considered in this section.

In our case, in which epitaxial thin films are obtained, the effect of the grain boundaries is diminished to a large extent (epitaxial thin films behave as a single crystal). Yet the electrode-film interface electric contribution cannot be neglected. Thus,

the real impedance response of the measurement is given by two *RC*-elements connected in series:

$$Z^*_{(R_iC_i,\mathrm{R_e}C_e)} = \frac{R_i}{1+i\cdot\omega R_iC_i} + \frac{R_e}{1+i\cdot\omega R_eC_e} \tag{3.10}$$

where R_i and R_e denote the intrinsic and extrinsic resistance, respectively, whereas C_i and C_e denote the intrinsic and extrinsic capacitance, respectively, of the equivalent *RC*-circuits. In the following, the intrinsic properties, R_i and C_i, refer to the dielectric properties of the dielectric film, while the extrinsic properties, R_e and C_e, refer to the dielectric properties of the interface capacitance.

By computing the complex dielectric constant, $\varepsilon^*=1/[i\cdot\omega\varepsilon_0 GZ^*]$, the real part, ε', no longer denotes the dielectric character solely as stated in expression 3.6, but follows a much more complex expression:

$$\varepsilon' = \frac{1}{\varepsilon_0 G\left(R_i+\mathrm{R}_e\right)} \frac{R_iC_i+\mathrm{R}_e\,Ce-\dfrac{R_i\,\mathrm{R}_e\left(C_i+C_e\right)}{R_i+\mathrm{R}_e}+\omega^2R_iC_i\,\mathrm{R}_e\,C_e\dfrac{R_i\,\mathrm{R}_e\left(C_i+C_e\right)}{R_i+\mathrm{R}_e}}{1+\omega^2\left(\dfrac{R_i\,\mathrm{R}_e\left(C_i+C_e\right)}{R_i+\mathrm{R}_e}\right)^2} \tag{3.11}$$

Therefore, it is no longer valid assuming that the measured real part of the complex dielectric response corresponds to the dielectric permittivity of the dielectric thin film.

The imaginary part follows:

$$\varepsilon'' = \frac{1}{\varepsilon_0 G\omega\left(R_i+R_e\right)} \frac{1-\omega^2R_iC_iR_eC_e+\omega^2\dfrac{R_iR_e\left(C_i+C_e\right)}{R_i+R_e}\left(R_iC_i+R_eC_e\right)}{1+\omega^2\left(\dfrac{R_iR_e\left(C_i+C_e\right)}{R_i+R_e}\right)^2} \tag{3.12}$$

In the following simulation, we have used the same example considered in Sect. 3.2.2, but adding an interfacial extrinsic resistance much larger than that of the film, $R_e >> R_i$, (as they behave as a highly resistive barriers [2, 4, 8, 16]) and an interfacial extrinsic capacitance of 10 nF, one order of magnitude larger than that of the film. Note

that interfacial thickness is much thinner than that of the core of the film, so that interfacial capacitance tend to be larger as inferred by the fact that the capacitance scales over the inverse of thickness, $C = \varepsilon A/(2t)$ [4]. The frequency dependence of real part, ε', of the dielectric response of the total system (extrinsic + intrinsic contribution) has been computed (Fig. 3.9). As observed, ε' greatly differs from the behaviour of the expected ε' of a pure leaky dielectric (Fig. 4). In this case, $\varepsilon'(\nu)$ is separated by two plateaus: high-frequency and low-frequency.

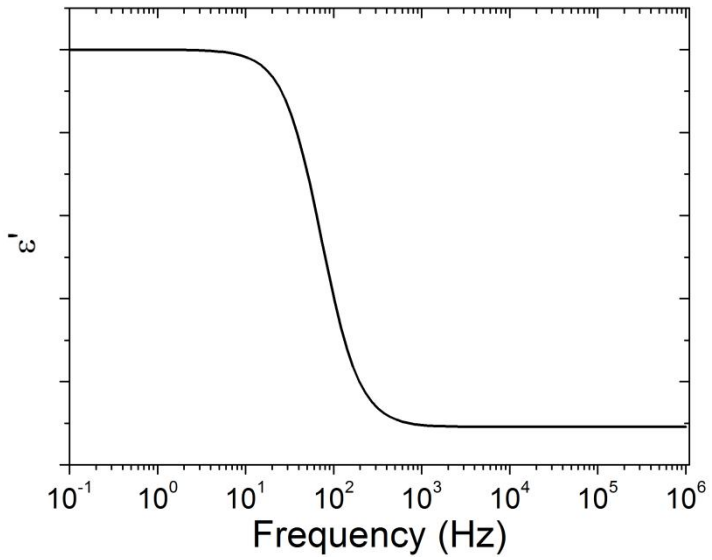

Fig. 3.9 – *Simulation of the real part of the complex dielectric response of a leaky dielectric film + interface electrode-film contribution.*

Computing the limit when $\omega \to \infty$ and when $\omega \to 0$ in expression 3.11, it can be deduced:

$$\varepsilon'_{\omega\uparrow\uparrow} \sim \frac{1}{\varepsilon_0 G}\frac{C_i C_e}{C_i + C_e}$$
$$\varepsilon'_{\omega\downarrow\downarrow} \sim \frac{1}{\varepsilon_0 G\left(R_i + R_e\right)^2}\left(R_i^2 C_i + R_e^2 C_e\right) \tag{3.13}$$

thus, the dielectric permittivity extracted from the high-frequency plateau corresponds to the equivalent capacitance of two capacitors, C_i and C_e, connected in series, *i.e.* the intrinsic and extrinsic capacitance; whereas the low-frequency dielectric response is highly altered by the interface and film resistivity.

Sometimes when analysing dielectric data, measurements are performed at one single-frequency and the real part of the complex dielectric constant is used to evaluate the dielectric permittivity of the material under test, using expression 3.6. This is misleading since, even at a high frequency, there is contribution of both extrinsic and intrinsic dielectric contributions. Only when $C_e >> C_i$, $\varepsilon'_{\omega\uparrow\uparrow}$ can be considered the intrinsic dielectric permittivity of the material under test. On the other hand, only when $C_e >> C_i$ and/or $R_e >> R_i$, $\varepsilon'_{\omega\downarrow\downarrow}$ signals the dielectric response of the interfacial parasitic capacitance. Note that in the example exposed in this section $R_e >> R_i$ is accomplished.

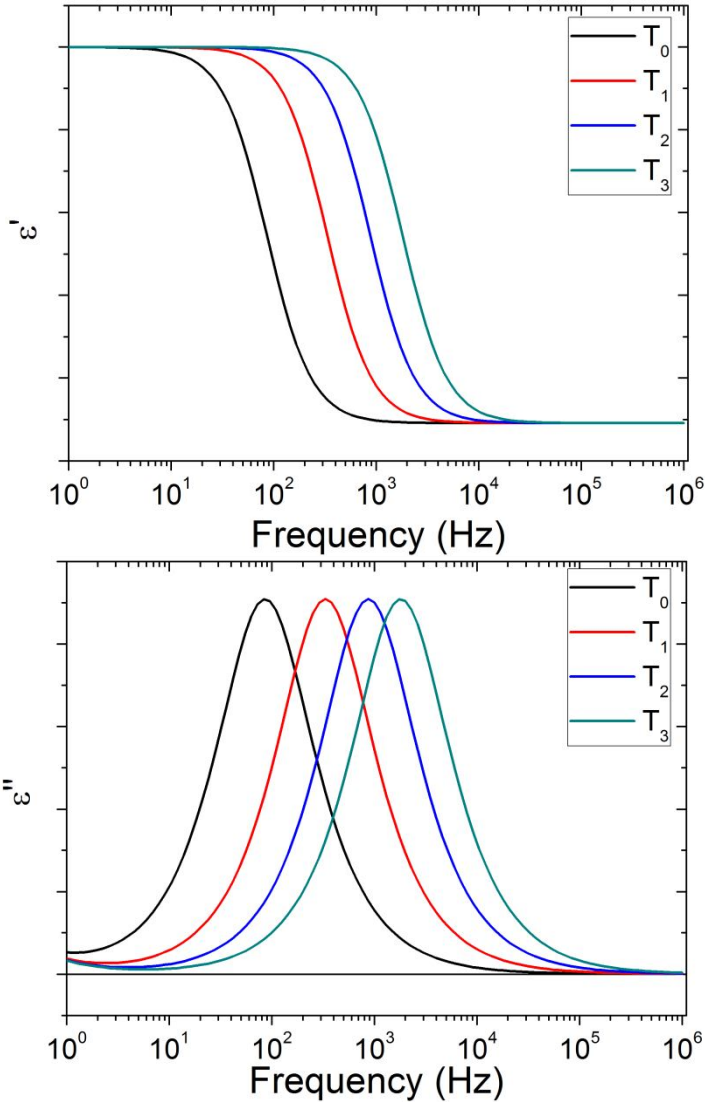

Fig. 3.10 – *Simulation of the dielectric response of a system formed by leaky dielectric film, with temperarture-dependent resistivity, and interface electrode-film, at different temperatures, $T_0 < T_1 < T_2 < T_3$, where $\Delta T = 20$ K.*

Assuming that the temperature dependence of the intrinsic resistivity of the dielectric material, R_i, is given by expression Eq. 3.3, whilst considering C_i, C_e and R_e temperature independent, the temperature evolution of $\varepsilon'(\nu)$ and $\varepsilon''(\nu)$ (expressions Eq.

3.11 and 3.12) are computed (Fig. 3.10). As observed, the dielectric response clearly resemblances to a temperature-dependent dielectric relaxation [14]. However, in this case no proper dielectric relaxation of electric dipoles is inferred as in this simulation C_i, *i.e.* the intrinsic dielectric permittivity of the material, $\varepsilon_r = 125$, is assumed temperature and frequency independent. Hence, as a matter of fact, two electric contributions in the dielectric response of a system (modelled by two *RC*-elements) can evoke an apparent dielectric relaxation. This kind of relaxation, which is quite often reported in many dielectric materials showing extrinsic contributions [2 – 6, 8, 13, 16, 24 – 27], is usually referred as a Maxwell-Wagner type. Moreover, the temperature evolution of this relaxation is driven by the temperature dependence of the resistance of either of each *RC*-element.

Thus, simulations in Fig. 3.9 and 3.10 unambiguously imply that attempts to determine the intrinsic dielectric permittivity by single fixed frequency measurements in the presence of an extrinsic dielectric contribution may generally be doubtful, especially at elevated temperature and/or low frequency.

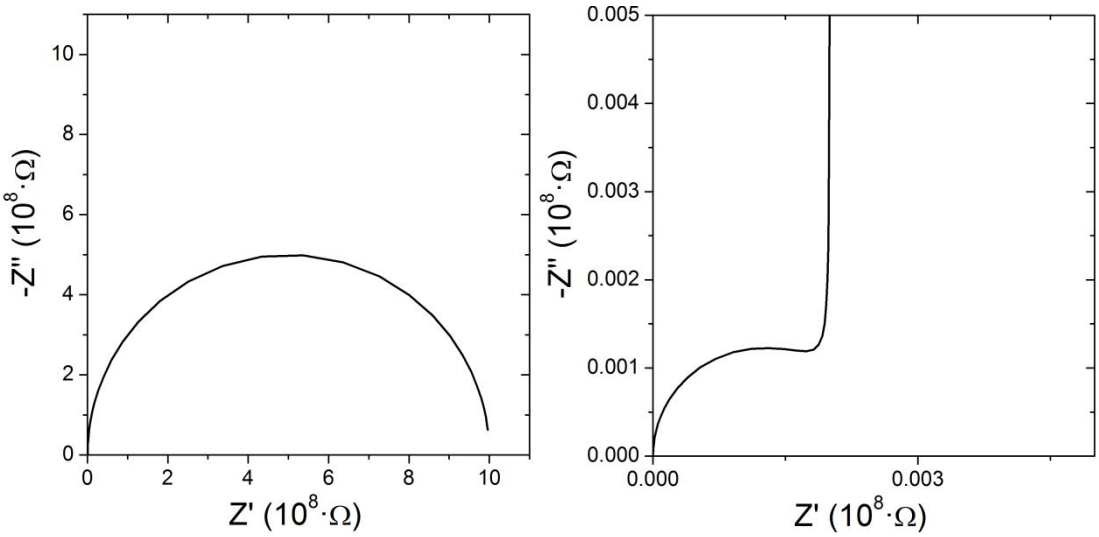

Fig. 3.11 – *Simulation of the impedance response of a system formed by leaky dielectric film and an interface electrode-film. Right figure shows the high-frequency region, zoomed from the left figure.*

As each electric contribution (intrinsic dielectric material, interface capacitances, grain boundaries, ...) will be signalled by semicircle in the Nyquist plots (Fig. 3.6), a

very useful way to determine the number of electric contributions present in the system under test consists of plotting the measured impedance data as –Z" as a function of Z'. In the particular case treated in this section, in which we have considered two electric contributions (interfacial capacitance and dielectric film), computing Eq. 3.10 will give as a result two incomplete semicircles in the impedance complex planes (Fig. 3.11). Note that as we have assumed $R_e >> R_i$, low-frequency semicircle is much larger than that of high-frequency. As a consequence the high-frequency semicircle is only able to be observed by zooming the high frequency region of the Nyquist plot (Fig. 3.11 right).

It is also worth mentioning that the experimental set up may also contribute to the impedance response of the measurement. This contribution consists, basically, of the resistance of the measurement probes and cables and the inductance of the cables. The former can be accounted by adding a single resistor, R_0, in series to the equivalent circuit of the system, whereas the latter can be accounted by adding a single inductance element, L_0, in series [8].

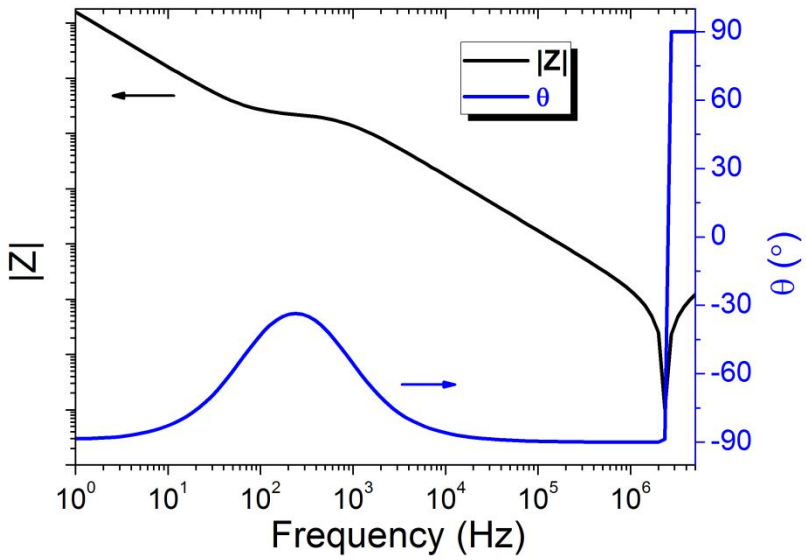

Fig. 3.12 – *Effect of the inductance of the experimental set up in the frequency response of the impedance of a system formed by a leaky dielectric film and an interface capacitance. The blue solid line signals the phase of the impedance, whereas the black solid line the modulus of the impedance.*

It is worth noting that inductance of cables may have a significant contribution at high frequencies (as $Z_L = i \cdot \omega L$), which can mask the high frequency dielectric data and thus giving rise to misleading interpretation of the results. In our experimental set up L_0

was found to be ~10^{-6} H. Adding this L_0 value to the system of interface capacitance and dielectric film, the impedance response is given in Fig. 3.12. As observed, at low frequencies and intermediate-high frequencies the phase of the complex impedance is close to -90º, signalling C_e and the equivalent capacitance of C_e and C_i in series, respectively. These two frequencies regimes are separated by a phase peak, indicating the Maxwell-Wagner relaxation. However, at the highest frequencies, the phase is rapidly increasing toward +90º, pointing out that the inductance is completely dominating the frequency spectra of the impedance data. This fact limits, to a large extent, extracting the intrinsic dielectric properties at high frequencies.

3.2.4 Magnetocapacitance measurements.

As stated in Sect. 1.1.3, one indirect consequence of the coupling between the magnetic and the ferroelectric order is the magnetic dependence, H, of the dielectric permittivity, ε. This fact has promoted a flurry of research based on magnetocapacitance measurements, *i.e.* measuring ε under different H, of possible candidates to display magnetoelectric coupling such us multiferroics or nanocomposites formed by ferroelectric and magnetic materials [10, 28 – 36]. Magnetocapacitance data is usually shown as a relative change of the dielectric permittivity, *i.e.* MC = $[\varepsilon(H)- \varepsilon(0)]/\varepsilon(0)]$.

It is clear, though, that having a Maxwell-Wagner relaxation, as described in Sect. 3.2.3, magnetocapacitance can also be arisen from changes in the resistivity as long as the resistivity displays magnetic-field dependence (Eq. 3.11). Hence, and important to be noted, magnetocapacitance alone is not a sufficient criterion to signal the occurrence of the coupling between the ferroelectric and magnetic order [4, 35, 37].

For the sake of example, let's assume that the resistivity of the dielectric film of the example exposed in Sect. 3.2.3 decreases on increasing H (*i.e.* displaying negative magnetoresistance), following the relation $\rho(H) \sim \rho(0)\exp(-H/H_0)$, where H_0 is a scaling parameter. Note that this expression is found in well known magnetoresistive materials like (La,Ca)MnO_3 [38]. Assuming H_0 = 20 kOe [38], Fig. 3.13 shows the frequency dependence of the complex dielectric response of the system formed by an interface capacitance and a dielectric film (Sect. 3.2.3).

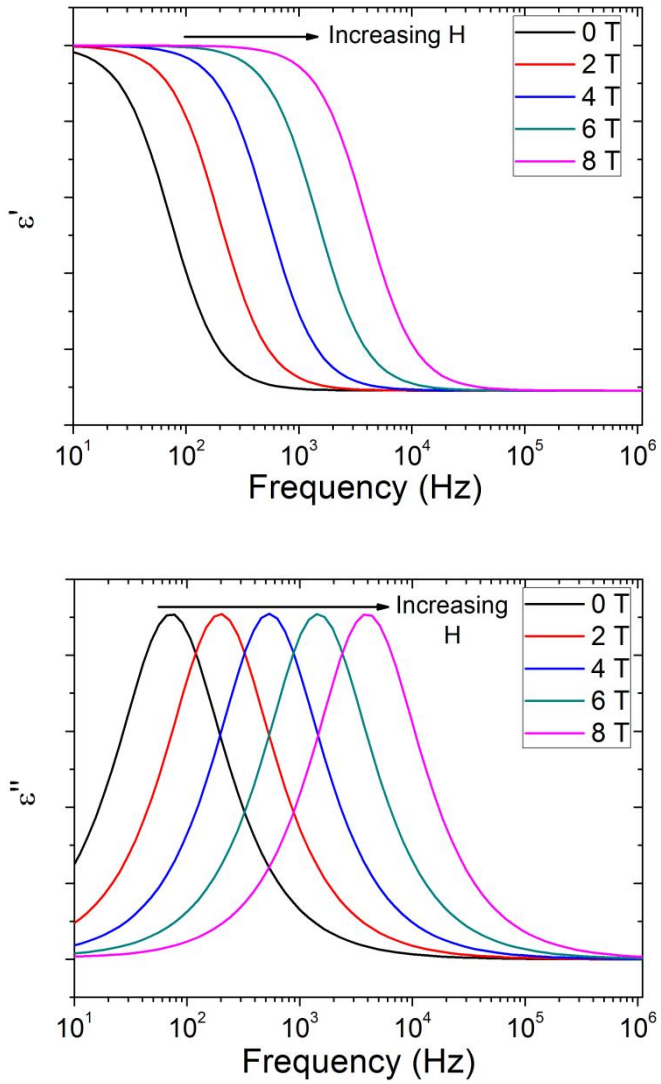

Fig. 3.13 – *Simulation of the frequency dependence of the dielectric response of a system formed by leaky dielectric film, with magnetic-field-dependent resistivity, and interface electrode-film, at different magnetic fields.*

Therefore, according to the simulation shown in Fig. 3.13, measuring the magnetic-field dependence of ε' at one-single frequency will give rise to a positive magnetocapacitance effect, yet not due to a multiferroic coupling but because of the negative magnetoresistance. Note that irrespective of the relation that follows the magnetoresistance (the expression used above does not have to apply for all materials), a negative magnetoresistance would produce a positive magnetocapacitance effect and, conversely, a positive magnetoresistance would produce a negative magnetocapacitance effect, as long as a Maxwell-Wagner relaxation occurs.

A useful way to disentangle magnetoresistive effects from genuine magnetoelectric coupling consist of performing the aforementioned impedance spectroscopy, by means of which, not only the extrinsic dielectric contributions can be determined and consequently ruled out, but also allows deconvoluting the resistive and dielectric character of the dielectric material that is under test.

3.3 Electric characterisation of the ferroelectric properties

The common electric characterisation of the ferroelectric properties consists of recording the polarisation, *P*, on cycling (Fig. 3.14) an applied electric field, *E*, *i.e.* the ferroelectric hysteresis loop.

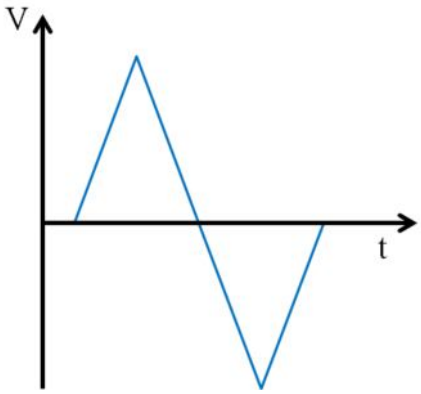

Fig. 3.14 – *Applied triangular voltage signal in a ferroelectric hysteresis loop.*

Nonetheless, what is measured on applying voltage is not the polarisation itself, but the current, *I*. The polarisation is computed by $P = Q/A$ where A is the area of the top electrodes and Q is the measured charge, which is obtained by integrating the measured current over time during the cycle:

$$Q = \int I(t)dt \tag{3.14}$$

In an ideal condition, *i.e.* a perfect insulator, the measured current should correspond to the displacement current, I_{DE} (Fig. 3.3), which, in a ferroelectric, basically consists of the charging current of the capacitor, I_{ε}, and the current related to the ferroelectric domain switching, I_{FE}, *i.e.* $I_{DE} = I_{\varepsilon} + I_{FE}$. Note that I_{ε}, arisen from the

induced polarisation, is responsible for the characteristic non-saturated hysteresis loops in ferroelectrics [39].

However, as pointed out in previous sections, as leakage is present in any dielectric (Fig. 3.3), the current related to the conductive part of the sample, $I_{leakage}$, is also recorded in the measurement, so that the integrated charge is given by:

$$Q = \int I_{DE}(t)dt + \int I_{leakage}(t)dt \tag{3.15}$$

This is one of the main sources of measuring apparent ferroelectric hysteresis loops in non-ferroelectric materials [39 – 41], as described on the following.

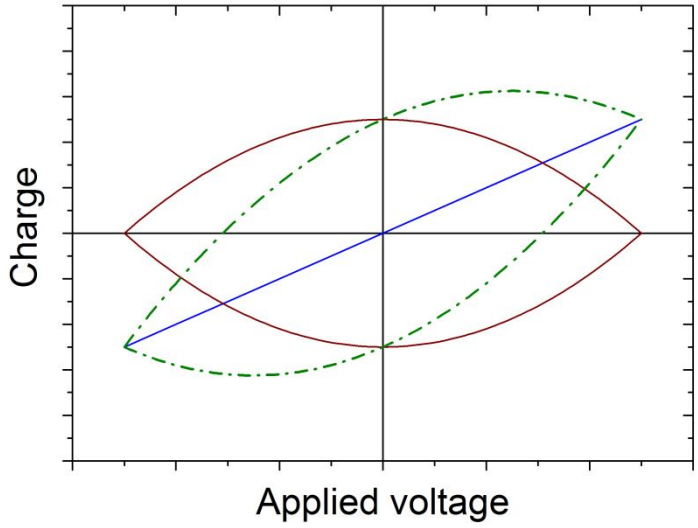

Fig. 3.15 – *Charge as a function of the applied voltage for a resistor (red solid line), a linear dielectric (blue solid line) and a leaky linear dielectric (green dashed-dotted line).*

Considering a pure resistor, $I_{leakage}$ will be proportional to the applied voltage ($I = V/R$), and thus, also to time as we are applying a triangular signal. Then it follows:

$$Q_{leakage} = \int I_{leakage}(t)dt \sim t^2 + K \sim V^2 + K' \tag{3.16}$$

(where K and K' are integration constants) *i.e.* $Q_{leakage}(V)$ will show two parabolas (Fig. 3.15, red solid line), whose concavity is different for the negative and positive slopes of

the voltage signal, giving rise to the characteristic 'rugby-shape' form. Note that the charge at the beginning and at the end of the voltage cycle is not zero. This is due to the algorithm used in the software of the ferroelectric testers that positions the curve symmetrically to the polarisation values (or, equivalently, charge values). The recollected $Q_{leakage}$ will increase on increasing the period of the cycle. Conversely, considering a pure linear dielectric, C, (with no ferroelectric order), the charge will be proportional to the applied voltage ($Q_\varepsilon = CV$), *i.e.* the slope will indicate the capacitance (or, equivalently, the dielectric permittivity) of the dielectric (Fig. 3.15, blue solid line). Hence, it is clear that a leaky linear dielectric ($Q_\varepsilon + Q_{leakage}$) will produce a closed $Q(V)$ loop, resembling a ferroelectric hysteresis loop (Fig. 3.15, green dashed-dotted line). This loop will be increasingly open on increasing the measuring time, *i.e.* the period of the cycle, as $Q_{leakage}$ will increase, contrarily to real ferroelectric hysteresis loop, in which the coercive electric field decreases on increasing the measuring time [39].

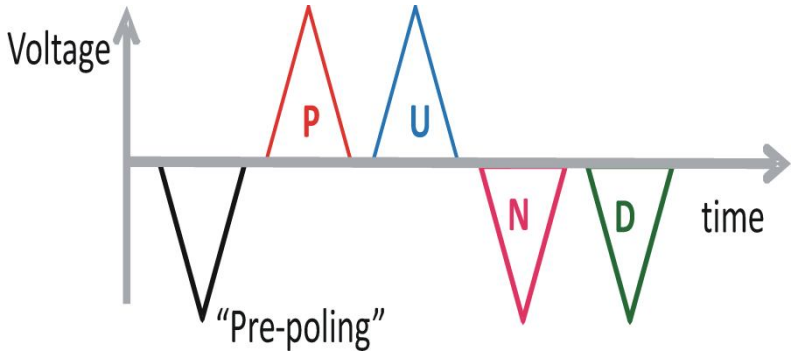

Fig. 3.16 – *Schematic representation of a PUND measurement.*

In order to avoid parasitic contributions, $Q_{leakage}$, to the measured ferroelectric hysteresis loop, the so-called positive-up-negative-down (PUND) technique [42 – 44] tend to be used. PUND technique consists of 5 voltage pulses (Fig. 3.16), in which the current is simultaneously recorded (except for the first pulse). The first one, labelled as 'pre-poling', is negative and serves to polarise the sample to $-P$. The current recorded during the second pulse, which is positive, labelled as P, contains all the contributions: I_ε, I_{FE} and $I_{leakage}$. Instead, the current recorder in the third pulse, labelled as U, only contains I_ε and $I_{leakage}$, as U is also positive and the sample is already polarised, $+P$ (*i.e.* no current is recorded for the ferroelectric domain switching). Using the same arguments, the current recorded in the pulses N and D, I_N and I_D, respectively, follows $I_N = I_\varepsilon + I_{FE} + I_{leakage}$ and $I_D = I_\varepsilon + I_{leakage}$. Thus, by subtracting the current resulting from

the U pulse from that of the P pulse (and similarly D from N) we only obtain the current related to the switching of the ferroelectric domains, I_{FE}.

Thus, by integrating I_{FE} over the measuring time (Eq. 3.14) we obtain the ferroelectric hysteresis loop, $P(E)$. Note that the ferroelectric hysteresis loops computed from PUND measurements are rectangular-shaped (*i.e.* saturated), as not only $I_{leakage}$ is suppressed, but also I_{ε}. Therefore, this technique directly gives the remanent polarisation values.

It is worth recalling that for the ferroelectric hysteresis loops, the parallel-plate capacitors configuration was used [see Sect. 3.1]. Thus, it follows that $E = V/(2 \cdot t)$, where V is the applied voltage from top to top electrode and t is the film thickness.

References

[1] J. R. Macdonald, *Impedance Spectroscopy*, Wiley, New York, 1987.

[2] J. T. S. Irvine, D. C. Sinclair and A. R. West, Adv. Mater. **2** 132 (1990).

[3] J. Yu, P. Paradis, T. Ishikawa and S. Yoda, Appl. Phys. Lett. **85** 2899 (2004).

[4] G. Catalan, Appl. Phys. Lett. **88** 102902 (2006).

[5] N. Ortega, A. Kumar, P. Bhattacharya, S. B. Majumder and R. S. Katiyar, Phys. Rev. B **77** 014111 (2008).

[6] M. Li, D. C. Sinclair and A. R. West, J. Appl. Phys. **109** 084106 (2011).

[7] W. Eerenstein, F. D. Morrison, J. F. Scott and N. D. Mathur, Appl. Phys. Lett. **87** 101906 (2005).

[8] R. Schmidt, W. Eerenstein, T. Winiecki, F. D. Morrison and P. A. Midgley, Phys. Rev. B **75** 245111 (2007).

[9] M. Sakai, A. Masuno, D. Kan, M. Hashisaka, K. Takata, M. Azuma, M. Takano and Y. Shimakawa, Appl. Phys. Lett. **90** 072903 (2007).

[10] T. Kimura, S. Kawamoto, I. Yamada, M. Azuma, M. Takano and Y. Tokura, Phys. Rev. B **67** 180401(R) (2003).

[11] Note that conventional ferroelectric materials, like $BaTiO_3$ or $Ba(Ti,Zr)O_3$, or incipient ferroelectric materials, like $SrTiO_3$, tend to show much larger dielectric permittivity than the exposed in the simulation of this chapter [see for example T. Tsurumi *et al*. Appl. Phys. Lett. **91** 182905 (2007)]. Yet dielectric permittivity in multiferroic materials is usually found to be much smaller, in agreement with the one used in the simulation [see refs. above and T. Kimura *et al*. Phys. Rev. B **71** 224425 (2005)].

[12] C. Kittel, *Introduction to Solid State Physics*, Wiley, Hoboken, NJ, 2004.

[13] G. Catalan, D. O'Neil, R. M. Bowman and J. M. Gregg, Appl. Phys. Lett. **77** 3078 (2000).

[14] A. K. Jonscher, *Dielectric Relaxations in Solids*, Chelsea Dielectrics Press, London, 1983.

[15] A. R. West, D. C. Sinclair and N. Hirose, J. Electroceramics 1:1 65 (1997).

[16] P. Lunkenheimer, V. Bobnar, A. V. Pronin, A. I. Ritus, A. A. Volkov and A. Loidl, Phys. Rev. B **66** 052105 (2002).

[17] F. D. Morrison, D. J. Jung and J. F. Scott, J. Appl. Phys. **101** 094112 (2007).

[18] R. Schmidt and A. W. Brinkman, J. Appl. Phys. **103** 113710 (2008).

[19] L. Hsu, G. Y. Guo, J. D. Denlinger and J. W. Allen, Phys. Rev. B **63** 155105 (2001).

[20] F. Berkemeier, M. R. S. Abouzari and G. Schmitz, Phys. Rev. B **76** 024205 (2007).

[21] A. Kukol, P. Li, P. Estrela, P. Ko-Ferrigno and P. Migliorato, Anal. Biochem. **374** 143 (2008).

[22] T. Tsurumi, J. Li, T. Hoshina, H. Kakemoto, M. Nakada and J. Akedo, Appl. Phys. Lett. **91** 182905 (2007).

[23] T. Teranishi, T. Hoshina, T. Tsurumi, Mater. Sci. Eng. B **161** 55 (2009).

[24] D. O'Neil, R. Bowman and J. M. Gregg, Appl. Phys. Lett. **77** 1520 (2000).

[25] L. He, J. B. Neaton, M. H. Cohen, D. Vanderbilt and C. C. Homes, Phys. Rev. B **65** 214112 (2002).

[26] N. Biškup, A. de Andrés, J. L. Martínez, C. Perca, Phys. Rev. B **72** 024115 (2005).

[27] J. Liu, C. Duan, W. N. Mei, R. W. Smith and J. R. Hardy, J. Appl. Phys. **98** 093703 (2005).

[28] T. Goto, T. Kimura, G. Lawes, A. P. Ramirez and Y. Tokura, Phys. Rev. Lett. **92** 257201 (2004).

[29] J. Hemberger, P. Lunkenheimer, R. Fichtl, H. –A. Krug von Nidda, V. Tsurkan and A. Loidl, Nature **434** 364 (2005).

[30] M. P. Singh, W. Prellier, L. Mechin and B. Raveau, Appl. Phys. Lett. **88** 012903 (2006).

[31] H. J. Xiang and M. –H. Whangbo, Phys. Rev. Lett. **98** 246403 (2007).

[32] P. Padhan, P. LeClair, A. Gupta and G. Srinivasan, J. Phys.: Condens. Matter **20** 355003 (2008).

[33] F. Schrettle, P. Lunkenheimer, J. Hemberger, V. Y. Ivanov, A. A. Mukhin, A. M. Balbashov and A. Loidl, Phys. Rev. Lett. **102** 207208 (2009).

[34] X. Martí, I. Fina, V. Skumryev, C. Ferrater, M. Varela, L. Fàbrega, F. Sánchez and J. Fontcuberta, Appl. Phys. Lett. **95** 142903 (2009).

[35] I. Fina, N. Dix, L. Fàbrega, F. Sánchez and J. Fontcuberta, Thin Solid Films **518** 4638 (2010).

[36] K. Raidongia, A. Nag, A. Sundaresan and C. N. R. Rao, Appl. Phys. Lett. **97** 062904 (2010).

[37] M. Maglione, J. Phys.: Condens. Matter **20** 32302 (2008).

[38] M. F. Hundley, J. J. Neumeier, R. H. Heffner, Q. X. Jia, X. D. Wu and J. D. Thompson, J. Appl. Phys. **79** 4535 (1996).

[39] M. E. Lines and A. M. Glass, *Principles and Applications of Ferroelectric and related materials*, Clarendon Press, Oxford, 1977.

[40] M. Dawber, K. M. Rabe, J. F. Scott, Rev. Modern Phys. **77** 1083 (2005).

[41] J. F. Scott, J. Phys.: Condens. Matter **20** 021001 (2008).

[42] J. F. Scott, L. Kammerdiner, M. Parris, S. Traynor, V. Ottenbacher, A. Shawabkeh and W. F. Oliver, J. Appl. Phys. **64** 787 (1988).

[43] K. M. Rabe, C. H. Ahn, J-M. Triscone, *Physics of Ferroelectrics: A Modern Perspective*, Springer-Verlag, Berlin Heidelberg, 2007.

[44] M. Dawber, N. Stucki, C. Lichtensteiger, S. Gariglio, P. Ghosez and J-M. Triscone, Adv. Mater. **19** 4153 (2007).

Chapter 4

$BiMnO_3$ thin films

4.1 Single-phase stabilisation

The stabilisation of single phase Bi-based manganite-family perovskites has been, in general, difficult to achieve because of their tendency of multiphase formation and the high volatility of bismuth [1 – 4]. Indeed, $BiMnO_3$ in bulk form is only achieved in extreme sintering conditions, *i.e.* between 3 and 6 GPa and between 600 ºC and 700ºC of mechanical pressure and temperature, respectively [5 – 9]. Heating at ambient pressure a mixture of bismuth oxide and manganese oxide leads to the formation of $Bi_{12}MnO_{20}$ and $Bi_2Mn_4O_{10}$ compounds, much more stable than the perovskite $BiMnO_3$ [9].

Still, as explained in Sect. 1.3, metastable compounds can be formed by replacing the mechanical pressure by the epitaxial stress, *i.e.* using substrates with similar structures and whose lattice parameters show a low mismatch with those of the compound that is to be formed. Here, the perovskite oxide $SrTiO_3$ was used as a substrate, whose crystal structure is cubic (a = 3.905 Å). The small lattice mismatch (table 4.1) with regard to a and c $BiMnO_3$ lattice parameter (pseudo-cubic representation: a ≈ c ≈ 3.935 Å, b ≈ 3.989 Å, α ≈ γ ≈ 91.46º, β ≈ 90.96º [5]) evidences the suitability of $SrTiO_3$ substrate for the epitaxial stress needed to synthesise the compound.

Substrate	Structure and orientation	Lattice parameter (Å)	Mismatch with *a* parameter of $BiMnO_3$	Mismatch with *b* parameter of $BiMnO_3$	Mismatch with *c* parameter of $BiMnO_3$
$SrTiO_3$	Cubic perovskite (001)	3.905	0.77%	2.15%	0.77%

Table 4.1 – *In-plane lattice parameter and orientation of the substrate and mismatch* $\left(\frac{a(b,c)_{BiMnO_3} - a_{SrTiO_3}}{a_{SrTiO_3}}\right)$ *with the lattice parameters of* $BiMnO_3$.

$BiMnO_3$ thin films were grown by PLD (Sect. 2.1) from non-stoichiometric targets, *i.e.* the mixture containing Bi/Mn oxides was 10% atomically Bi-rich in order to compensate for the Bi volatility. According to the mismatch with $SrTiO_3$ substrate

(table 4.1), $BiMnO_3$ thin films are expected to grow (010)-oriented, *i.e.* with the *b*-axis as the out-of-plane direction, as *b* parameter shows the largest mismatch. Thus, only (0*k*0) reflexions of $BiMnO_3$ are to be found in the symmetric θ/2θ XRD diffractograms.

In order to optimise the deposition conditions for the single-phase stabilisation, the substrate temperature and the oxygen pressure during the growth process were assessed as well as the role of the thickness.

4.1.1 Dependence on temperature

By keeping the rest of the PLD deposition conditions fixed (see Sect. 2.1), we grow different samples at different substrate temperatures, ranging from 590ºC to 700ºC.

In Fig. 4.1, XRD $\theta/2\theta$ scans of 50-nm thick films grown at 0.1 mbar at various illustrative temperatures are shown. The (0*k*0) reflections of the $BiMnO_3$ phase can be clearly observed, which take place at 2θ values slightly smaller than the (00*l*) reflexions of $SrTiO_3$, as expected since *b* lattice parameter of $BiMnO_3$ is larger than that of $SrTiO_3$ [note that, having in mind the Bragg diffracion law (Eq. 2.1), the interplanar distance of the (0*k*0) reflexions, $d_{0k0} = b/k$ (Appendix XRD), is larger in the case of $BiMnO_3$ films]. The lattice parameters will be assessed in sect. 4.2.2.

However, in addition to the (0*k*0) reflexions of $BiMnO_3$, the diffractograms reveal the presence of other phases of the Bi – Mn – O ternary system (Fig. 4.1). Importantly enough, a correlation between these parasitic phases and the substrate temperature is observed. In the samples prepared at lower temperatures than 630ºC, Bi-rich phases, such as Bi_2O_3 and $Bi_{12}MnO_{20}$ coexist with $BiMnO_3$. The presence of these phases is monotonously reduced on increasing temperature and eventually disappearing at around 630ºC. Conversely, in the samples prepared at temperatures higher than 630ºC, it is the Mn-rich phases, such as Mn_3O_4 and $Bi_2Mn_4O_{10}$, the ones that coexists with $BiMnO_3$ phase. Moreover, the presence of these Mn-rich phases is enhanced on increasing temperature. It is only the XRD patterns of the films prepared at the intermediate temperatures around 630ºC which displays the (0*k*0) reflexions of $BiMnO_3$ without traces of spurious phases.

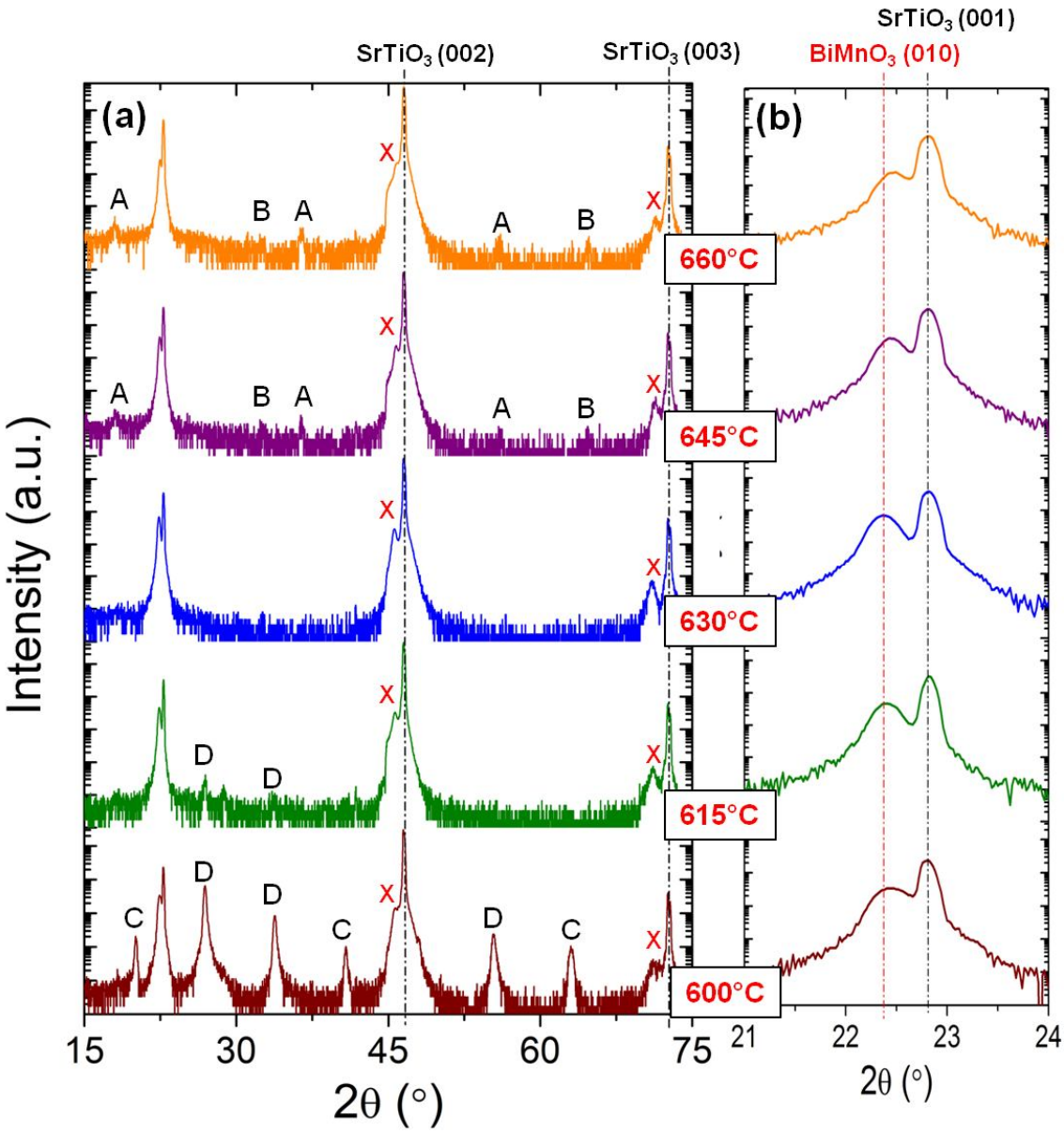

Fig. 4.1 – (a) *XRD θ/2θ scans of $BiMnO_3$ thin films (50 nm thick) grown at 0.1 mbar of O_2 and at different temperatures. (X) denotes the (0k0) reflexions of $BiMnO_3$ phase. Parasitic phases belonging to the Bi – Mn – O system are signalled by capital letters: (A) Mn_3O_4; (B) $Bi_2Mn_4O_{10}$; (C) $Bi_{12}MnO_{20}$; (D) Bi_2O_3.* **(b)** *Zoom of the (001) reflexion of $SrTiO_3$ and (010) reflexion of $BiMnO_3$.*

On the other hand, as observed in Fig. 4.1 (b), the (0*k*0) reflexions of $BiMnO_3$ shifts toward higher 2θ values on increasing temperature above 630ºC. Hence, according to the Bragg's law (Eq. 2.1), the interplanar distance of the (0*k*0) reflexions, d_{0k0}, is reduced at higher temperatures and consequently the out-of-plane lattice parameter, *b* (Appendix XRD), as shown in Fig. 4.2. Considering that the in-plane lattice parameter

of $BiMnO_3$ is fully strained on $SrTiO_3$, as will be inferred in Sect. 4.2.2, and hence it adopts the $SrTiO_3$ lattice parameter, the unit cell volume is monotonously reduced at high temperatures (right axis), signalling a change in the film composition. A variation of the oxygen concentration is possible, but the presence of anion vacancies is known to produce an enlargement of the unit cell volume [10 – 12]. Conversely, cation vacancies produce a reduction of the unit cell volume, as proved in either $LaMnO_3$ [13] or $BiMnO_3$ [3]. Taking into account the high Bi volatility compared to Mn, it is reasonable to argue that this unit cell volume reduction at high temperatures is driven by the presence of Bi vacancies.

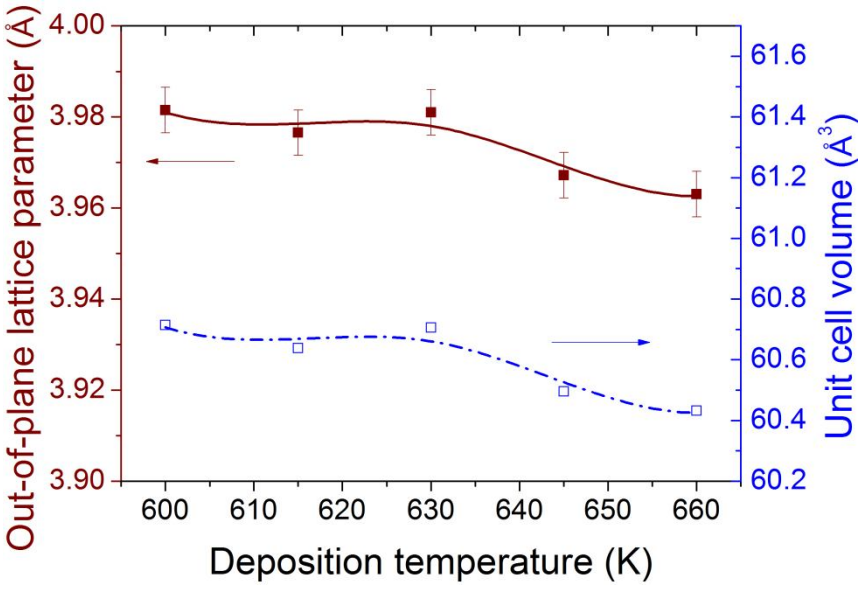

Fig. 4.2 – *Evolution of the lattice parameter (left axis) and unit cell volume (right axis) of $BiMnO_3$ as a function of the deposition temperature. In computing the unit cell volume the in-plane lattice parameter of $BiMnO_3$ is assumed to be coincident with that of $SrTiO_3$ (see Sect. 4.2), thus assuming a tetragonal unit cell for $BiMnO_3$.*

Thus, XRD results suggest that the Bi-content in the films decreases on increasing the deposition temperature (substrate temperature), in agreement with the high volatility of this element. In order to bear out this tendency, the chemical composition of the films prepared at different temperatures was assessed by X-ray wavelength dispersive spectroscopy technique (described in Sect. 2.4.2). The results can be summarised in Fig. 4.3, in which the evolution of the [Bi]/[Mn] atomic ratio as a function of the deposition temperature is depicted. As observed, there is a slight monotonic reduction

of the Bi content when the deposition temperature varies from 600ºC to 630ºC, in agreement with a slightly increase of the Bi desorption rate upon temperature. However, above 630ºC Bi amount is severely reduced, attaining 50 % of the nominal value at 645ºC and 25% at 660ºC. This finding evidences a substantial change in the Bi desorption rate (*i.e.* a strong increase) during growth occurring when depositing at higher temperatures than 630ºC, giving rise to largely Bi-deficient samples. Very similar behaviour was found, indeed, for the Bi-content in columnar nanocomposites $BiFeO_3$-$CoFe_2O_4$ [14].

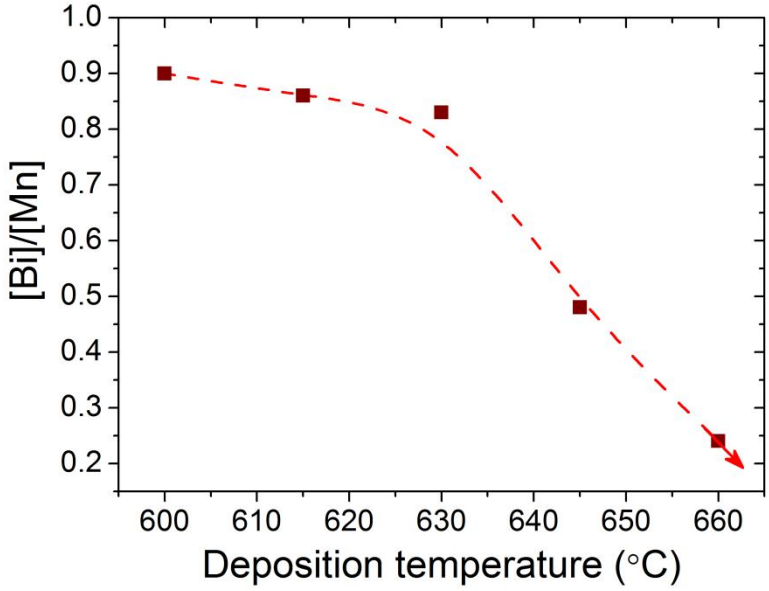

Fig. 4.3 – *Cationic composition ratio, [Bi]/[Mn], of Bi – Mn – O films as a function of the deposition temperature. Data are subjected to a 10% of experimental error.*

Thus, as expected, the appearance of Mn-rich phases in the XRD patterns of the samples prepared at high temperatures (Fig. 4.1) is promoted by the large Bi loss in Bi – Mn – O system. However, the samples prepared at low temperatures do not show an excess of Bi-content, as expected for the appearance of Bi-rich phases, but shows [Bi]/[Mn] ratio slightly below the nominal value 1:1 (Fig. 4.3). The Bi – Mn – O multiphase formation at low temperatures is likely caused by the incomplete reaction or low mobility of the arriving species (Bi and Mn oxides) at the substrate surface to form $BiMnO_3$. The temperature dependence of the reaction rate, r, tend to follow an Arrhenius law, *i.e.* $r \sim \exp(-E_a/k_BT)$ [4], where E_a is the activation energy of the reaction and k_B is the Boltzman constant. E_a depends on the reaction. Hence, in order to achieve

a complete reaction of the Bi and Mn oxides to form $BiMnO_3$, overcoming the more stable phases Bi_2O_3 and $Bi_{12}MnO_{20}$, it is necessary to increase the thermal energy k_BT. However, the Bi desorption rate from the substrate surface also increases on increasing temperature following $r_{des} \sim \exp(-E_{des}/k_BT)$ [4], where E_{des} is the activation energy of the desorption process (which is very small for volatile elements like Bi as inferred from Fig. 4.3) [4]. The high desorption rate is responsible for the highly Bi-deficient samples prepared at high temperatures and consequently the formation of Mn-rich phases. As a result, obtaining single phase $BiMnO_3$ in the Bi – Mn – O system is a very delicate balance between the reaction rate of the arriving species and the Bi desorption rate, leading to a very narrow window of deposition temperatures in which it is achieved (around 630ºC in our case). It is worth mentioning, though, that this narrow window of deposition temperatures in which single phase $BiMnO_3$ is obtained is not an universal recipe as it may greatly differ or even disappear depending on the target composition (*i.e.* the Bi:Mn ratio in the target), the deposition rate (the higher the lower Bi-desorption due to the shorter time of the growth process), the laser ablation fluency, ...

4.1.2 Dependence on O_2 pressure

By keeping the rest of the PLD deposition conditions fixed (see Sect. 2.1), we grow different samples at 630ºC for different O_2 pressures inside the chamber, ranging from vacuum to 0.3 mbar.

In Fig. 4.4, XRD $\theta/2\theta$ scans of 50-nm thick films grown at 630ºC under various illustrative oxygen pressures are shown. The (0k0) reflections of the $BiMnO_3$ phase can be clearly observed in all the oxygen pressure range except for the sample prepared in vacuum, in which $BiMnO_3$ compound is not formed. This latter is likely due to a large oxygen deficiency, evidencing the requirement of using partial oxygen pressures when growing complex oxides. Moreover, in the XRD patterns of the films prepared in vacuum traces of Mn_3O_4 phase appear, similar to what is found for samples prepared at high temperatures (Fig. 4.1), which signals a similar Bi-deficiency but driven in this case by heating in vacuum conditions.

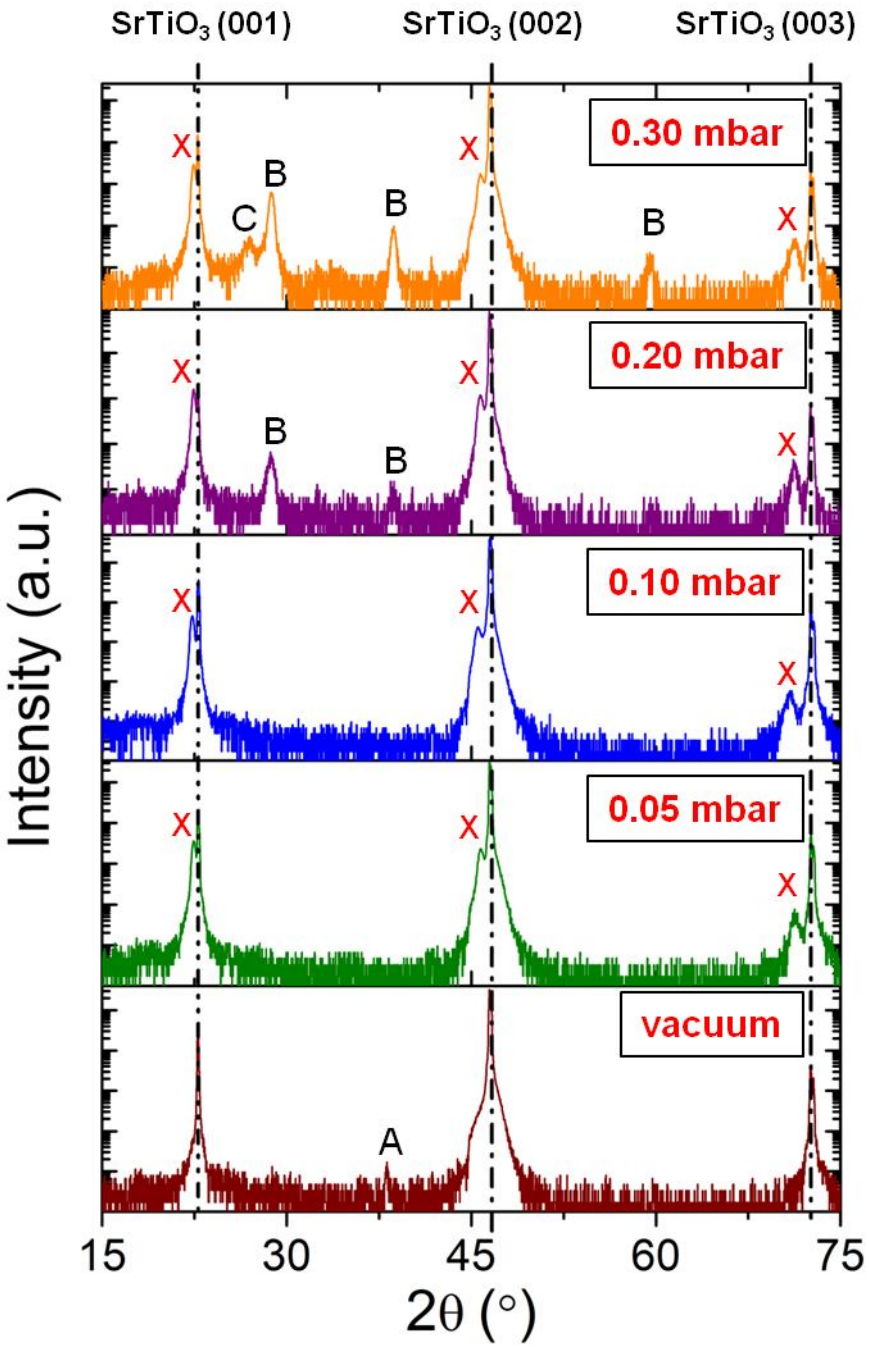

Fig. 4.4 – *XRD θ/2θ scans of $BiMnO_3$ thin films (50 nm thick) grown at 630ºC and at different O_2 pressures. (x) denotes the (0k0) reflexions of $BiMnO_3$ phase. Parasitic phases belonging to the Bi – Mn – O system are signalled by capital letters: (A) Mn_3O_4; (B) MnO_2; (C) Bi_2O_3.*

For the samples prepared in the range of O_2 pressures comprised between 0.05 and 0.1 mbar, single phase $BiMnO_3$ thin films are obtained. Yet when further increasing the partial oxygen pressure in the deposition process, XRD patterns show additional

reflexions corresponding to parasitic phases (Fig. 4.4). This fact reveals the pronounced multiphase character of the Bi – Mn – O system. It is worth noting that the presence of MnO_2 phase, which corresponds to Mn^{4+} of oxidation state, is increasingly enhanced upon O_2 pressure. An over-oxidation of the films will produce an increase of the valence state of the transition metals, *i.e.* from Mn^{3+} (the appropriate oxidation state for $BiMnO_3$ compound) to Mn^{4+}, in order to maintain the electric equilibrium. According to XRD results (Fig. 4.4), an over-oxidation of Bi – Mn – O system seems to lead to phase segregation, *i.e.* the formation of Mn^{4+}-phases with the excess of Mn^{4+}, rather than producing single-phase $BiMnO_3$ containing multivalent Mn^{3+}/Mn^{4+} at the B-site. Additionally, the samples prepared at the highest oxygen pressure (0.3 mbar), Bi_2O_3 phase is also detected in the XRD patterns (Fig. 4.4), which might be the result of a smaller Bi desorption rate due to the higher pressure inside the chamber. Similar Bi-rich phases were detected either at low deposition temperature or at high oxygen pressure when growing $BiFeO_3$ films due to a larger [Bi]/[Fe] cationic ratio in either case [15].

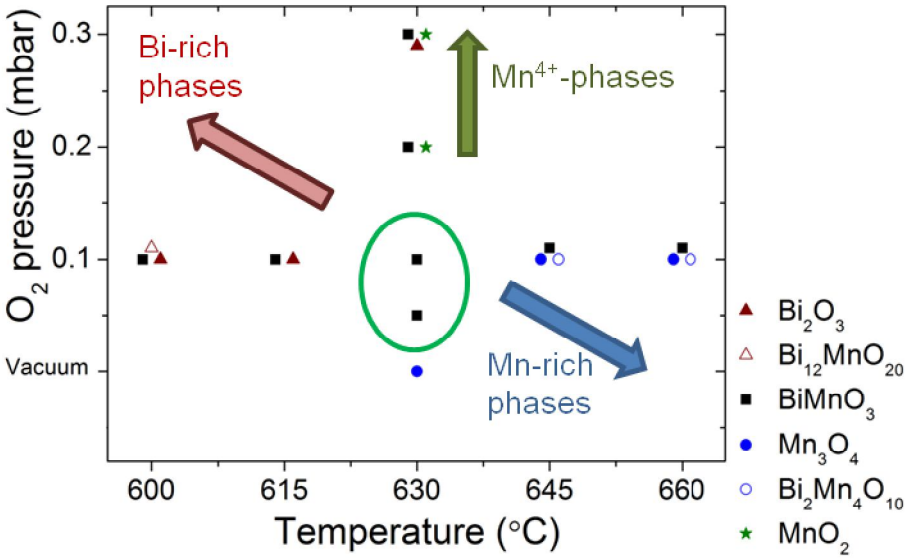

Fig. 4.5 – *Phase diagram of Bi – Mn – O films grown on (001)-oriented $SrTiO_3$ as a function of the deposition temperature and the oxygen pressure during the growth process. The green solid line signals the window of deposition conditions in which single-phase $BiMnO_3$ is achieved.*

As a summary, from the XRD results a partial phase diagram of Bi – Mn – O films can be deduced as a function of the deposition temperature and oxygen pressure during the growth process, which is shown in Fig. 4.5. As observed, either at low high

temperatures or at high pressures, Bi-rich phases appear together with the $BiMnO_3$ phase. Conversely, the films prepared either at high temperatures or low oxygen pressure show Mn-rich phases consistent with a larger Bi-deficiency. Thus, only in a narrow window of deposition conditions (marked by a green solid line in Fig. 4.5) single-phase $BiMnO_3$ is achieved. Yet, as aforementioned, different target stoichiometry, laser fluence, etc may modify this narrow window and the phase diagram of Bi – Mn – O system.

4.1.3 Dependence on thickness

In this section we have investigated the influence of the thickness of Bi – Mn – O films on the single-phase stabilisation of $BiMnO_3$ phase. The samples that have been studied correspond to those grown in the narrow deposition conditions determined in Sect. 4.2.1 and 4.2.2, in which single-phase $BiMnO_3$ is achieved in 50-nm thick films, *i.e.* at 630ºC and 0.1 mbar of O_2 pressure.

In Fig. 4.6 XRD $\theta/2\theta$ scans of three illustrative samples of different thickness, *i.e.* 30, 60 and 100 nm are plotted. As observed, the thickest film displays a clear multiphase character, despite being grown at the narrow window of deposition conditions for the single-phase stabilisation (see Sect. 4.21 and 4.2.2). This multiphase tendency upon thickness could be due to a kind of mechanism of strain relaxation, instead of the common one which would consist of $BiMnO_3$ film lattice parameters becoming closer to those of the bulk upon thickness [16]. However, as a matter of fact, the parasitic phases that arise in the thickest films are all Mn-rich, *i.e.* Mn_3O_4 and $Bi_2Mn_4O_{10}$, similar to what is found in thinner Bi – Mn – O films grown at high temperatures (Sect. 4.2.1). This fact points out to the possibility of an increasing Bi-deficiency upon thickness.

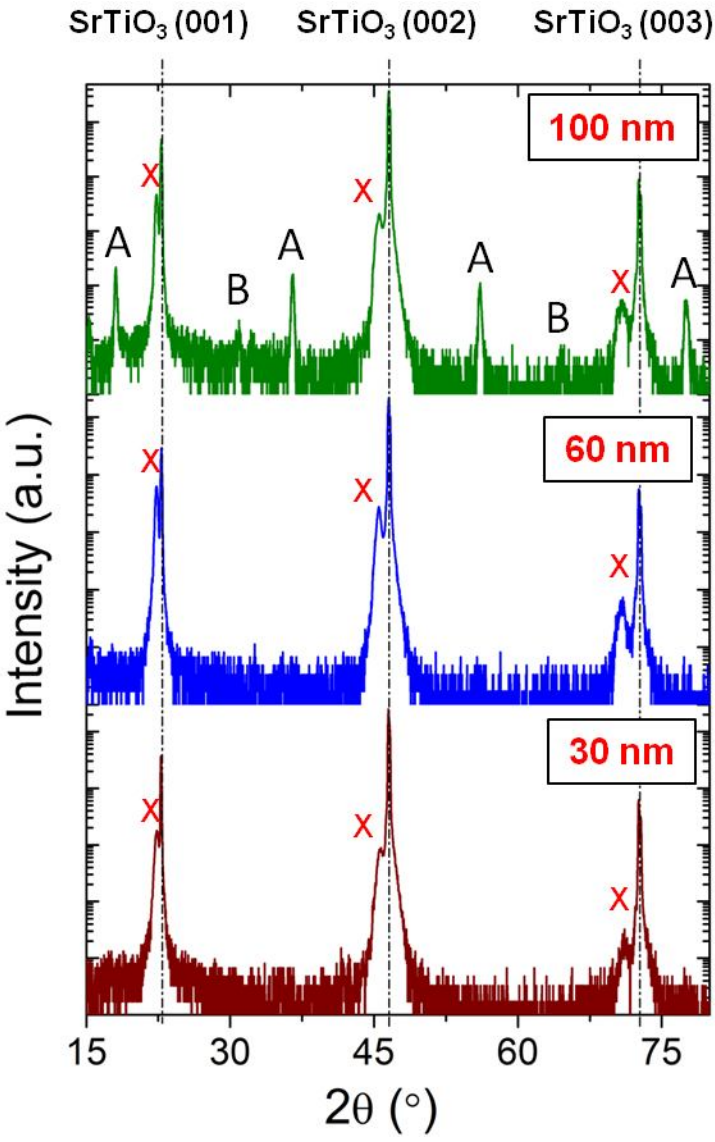

Fig. 4.6 – *XRD θ/2θ scans of Bi – Mn – O thin films (different thickness) grown at 630ºC and at 0.1 mbar of O_2 pressure. (x) denotes the (0k0) reflexions of $BiMnO_3$ phase. Parasitic phases belonging to the Bi – Mn – O system are signalled by capital letters: (A) Mn_3O_4; (B) $Bi_2Mn_4O_{10}$.*

In order to further study this possibility, thick films (90 nm – 120 nm) of Bi – Mn – O system were grown at different temperatures (at 0.1 mbar of O_2 pressure). The XRD $\theta/2\theta$ scans of some illustrative samples are shown in Fig. 4.7. The results show a multiphase tendency regardless the deposition temperature. Still, interesting enough, the spurious phases are all Mn-rich, even for the samples prepared at low temperatures (note that 50-nm thick Bi – Mn – O films deposited at 600ºC and 615ºC display Bi-rich phases, as shown in Fig. 4.1). Nonetheless, it is worth noting that the presence of

$Bi_2Mn_4O_{10}$ phase is larger than Mn_3O_4 phase the lower the deposition temperature is, in agreement with an increasing Mn enrichment of Bi – Mn – O films upon temperature as deduced in Sect. 4.2.1.

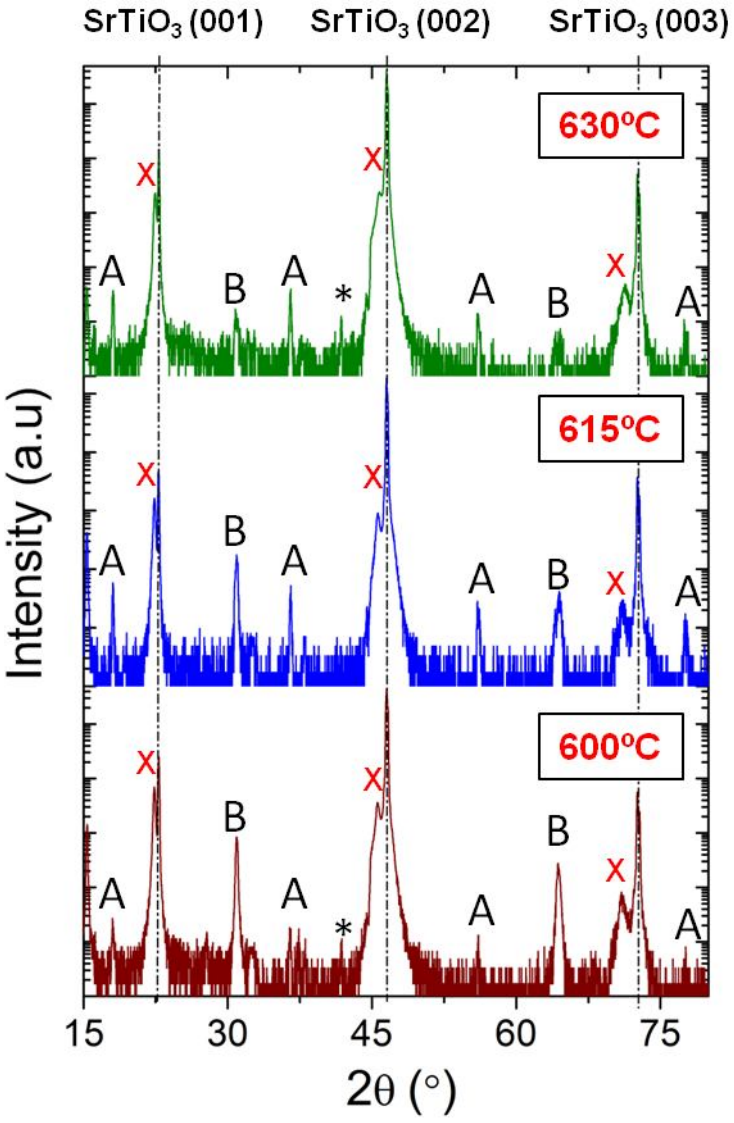

Fig. 4.7 – *XRD θ/2θ scans of Bi – Mn – O thin films (90 – 110 nm) grown at 0.1 mbar of O_2 pressure and at different temperatures. (x) denotes the (0k0) reflexions of $BiMnO_3$ phase. Parasitic phases belonging to the Bi – Mn – O system are signalled by capital letters: (A) Mn_3O_4; (B) $Bi_2Mn_4O_{10}$. (*) denotes the K_β of (002) $SrTiO_3$.*

Hence, according to the XRD results, the Bi – Mn – O films seem to be increasingly Bi-deficient the thicker they are, irrespective of the deposition temperature. Chemical analysis of the samples of different thickness was carried out by X-ray wavelength

spectroscopy, the results of which are summarised in Fig. 4.8. As observed the [Bi]/[Mn] cationic ratio of Bi – Mn – O films is strongly reduced on increasing thickness, proving the fact that the thicker the film the larger the Bi-deficiency. Thus, it might indicate that the Bi desorption rate, r_{des}, is higher than the incoming Bi ablated material, even for low deposition temperatures [r_{des} increases upon temperature, ~exp(-E_{des}/k_BT)]. Consequently, this deviation would be increasingly emphasised the longer the deposition time, *i.e.* the thicker the films (note that the pulsed laser repetition rate was maintained constant at 5 Hz, sect. 2.1), leading to increasingly Mn-rich films upon thickness.

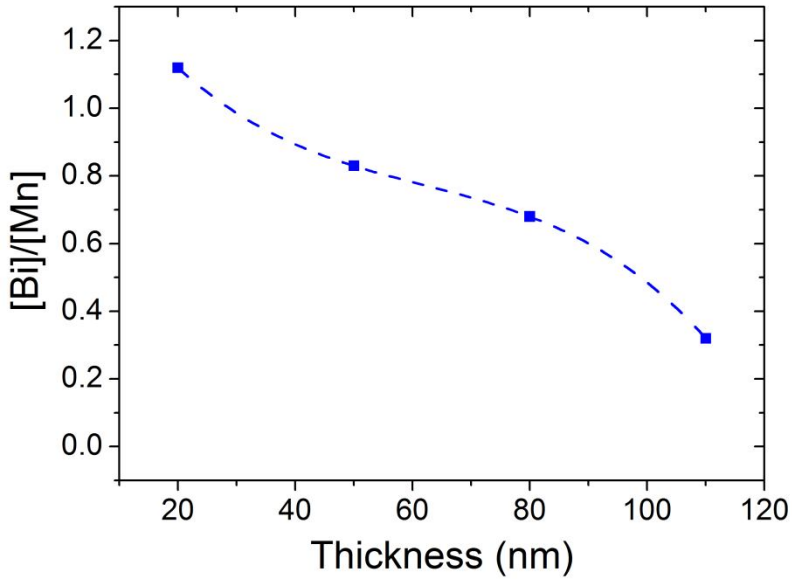

Fig. 4.8 – *Cationic composition ratio, [Bi]/[Mn], of Bi – Mn – O films grown at 630ºC and at 0.1 mbar of O_2 pressure as a function of film thickness. Data are subjected to a 10% of experimental error.*

Still, another plausible possibility is the fact that the ablated material from the target might be increasingly Bi-deficient during the growth process, as it would produce similar off-stoichiometric films as shown in Fig. 4.8. The laser-matter interaction produces local high temperatures, vaporising the volatile elements, *i.e.* Bi, from the target surface affected by the laser. Thus, the reiteration of the laser pulses onto the target surface will make it increasingly Mn-rich pulse after pulse, and hence the ablated material will become increasingly Bi-deficient on increasing the deposition time. In order to corroborate this argument, the composition of the surface of the target was also

assessed by X-ray wavelength spectroscopy, but analysing two different areas: a region that has been hit by the laser after deposition and another one that has not. The results (Table 4.2) show clear differences, *i.e.* whereas the region that is not altered by the laser displays a [Bi]/[Mn] cationic ratio close to the nominal composition of the target, that region that has been altered by the laser pulses (5000 pulses, ~ 100 nm) present clear Bi-deficiency (~ 50% of the nominal value).

Surface target composition	Nominal	Region non-altered by the laser	Region altered by the laser
[Bi]/[Mn] ratio	1.10	1.07	0.55

Table 4.2 – *[Bi]/[Mn] ratio of the target surface. Data are subjected to a 10% of experimental error.*

Thus, according to the composition results, the stoichiometry of the surface target is not preserved after the laser interaction, becoming increasingly Bi-deficient the longer the exposition time. Additionally, long deposition time leads to large Bi-desorption from the growing film and therefore increasingly Bi-deficient. Hence, the increasingly Bi-deficient Bi – Mn – O films upon thickness can be explained by a combination of these two factors: the increasingly Bi-deficient ablated material and the increasing Bi desorption from the growing film upon deposition time. In this sense the 2D phase diagram shown in Fig. 4.5 becomes quite much complicated as another variable (deposition time) should also be accounted.

4.2 Structural characterisation and surface topography

4.2.1 Texture of the films

First assessment of the crystal structure was focused on the dispersion of the out-of-plane lattice parameter of the film from the growth direction. As explained in Sec. 2.2.1, a way to quantify the so-called out-of-plane texture is by means of the FWHM of the

rocking curves (ω scans). In this work we have performed the rocking curves around the (001) Bragg reflexion [(010) in the case of $BiMnO_3$]. This figure of merit is compared with that of the substrate, as being the latter a single crystal with presumable high quality and free from form factor effects. Thus, the FWHM of the substrate Bragg reflexion may represent the estimate width to be achieved in a film for the instrumental width.

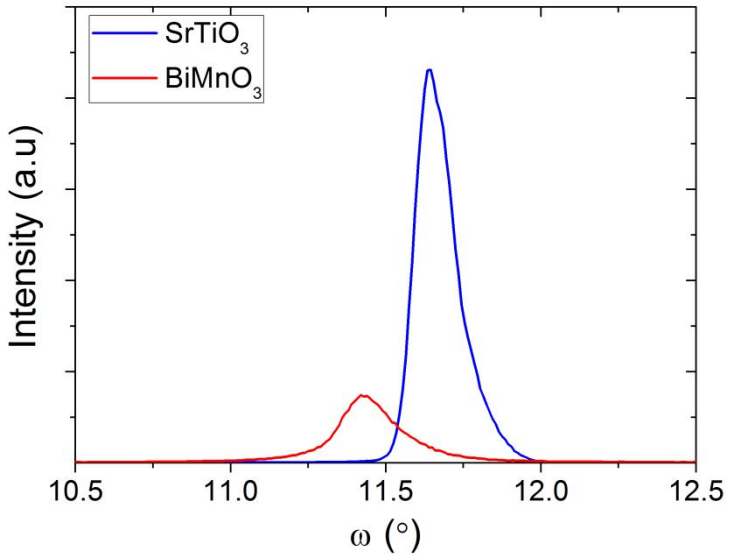

Fig. 4.9 – *Rocking curve of the (001) reflexion of $SrTiO_3$ substrate and 50-nm $BiMnO_3$ film grown at 630ºC and 0.1 mbar of O_2 pressure.*

Rocking curves of the (010) $BiMnO_3$ and (001) $SrTiO_3$ Bragg reflexions are illustrated in Fig. 4.9 of a 50-nm $BiMnO_3$ film grown in the optimised deposition conditions for single-phase formation. Comparison of the rocking curves reveals that the FWMH value of the $BiMnO_3$ peak (0.24º) is of the order of that of the substrate (0.15º), though substantially larger, which indicates a certain out-of-plane dispersion of the $BiMnO_3$ unit cells. The FWHM ratio between the rocking curve of $BiMnO_3$ and that of the substrate (~1.5) is extensive for the rest of the films up to 70 nm of thickness.

In-plane texture, *i.e.* how $BiMnO_3$ unit cells are in-plane oriented, is characterised by ϕ-scans of an asymmetric reflexion (see Sect. 2.2.1), which allows planes that are not parallel to the interface to diffract. When it comes to choosing an appropriate asymmetric reflexion, the criterion is based on using an easy in-plane axis, such as the [100] or [010] $SrTiO_3$ directions, which are equivalent as being a cubic structure.

However, due to the similarity of the lattice parameters of both $SrTiO_3$ and $BiMnO_3$, which means similar 2θ angle of the Bragg reflexions, a high-2θ reflexion was required in order to minimise the substrate contribution to the ϕ-scans of the film, since difference in 2θ is larger the higher the angle is. Thus, (103) reflexion [(130) in the case of $BiMnO_3$] was used, whose difference in 2θ between $BiMnO_3$ and $SrTiO_3$ is about 1.8º (see table 4.3).

XRD reflexion	**2θ(º)**	**ω(º)**	**ψ(º)**
(103) $SrTiO_3$	77.2	38.6	18.4
(130) $BiMnO_3$	75.4	37.7	18.2

Table 4.3 – *Four-circle diffractometer angles at which the (103) reflexion of $SrTiO_3$ and (130) reflexion of $BiMnO_3$ take place. ϕ angle is four times degenerated and 90º separated when tetragonal (cubic) in-plane crystal symmetry.*

Fig. 4.10 depicts the XRD ϕ-scans of the asymmetric (103) reflexion of substrate and (130) reflexion of $BiMnO_3$ film (50 nm thick) grown in the optimised deposition conditions for single-phase formation. As shown, only four 90º-ϕ-spaced peaks of the film are observed, which not only indicates that there are no contributions of misoriented in-plane family of crystallites of $BiMnO_3$, *i.e.* $BiMnO_3$ films are in-plane textured, but also that the crystal symmetry of $BiMnO_3$ films corresponds to that which allows an orthogonal in-plane unit cell base, *i.e.* orthorhombic, tetragonal or cubic. Moreover, the fact that $BiMnO_3$ ϕ peaks coincide in ϕ angle value with those of the substrate (Fig. 4.10) proves that $BiMnO_3$ films have grown cube-on-cube, *i.e.* the tetragonal base is coincident in orientation with that of the cubic substrate (see Sect. 2.2.1). Or, in other words, the [100] in-plane crystallographic direction of $BiMnO_3$ film is parallel to the [100] direction of $SrTiO_3$, which is normally represented by the epitaxial relationship $[100]BiMnO_3(010)//[100]SrTiO_3(001)$. The cube-on-cube growth is confirmed along thickness up to 70 nm.

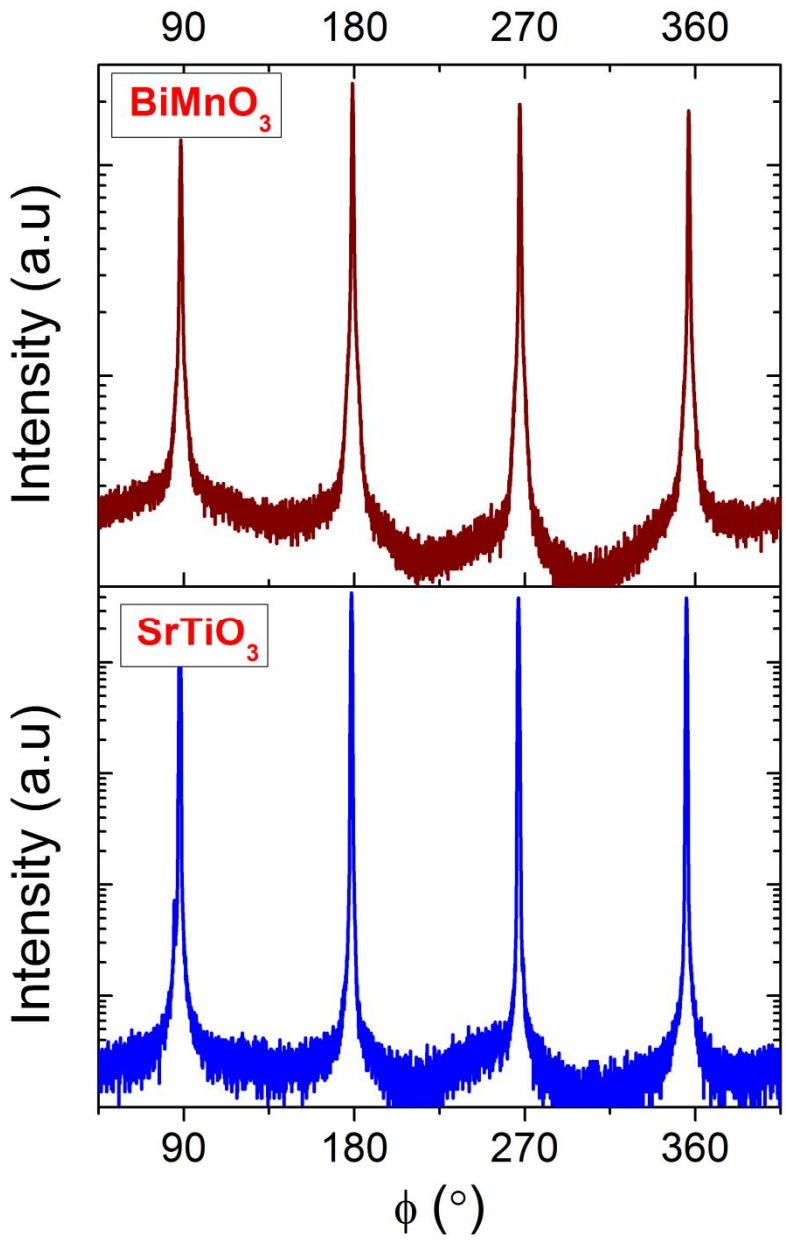

Fig. 4.10 – *XRD ϕ-scans around the (130) reflexion of $BiMnO_3$ film, 50-nm thick, grown at 630°C and 0.1 mbar of O_2 and (103) reflexion of $SrTiO_3$ substrate.*

4.2.2 Reciprocal space maps and lattice parameters

Reciprocal space maps (RSM) consists of plotting the out-of-plane component, q_{perp}, of the reciprocal space vector, $\vec{q}_{hkl}$, of the (*hkl*) XRD reflexion versus the in-plane component, $q_{parallel}$. They have been performed in order to determine the film lattice parameters (both the out-of-plane and in-plane lattice parameters, as long as an

asymmetric XRD reflexion is assessed) and the epitaxial strain of $BiMnO_3$ films (see Sect. 2.2.1). In the reciprocal space map, not only the film XRD reflexion is recorded but also that of the substrate, as the ($q_{parallel}$, q_{perp}) XRD peak position of the film compared to that of the substrate is used to evaluate the strain and extract the correct lattice parameters of $BiMnO_3$ films by accounting the instrumental error, as discussed in Appendix C.

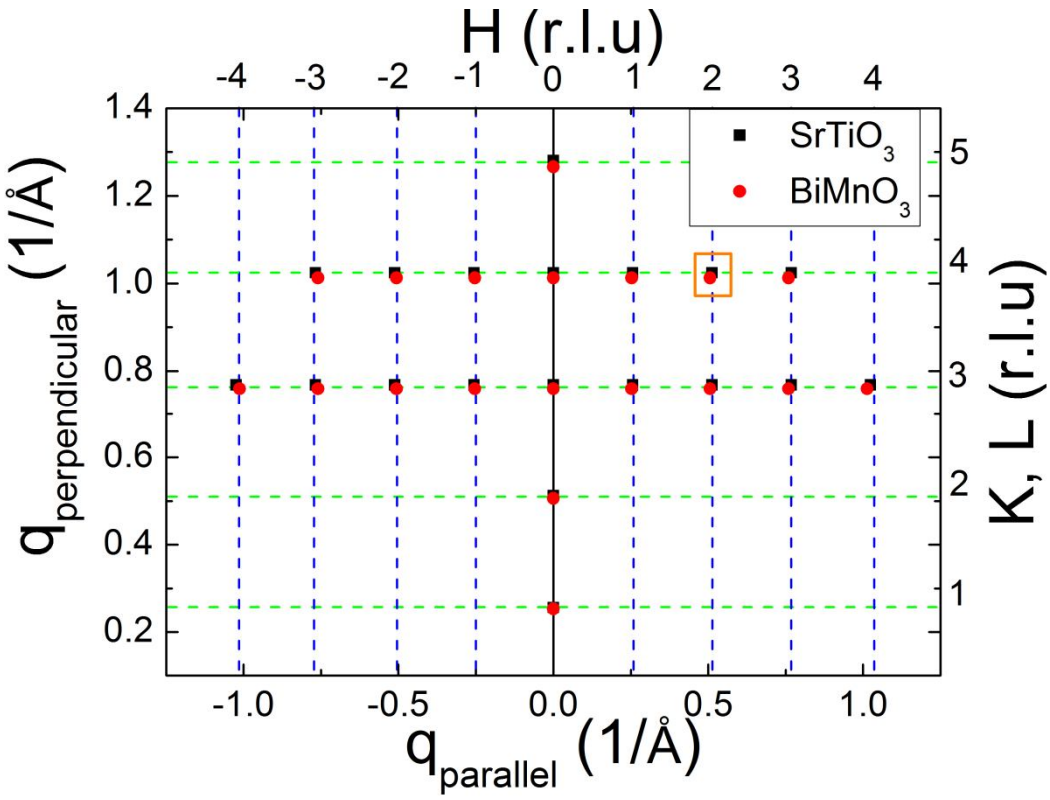

Fig. 4.11 – *Reciprocal space of the allowed XRD reflexions in the 4-circle diffractometer for both $BiMnO_3$ (solid circles) and $SrTiO_3$ (solid squares), when [100] and [001] ([010] for $BiMnO_3$) crystallographic directions are the in-plane and out-of-plane directions, respectively. Top and right axis indicates the corresponding in-plane and out-of-plane reciprocal lattice units of the XRD reflexions, respectively. The (204) XRD reflexion is pointed out (open orange square).*

According to the epitaxial relationship (Sect. 4.2.1), (*hkl*) reflexions of both $BiMnO_3$ and $SrTiO_3$ are coincident in ϕ angle and, due to the similar lattice of both compounds, they take place in similar 2θ and ω angle, which means similar $q_{parallel}$ and q_{perp} in the RSM. Thus, as in ϕ scans, the criterion of choosing the appropriate asymmetric reflexion is based on looking for a sufficiently intense XRD peak of the

film, but also with large enough angular separation with regard to the substrate reflexion in order to be able to discern between both contributions (film + substrate) in the reciprocal space map. Taking into account the geometric configuration of the 4-circle diffractometer (Fig. 2.4), and using [100] and [001] vectors as the in-plane and out-of-plane directions (note that for $BiMnO_3$ the out-of-plane direction is [010]), respectively, Fig. 4.11 depicts the allowed XRD reflexions in the reciprocal space, considering $BiMnO_3$ film relaxed, *i.e.* with bulk pseudocubic lattice parameter (~3.95 Å). It is worth recalling that both [100] and [001] directions are equivalent when it comes to characterising the in-plane lattice parameters since $BiMnO_3$ possesses a tetragonal structure according to the epitaxial relationship (see sect. 4.2.1). Thus, both (*hk0*) and (*0kl*) XRD reflexions of $BiMnO_3$, accomplishing $h = l$, are equivalent.

XRD reflexion	**2θ(º)**	**ω(º)**	**ψ(º)**
(204) $SrTiO_3$	123.8	35.3	0
(240) $BiMnO_3$	120.0	33.7	0

Table 4.4 – *Four-circle diffractometer angles at which the (204) reflexion of $SrTiO_3$ and (240) reflexion of $BiMnO_3$ takes place, when ψ is forced to be 0. ϕ angle is four times degenerated and placed at 0º, 90º, 180º and 270º.*

As shown in Fig. 4.11, $\vec{q}$ position of (*h0l*) and (*hk0*) XRD reflexions of substrate and film, respectively, are very similar. (204) and (240) XRD reflexion (substrate and film, respectively) was used (open orange square), which corresponds to a high-2θ reflexion, and hence the angular separation is large, but with enough intensity to be recorded. In RSM, instead of fulfilling the condition of $\omega = \theta$, as in the ϕ-scans, ω is modified as follows $\omega = \theta - \psi$ (see table 4.4), forcing $\psi = 0$, allowing the asymmetric (204) and (240) reflexion to diffract. Note that ψ angle corresponds to the angle between the out-of-plane direction and the perpendicular direction of the (204) crystallographic planes [(240) in the case of $BiMnO_3$], as shown in Fig. 2.4.

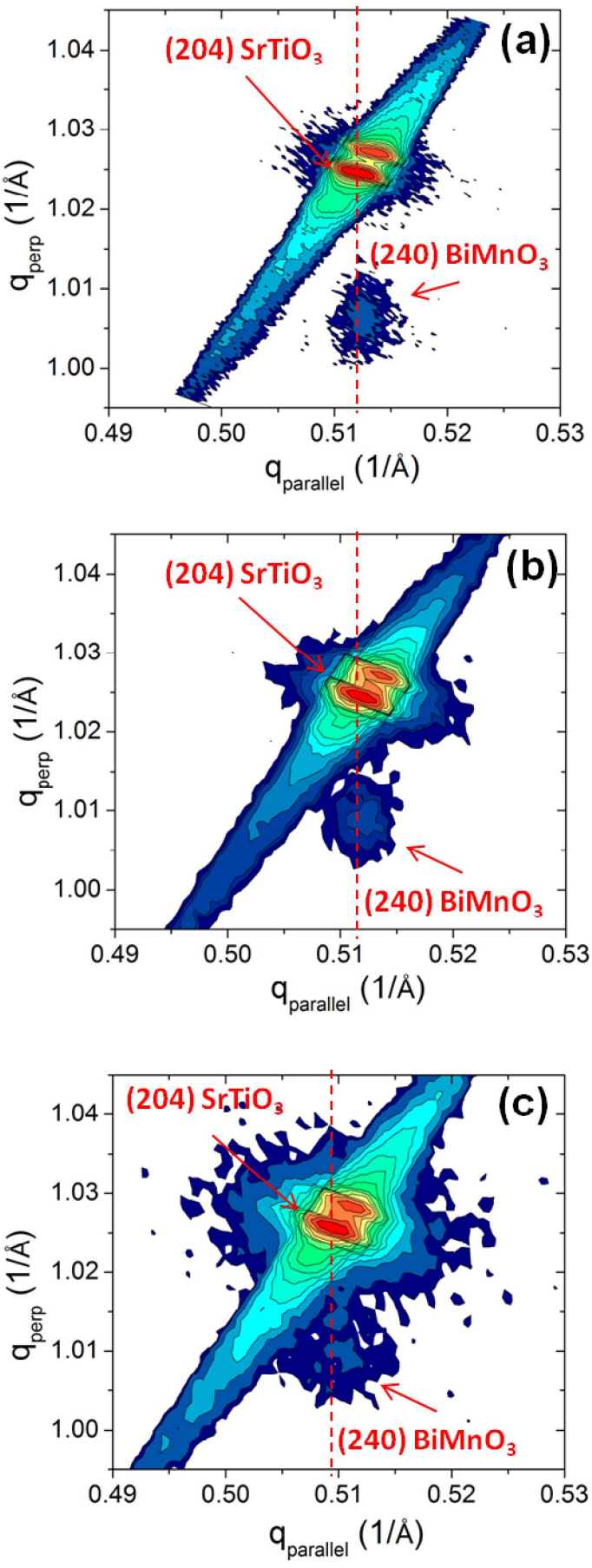

Fig. 4.12 – *Reciprocal space map around (204) XRD reflexion of $SrTiO_3$ and (240) XRD reflexion of $BiMnO_3$ phase of 50-nm thick films grown at 0.1 mbar of O_2 pressure and* **(a)** *630ºC,* **(b)** *645ºC and* **(c)** *660ºC*

In the RSM $\vec{q}$ is not directly measured, but, instead, several coupled $2\theta/\omega$ XRD scans are performed for different ω values, giving rise to a 2D $2\theta - \omega$ map of intensities. Then, using Eq. (2.8), q_{perp} and $q_{parallel}$ are obtained (see Sect. 2.1). As an illustrative example, Fig. 4.12 (a) shows the RSM of (204) and (240) XRD reflexions of $SrTiO_3$ substrate and 50-nm $BiMnO_3$ film (grown in the optimised deposition conditions for single-phase stabilisation, *i.e.* 630ºC and 0.1 mbar of O_2 pressure), respectively. As $q_{perp} = k/b = 4/b$ [see Eq. (2.6)], where b is the out-of-plane lattice parameter of $BiMnO_3$, $BiMnO_3$ peak is found at lower values of q_{perp} than that of the substrate since $SrTiO_3$ out-of-plane lattice parameter is smaller. Instead, $q_{parallel}$ of $BiMnO_3$ XRD reflexion is found to be coincident with that of the substrate (indicated by the two guide-to-eye dashed lines corresponding to $K_{\alpha 1}$ and $K_{\alpha 2}$). As $q_{parallel} = h/a = 2/a$ [see Eq. (2.6)], where a is the in-plane lattice parameter, it means that $BiMnO_3$ in-plane lattice parameter adopts the value of the $SrTiO_3$ lattice parameter (3.905 Å). As the film in-plane lattice parameter (3.905 Å) is smaller than that of the bulk (triclinic representation, 3.935 Å), $BiMnO_3$ films are compressive strained, about -0.76%, defined as following:

$$strain = \frac{a_{film} - a_{bulk}}{a_{bulk}} = -0.76\% \qquad (4.1)$$

where a_{film} and a_{bulk} are the in-plane lattice parameter for the film and for the bulk lattice parameter (triclinic representation) of $BiMnO_3$, respectively.

Exploring RSM for Bi – Mn – O films prepared at higher temperatures [Fig. 4.12 (b) and (c)], $BiMnO_3$ phase coherently grows on $SrTiO_3$, *i.e.* with the same in-plane lattice parameter, despite its coexistence with parasitic phases of Bi – Mn – O system (See Sect. 4.1.1). Nonetheless, q_{perp} component of $\vec{q}_{(240)}$ of $BiMnO_3$ is increasing on increasing temperature, which indicates that the out-of-plane lattice parameter of $BiMnO_3$ phase decreases upon temperature, as found in the symmetric $\theta/2\theta$ XRD scans (sect. 4.2.1). Fig. 4.13 (a) shows the in-plane (left axis) and the out-of-plane (right axis) lattice parameter, computed by means of the RSM, as a function of the deposition temperature. Note that the $BiMnO_3$ lattice parameters obtained by RSM are computed from $\Delta q_{parallel}$ and Δq_{perp} between $\vec{q}_{(240)}$ of $BiMnO_3$ and $\vec{q}_{(204)}$ of $SrTiO_3$, using that of $SrTiO_3$ as a reference, with lattice parameter (3.905 Å), accounting for the experimental

error (see Appendix C). As observed, whereas in-plane lattice constant is roughly constant around 3.905 Å (the $SrTiO_3$ lattice parameter), the out-of-plane lattice parameter is reduced at high deposition temperatures, which bears out the reduction of the $BiMnO_3$ unit cell volume at high temperatures [Fig. 4.13 (b)]. Nevertheless, the film unit cell is smaller than that of the bulk (marked with black dashed line in Fig. 4.14) in all temperature range, ranging from -1.2% to -1.8% in the samples prepared at the highest temperature. This unit cell volume reduction might be caused by the presence of Bi vacancies, even for samples prepared at low temperatures, as inferred by the chemical analysis (Fig. 4.3).

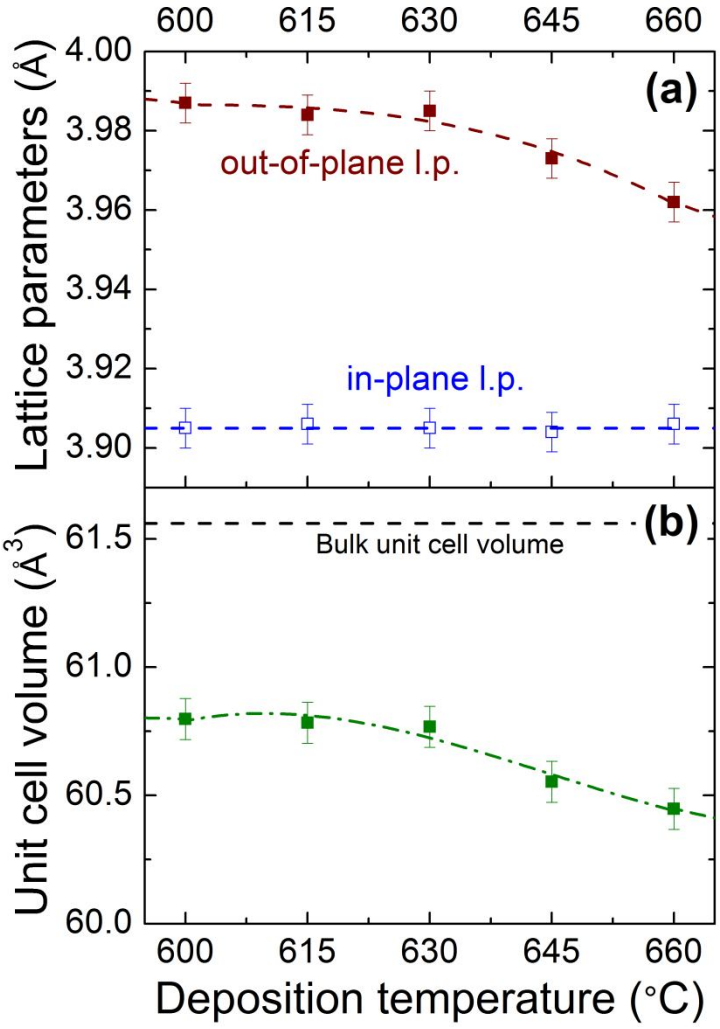

Fig. 4.13 – (a) *Lattice parameters of $BiMnO_3$ phase of Bi – Mn – O thin films as a function of the deposition temperature.* **(b)** *Unit cell volume of $BiMnO_3$ phase as a function of the deposition temperature. Black dashed line indicates the bulk unit cell volume.*

Exploring RSM for different thick films no relaxation is observed, *i.e.* $q_{parallel}$ of (240) $BiMnO_3$ reflexion and (204) $SrTiO_3$ reflexion are still coincident up to at least 70 nm (thicker films, with strong multiphase character, were not assessed). This is likely due to the small mismatch between lattice parameters of $BiMnO_3$ and $SrTiO_3$.

4.2.3 Surface topography

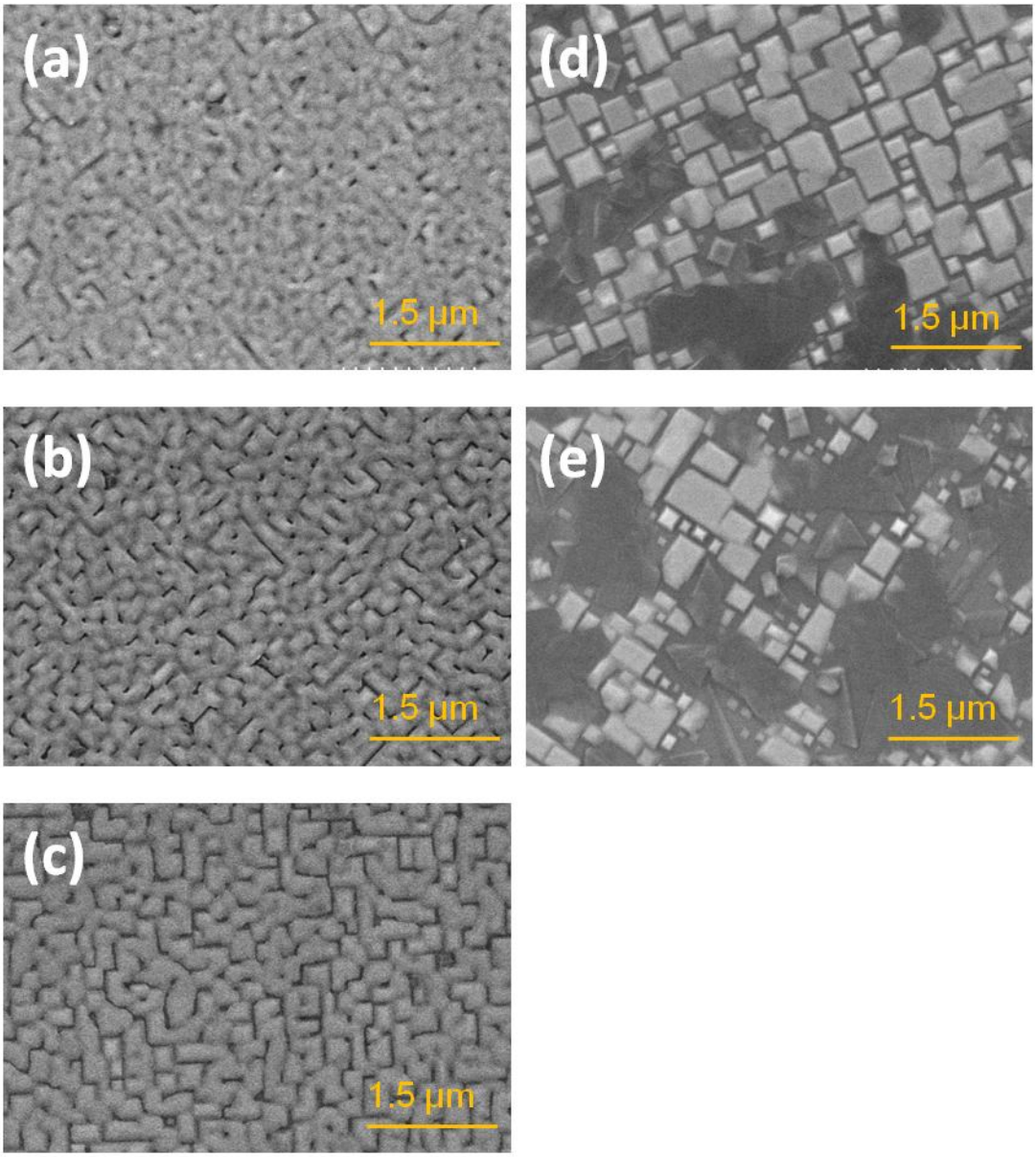

Fig. 4.14 – *Evolution of the surface topography (Field emission SEM images) as a function of the deposition temperature:* **(a)** *600ºC,* **(b)** *615ºC,* **(c)** *630ºC,* **(d)** *645ºC and* **(e)** *660ºC.*

Most of the applications in which a multilayer structure of nanometric films is required (tunnel junctions, spin valves, etc) the surface morphology plays an essential role. In addition, studying the surface topography contributes to the understanding of the growth mechanism of $BiMnO_3$ thin films on $SrTiO_3$, which may be extended to other similar substrates in perovskite structure with similar lattice parameters. Field

emission ESEM and AFM was used in the characterisation of surface topography, as explained in Sect. 2.3.1 and 2.3.2, respectively.

The effect of the deposition temperature on the surface morphology of the films is summarised in figure 4.14, in which, illustratively, is depicted 5 films of around 50 nm of thickness deposited at 600ºC, 615ºC, 630ºC, 645ºC and 660ºC, respectively. All the images suggest $BiMnO_3$ being formed from three dimensional (3D) growth mechanism as an evident island morphology is observed. Yet an evolution of the grains with the temperature can be also noticed. The size of the grains is enlarged on being increased the temperature. In addition, it can be also observed that the grains are increasingly defined and more faceted as the deposition temperature rises. These results are consistent with the thermodynamic aspects of nucleation as the critical nucleus size, from which the nucleation takes place, is enlarged when the temperature is increased [16]. It can also be understood as a better arrangement of the arriving species when the temperature increases since their mobility on the surface increases as well.

Nevertheless, just as at lower temperatures than around slightly above 630ºC only one modal of distribution of grains is observed, at higher temperatures the films present a bimodal distribution of grains as well as regions on which there is not a clear defined morphology. Most of the crystallites on the films deposited at higher temperatures have a flat surface, corresponding to the same crystallites formed at lower temperatures, but there is a minor second family of grains which has a pyramidal-like shape. This second family of crystallites might be related to the presence of Mn-rich parasitic phases as at higher temperatures XRD scans has revealed the formation of Mn_3O_4 and $Bi_2Mn_4O_{10}$, apart from $BiMnO_3$. What is more, this minor second family has a greater presence at 660ºC than at 645ºC, which would be in agreement with the increasing intensity of diffracted peaks of the Mn-rich phases upon temperature (Fig. 4.1). The presence of different family of crystallites for $BiMnO_3$ and Mn_3O_4 in the ternary Bi – Mn – O films is also reported by Fujino *et al.* [2]. Interestingly enough is the fact that the presence of regions with no clear morphology increases upon temperature, which might be related to amorphous/polycrystalline Mn-rich regions due to the small [Bi]/[Mn] cationic ratio of the films prepared at the highest temperatures (Fig. 4.3). However, the multiphase character of Bi – Mn – O films at low temperatures shown in the XRD scans cannot be observed from the surface morphology images.

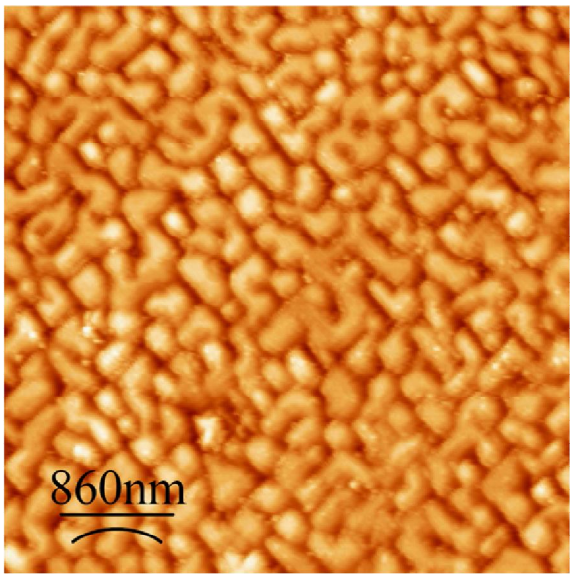

Fig. 4.15 – *Illustrative AFM topographic image of 60-nm thick $BiMnO_3$ thin film grown at 630°C and 0.1 mbar of O_2 on (001)-oriented $SrTiO_3$ substrate.*

AFM topographic images bear out the clear island surface morphology of $BiMnO_3$ thin films grown on $SrTiO_3$ (Fig. 4.15), indicative of a 3D growth mode. Consequently, notably rough surfaces are found, with typically root-mean-square (rsm) surface roughness of 5 nm (3 nm in the best-case scenario).

4.3 Magnetic properties of Bi – Mn – O films

As explained in chapter 1, the ferromagnetic order in $BiMnO_3$ results from a peculiar e_g orbital ordering of Mn^{3+} cations, which makes ferromagnetic interactions dominate over the antiferromagnetic ones [5]. Nonetheless, this delicate balance between antiferromagnetic and ferromagnetic may substantially be modified as a consequence of the epitaxial strain [17]. Moreover, Bi-deficient samples [3] and multiphase character of Bi – Mn – O system [2] makes the magnetic characterisation even more complicated. Here we study the magnetic properties of both single-phase $BiMnO_3$ films and multiphase Bi – Mn – O films, carried out by the SQUID magnetometer (Sect. 2.5.1). The applied magnetic field, H, has been applied along an

in-plane direction. The large diamagnetic contribution of the substrate $SrTiO_3$ was removed from the raw data (see Appendix D).

The temperature dependence of the magnetisation, $M(T)$, of single-phase 50-nm $BiMnO_3$ is illustrated in Fig. 4.16 (c), whose XRD pattern is shown in Fig. 4.16 (a). The sample was cooled down under an applied in-plane magnetic field, H, of 1000 Oe. The ferromagnetic transition temperature occurs at $T_{FM} \sim 100$ K, in close agreement with the reported bulk value ~105 K [7], as inferred by the differentiated inverse of the volume magnetic susceptibility $1/\chi_v$ (Fig. 4.16 (c); right axis). Note that χ_v is computed by M/H once the diamagnetic contribution of $SrTiO_3$ substrate is removed. Quite different magnetic behavior is found for thicker films, Fig. 4.16 (d), in which strong multiphase character is found, Fig. 4.16 (b). The differentiated $1/\chi_v$ (Fig. 4.16 (d); right axis) shows two maxima, indicating two ferromagnetic transition temperatures, *i.e.* at ~50 K and ~100 K of Bi – Mn – O system. Whereas the higher transition temperature must be related to the $BiMnO_3$ phase, that at 45-50 K must correspond to the Mn_3O_4 phase [clearly present in the XRD pattern, Fig. 4.16 (b)], as this compound, with spinel structure AB_2O_4: Mn^{2+} (at the A-site) and Mn^{3+} (at the B-site), orders antiferromagnetically below ~45 K [18 – 20], giving rise to net magnetic moment (*i.e.* ferrimagnetism, no compensated spins of Mn^{2+} and Mn^{3+}).

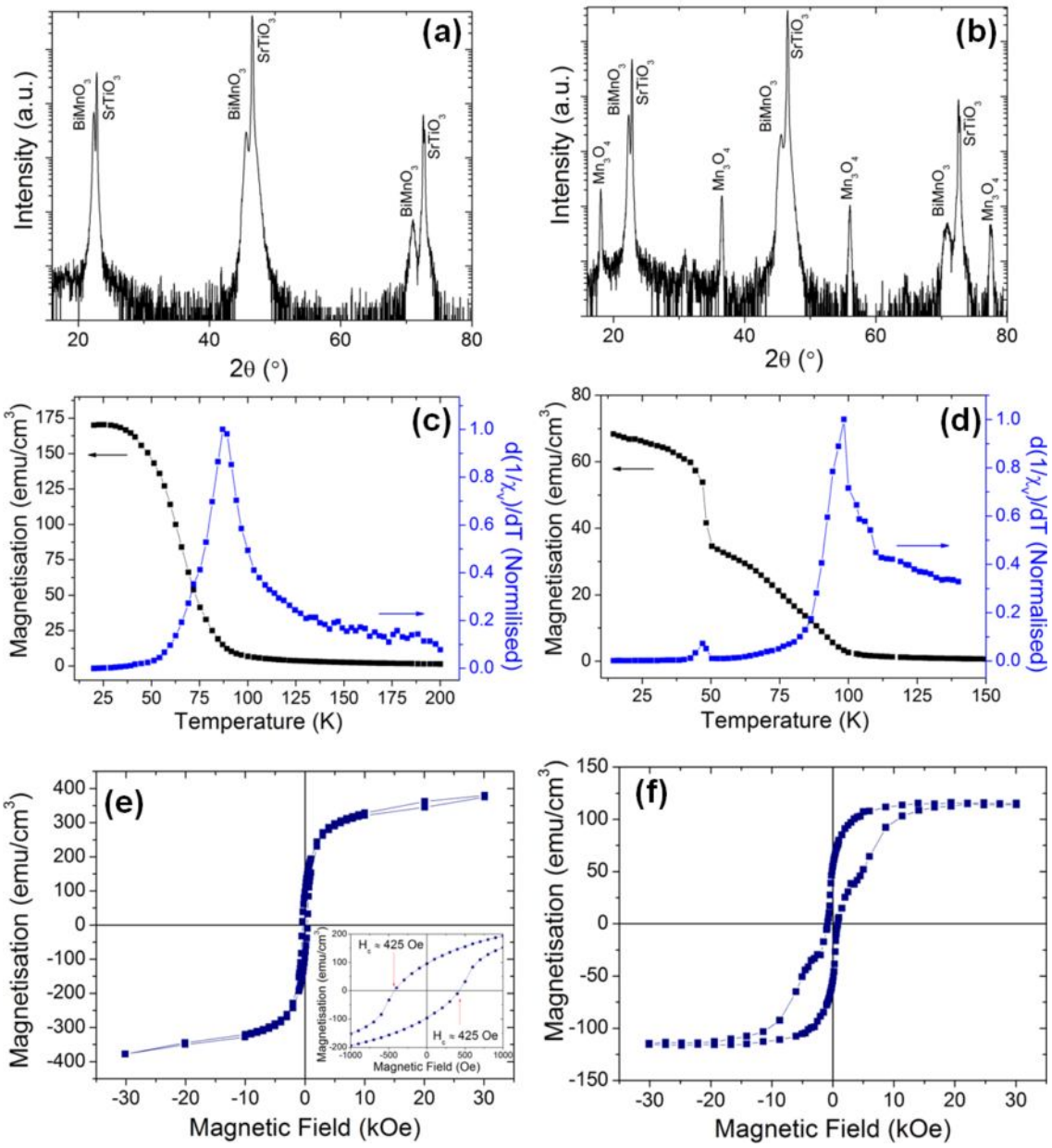

Fig. 4.16 – *Magnetic properties of Bi – Mn – O films grown at 630ºC and 0.1 mbar of O_2 pressure of 50 nm* **(a, c, e)** *and 100 nm* **(b, d, f)** of thickness. *θ/2θ XRD scan of single-phase $BiMnO_3$ film* **(a)** *and multiphase Bi – Mn – O film* **(b)**. *Temperature dependence of the magnetization (left axis) and derivative of the inverse susceptibility (right axis) of $BiMnO_3$ thin film* **(c)** *[the corresponding XRD pattern in (a)] and Bi – Mn – O film* **(d)** *[the corresponding XRD pattern in (b)] under an in-plane applied magnetic field of 1000 Oe.* **(e)** *Magnetic field dependence of the magnetization of $BiMnO_3$ thin film [the corresponding XRD pattern in (a)] at 10 K. Bottom panel: Zoom of the low field region.* **(f)** *Magnetic field dependence of the magnetization of Bi – Mn – O film [the corresponding XRD pattern in (b)] at 10 K.*

Fig. 4.16 (e) shows magnetisation data versus applied magnetic field, $M(H)$, recorded at 10 K, for single-phase $BiMnO_3$ films [XRD pattern Fig. 4.16(a)], in which an hysteretic $M(H)$ behaviour can clearly be observed, confirming the ferromagnetic character of $BiMnO_3$ thin films, with a coercive field, H_c, found to be around 425 Oe. Yet the multiphase Bi – Mn – O film [XRD pattern Fig. 4.16 (b)] shows a quite broader $M(H)$ curve [Fig. 4.16 (f)], reflecting the contribution of the ferrimagnetic Mn_3O_4 phase, which displays larger coercive fields [18 – 20], and the likely magnetic coupling with the ferromagnetic $BiMnO_3$ phase. Moreover, $M(H)$ curve of Bi – Mn – O films [Fig. 4.16 (f)] shows lower saturated magnetisation (~120 emu/cm^3) than that of pure $BiMnO_3$ phase (~375 emu/cm^3) [Fig. 4.16 (e)], which is due to the reduced magnetic moment of Mn_3O_4 phase (1.5 – 1.8 μ_B/f.u.) [18 – 20] compared to that of $BiMnO_3$ (~3.6 μ_B/f.u. in bulk [7]).

It is worth noting, though, that the saturated magnetisation for single-phase $BiMnO_3$ films [Fig. 4.16 (e)] is found to be much lower (375 emu/cm^3 corresponds to ~2.5 μ_B/f.u.) than that of bulk specimens. Similar low magnetisation values were reported for $BiMnO_3$ thin films (1.5 – 2.5 μ_B/f.u. [2, 3, 17, 21 – 23]). The smaller saturation moment in thin film was argued to be driven by the enhancement of the inherent magnetic frustration in $BiMnO_3$ [17]. It is to be noted that in bulk $BiMnO_3$ two out of three magnetic interactions are ferromagnetic, dominating over the antiferromagnetic ones [5]. Yet the strength of the ferromagnetic and antiferromagnetic interactions can be modified by the epitaxial strain as it changes the inter-ion distances and angles, unbalancing the bulk equilibrium between the two kinds of magnetic interactions [17]. However, on the other hand, off-stoichiometric films, in particular Bi-deficient samples may also produce a strong reduction of the magnetisation of $BiMnO_3$ films [3]. By electric equilibrium of the compound each Bi vacancy originates three Mn^{4+} neighbouring ions, which are not subjected to Jahn-Teller distortion like Mn^{3+} and consequently contribute to the local disruption of the peculiar orbital ordering of Mn^{3+} ions responsible for the ferromagnetic ground state of $BiMnO_3$. Moreover, each Mn^{4+} ($t_{2g}^3 e_g^0$) may couples either antiferromagnetic or ferromagnetic with the surrounding Mn^{3+} ($t_{2g}^3 e_g^1$) depending on the local configuration, *i.e.* weather empty e_g orbital points toward empty e_g orbital or half-filled e_g orbital, respectively (Sect. 1.2.3). The local competing ferromagnetic/antiferromagnetic interactions lead to a strong spin frustration. Indeed, not only Mn^{4+} couples antiferromagnetically with the Mn^{3+} matrix, but also

several first neighbour Mn^{3+} ions in the vicinity of a Bi vacancy [3]. Taking into account the high Bi volaitility and that just 0.05% of Mn^{4+} concentration can produce a ~40% reduction of the magnetisation [3], this latter scenario seems to be the most plausible when it comes to describe the magnetic properties of our $BiMnO_3$ films. Note that this small amount of Mn^{4+} is hardly detectable by chemical analysis techniques. However, both chemical composition (Sect. 4.1.1) and structure characterisation (Sect. 4.2) suggest some Bi-deficiency in $BiMnO_3$ films, which would be in agreement with the small recorded magnetisation. Indeed, the fact that all reported magnetisation data of $BiMnO_3$ films [2, 3, 17, 21 – 23] display reduced magnetic moments evidences the difficulty in obtaining high-quality stoichiometric $BiMnO_3$ thin films.

4.4 Electric and magnetoelectric properties

4.4.1 Background

One of the interesting features multiferroic materials may exhibit is the so-called magnetoelectric coupling (as explained in Sect. 1.1.3), which consists of the coupling between the ferroelectric and the magnetic order. A common route to investigate the magnetoelectric character consists of studying the effect on the dielectric permittivity, ε, of changes of the magnetic state of the magnetic layer, either by applying a magnetic field, the so-called magnetocapacitance (or magnetodielectric response), $\varepsilon(H)$, or by searching for variations of ε in the temperature dependence, $\varepsilon(T)$, in the vicinity of the magnetic transition temperature (see Sect. 1.1.3).

$BiMnO_3$ bulk polycrystalline samples were reported to display a modest dielectric permittivity (ε_r ~ 25) at low temperatures (50 K – 170 K) [7]. The reported dielectric constant shows an steady increasing value upon temperature. Interesting enough, the dielectric permittivity of $BiMnO_3$ bulk polycrystalline samples displayed a slight anomaly (a subtle peak increase) around the ferromagnetic transition temperature (T_{FM} ~ 100 K) [7]. Moreover, the dielectric response showed a weak magnetic field dependence, in which the magnetodielectric effect, MC = [ε(H)-ε(0)]/ε(0), scales with

the square of the magnetisation, M^2, being maximum (0.6%) at $T \sim T_{FM}$ [7]. Both features suggested that the two ferroic orders of $BiMnO_3$ are coupled. On the other hand, the dielectric behaviour of $BiMnO_3$ thin films were analysed by impedance spectroscopy [24, 25], in which, despite discrepancies on the value of the dielectric permittivity with regard to that of bulk samples, similar anomalies were found around T_{FM}. Yet the magnetic dependency of the dielectric properties of $BiMnO_3$ thin films remains to be elucidated.

Here in this section we performed an exhaustive study of the dielectric properties of $BiMnO_3$ thin films, in which temperature dependent impedance spectroscopy (see Sect. 3.2) was used to disentangle extrinsic and intrinsic contributions to the measured permittivity. At the end of the section, the intrinsic magnetoelectric response of $BiMnO_3$ thin films is obtained by deconvoluting magentodielectric and magnetoresistive effect (see Sect. 3.2.4). To performed the dielectric measurements, Pt/$BiMnO_3$/Nb:SrTiO3 capacitors were fabricated (see Sect. 3.1). $BiMnO_3$ samples were grown at the optimised conditions for single-phase formation (*i.e.* at 630 ºC and 0.1 mbar of O_2 pressure). The thickness of the set of samples was comprised between 40 and 60 nm.

4.4.2 Complex dielectric constant and ac conductivity. Qualitative analysis

Fig. 4.17 shows the temperature, T, evolution of the dielectric permittivity at different frequencies, assuming that the measured capacitance is only due to the dielectric response of $BiMnO_3$ film, *i.e.* $C = \varepsilon'\varepsilon_0 A/(2t)$ (see chapter 3). As observed, $\varepsilon'(T)$ displays a clear step-like increase on increasing temperature. Moreover, this step-like feature moves toward higher temperatures on increasing the measuring frequency. As a result, $\varepsilon'(T)$ shows two plateaus: at high and low temperatures. Whereas the value of the dielectric permittivity at low temperatures is almost frequency independent and close to the bulk values (~ 25), that of the high temperatures is anomalous high and highly frequency dependent. As described in sect. 3.2, these features are clearly indicating that extrinsic contributions are likely altering the dielectric response of $BiMnO_3$ films.

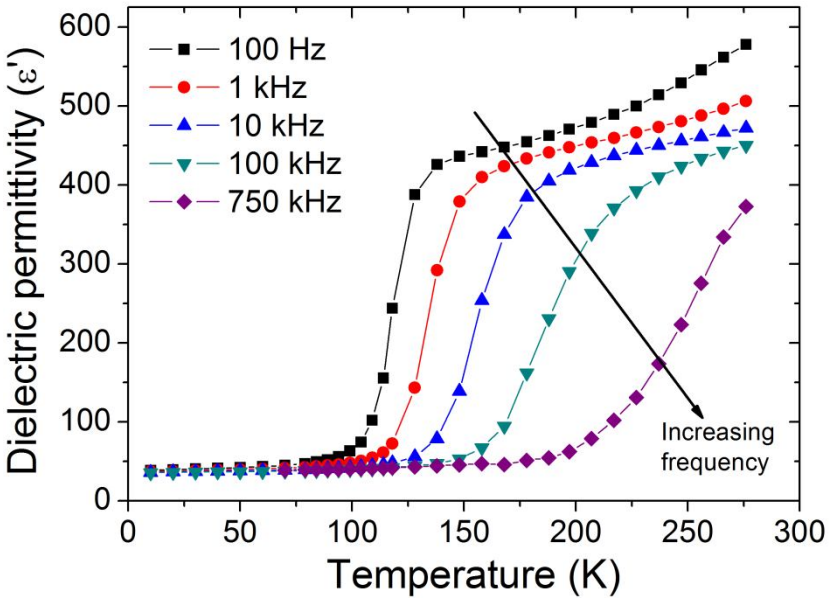

Fig. 4.17 – *Temperature dependence of the dielectric response of Pt/$BiMnO_3$/Nb:$SrTiO_3$ system measured at different frequencies.*

In order to assess the frequency response, the complex representation of the dielectric constant, $\varepsilon^* = \varepsilon' - i\varepsilon''$, will be used (see Sect. 3.2.2). Fig. 4.18 depicts the frequency dependence, ν, of the real part (top panel), ε', and the imaginary part (bottom panel), ε'', of the complex dielectric constant. The measured ε' of Pt/$BiMnO_3$/Nb:$SrTiO_3$ capacitors shows two frequency regimes, where $\varepsilon'(\nu)$ is rather constant, separated by a step-like region which is accompanied by a peak in $\varepsilon''(\nu)$. Both the sharp increase in $\varepsilon'(\nu)$ and the peak in $\varepsilon''(\nu)$ shift toward higher frequencies on increasing temperature. At first sight, this behaviour shows a clear resemblance of a thermally activated Debye-like dielectric relaxation dominating the frequency dependence of $\varepsilon'(\nu)$ [26]. Yet, as described in Sect. 3.2.3, a Maxwell-Wagner relaxation type, in which two electric contributions (characterised by two *RC*-elements) to the dielectric properties of the system is found, may reproduce identical dielectric behaviour, following the same temperature evolution depicted in Fig. 4.18 if the resistance of either of each *RC*-element decreases upon temperature. Indeed, the measured value of ε' in the low frequency plateau is anomalous large (~ 450 – 500), whereas that obtained from the high frequency plateau (~ 35 – 40) is in a similar range of the dielectric permittivity found in $BiMnO_3$ bulk samples [7], thus indicating a more plausible intrinsic character.

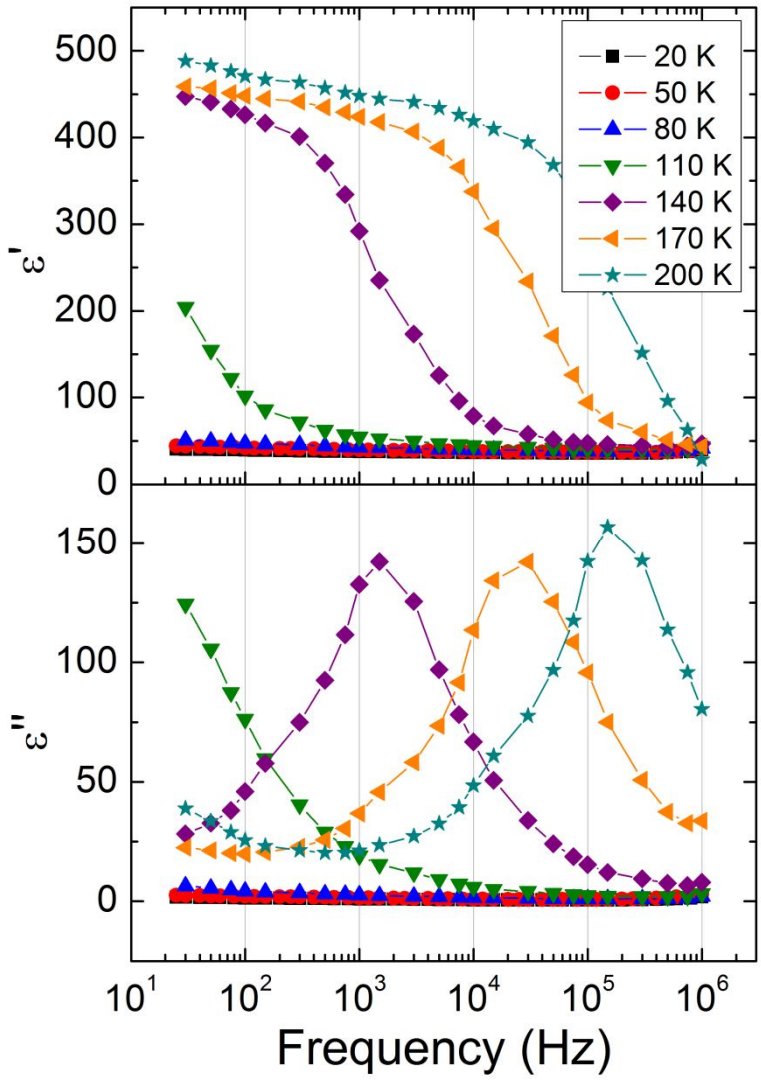

Fig. 4.18 – *Frequency dependence of the real part (top panel) and the imaginary part (bottom panel) of the complex dielectric constant of Pt/$BiMnO_3$/Nb:$SrTiO_3$ capacitors measured at different temperatures.*

For an ideal dielectric behaviour ε' should be frequency independent (see Fig. 3.7 in Sect. 3.2.2). Yet it is worth noting that $\varepsilon'(\nu)$ modestly decreases on increasing frequency in the high-frequency plateau, following the same trend described for non-ideal dielectrics (see Fig. 3.8 in Sect. 3.2.2). This non-ideality can better be appreciated in the complex conductivity, $\sigma^* = i \cdot \omega \varepsilon_0 \varepsilon^*$, in which the real part, σ', of σ^* at various illustrative temperatures is plotted in Fig. 4.19. In the log-log scale of $\sigma'(\nu)$, Fig. 4.19, at high-frequencies there is a power-like frequency dependence, $\sim \nu^{\alpha}$, which is in agreement with the Jonscher's universal dielectric response of non ideal dielectrics [26 – 28]. This frequency dependent term is superimposed to a non-frequency dependent term, the

corresponding leakage of the sample: σ_{dc}, responsible for the flattening of $\sigma'(\nu)$ at intermediate frequencies. Thus it reasonably follows $\sigma' = \sigma_{dc} + \sigma_0 \cdot \omega^{\alpha}$, where ω stands for the angular frequency ($2\pi\nu$), marked with dashed line in Fig. 4.19, as described in Sect. 3.2.2 for non-ideal dielectrics. However, when further lowering ν, conductivity is steeply reduced, deviating for the ideal behaviour marked in dashed lines. As shown by data in Fig. 4.19, this drop is also temperature dependent, and shifts toward higher frequencies as temperature rises. Not surprisingly, it coincides with the large enhancement of the dielectric constant and the peak of ε'' shown in Fig. 4.18.

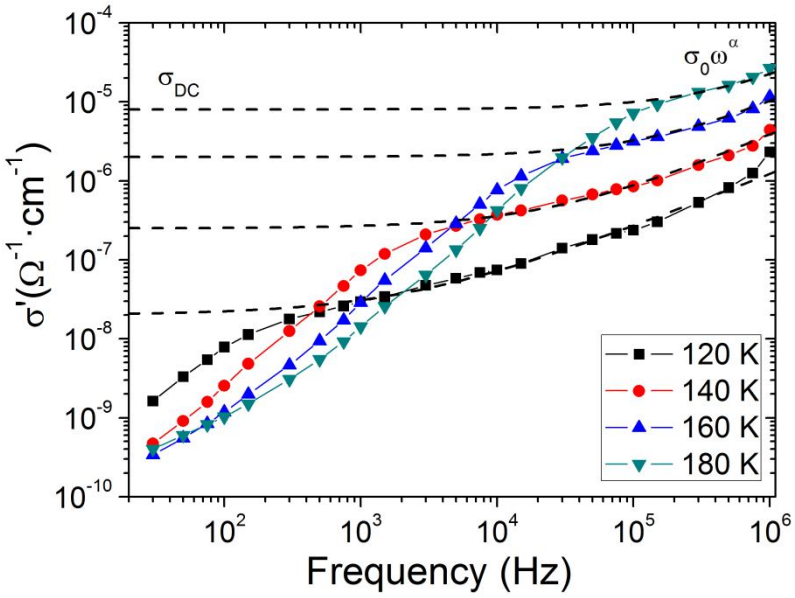

Fig. 4.19 – *Frequency dependence of σ' at different temperatures. The dashed line indicates the non-ideal dielectric behaviour, $\sigma' = \sigma'_{dc} + \sigma'_0\omega^{\alpha}$ (see text).*

In the following it will be shown that both, the low-frequency region as well as the step-like region are not-intrinsic properties of $BiMnO_3$ film but result from the contribution of interface effects.

4.4.3 Impedance spectroscopy. Quantitative analysis

To obtain a more quantitative insight into the dielectric response of the sample, to investigate the number of electrical responses present and to determine the intrinsic

properties of the film, complex impedance ($Z^* = Z' + iZ''$) spectroscopy was performed as described in Sect. 3.2.1.

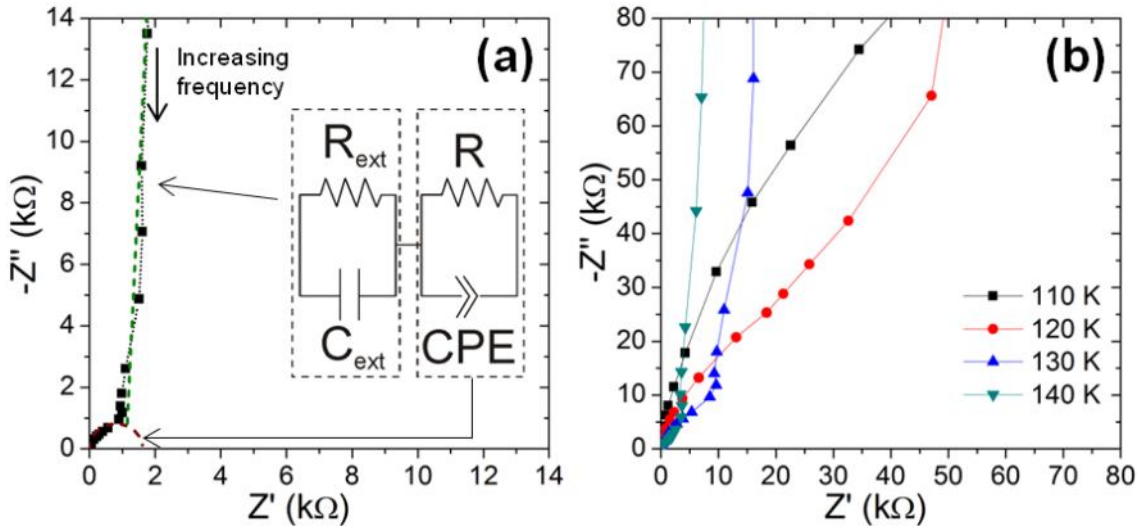

Fig. 4.20 – (a) *Impedance complex plane (–Z'' – Z' plots) from impedance data measured at 150 K. The visual guide of the dashed line indicates the two semicircles at high and low frequency. The inset sketch depicts the equivalent circuit, describing the different electrical responses present in Pt/$BiMnO_3$/Nb:$SrTiO_3$ capacitors (see text for symbols).* **(b)** *–Z'' – Z' data plots measured at different temperatures.*

In Fig. 4.20 (a) illustrative *–Z''* - *Z'* plot of the impedance measured at 150 K is shown. Data signals the existence of two incomplete semicircles (marked with dashed lines as guide-to-eyes) at high and low frequency, respectively. The existence of these two semicircles can be explained by the presence of two electrical contributions to the dielectric data in Pt/$BiMnO_3$/Nb:$SrTiO_3$ capacitors. Thus, as suspected, the dielectric response observed in Sect. 4.4.2 does not only come from the intrinsic dielectric properties of $BiMnO_3$ film, which would produce a unique semicircle (Sect. 3.2.1). This behaviour is hence consistent with a Maxwell-Wagner relaxation, as explained in Sect. 3.2.3, in which extrinsic dielectric contribution is affecting the measurement. Nonetheless, it is worth mentioning here that for temperatures lower than ~90 K, only the high frequency contribution is observed as the low frequency contribution is out of the frequency range, *i.e.* it appears at frequencies lower than 20 Hz. Instead, for temperatures higher than 200 K, only the low frequency contribution is found in the

frequency spectra as the high frequency contribution appears at frequencies higher than 1 MHz, *i.e.* not experimentally available.

On the other hand, it can be appreciated in Fig. 4.20 (a) that the radius of the low-frequency semicircle is much larger than the high-frequency one; this reflects that the low-frequency contribution is much more resistive than that of the high-frequency contribution. Additionally, inspection of the impedance data at different temperatures, shown in Fig. 4.20 (b), indicates that the high frequency semicircle significantly decreases on increasing temperature, evidencing that the resistivity of the high frequency contribution decreases as temperature rises, according to data of the conductivity shown in Fig. 4.19.

Thus, according to Fig. 4.20, the most natural explanation of the dielectric behaviour shown in section 4.4.2 comes from the formation of a capacitive layer at the interface and by the temperature dependence of the resistivity of the core of the film, as deduced in Sect. 3.2.3. The band bending caused by the difference between the work function of the metal and the electronic affinity of the dielectric gives rise to charge depletion/accumulation region at the interface [24, 27, 29, 30], which forms a relatively thin layer, behaving as a high resistive barrier, modelled as a capacitor, C_{ext}, and a low conductance, R_{ext}^{-1}, connected in parallel as illustrated by the circuit-model sketched in Fig. 4.40 (a). At high frequency, charge carriers have no time to follow the alternating electric field and the measured capacitance is the film and the interface capacitances in series (Fig. 4.21). However, at low frequencies, charge carriers do respond to the electric field in the low resistive part, *i.e.* the core of the film [modelled as R inset Fig. 5.42 (a)], forming an electric current. This entails that the drop of the electric field is mostly taking place at the interface barrier, yielding the apparent high dielectric constant shown in Fig. 4.18 because of the apparent reduction of the dielectric thickness (measured capacitance ~ $1/t'$) as shown in Fig. 4.21 [29]. On increasing temperature, the film resistivity decreases [so leakage, σ_{dc}, increases (Fig. 4.19)] and charge carriers can respond to faster alternation of the electric field. Thus, the apparent enhancement of the dielectric constant due to the apparent reduction of the dielectric thickness is shifting toward higher frequencies on increasing temperature, consistent with the observed temperature evolution of data of Fig. 4.18. The cut-off frequency, ω_{max}, at which losses

(~ε'') show a peak [Fig. 4.18] is given by the condition $\omega_{max}(T) = [R(T)\cdot C]^{-1}$ [29] and is therefore temperature dependent. Hence, the thermal activation of this apparent dielectric relaxation is driven by the temperature-dependence of the resistivity, instead of permanent dielectric dipoles. Indeed, the dielectric relaxation of permanent dipole moments tends to occur at much higher frequencies, in the range of the microwaves [31], as indicated in Sect. 3.2.2.

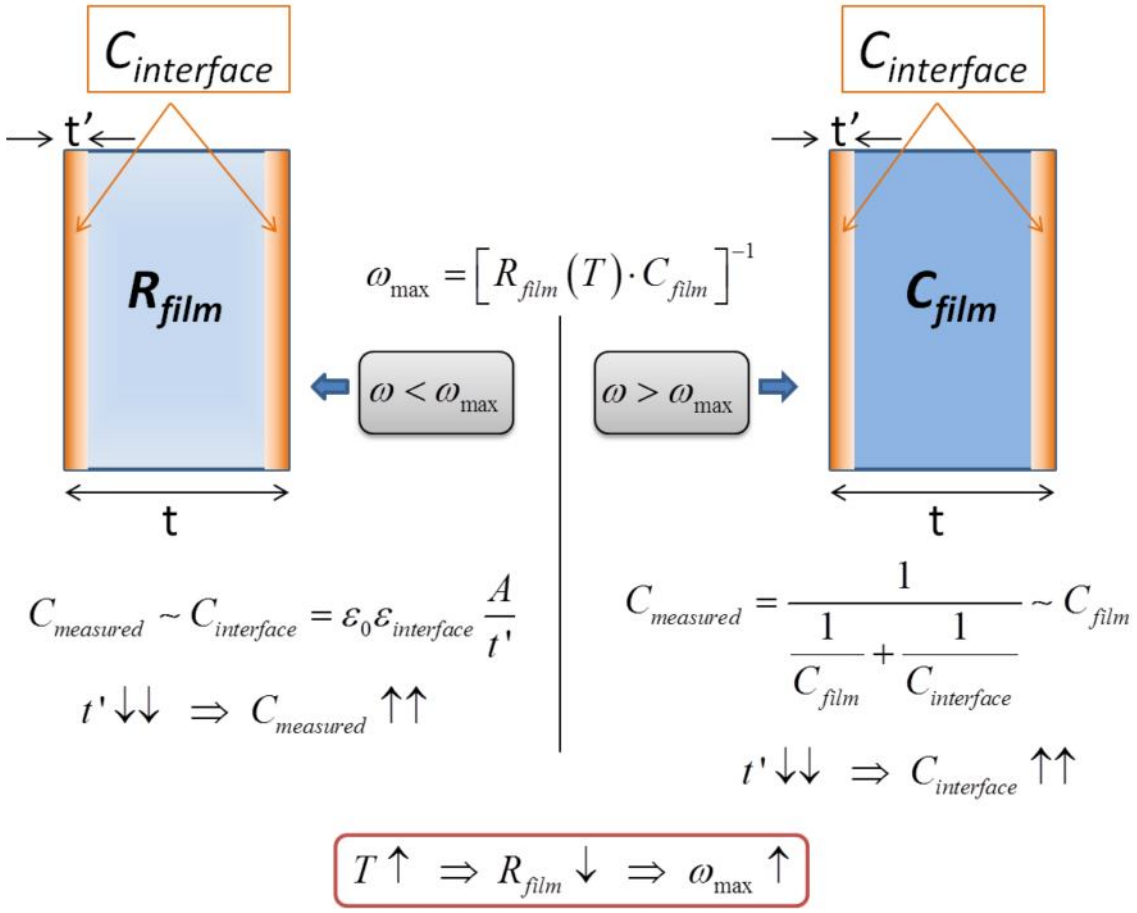

Fig. 4.21 – *Sketch of the dielectric behaviour of $BiMnO_3$ thin films when the resistivity of the film and interface parasitic capacitance interfer.*

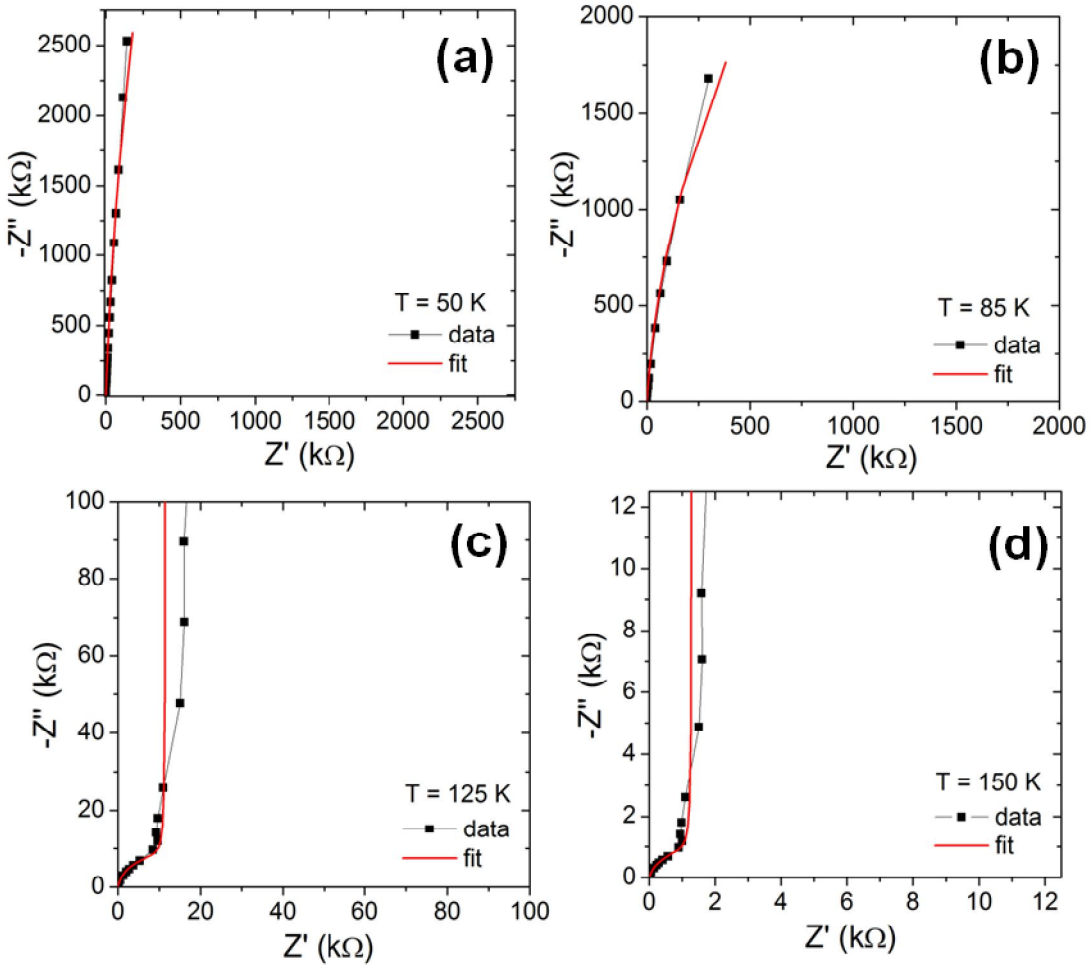

Fig. 4.22 – *Experimental data (black solid symbols) and fitting (red solid line) using the model of Eq. 4.2 for some illustrative temperatures.*

The impedance of $Pt/BiMnO_3/Nb:SrTiO_3$ system, in which the intrinsic film and the interface contributions are accounted, is given by adapting of Eq. 3.10 in Sect. 3.2.3:

$$Z^*(R-CPE, R_{ext}-C_{ext}) = \frac{R}{1+R\cdot Q\cdot(i\omega)^{\alpha}} + \frac{R_{ext}}{1+i\omega\cdot R_{ext}\cdot C_{ext}} \qquad (4.2)$$

where the first and the second terms correspond to the film and the extrinsic contributions, respectively. A *CPE* element (see Sect. 3.2.1) is used for the film contribution accounting for the non-ideality of the dielectric behaviour of $BiMnO_3$ film shown in the previous section. Yet for temperatures lower than 110 K, only the intrinsic

R–CPE circuit was used as only one electric contribution to the impedance data was found in the frequency range:

$$Z^*(R-CPE)=\frac{R}{1+R\cdot Q\cdot(i\omega)^{\alpha}} \tag{4.3}$$

Eq. 4.2 and 4.3 was used to fit impedance data in order to validate the proposed model. Fig. 4.22 shows some illustrative results of the fits to -Z''– Z' data at different temperatures. As observed, model (solid lines) and data match very reasonably, which is also extensive for the rest of temperatures up to 160 K. Above this temperature the low-frequency contribution dominates almost completely the experimentally available frequency range (up to 1 MHz), and reliable determining the intrinsic properties (high-frequency contribution) was unfeasible. The fitting values of the *R–CPE* (*Q*, *R*, *α*) corresponding to the film contribution are summarised in table 4.5.

Temperature (K)	***Q* [$Fs^{\alpha-1}$]**	**error *Q* [%]**	***R* [Ω]**	**error *R* [%]**	***α***	**error *α* [%]**
20	$2.44\cdot10^{9}$	0.3	$9.29\cdot10^{7}$	13.3	0.986	0.03
30	$2.52\cdot10^{9}$	0.4	$7.82\cdot10^{7}$	13.2	0.984	0.04
40	$2.61\cdot10^{9}$	0.4	$7.38\cdot10^{7}$	14.3	0.982	0.04
50	$2.70\cdot10^{9}$	0.5	$6.84\cdot10^{7}$	15.1	0.980	0.05
60	$2.82\cdot10^{9}$	0.6	$6.12\cdot10^{7}$	16.0	0.978	0.05
70	$2.97\cdot10^{9}$	1.1	$3.09\cdot10^{7}$	19.5	0.975	0.11
79	$3.22\cdot10^{9}$	1.5	$1.86\cdot10^{7}$	16.0	0.970	0.15
84	$3.45\cdot10^{9}$	1.8	$1.14\cdot10^{7}$	12.6	0.965	0.18
89	$3.76\cdot10^{9}$	2.3	$6.59\cdot10^{6}$	9.8	0.959	0.23
94	$4.21\cdot10^{9}$	3.1	$3.57\cdot10^{6}$	7.8	0.951	0.31
99	$5.04\cdot10^{9}$	4.7	$1.89\cdot10^{6}$	7.4	0.939	0.47
104	$6.41\cdot10^{9}$	7.6	$9.36\cdot10^{5}$	7.7	0.921	0.76
109	$7.23\cdot10^{9}$	6.5	$1.74\cdot10^{5}$	4.6	0.927	0.61
114	$8.11\cdot10^{9}$	7.9	$8.94\cdot10^{4}$	4.4	0.918	0.73
118	$9.21\cdot10^{9}$	9.3	$4.42\cdot10^{4}$	4.6	0.909	0.90
126	$1.22\cdot10^{8}$	9.8	$1.15\cdot10^{4}$	4.3	0.894	1.10
138	$1.76\cdot10^{8}$	10.1	$3.50\cdot10^{3}$	4.4	0.874	1.35
148	$2.98\cdot10^{8}$	12.0	$1.29\cdot10^{3}$	4.2	0.844	1.52
158	$7.61\cdot10^{8}$	13.1	$5.43\cdot10^{2}$	4.6	0.789	1.98

Table 4.5 – *Fitting results of the high-frequency R-CPE element, sketched in Fig. 4.20 (a).*

It is worth noting that the CPE exponent, α, decreases upon temperature (Fig. 4.23), signalling an increasing non-ideality of the dielectric behaviour of $BiMnO_3$ film on increasing temperature. Remarkably enough, α shows an anomaly around 100 K, possibly reflecting the set of the magnetic order.

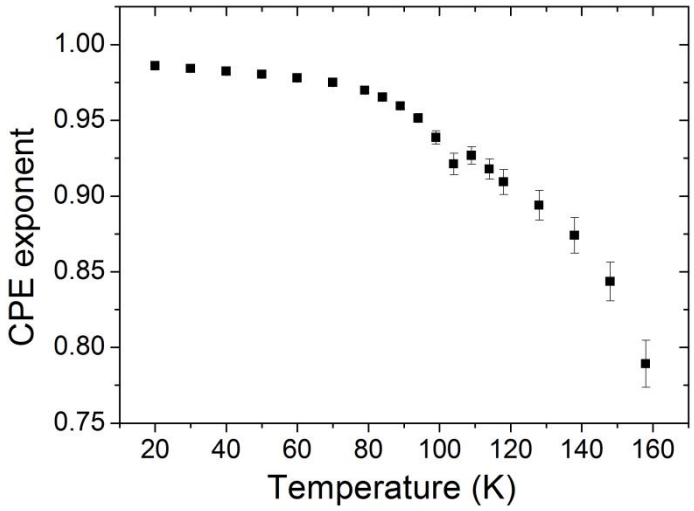

Fig. 4.23 – *Temperature dependence of the CPE exponent.*

From the fitting values (Q, R, α), the intrinsic dielectric permittivity [$\varepsilon = C\cdot(2t/\varepsilon_0 A)$, where $C = (Q\cdot R)^{(1/\alpha)}/R$, see Appendix C] and the intrinsic resistivity [$\rho = A\cdot R/(2t)$] of $BiMnO_3$ film can be computed at each temperature, as shown in Fig. 4.24 and 4.25, respectively. For the sake of clarity in the text, in the following dielectric permittivity and resistivity stand for the intrinsic ones of $BiMnO_3$ films, computed by impedance spectroscopy as stated above.

The temperature dependence of dielectric permittivity, $\varepsilon(T)$, of $BiMnO_3$ films (Fig. 4.24, top panel) shows a modest steady increase up to ~70 K, consistent with the slight increase found in the dielectric permittivity of bulk specimens in similar range of temperatures [7]. However, above ~80 K, $\varepsilon(T)$ upturns, displaying a peak structure around 105 K, close to the ferromagnetic temperature. This anomaly can be better appreciated in the derivative of the dielectric permittivity with respect to temperature (Fig. 4.24, bottom panel), in which clearly there is a pronounced change around the magnetic transition temperature (marked with dashed line). This peak in $\varepsilon(T)$ is in close agreement with previous work, both in thin films [25] and bulk [7], and it may well

represent the intrinsic magnetoelectric coupling of $BiMnO_3$ compound. Note that extrinsic contributions cannot be the origin of this anomaly as they have been previously disentangled from the raw impedance data.

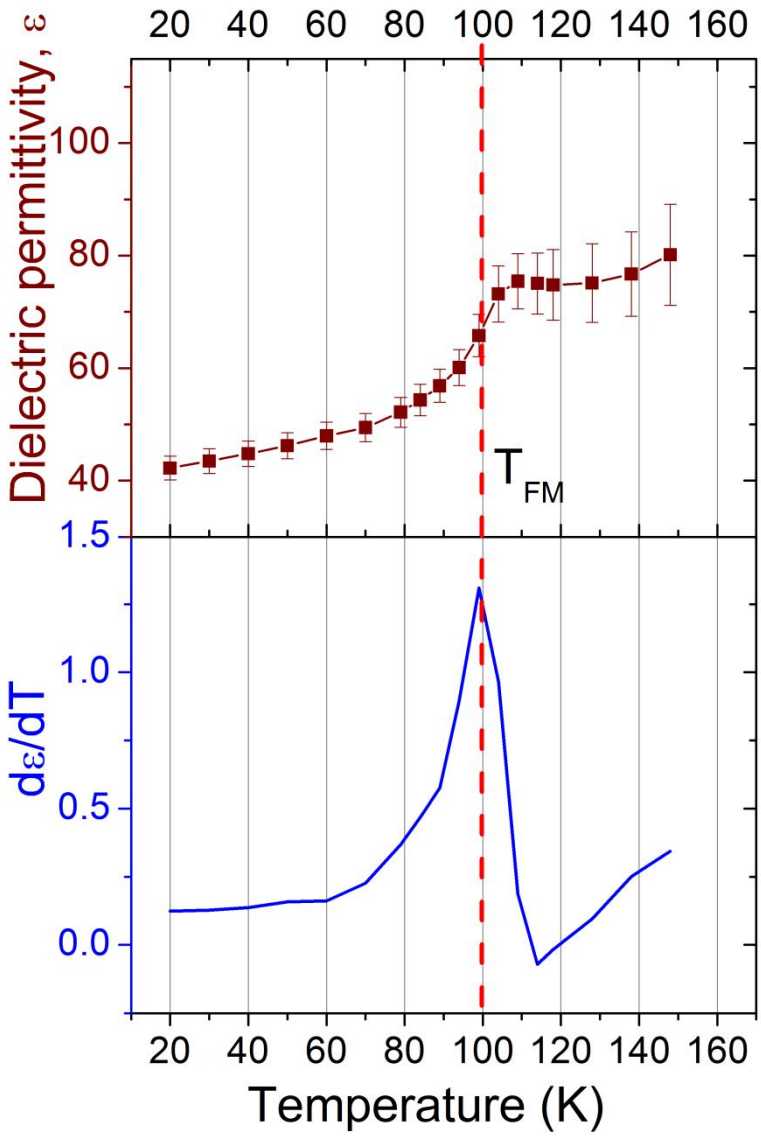

Fig. 4.24 – *Temperature dependence of the dielectric permittivity (top panel) and its derivative (bottom panel) of $BiMnO_3$ thin films. The dashed line indicates the ferromagnetic transition temperature.*

The temperature dependence of the resistivity, $\rho(T)$, of $BiMnO_3$ thin films (Fig. 4.25) shows a semiconductor-like behaviour, similar to what has been reported in previous work and related perovskite oxides [7, 8, 22, 24, 32]. The resistivity values are

found to decrease upon temperature, from ~10^{10} Ω·cm at 20 K to ~10^5 Ω·cm at 160 K. Yet data shows two different regimes for low and high temperatures reflecting a change in the predominant conduction mechanism:

i) Above ~100 K, the conduction mechanism is thermally activated, for which $\rho(T)$ follows an Arrhenius law (indicated as dashed line in Fig. 4.25), $\rho(T) = \rho_0 \exp[-E_a/(k_B T)]$, with an activation energy value E_a ~ 184 meV.

ii) Below ~100 K, instead, $\rho(T)$ monotonously deviates from the Arrhenius law, in which the thermal activation of charge transport is weakened or becoming negligible as inferred by the reduced slope of the ρ vs 1/T curve.

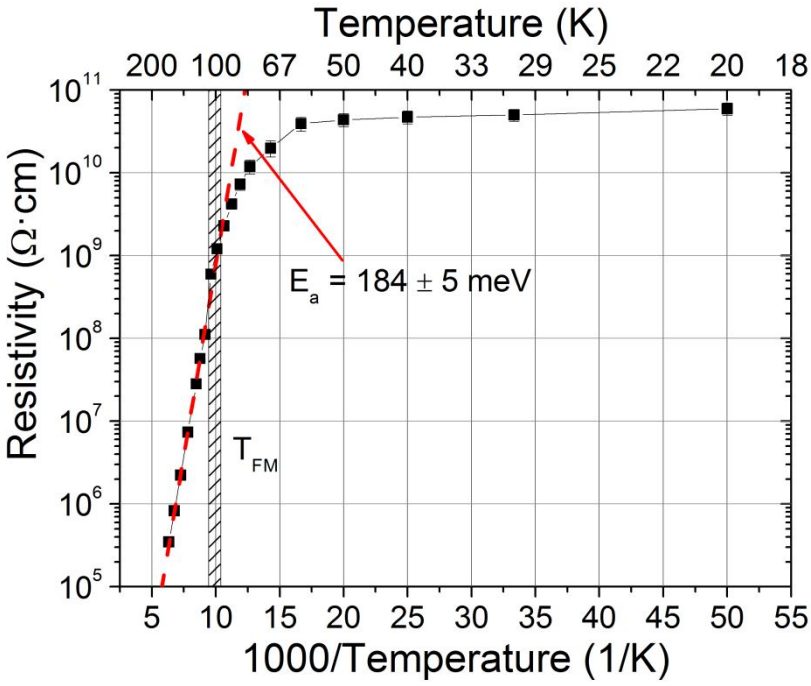

Fig. 4.25 – *Temperature dependence of the resistivity of $BiMnO_3$ films. The dashed line shows the Arrhenius fitting (see text). Dashed region indicates the magnetic Curie temperature.*

In order to fit the $\rho(T)$ data in all experimental temperature range, alternative conduction mechanism, such Mott's Variable-Range-Hopping (VRH) or Efros and Shklovskii VRH conduction mechanisms [$\rho(T) = \rho_0 \exp(T_0/T^{1/\gamma})$, $\gamma = 4$ or 2, respectively]

have been considered [33 - 37]. Yet it is found that none of these models (Fig. 4.26) allow describing satisfactorily the whole temperature range, either. Moreover, VRH model, in which electron hopping is not produced between first neighbour ions but there is an optimum hopping distance that maximise the hopping probability [37], is proposed for either disordered systems or with doping impurities, in which localised states are found. As this case is not expected in $BiMnO_3$ films, the conduction mechanism shown in Fig. 4.25 has more physical meaning. In any case, data in Fig. 4.25 suggests either a change of the transport mechanism or the relevant energy for activated transport occurring at about 100 K. Remarkably enough, this change in the conduction mechanism appears close to the ferromagnetic transition temperatures, indicating that the set of the magnetic order may have some influence in the conductivity of $BiMnO_3$ compound.

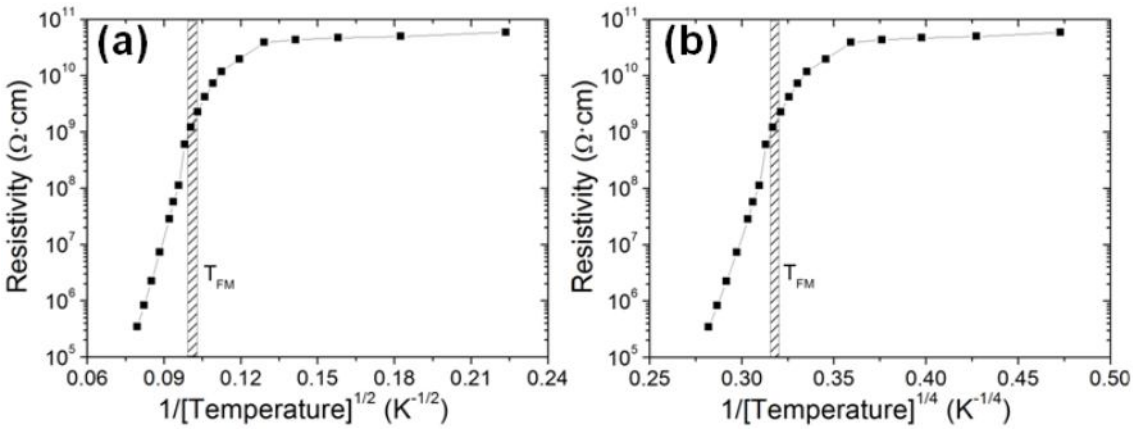

Fig. 4.26 – *Resistivity of $BiMnO_3$ films as a function of (1/Tempereture)$^{1/\gamma}$, being γ =2* **(a)** *and γ = 4* **(b)**. *The dashed region indicates the ferromagnetic Curie temperature.*

Above 100 K, the activation energy (E_a ~0.18 eV) of the semiconducting behaviour of $BiMnO_3$ films gives an estimation of the energy gap between the conduction and valence bands. Similar activation energies are found in previous work on BiMnO3 thin films [22, 24, 25]. Yet it is worth noting that optical measurements reveal a much larger band gap in $BiMnO_3$ compounds, around 1.1 eV [23].

4.4.4 Magnetoelectric response

Data shown in previous section points to the occurrence of magnetoelectric coupling in $BiMnO_3$ films as inferred from the clear anomaly of $\varepsilon(T)$ curve around the magnetic transition temperature (Fig. 4.24). In order to bear out this plausible magnetoelectric effect, magnetic field, H, dependent dielectric measurements were performed. Yet it is also clear form data in previous section the presence of extrinsic and intrinsic electric contributions in $Pt/BiMnO_3/Nb:SrTiO_3$ capacitors. This fact, together with the possibility of $BiMnO_3$ displaying a certain degree of magnetoresistence, can evoke an apparent magnetic-field dependent dielectric permittivity without magnetoelectric coupling (see Sect. 3.2.4). In order to avoid any misleading interpretation and to be able to disentangle between genuine magnetoelectric coupling –*i.e.* genuine changes in $\varepsilon(H)$– from pure magnetoresistive effects, impedance spectroscopy was performed at selected fixed temperatures under different magnetic fields (see Sect. 3.2.4).

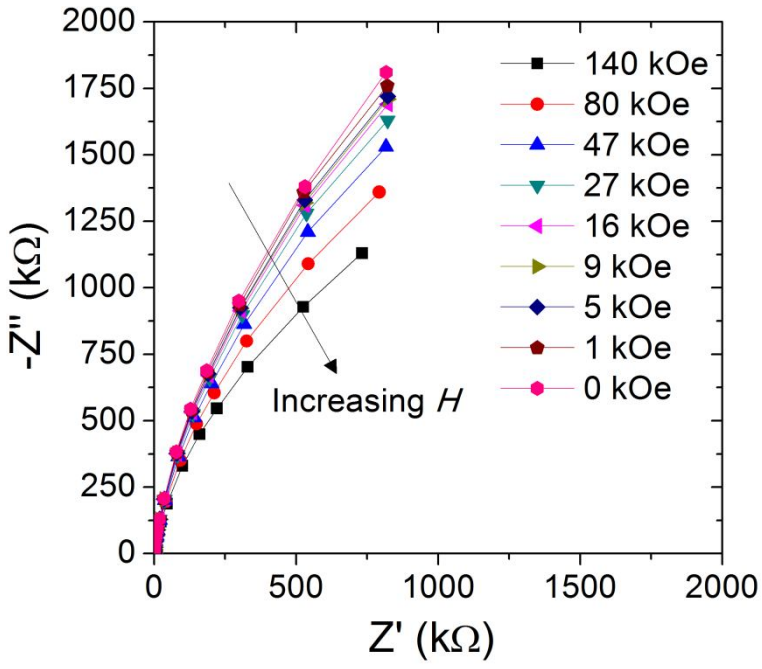

Fig. 4.27 – *Impedance complex plane (–Z'' – Z' plots) from impedance data measured at 95 K under different magnetic fields, H.*

Fig. 4.27 depicts the magnetic field dependence of the impedance data of $Pt/BiMnO_3/Nb:SrTiO_3$ capacitors measured at 95 K. Note that this temperature was selected for being close to the magnetic Curie temperature, thus expecting large magnetoelectric effect as indicated in Fig. 4.24. Qualitatively, as observed in Fig. 4.27, on increasing the applied magnetic field, the semicircle diameter of the $-Z'' - Z'$ plots decreases, signalling that the resistivity of $BiMnO_3$ decreases upon applied magnetic field. Using the same procedures as described in previous section, *i.e.* using Eq. 4.3 to fit the impedance data under the different magnetic fields, the fitting values (Q, R, α) of the *R–CPE* element can be determined at each magnetic field. As discussed in previous section, these values are used to compute the magnetic field dependence of the intrinsic resistivity, $\rho(H)$, and dielectric permittivity of $BiMnO_3$ films, which are assessed in the following.

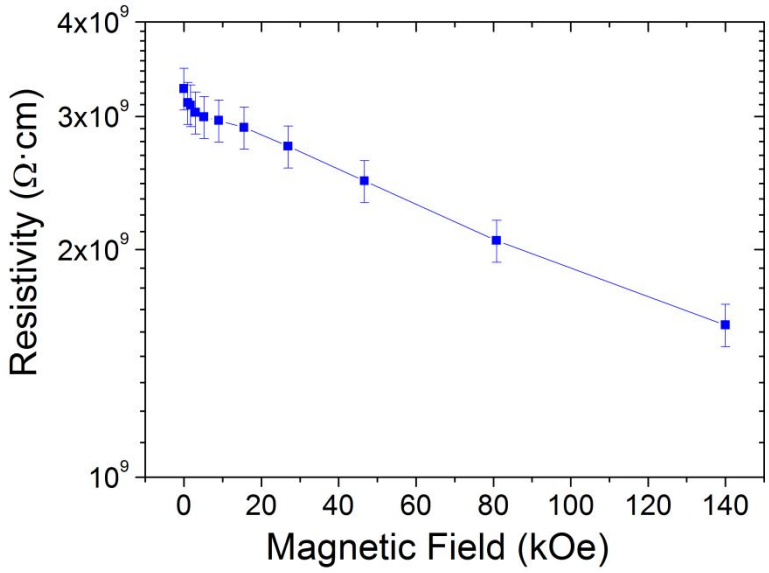

Fig. 4.28 – *Magnetic-field dependence of the resistivity of $BiMnO_3$ films at 95 K*

The magnetic field dependence of the $BiMnO_3$ resistivity at 95 K is shown in Fig. 4.28. As observed, $\rho(H)$ decreases on increasing H, confirming the behaviour shown in Fig. 4.27. Thus, $BiMnO_3$ indeed displays a negative magnetoresistance. The influence of the magnetic field on the resistivity of $BiMnO_3$ was also inferred in Fig. 4.25, in which a notably change in the conduction mechanism is observed around the magnetic transition temperature. Once the magnetoresistive effect is disentangled from the impedance data, we focus on the possible changes of the dielectric permittivity of

$BiMnO_3$ on applying a magnetic field. As shown in the upper part of Fig. 4.29, in which the $\varepsilon(H)$ measured at 95 K is plotted, the dielectric permittivity continuously increases on increasing the magnetic field, thus displaying a positive magnetocapacitance effect. This contrasts to the negative magnetocapacitance effect reported for bulk $BiMnO_3$ [7]. It is worth noting that no magnetoresistive artefacts, as described in Ch. 3, are the origin of this magnetocapacitance, as the resistive and dielectric character have been disentangled from the raw impedance data previously. Moreover, $\varepsilon(H)$ curve shows a modest hysteretic behaviour, *i.e.* $\varepsilon(H)$ does not follow the same path when increasing H as when decreasing H. Yet it should be mentioned that error bars (around 5 %) may mask this hysteretic behaviour. In order to crosscheck the hysteresis in $\varepsilon(H)$ curves, impedance data at different magnetic fields was also recorded at 50 K, from which the intrinsic dielectric permittivity of $BiMnO_3$ film was obtained by fitting data by Eq. 4.3, as described previously. The results are shown in the lower part of Fig. 4.29, in which the $\varepsilon(H)$ curve clearly follows the same hysteretic trend as that of 95 K, though in a more modest fashion probably due to the fact that the closer to the magnetic Curie temperature the stronger the magnetoelectric effect (see Sect. 1.1.3).

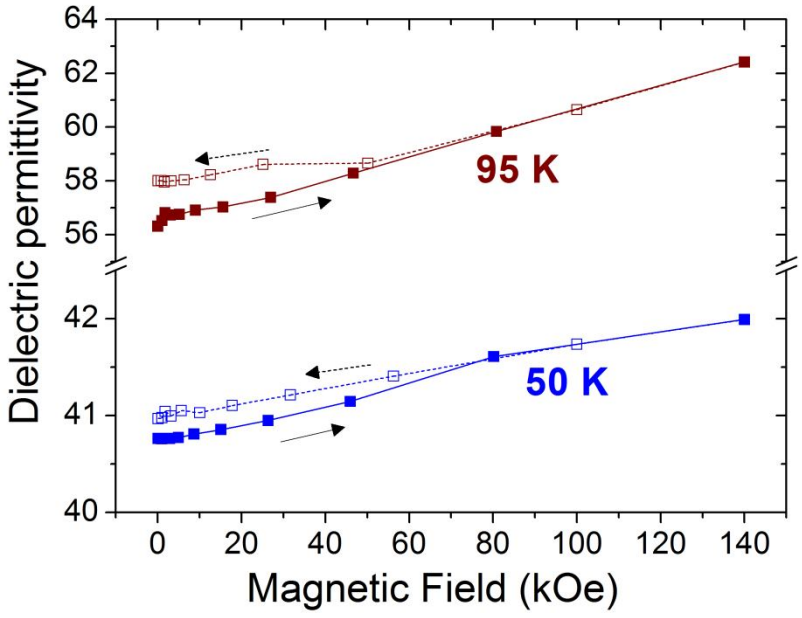

4.29 – *Magnetic field dependence of the dielectric permittivity of $BiMnO_3$ films. Solid (open) symbols are obtained on increasing (decreasing) magnetic field.*

Thus, despite the fact that error bars of the fitting inhibit from conclusively stating the magnetoelectric coupling, especially giving reliable quantitative values, all

evidences point to this feature being realised in $BiMnO_3$ compounds. In fact, the hysteretic behaviour of $\varepsilon(H)$ can only be understood as an effect of the magnetic state of $BiMnO_3$ film on the dielectric permittivity. In particular, as shown in Fig. 4.29, increasing the magnetic ordering of the spins of Mn^{3+} (*i.e.* increasing the magnetisation by applying a magnetic field) in $BiMnO_3$, the dielectric permittivity increases. Due to the ferromagnetic character of $BiMnO_3$, when the magnetic field is removed, there is still a remanent magnetisation in the film, which is responsible for the relatively larger dielectric permittivity with regard to that at the beginning of the H cycle (*i.e.* when the film is not magnetised).

4.4 Ferroelectric properties

By electric characterisation the ferroelectric character of $BiMnO_3$ was not possible to be confirmed in this work. Conduction current was too large with regard to the ferroelectric domain switching current that masked any footprint of ferroelectricity. It is worth mentioning that the recorded saturated polarisation of $BiMnO_3$, though from a not conclusively ferroelectric hysteresis loop, was of the order of a few nC/cm^2 [6], *i.e.* a very low value. Thus, this points to a small ferroelectric domain switching current, if any, which becomes negligible in comparison to the leakage current. Moreover, the latter is even more significant taking into account that thick (thicker than 80 nm) single-phase $BiMnO_3$ films were not feasible to be grown due to the large Bi-deficiency (see Sect. 4.1).

References

[1] A. F. Moreira dos Santos, A. K. Cheetham, W. Tian, X. Pan, Y. Jia, N. J. Murphy, J. Lettieri and D. G. Schlom, Appl. Phys. Lett. **84** 91 (2004).

[2] S. Fujino, M. Murakami, S. –H. Lim, L. G. Salamanca-Riba, M. Wuttig and I. Takeuchi, J. Appl. Phys. **101** 013903 (2007).

[3] M. Gajek, M. Bibes, F. Wyczisk, M. Varela, J. Fontcuberta and A. Barthélémy, Phys. Rev. B **75** 174417 (2007).

[4] S. Havelia, S. Wang, M. Skowronski and P. A. Salvador, J. Appl. Phys. **106** 123509 (2009).

[5] T. Atou, H. Chiba, K. Ohoyama, Y. Yamaguchi and Y. Syono, J. Sol. State Chem. **145** 639 (1999).

[6] A. Moreira dos Santos, S. Parashar, A. R. Raju, Y. S. Zhao, A. K. Cheetham and C. N. R. Rao, Sol. State. Comm. **122** 49 (2002).

[7] T. Kimura, S. Kawamoto, I. Yamada, M. Azuma, M. Takano and Y. Tokura, Phys. Rev. B **67** 180401 (2003).

[8] Z. H. Chi, C. J. Xiao, S. M. Feng, F. Y. Li and C. Q. Jin, J. Appl. Phys. **98** 103519 (2005).

[9] E. Montanari, L. Righi, G. Calestani, A. Migliore, E. Gilioli and F. Bolzon, Chem. Mater. **17** 1765 (2005).

[10] H. Okamoto, H. Fjellvåg, H. Yamauchi and M. Karppinen, Sol. State Comm. **137** 522 (2006).

[11] T. Zhao, F. Chen, H. Lu, G. Yang and Z. Chen, J. Appl. Phys. **87** 7442 (2000).

[12] C. H. Park and D. J. Chadi, Phys. Rev. B **57** R13961 (1998).

[13] J. M. D. Coey, M. Viret and S. von Molnár, Adv. Phys. **48** 167 (1999).

[14] N. Dix, R. Muralidharan, B. Warot-Fonrose, M. Varela, F. Sánchez and J. Fontcuberta, Chem. Mater. **21** 1375 (2009).

[15] L. Bi, A. R. Taussig, H-S. Kim, L. Wang, G. F. Dionne, D. Bono, K. Persson, G. Ceder and C. A. Ross, Phys. Rev. B **78** 104106 (2008).

[16] M. Ohring, Materials Science of Thin Films: Deposition and Structure, Academic Press, San Francisco, 2002.

[17] C. –H. Yang, T. Y. Koo, S. –H. Lee, C. Song, K. –B. Lee and Y. H. Jeong, Europhys. Lett. **74** 348 (2006).

[18] K. Dwight and N. Menyuk, Phys. Rev. **119** 1470 (1960).

[19] G. B. Jensen and O. V. Nielsen, J. Phys. C.: Sol. State Phys. **7** 409 (1974)

[20] L. W. Guo, D. L. Peng, H. Makino, K. Inaba, H. J. Ko, K. Sumiyama, T. Yao, J. Mag. Mag. Mater. **213** 321 (2000).

[21] M. Gajek, M. Bibes, A. Barthélémy, K. Bouzehouane, S. Fusil, M. Varela, J. Fontcuberta and A. Fert, Phys. Rev. B **72** 020406(R) (2005).

[22] W. Eerenstein, F. D. Morrison, J. F. Scott and N. D. Mathur, Appl. Phys. Lett. **87** 101906 (2005).

[23] J. H. Lee, X. Ke, R. Misra, J. F. Ihlefeld, X. S. Xu, Z. G. Mei, T. Heeg, M. Roeckerath, J. Schubert, Z. K. Liu, J. L. Musfeldt, P. Schiffer and D. G. Schlom, Appl. Phys. Lett. **96** 262905 (2010).

[24] R. Schmidt, W. Eerenstein, T. Winiecki, F. D. Morrison and P. A. Midgley, Phys. Rev. B **75** 245111 (2007).

[25] R. Schmidt, W. Eerenstein and P. A. Midgley, Phys. Rev. B **79** 214107 (2009).

[26] A. K. Jonscher, *Dielectric Relaxations in Solids*, Chelsea Dielectrics Press, London, 1983.

[27] P. Lunkenheimer, V. Bobnar, A. V. Pronin, A. I. Ritus, A. A. Volkov and A. Loidl, Phys. Rev. B **66** 052105 (2002).

[28] R. Schmidt and A. W. Brinkman, J. Appl. Phys. **103** 113710 (2008).

[29] G. Catalan, Appl. Phys. Lett. **88** 102902 (2006).

[30] D. O'Neill, R. M. Bowman and J. M. Gregg, Appl. Phys. Lett. **77** 1520 (2004).

[31] T. Tsurumi, J. Li, T. Hoshima, H. Kakemoto, M. Nakada and J. Takedo, Appl. Phys. Lett. **91** 182905 (2007).

[32] H. Chiba, T. Atou and Y. Syono, J. Solid State Chem. **132** 139 (1997)

[33] A. Seeger, P. Lunkenheimer, J. Hemberger, A. A. Mukhin, V. Y. Ivanov, A. M. Balbashov and A. Loidl, J. Phys.: Condens. Matter **11** 3273 (1999).

[34] A. L. Efros and B. I. Shklovskii, J. Phys. C. Solid State Phys. **8** L49 (1975).

[35] J. M. D. Coey, M. Viret, L. Ranno and K. Ounadeja, Phys. Rev. Lett. **75** 3910 (1995).

[36] J. Fontcuberta, B. Martínez, A. Seffar, S. Piñol, J. L. García-Muñoz and X. Obradors, Phys. Rev. Lett. **76** 1122 (1996).

[37] D. Yu, C. Wang, B. L. Wehrenberg and P. Guyot-Sionnest, Phys. Rev. Lett. **92** 216802 (2004).

Chapter 5

$(Bi_{0.9}La_{0.1})_2NiMnO_6$ thin films

5.1 Single-phase stabilisation

The stabilisation of single phase Bi-based manganite-family perovskites has been, in general, difficult to achieve because of their tendency of multiphase formation and the high volatility of bismuth [1 – 4]. Indeed, in bulk form Bi_2NiMnO_6 is only achieved in extreme sintering conditions, *i.e.* at 6 GPa and 800 ºC of mechanical pressure and temperature, respectively [5].

Still, as explained in Sect. 1.3.1, metastable compounds can be formed by replacing the mechanical pressure by the epitaxial stress, *i.e.* using substrates whose lattice parameters show a low mismatch with those of the compound that is to be formed. Thus, as pseudo-cubic lattice parameter of Bi_2NiMnO_6 is a ~ 3.877 Å, $SrTiO_3$ (001)-oriented substrates were used, which presented 0.71 % of tensile stress (See table 4.1).

Substrate	Structure and orientation	Latt. parameter (Å)	Mismatch with pseudo-cubic latt. parameter of Bi_2NiMnO_6
$SrTiO_3$	Cubic perovskite (001)	3.905	$\frac{a_{Bi_2NiMnO_6} - a_{SrTiO_3}}{a_{SrTiO_3}} = -0.71\%$

Table 5.1 – *Substrate and mismatch with Bi_2NiMnO_6.*

On the other hand, partial replacement of Bi^{3+} cations by La^{3+} cations at the A-site has been proved to facilitate single-phase stabilisation in bismuth manganite compounds [3], because of the slightly smaller ionic radius of La^{3+} with regard to Bi^{3+} (0.130 nm and 0.131 nm, respectively [6]). It gives rise to a slightly reduced unit cell volume, without changing the lattice parameters significantly, but exerting the so-called chemical pressure (see Sect. 1.2.6) which contributes to prevent Bi^{3+} cations from desorption during the growth process. Still, in bulk the solid solution $(Bi_{1-x}La_x)_2NiMnO_6$ remains non-centrosymmetric for $x < 0.2$ [7], so that 10% of La-doping was used, allowing the possibility of ferroelectricity to be established.

$(Bi_{0.9}La_{0.1})_2NiMnO_6$ thin films were grown by PLD (See Sect. 2.1) from stoichiometric targets, in which the primary oxides are found, not the compound itself. As $SrTiO_3$ is (001)-oriented, we expect $(Bi_{0.9}La_{0.1})_2NiMnO_6$ thin films to grow with the

c-axis as the out-of-plane direction, *i.e.* we expect to find only (00*l*) reflexions in the symmetric $\theta/2\theta$ XRD diffractograms.

In order to optimise the deposition conditions, the substrate temperature, the oxygen pressure during the growth process and the thickness of the films were assessed.

5.1.1 Dependence on Temperature

By keeping the rest of the PLD deposition conditions fixed (see Sect. 2.1), we grow different samples at different substrate temperatures, ranging from 590ºC to 700ºC.

In Fig. 5.1, XRD $\theta/2\theta$ scans of films grown at 0.5 mbar at various illustrative temperatures are shown. The (00*l*) reflexions of the $(Bi_{0.9}La_{0.1})_2NiMnO_6$ phase can clearly be observed for temperatures lower than 660 ºC, which take place at 2θ values slightly higher than the (00*l*) reflexions of $SrTiO_3$, as expected since the pseudocubic lattice parameter of $(Bi_{0.9}La_{0.1})_2NiMnO_6$ is smaller than that of $SrTiO_3$. Note that, having in mind the Bragg Diffracion law (Eq. 2.1), the interplanar distance of the (00*l*) reflexions, $d_{00l} = c/l$, where c is the out-of-plane lattice parameter, is shorter in the case of $(Bi_{0.9}La_{0.1})_2NiMnO_6$ compound than in $SrTiO_3$ (see Appendix A). The lattice parameters will be discussed in sect. 5.2.2.

For films deposited at 660ºC and above, $(Bi_{0.9}La_{0.1})_2NiMnO_6$ reflexions are not found, which should be due to the fact that they might present such a great deficiency in Bi content –as this element is very volatile– that makes unfeasible the $(Bi_{0.9}La_{0.1})_2NiMnO_6$ formation or leads to polycrystalline compound. In addition to the $(Bi_{0.9}La_{0.1})_2NiMnO_6$ reflections, in the patterns of samples prepared at higher and lower temperatures than 620ºC the NiO phase, (002) reflection, occurring at about $2\theta \sim 43.4^\circ$ can clearly be observed. The existence of parasitic lines arising from the transition metal oxides in the Bi – Mn – Ni – O system in the patterns of samples prepared at higher temperatures should be expected as a consequence of Bi deficits. Although a compositional study of the $(Bi_{0.9}La_{0.1})_2NiMnO_6$ films grown at different temperatures has not been carried out, they are expected to behave similar to $BiMnO_3$ films, in which the Bi-content decay significantly above 640ºC (see Sect. 4.1.1).

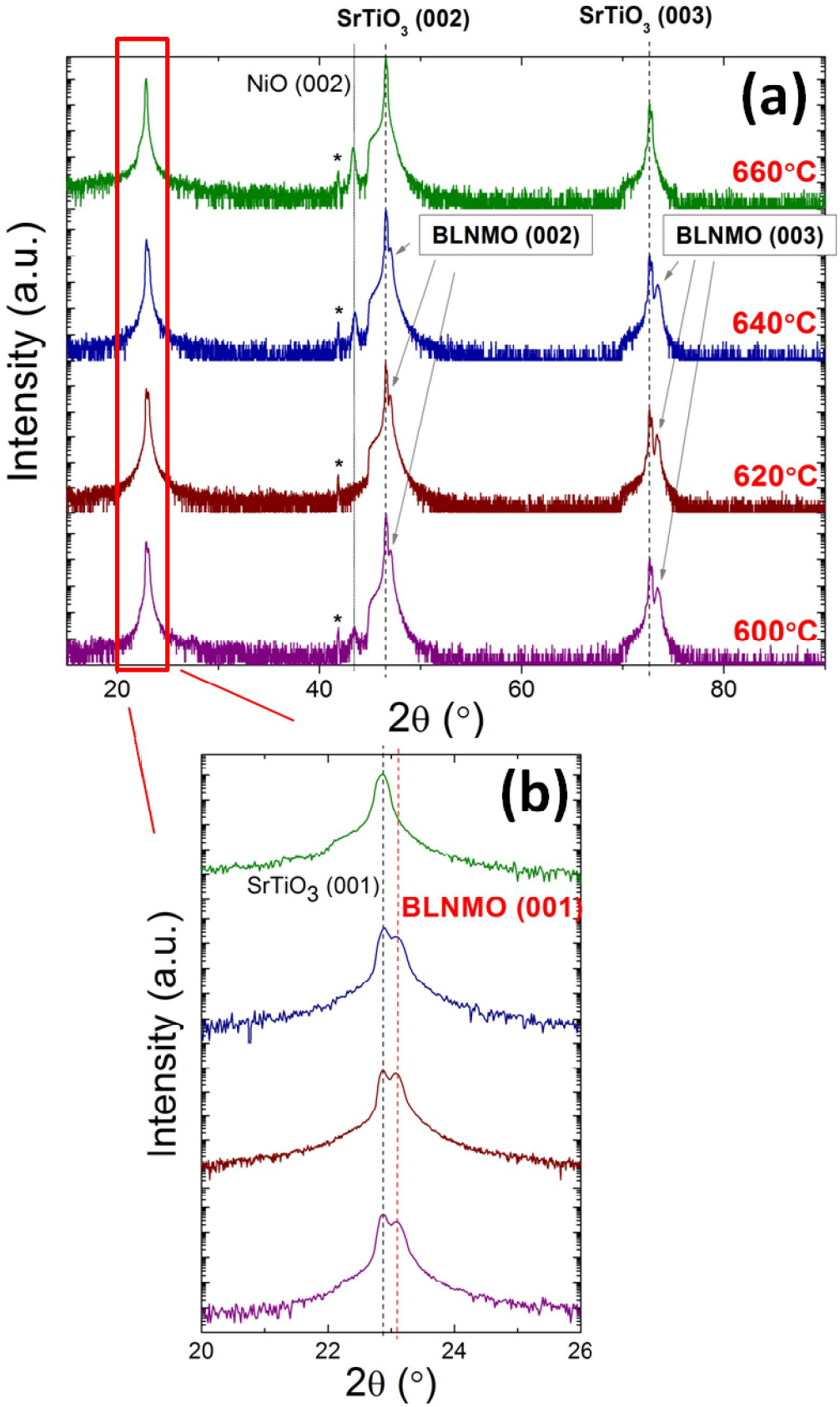

Fig. 5.1 – (a) *XRD θ/2θ scans of $(Bi_{0.9}La_{0.1})_2NiMnO_6$ thin films (ranging from 60 to 70 nm) grown at 0.5 mbar of O_2 and at different temperatures. * denotes the K_β of (002) $SrTiO_3$.* **(b)** *Zoom of the (001) reflexion of both $SrTiO_3$ and $(Bi_{0.9}La_{0.1})_2NiMnO_6$.*

The reason of the existence of NiO phase at lower temperatures is more uncertain, although it may result from the lower mobility of the arriving species onto the substrate which might lead to phase segregations. It is worth noting here the multiphase tendency of Bi-based manganite family compounds [1 – 4] and the fact that the target does not contain the compound itself but the mixture of the primary oxides. Metastable $(Bi_{0.9}La_{0.1})_2NiMnO_6$ compound requires relatively high temperature, thus the use of low temperatures may result in an incomplete formation of the compound in the Bi – Mn – Ni – O system.

The XRD pattern of the film prepared at the intermediate temperature (620ºC) displays only reflections associated to the $(Bi_{0.9}La_{0.1})_2NiMnO_6$ phase without traces of spurious phases. Hence, single-phase $(Bi_{0.9}La_{0.1})_2NiMnO_6$ is only obtained when the film is grown at around 620ºC, slightly lower value than the optimal temperature found by Sakai *et al.*, 630ºC, for Bi_2NiMnO_6 thin films grown at similar oxygen pressure (0.53 mbar) [8].

5.1.2 Dependence on O_2 pressure

By keeping the rest of the PLD deposition conditions fixed (see Sect. 2.1), we grow different samples at different O_2 pressures, ranging from 0.3 mbar to 0.6 mbar.

In terms of single phase formation of $(Bi_{0.9}La_{0.1})_2NiMnO_6$, the oxygen pressure does not seem to be such a critical deposition parameter (as the temperature is) in the range we have worked. As illustrated by data in Fig. 5.2 the XRD θ/2θ diffractograms of films grown at 620 ºC for different oxygen pressures show no evidence of any parasitic phase and only the (00*l*) reflexions of $(Bi_{0.9}La_{0.1})_2NiMnO_6$ phase is obtained. This behaviour greatly contrasts with the single-phase formation of the parental compound $BiMnO_3$, which was very sensitive to the O_2 pressure (see Sect. 4.1.2). It is worth remarking that the standard procedure of cooling down the sample after the deposition is finished consists of introducing O_2 pressure immediately, attaining $1 \cdot 10^3$ mbar of pressure when the film is at 600ºC and keeping that O_2 pressure during the rest of the cooling down process. Yet we have investigated the effects on the single-phase formation of annealing the sample at $1 \cdot 10^3$ mbar of O_2 pressure and at 450ºC for 1 hour. At any event, single-phase is achieved (Fig. 5.3).

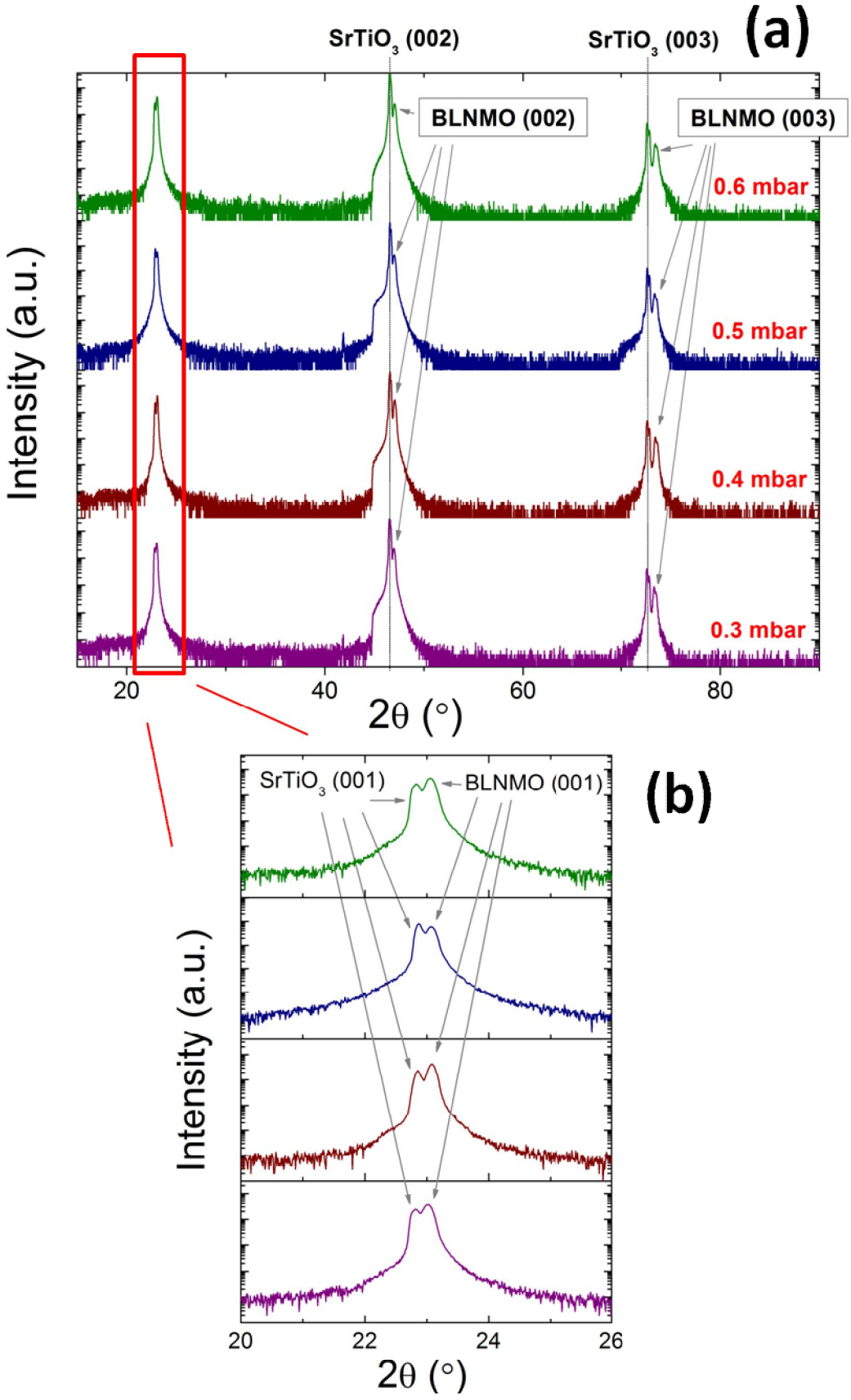

Fig. 5.2 – (a) *XRD θ/2θ scans of $(Bi_{0.9}La_{0.1})_2NiMnO_6$ thin films (ranging from 90 to 120 nm) grown at 620 ºC and at different O_2 pressures.* **(b)** *Zoom of the (001) reflexion.*

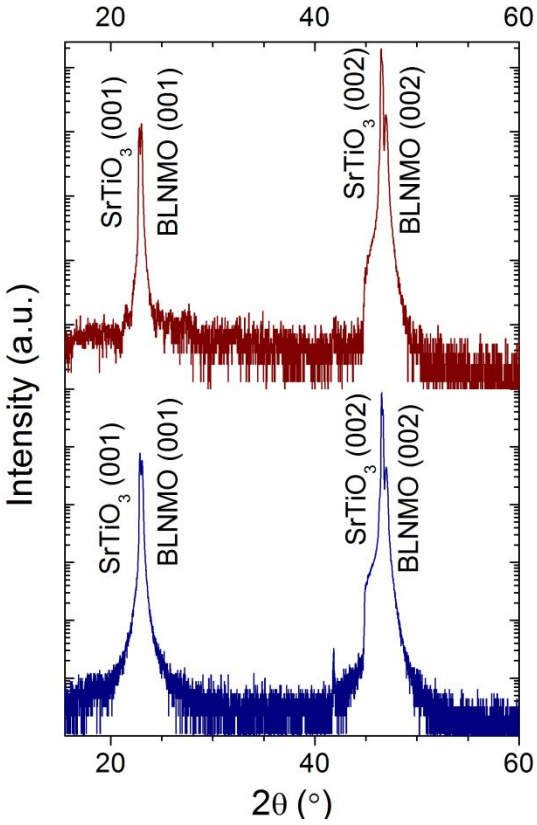

Fig. 5.3 – *XRD θ/2θ scans of BLNMO thin films of different thickness grown at 620ºC and 0.5 mbar of O_2 pressure. Whereas bottom diffractogram shows a non-annealed sample, upper diffractogram shows an annealed sample at 450ºC and at 10^3 mbar of O_2 pressure for 1 hour.*

5.1.3 Dependence on thickness

By keeping the rest of the PLD deposition conditions fixed (see Sect. 2.1), and setting the substrate temperature and the oxygen pressure at 620ºC and 0.5 mbar, respectively, we grow different samples at different number of laser pulses, *i.e.* different thicknesses (ranging from 20 to 140 nm in this work).

In Fig. 5.4, XRD $\theta/2\theta$ scans of films of various illustrative thicknesses are depicted. In contrast to the clear thickness dependence of the single-phase stabilisation of $BiMnO_3$ films (Sect. 4.1.3), single-phase stabilisation in $(Bi_{0.9}La_{0.1})_2NiMnO_6$ is not that sensitive and it is achieved, at least, up to 140 nm, indicative as a lower bound.

Laue oscillations of the (001) Bragg diffraction peak of 20-nm $(Bi_{0.9}La_{0.1})_2NiMnO_6$ film can be made out [Fig. 5.4 (b)], which points out the existence of crystalline coherence along the full thickness of the film. They are normally observed for thin films (few tens of nm) when showing high crystal quality, as it will be borne out in the following section.

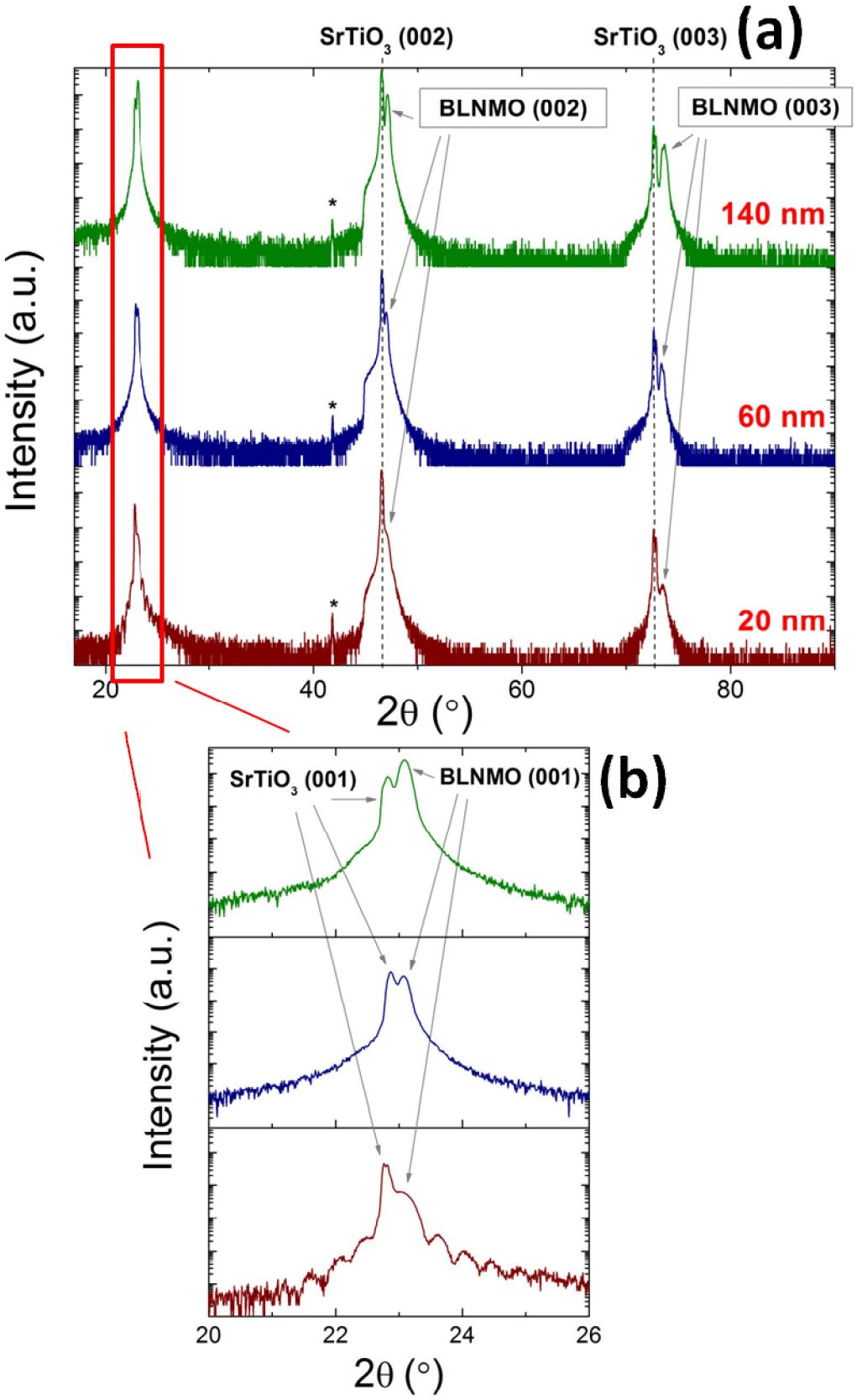

Fig. 5.4 – (a) *XRD θ/2θ scans of $(Bi_{0.9}La_{0.1})_2NiMnO_6$ thin films of different thickness grown at 620°C and 0.5 mbar of O_2 pressure. * denotes the K_β of (002) $SrTiO_3$.* **(b)** *Zoom of the (001) reflexion.*

5.2 Structural characterisation and surface topography

5.2.1 Texture of the films

First assessment of the crystal quality was focused on the out-of-plane texture of the film. As explained in Sec. 2.2.1, a way to quantify it is by means of the FWHM of the rocking curves (ω scans). In this work we have performed the rocking curves around the (001) Bragg reflexion. This figure of merit is compared to that of the substrate, as being the latter a single crystal with presumable high quality and free from form factor effects. Thus, the FWHM of the substrate Bragg reflexion accounts for the instrumental width.

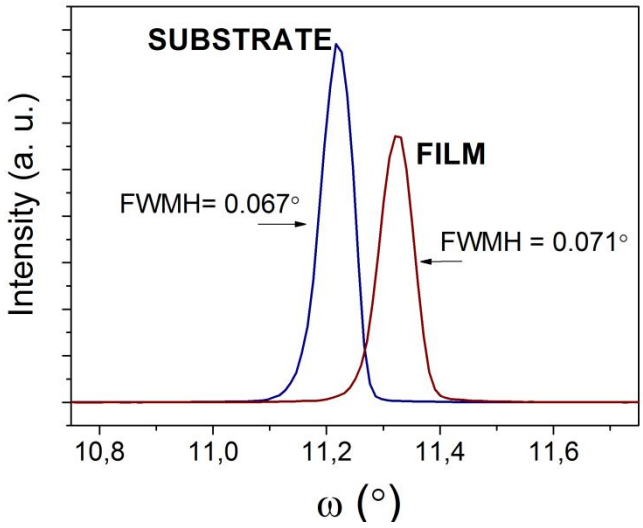

Fig. 5.5 – *Rocking curve of the (001) reflexion of both $SrTiO_3$ substrate and 60-nm $(Bi_{0.9}La_{0.1})_2NiMnO_6$ film grown at 620ºC and 0.5 mbar of O_2 pressure.*

Rocking curves of the (001) $(Bi_{0.9}La_{0.1})_2NiMnO_6$ and (001) $SrTiO_3$ Bragg reflexions are illustrated in Fig. 5.5, of a 60-nm $(Bi_{0.9}La_{0.1})_2NiMnO_6$ film grown in the optimised deposition conditions for single-phase formation. Comparison of the rocking curves reveals that the FWMH value of the $(Bi_{0.9}La_{0.1})_2NiMnO_6$ peak (0.071º) is comparable to that of the substrate (0.067º), which is extensive for the rest of film thicknesses up to 140 nm, attaining FWHM values inferior to 0.09º. Thus, $(Bi_{0.9}La_{0.1})_2NiMnO_6$ films show a very low out-of-plane dispersion of the unit cells, indicating a high crystalline quality.

In-plane texture, *i.e.* how $(Bi_{0.9}La_{0.1})_2NiMnO_6$ unit cells are in-plane oriented, is characterise by pole figures and ϕ-scans of an asymmetric reflexion (see Sect. 2.2.1), which allows planes that are not parallel to the interface to diffract. When it comes to choosing an appropriate asymmetric reflexion, the criterion is based on using an easy in-plane axis, such as the [100] or [010] $SrTiO_3$ directions, which are equivalent as being a cubic structure. However, due to the similarity of the lattice parameters of both $SrTiO_3$ and $(Bi_{0.9}La_{0.1})_2NiMnO_6$, which means similar 2θ angle of the Bragg reflexions, a high-2θ reflexion was required in order to minimise the substrate contribution to the pole figures and ϕ-scans of the film, since discernition in 2θ is larger the higher the angle is. Thus, (204) reflexion was used, whose difference in 2θ between that of $(Bi_{0.9}La_{0.1})_2NiMnO_6$ and that of $SrTiO_3$ is about 1.5º (see table 5.2).

(204) reflexion	2θ(º)	ω(º)	ψ(º)
$SrTiO_3$	123.8	61.9	26.6
BLNMO	125.3	62.7	25.9

Table 5.2 – *Four-circle diffractometer angles at which the (204) reflexion of both $SrTiO_3$ and $(Bi_{0.9}La_{0.1})_2NiMnO_6$ (BLNMO) takes place. ϕ angle is four times degenerated and 90º separated when orthogonal in-plane crystal symmetry.*

Fig. 5.6 depicts the XRD ϕ-scans of the assymetric (204) reflexion of both substrate and film of a 125-nm $(Bi_{0.9}La_{0.1})_2NiMnO_6$ film grown in the optimised deposition conditions for single-phase formation. As shown, only four 90º-ϕ-spaced peaks of the film are observed, which not only indicates that there are no contributions of misoriented in-plane family of crystallites of $(Bi_{0.9}La_{0.1})_2NiMnO_6$, *i.e.* $(Bi_{0.9}La_{0.1})_2NiMnO_6$ films are in-plane textured, but also that the crystal symmetry of $(Bi_{0.9}La_{0.1})_2NiMnO_6$ films corresponds to that which allows an orthogonal square in-plane unit cell base, *i.e.* tetragonal or cubic. In order to ensure the in-plane texture of the film, pole figures was performed, in which ψ was scanned from 0 to 30, as illustrated in Fig. 5.7 for a 60-nm $(Bi_{0.9}La_{0.1})_2NiMnO_6$ film grown in the optimised deposition conditions for single-phase stabilisation. In agreement with the ϕ-scans, Fig. 5.7 reproduces the four 90º-ϕ-spaced peaks of the film, confirming the tetragonal (cubic) symmetry.

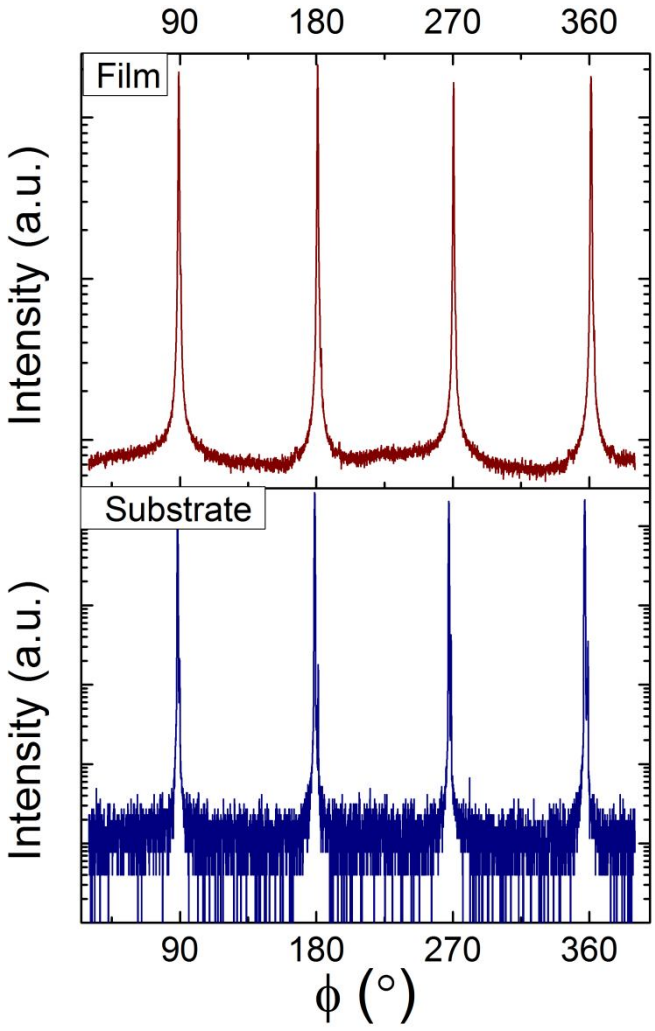

Fig. 5.6 – *XRD ϕ-scans around the (204) reflexion of both $(Bi_{0.9}La_{0.1})_2NiMnO_6$ film and $SrTiO_3$ substrate, of 125-nm thick, grown at 620ºC and 0.5 mbar of O_2.*

Moreover, the fact that $(Bi_{0.9}La_{0.1})_2NiMnO_6$ ϕ peaks coincide in ϕ angle value with those of the substrate [Fig. 5.6 (bottom panel) and Fig. 5.7 (a)] shows that $(Bi_{0.9}La_{0.1})_2NiMnO_6$ films have grown cube-on-cube, *i.e.* the tetragonal base is coincident in orientation with that of the cubic substrate (see Sect. 2.2.1). Or, in other words, the [100] in-plane crystallographic direction of $(Bi_{0.9}La_{0.1})_2NiMnO_6$ film is parallel to the [100] direction of $SrTiO_3$, which is normally represented by the epitaxial relationship [100]BLNMO(001)//[100]$SrTiO_3$(001). The cube-on-cube growth is confirmed along thickness up to 140 nm.

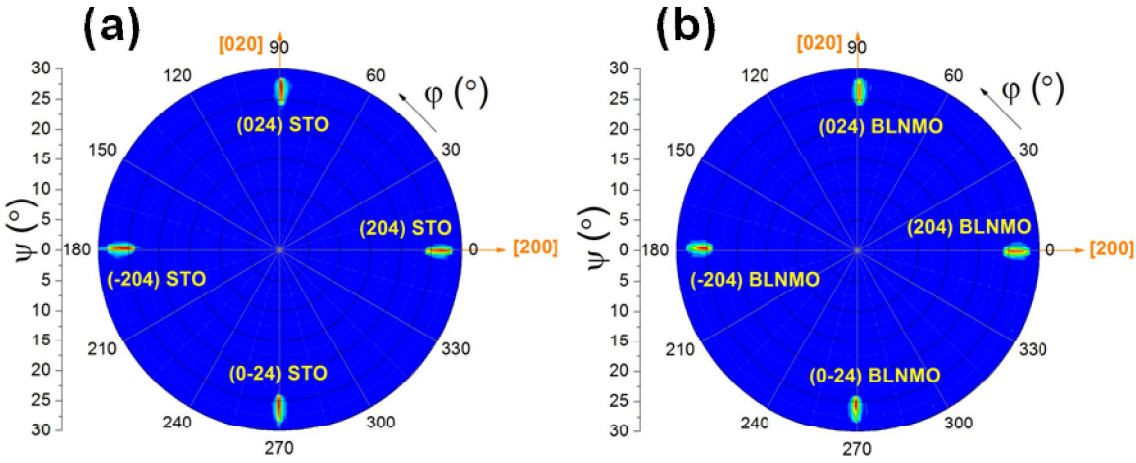

Fig. 5.7 – *XRD pole figure around the (204) reflexion of* **(a)** *$SrTiO_3$ (STO) substrate* **(b)** *$(Bi_{0.9}La_{0.1})_2NiMnO_6$ (BLNMO) film, of 60-nm thick, grown at 620ºC and 0.5 mbar of O_2.*

Both out-of-plane and in-plane texture characterisation suggest BLNMO films have a high epitaxial quality.

5.2.2 Reciprocal space maps and lattice parameters

Reciprocal space maps (RSM), where q_{perp} component (related to the out-of-plane lattice parameter) of the reciprocal space vector $\vec{q}$ is plotted versus $q_{parallel}$ component (related to the in-plane lattice parameter), were performed in order to determine the film lattice parameters (both the out-of-plane and in-plane lattice parameters, as long as an asymmetric XRD reflexion is assessed) and the epitaxial strain of $(Bi_{0.9}La_{0.1})_2NiMnO_6$ films (see Sect. 2.2.1). In the reciprocal space map, not only the film reflexion is recorded but also that of the substrate, as the ($q_{parallel}$, q_{perp}) XRD peak position of the substrate is used to account for the instrumental error (see Appendix A) in order to determine the correct lattice parameters of $(Bi_{0.9}La_{0.1})_2NiMnO_6$ films.

According to the epitaxial relationship (Sect. 5.2.1), (*hkl*) reflexions of both $(Bi_{0.9}La_{0.1})_2NiMnO_6$ and $SrTiO_3$ are coincident in ϕ angle and, due to the similar lattice of both compounds, they take place in similar 2θ and ω angle, which means similar $q_{parallel}$ and q_{perp} in the RSM. Thus, as in the pole figures and ϕ scans, the criterion of choosing the appropriate asymmetric reflexion is based on looking for a sufficiently

intense XRD peak of the film, but also with large enough angular separation with regard to the substrate reflexion in order to discern between both contributions (film + substrate) in the reciprocal space map. Taking into account the geometric configuration of the 4-circle diffractometer (Fig. 2.4), and using [100] and [001] vectors as the in-plane and out-of-plane directions, respectively, Fig. 5.8 depicts the allowed XRD reflexions in the reciprocal space, considering $(Bi_{0.9}La_{0.1})_2NiMnO_6$ film relaxed, *i.e.* with bulk pseudocubic lattice parameter ~3.877 Å. It is worth recalling that both [100] and [010] directions are equivalent when it comes to characterising the in-plane lattice parameters since $(Bi_{0.9}La_{0.1})_2NiMnO_6$ possesses a tetragonal structure according to the epitaxial relationship. Thus, both (*h0l*) and (*0kl*) XRD reflexions, accomplishing $h = k$, are equivalent.

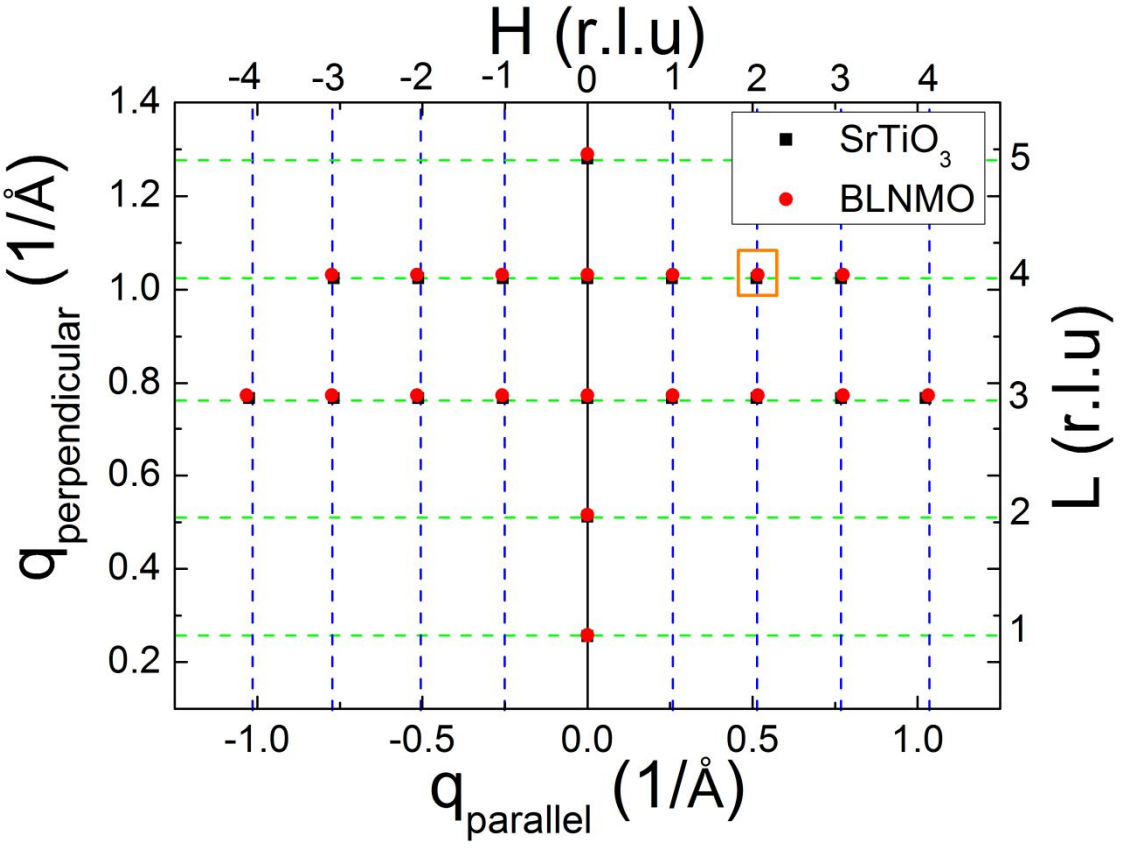

Fig. 5.8 – *Reciprocal space of the allowed XRD reflexions in the 4-circle diffractometer for both $(Bi_{0.9}La_{0.1})_2NiMnO_6$ (BLNMO) (solid circles) and $SrTiO_3$ (solid squares), when [100] and [001] crystallographic directions are the in-plane and out-of-plane directions, respectively. Top and right axis indicates the corresponding in-plane and out-of-plane reciprocal lattice units of the XRD reflexions, respectively. The (204) XRD reflexion is marked by an orange square.*

As shown in Fig. 5.8, $\vec{q}$ position of (*h0l*) XRD reflexions of both substrate and film are very similar, so that (204) XRD reflexion was used (orange square), which corresponds to a high-2θ reflexion, and hence with a larger angular separation, but with enough intensity to be recorded. It is to be noted that (204) reflexion is that used in the in-plane texture characterisation; however, in the RSM, ψ angle remains at zero. Then, instead of fulfilling the condition of $\omega = \theta$, as in the pole figures (or ϕ-scans), ω is modified as follows $\omega = \theta - \psi$ (see table 5.3), allowing the asymmetric (204) reflexion to diffract. Note that ψ angle corresponds to the angle between the out-of-plane direction and the perpendicular direction of the (204) crystallographic planes (see Fig. 2.4).

(204) reflexion	2θ(º)	ω(º)	ψ(º)
$SrTiO_3$	123.8	35.3	0
BLNMO	125.3	36.8	0

Table 5.3 – *Four-circle diffractometer angles at which the (204) reflexion of both $SrTiO_3$ and $(Bi_{0.9}La_{0.1})_2NiMnO_6$ (BLNMO) takes place, when ψ is forced to be 0. ϕ angle is four times degenerated and placed at 0º, 90º, 180º and 270º.*

In the RSM $\vec{q}$ is not directly measured, but, instead, several coupled $2\theta/\omega$ XRD scans are performed for different ω values, giving rise to a 2D $2\theta - \omega$ map of intensities. Then, using Eq. 2.8, q_{perp} and $q_{parallel}$ are obtained (see Sect. 2.2.1). As an illustrative example, Fig. 5.9 (a) shows the RSM of (204) reflexion of both $SrTiO_3$ substrate and 60-nm $(Bi_{0.9}La_{0.1})_2NiMnO_6$ film (grown in the optimised deposition conditions for single-phase stabilisation). As $q_{perp} = l/c = 4/c$ [see Eq. 2.6], where c is the out-of-plane lattice parameter, $(Bi_{0.9}La_{0.1})_2NiMnO_6$ peak is found at higher values of q_{perp} than that of the substrate, as $(Bi_{0.9}La_{0.1})_2NiMnO_6$ unit cell is smaller than that of the $SrTiO_3$ (Fig. 5.9). Instead, $q_{parallel}$ of (204) $(Bi_{0.9}La_{0.1})_2NiMnO_6$ reflexion is found to be coincident with that of the substrate (indicated by the two guide-to-eye dashed lines corresponding to $K_{\alpha1}$ and $K_{\alpha2}$). As $q_{parallel} = h/a = 2/a$ [see Eq. 2.6], where a is the in-plane lattice parameter, it means that $(Bi_{0.9}La_{0.1})_2NiMnO_6$ in-plane lattice parameter adopts the value of the $SrTiO_3$ lattice parameter (3.905 Å).

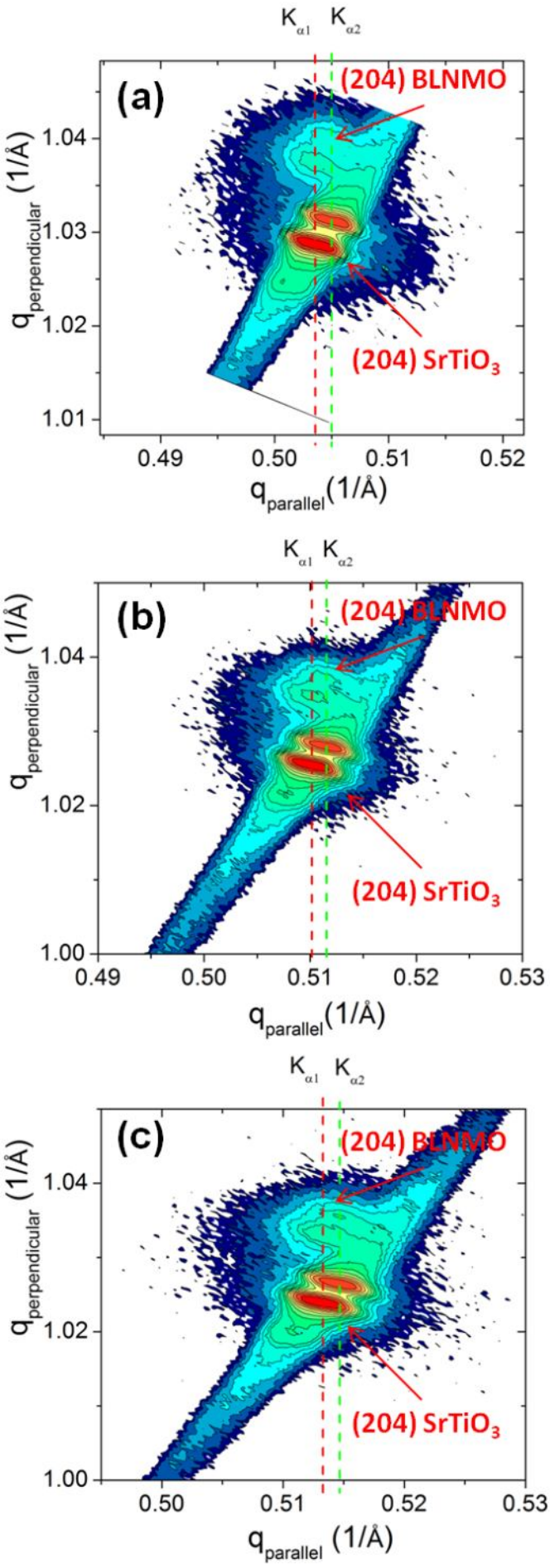

Fig. 5.9 – *Reciprocal space map of the (204) reflexion of $SrTiO_3$ and (204) reflexion of a 60-nm* **(a)** *100-nm* **(b)** *and 130-nm* **(c)** *$(Bi_{0.9}La_{0.1})_2NiMnO_6$ (BLNMO) thin film (grown at 620ºC and 0.5 mbar of O_2). The red dashed and blue dashed line ($K_{\alpha1}$ and $K_{\alpha2}$, respectively) are guide-to-eye lines showing that the in-plane lattice parameter of BLNMO is coincident with the $SrTiO_3$ lattice parameter.*

Exploring RSM for thicker films [Fig. 5.9 (b) and (c)], no relaxation is observed, *i.e.* $q_{parallel}$ of (204) $(Bi_{0.9}La_{0.1})_2NiMnO_6$ reflexion and (204) $SrTiO_3$ reflexion are still coincident. This is likely due to the small mismatch between lattice parameters of $(Bi_{0.9}La_{0.1})_2NiMnO_6$ and $SrTiO_3$ (see table 5.1). Thus, $(Bi_{0.9}La_{0.1})_2NiMnO_6$ films grow coherently on $SrTiO_3$ substrates up to 130 nm of thickness (lower bound), adopting the $SrTiO_3$ lattice parameter as the in-plane lattice parameter. Hence, $(Bi_{0.9}La_{0.1})_2NiMnO_6$ films are tensile strained, about 0.72%, defined as following:

$$strain = \frac{a_{film} - a_{bulk}}{a_{bulk}} = 0.72\% \tag{5.1}$$

where a_{film} and a_{bulk} are the film in-plane lattice parameter and the bulk pseudocubic lattice parameter of $(Bi_{0.9}La_{0.1})_2NiMnO_6$, respectively.

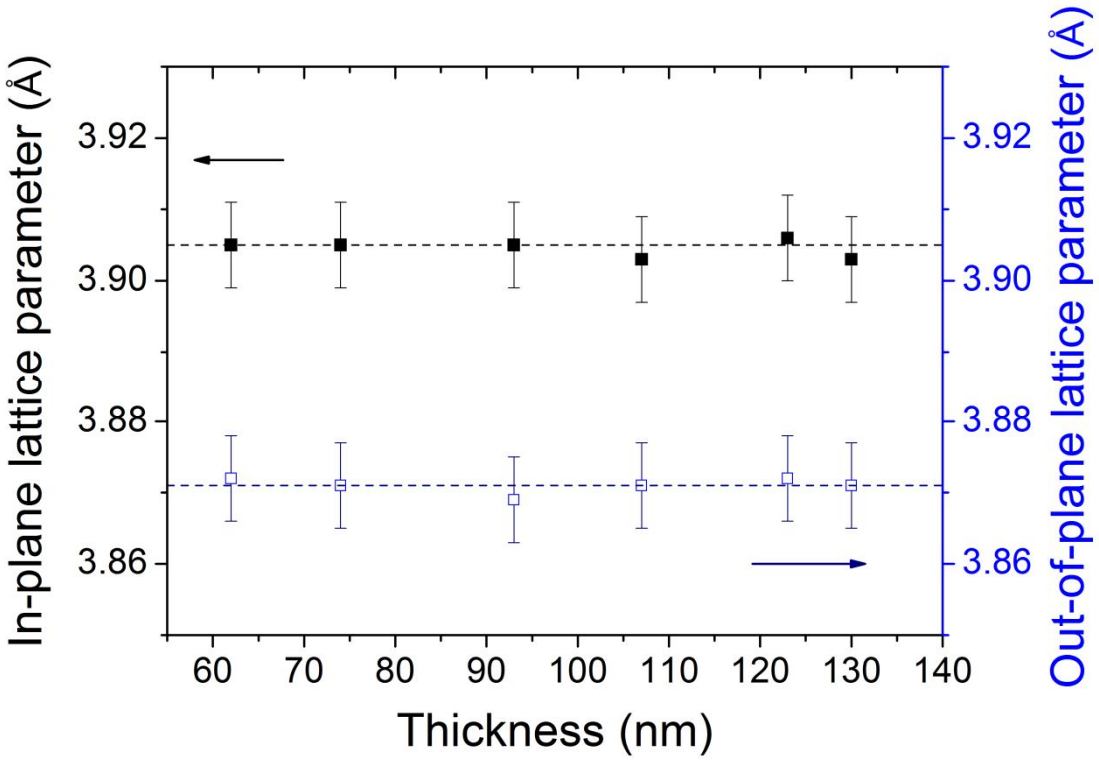

Fig. 5.10 – *Thickness dependence of in-plane (solid square symbols) and out-of-plane (open square symbols) lattice parameters of $(Bi_{0.9}La_{0.1})_2NiMnO_6$ films (grown at 620ºC and 0.5 mbar of O_2 pressure). Upper dashed line indicates the lattice parameter of $SrTiO_3$ (3.905 Å), whereas bottom dashed line indicates the average value of the out-of-plane lattice parameter (3.871 Å).*

In Fig. 5.10 (left axis) in-plane lattice parameter computed by means of the RSM as a function of $(Bi_{0.9}La_{0.1})_2NiMnO_6$ thickness is depicted, which is roughly constant around the value of $SrTiO_3$ lattice parameter. The out-of-plane lattice parameter, determined by RSM [Fig. 5.10 (right axis)] is roughly constant along thickness (~ 3.87 Å), as expected when no relaxation takes place. Note that the $(Bi_{0.9}La_{0.1})_2NiMnO_6$ lattice parameters obtained by RSM are computed from $\Delta q_{parallel}$ and Δq_{perp} between $\vec{q}_{(204)}$ of $(Bi_{0.9}La_{0.1})_2NiMnO_6$ and $\vec{q}_{(204)}$ of $SrTiO_3$, using that of $SrTiO_3$ as a reference, with lattice parameter (3.905 Å), accounting for the experimental error (see Appendix A).

Thus, the unit cell volume of $(Bi_{0.9}La_{0.1})_2NiMnO_6$ films [$V_{u.c} = a^2 \cdot c$; as $(Bi_{0.9}La_{0.1})_2NiMnO_6$ film have a tetragonal structure] is maintained constant along thickness. However, contrary to the common assumption that epitaxial strain preserves the bulk unit cell volume, $(Bi_{0.9}La_{0.1})_2NiMnO_6$ films possess a noticeable larger unit cell volume (~59.03 $Å^3$) than that of the bulk (58.29 $Å^3$). Yet this is a rather common result in many epitaxial films.

On the other hand, the out-of-plane lattice parameter of $(Bi_{0.9}La_{0.1})_2NiMnO_6$ films can also be computed by the symmetric XRD reflexions (Fig. 5.11), *i.e.* from the $\theta/2\theta$ XRD scans, as described in Sect. 2.2.1. In the symmetric XRD reflexions only the crystallographic planes (*hkl*) that are parallel to the surface of the film are allowed to diffract, in our case the (00*l*) family of planes. Hence, the interplanar distance of this family of planes are directly related to the out-of-plane lattice parameter (denoted as *c*): $d_{00l} = c/l$ (see Appendix A). Note that in order to account for the instrumental error, the 2θ position of the (00*l*) XRD reflexions of $SrTiO_3$ were also computed and used the lattice parameter of $SrTiO_3$ (3.905 Å) as a reference (see Appendix A). Fig. 5.11 (a) shows the out-of-plane lattice parameter, computed by the symmetric XRD patterns, of $(Bi_{0.9}La_{0.1})_2NiMnO_6$ films grown at different temperatures when the oxygen pressure during growth is maintained constant at 0.5 mbar. Despite the fact that at lower and higher temperatures than 620ºC spurious phases are formed (NiO) together with $(Bi_{0.9}La_{0.1})_2NiMnO_6$ phase (Fig. 5.1), the out-of-plane lattice parameter of $(Bi_{0.9}La_{0.1})_2NiMnO_6$ phase are roughly constant (~3.87 Å) along the temperature range. This contrasts with $BiMnO_3$ phase (see Sect. 4.1.1), in which the out-of-plane lattice

parameter monotonously reduces upon deposition temperature, associated with an increasing presence of Bi vacancies.

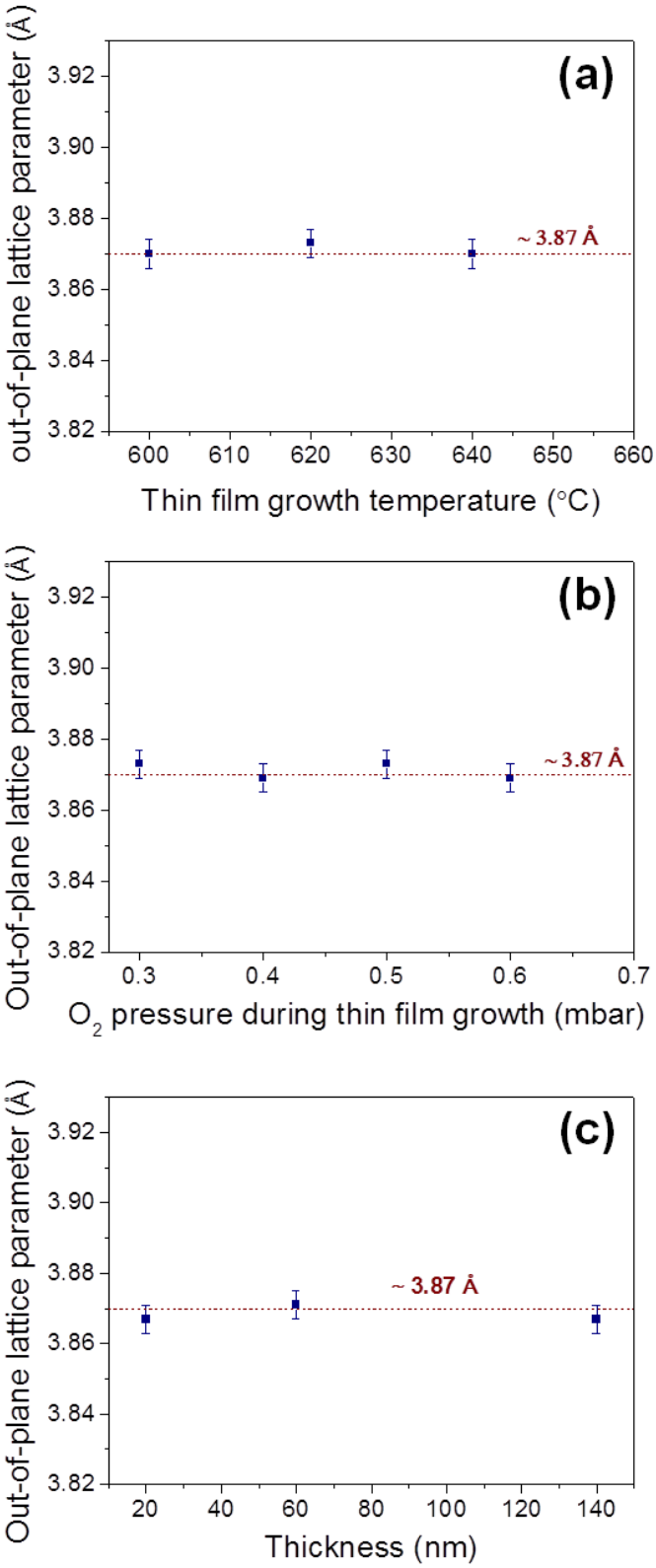

Fig. 5.11 – *Out-of-plane lattice parameter of $(Bi_{0.9}La_{0.1})_2NiMnO_6$ thin films as a function:* **(a)** *the deposition temperature (O_2 pressure maintained at 0.5 mbar);* **(b)** *the O_2 pressure during the thin film growth (temperature maintained at 620ºC); and* **(c)** *thickness (grown at 620ºC and 0.5 mbar of O_2 pressure).*

The dependence of the out-of-plane lattice parameter on the oxygen pressure during the thin film growth is also negligible [Fig. 5.11 (b)], in which a value around 3.87 Å is also recorded in the whole range (from 0.3 mbar to 0.6 mbar). In addition, thickness, *t*, dependence of the out-of-plane lattice parameter, *c*(*t*), was also assessed by the symmetric (00*l*) XRD reflexion [Fig. 5.11 (c)]. As shown, *c*(*t*) remains invariant (~3.87 Å) along thickness, in agreement with the out-of-plane lattice parameter extracted from the reciprocal space maps, which gives an additional evidence of the lack of relaxation process of $(Bi_{0.9}La_{0.1})_2NiMnO_6$ films grown on $SrTiO_3$.

Hence, as a conclusion, $(Bi_{0.9}La_{0.1})_2NiMnO_6$ films grow fully tensile strained on $SrTiO_3$ substrates, thus, with *a* lattice parameter (in-plane) around 3.905 Å, and *c* lattice parameter (out-of-plane) is found around 3.87 Å.

5.2.3 Microstructure characterisation by transmission electron microscopy

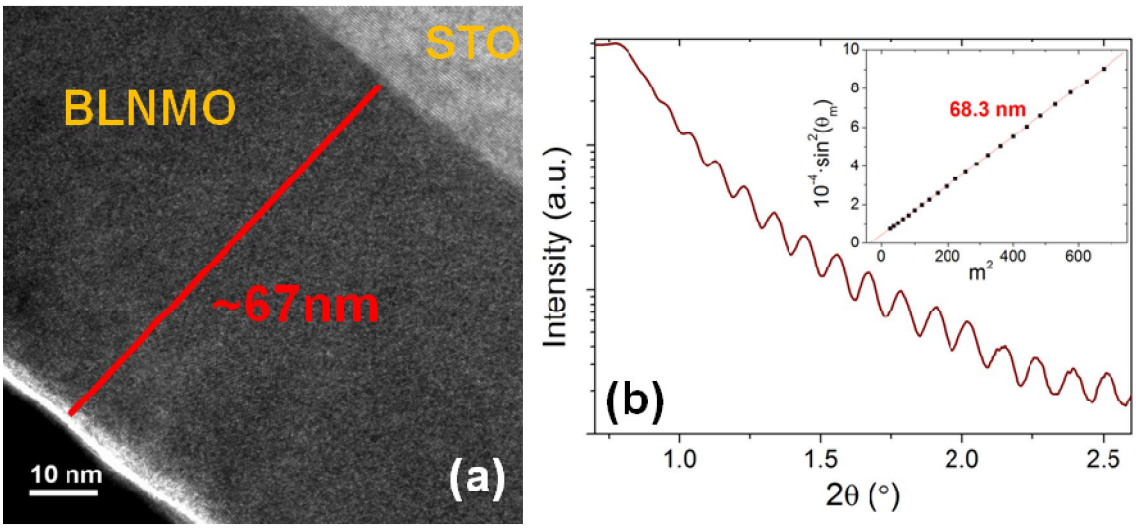

Fig. 5.12 – (a) *General view of cross-section TEM image of* $(Bi_{0.9}La_{0.1})_2NiMnO_6$ *(BLNMO) film. STO stands for* $SrTiO_3$ *substrate. The measured thickness is in good agreement with that obtained by X-ray reflectivity* **(b)**, *using the expression 2.10 deduced in Ch. 2, in which the slope of the* $\sin^2\theta_m$ *versus* m^2 *corresponds to* $[\lambda/(2\cdot t)]^2$, *where* θ_m *and m are the* θ *position of the minimum of order m; and t and* λ *are the film thickness and the wavelength of* K_α *of Cu, respectively.*

Transmission electron microscopy (TEM) was used to assess the substrate-film interface, as well as the homogeneity of the film, the crystal quality and the epitaxial growth of the film. TEM samples were prepared in cross-section geometry by focused ion beam, as explained in Sect. 2.2.2 (Ch. 2). The sample investigated was a 68-nm $(Bi_{0.9}La_{0.1})_2NiMnO_6$ film grown at the optimised deposition conditions for single phase stabilisation (620ºC and 0.5 mbar of O_2 pressure). The thickness determined by TEM [Fig. 5.12 (a)] is in close agreement with that extracted by X-Ray reflectivity [Fig. 5.12 (b)].

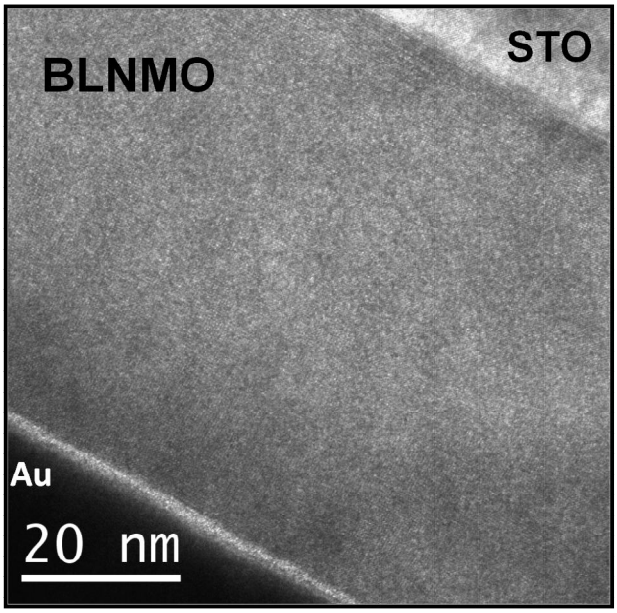

Fig. 5.13 – *Cross-section along [100] direction TEM image of BLNMO and $SrTiO_3$ (STO).*

Low magnification TEM image is shown in Fig. 5.13, which evidences the homogeneity of the film along thickness.

High-resolution TEM (HRTEM) images [Fig. 5.14 (a) and (b)] were adquired in order to obtain information about the microstructure and crystallographic features of $(Bi_{0.9}La_{0.1})_2NiMnO_6$ films. Accordingly, high crystalline quality can be appreciated, in which no misfit dislocations are observed, as expected for a fully strained film with no relaxation according to the XRD results. The high crystal quality is also in agreement with the sharp rocking curves of $(Bi_{0.9}La_{0.1})_2NiMnO_6$ films compared with that of the substrate, as assessed by XRD measurements (Sect 5.2.1). Additionaly, Fig. 5.14 (b)

shows that the $(Bi_{0.9}La_{0.1})_2NiMnO_6/SrTiO_3$ interface is strikingly sharp, which indicates no cationic interdifusion across the interface, as will be deeper discussed in Sect. 5.3., in composition analysis of $(Bi_{0.9}La_{0.1})_2NiMnO_6$ films.

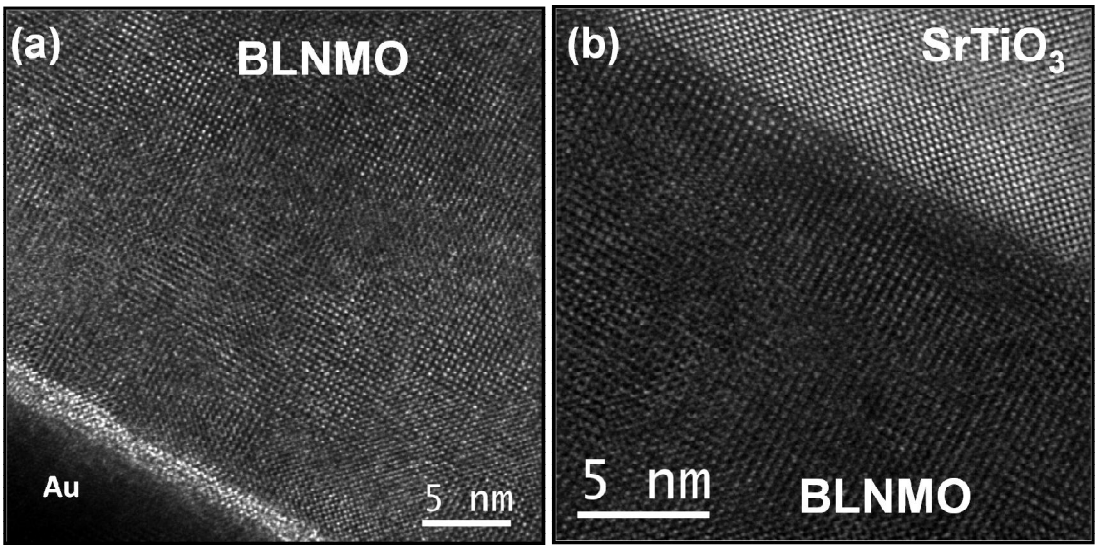

Fig. 5.14 – (a) *HRTEM image of $(Bi_{0.9}La_{0.1})_2NiMnO_6$ (BLNMO) film prepared in cross-section geometry along [100] direction.* **(b)** *Higher magnification HRTEM image of BLNMO/$SrTiO_3$ interface.*

Fast Fourier Transmforms (FFTs) of selected areas of the HRTEM images were computed in order to assess the periodicity of the crystal lattice. According to the FFTs of selected areas of substrate and film [Fig. 5.15 (b) and (c), respectively, from the selected areas marked by a green and blue square, respectively, in Fig. 5.15 (a)] the crystallographic directions of both substrate and film are coincident, accomplishing the epitaxial relationship $[100](Bi_{0.9}La_{0.1})_2NiMnO_6(001)//[100]SrTiO_3(001)$, in agreement with XRD measurements. Thus, $(Bi_{0.9}La_{0.1})_2NiMnO_6$ films grow well adapted on $SrTiO_3$ substrates.

To sum up, TEM characterisation, apart from indicating $(Bi_{0.9}La_{0.1})_2NiMnO_6$ film being defect-free and a sharp interface between film and $SrTiO_3$ substrate, bears out the high crystal quality of $(Bi_{0.9}La_{0.1})_2NiMnO_6$ films and the epitaxial relationship $[100](Bi_{0.9}La_{0.1})_2NiMnO_6(001)//[100]SrTiO_3(001)$, as proved by XRD measurements.

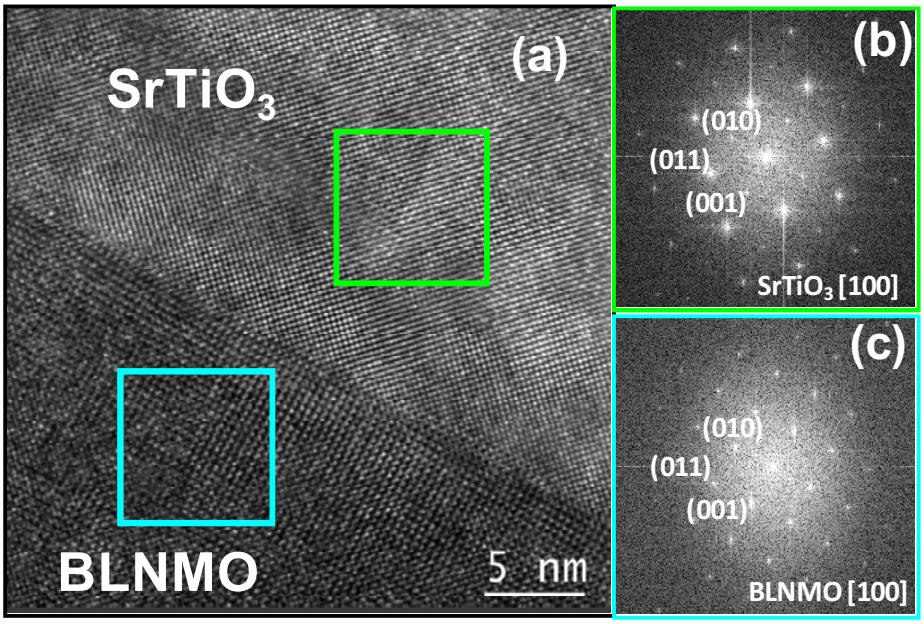

Fig. 5.15 – (a) *HRTEM image of $(Bi_{0.9}La_{0.1})_2NiMnO_6$ (BLNMO) and $SrTiO_3$ substrate prepared in cross-section geometry along [100] direction. The green (blue) square mark signals the selected area of the substrate (film) where FFT is taken. FFT of $SrTiO_3$ substrate* **(b)** *and BLNMO film* **(c)**.

5.2.4 B-site order

In double-perovskite Bi_2NiMnO_6, the B-site order, *i.e.* how the Ni^{2+} and Mn^{4+} cations are placed in the structure regarding one another, is strongly influential on the magnetic properties. Whereas Ni – O – Ni and Mn – O – Mn bonds give rise to antiferromagnetic superexchange interaction, Ni – O – Mn bond give rise to ferromagnetic superexchange interaction (see Sect. 1.2.5).

Thus, for a long-range ferromagnetic interaction, Ni and Mn cations are required to be located alternatively along the [100], [010] and [001] crystallographic directions (Fig. 5.16). In this work long-range B-site order is defined as the fulfilment of this periodicity, also known as rock-salt structure of the double-perovskite [5, 9, 10]. This periodicity results in the alternation of Ni-planes and Mn-planes along the [111] direction (along the eight equivalent directions: [1-11], [11-1], [-111], [1-1-1], [-11-1], [-1-11], [-1-1-1], [111]), as shown in Fig. 2.13 in Ch. 2. As a consequence, occurrence of the (1/2 1/2 1/2) superstructure XRD reflexion should be expected. However, as the

atomic scattering factor of Ni^{2+} and Mn^{4+} are very similar, the superstructure XRD reflexion in Bi_2NiMnO_6 is very weak. Note that should B cations be identical, like in $SrTiO_3$, systematic XRD cancellation occurs and no superstructure XRD reflexion is to be observed, so that the larger the difference in the atomic scattering factor of the B cations, the higher the intensity of the superstructure XRD reflexion.

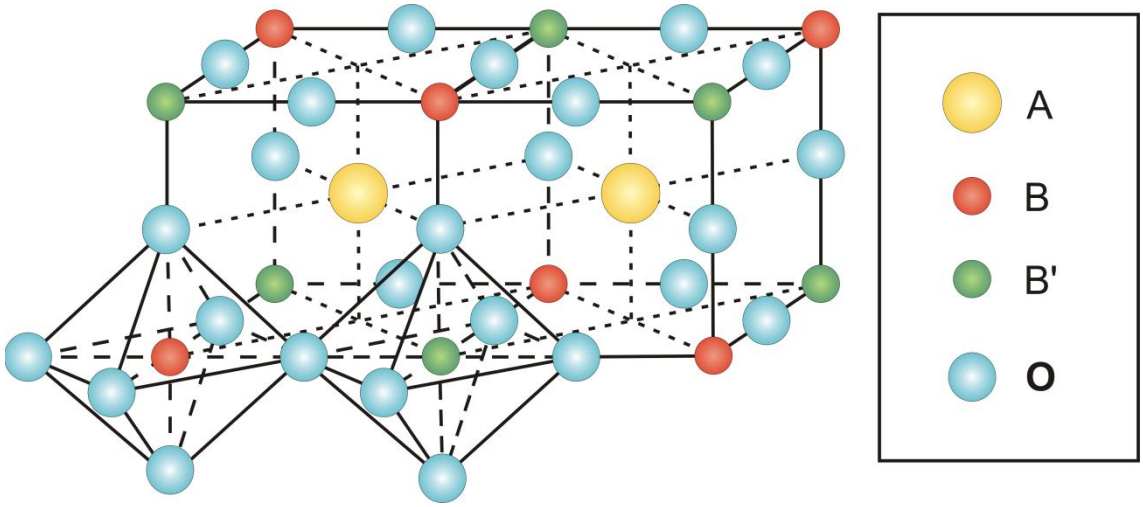

Fig. 5.16 – *Scheme of the double-perovskite structure in the rock-salt configuration*

In order to observe this weak superstructure XRD reflexion, first X-ray diffraction using synchrotron radiation was used, which provides an intense source of X-rays, allowing detecting the weak XRD reflexion (for experimental details see Sect. 2.4 of Ch. 2). Second, electron diffraction using TEM and computing FFT's HRTEM images were used in order to corroborate the synchrotron XRD results. The samples used for the B-site order characterisation were those grown at the optimal deposition conditions for single-phase stabilisation, *i.e.* at 620ºC and 0.5 mbar of O_2 pressure.

Fig. 5.17 (a) and (b) depict $\theta/2\theta$ synchrotron XRD scan around (111) and (1/2 1/2 1/2) $(Bi_{0.9}La_{0.1})_2NiMnO_6$ reflexions, respectively, of a 100-nm film. Due to the similar lattice parameters of $(Bi_{0.9}La_{0.1})_2NiMnO_6$ and $SrTiO_3$, Fig. 5.17 (a) shows the contribution of the fundamental perovskite (111) reflexion of both film and substrate ($2\theta_{film} \sim 32.62º$ and $2\theta_{susbtrate} \sim 32.59º$, respectively). In contrast, as superstructure order is absent in $SrTiO_3$, the sole contribution observed in Fig. 5.17 (b) should correspond to (1/2 1/2 1/2) $(Bi_{0.9}La_{0.1})_2NiMnO_6$ XRD reflexion. Indeed, the peak appears around $2\theta \sim 16.14º$, as expected, since, according to the Bragg's law [Eq. 2.1, Ch. 2], it must fulfil

the relation $sin(\theta_{(1/2\ 1/2\ 1/2)}) = (1/2)\cdot sin(\theta_{(111)})$, given the fact that the distance between (111) planes and (1/2 1/2 1/2) planes is $d_{(1/2\ 1/2\ 1/2)} = 2\cdot d_{(111)}$. Therefore, Fig. 5.17 (b) unequivocally reveals the long-range B-site order of $(Bi_{0.9}La_{0.1})_2NiMnO_6$ thin films.

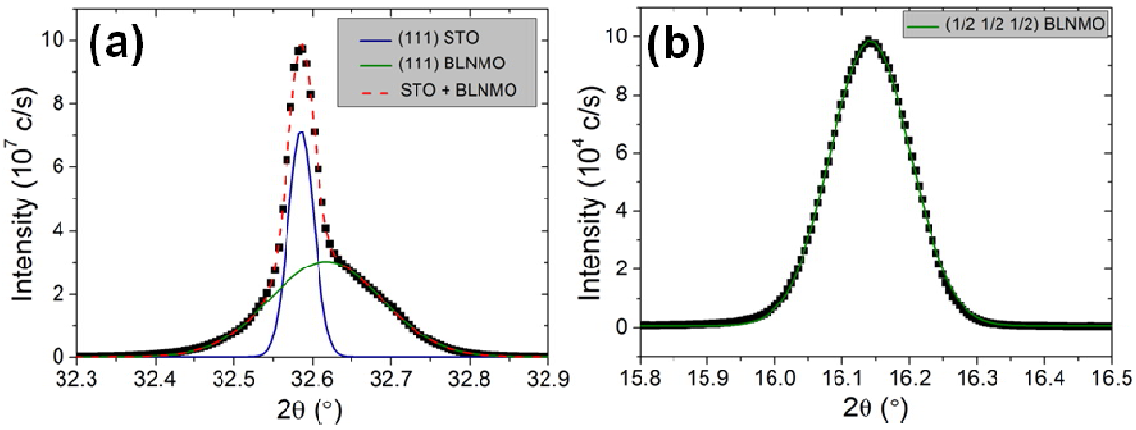

Fig. 5.17 – (a) *θ/2θ synchrotron XRD scan around the fundamental perovskite (111) reflexion of* $(Bi_{0.9}La_{0.1})_2NiMnO_6$ *(BLNMO) and* $SrTiO_3$. **(b)** *θ/2θ synchrotron XRD scan around the (1/2 1/2 1/2) superstructure reflexion of BLNMO. The diffraction intensity peaks were fitted using Gaussian functions.*

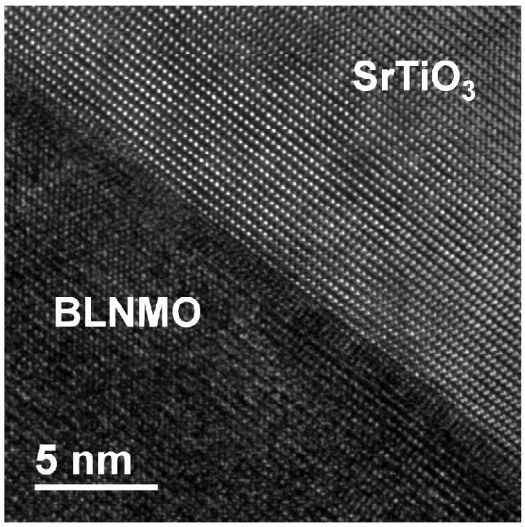

Fig. 5.18 – *HRTEM image of BLNMO and* $SrTiO_3$ *in cross-section geometry prepared along* $[1\bar{1}0]$ *direction.*

In order to detect the superstructure diffraction peaks by TEM, cross sections were to be prepared along the [1-10] zone axis (instead of the common [100] zone axis as

prepared in Sect. 5.2.3) as this cross-section geometry enables the observation of the reflexions related to the {111} crystallographic planes. Fig. 5.18 shows the HRTEM image of a cross-section prepared along [1-10] zone axis of a 68-nm $(Bi_{0.9}La_{0.1})_2NiMnO_6$ film, showing both the film and the substrate, in which the high crystal quality and sharp interface between $(Bi_{0.9}La_{0.1})_2NiMnO_6$ and $SrTiO_3$ are appreciated, corroborating the results obtained for cross-sections prepared along [100] crystallographic direction (Sect. 5.2.3).

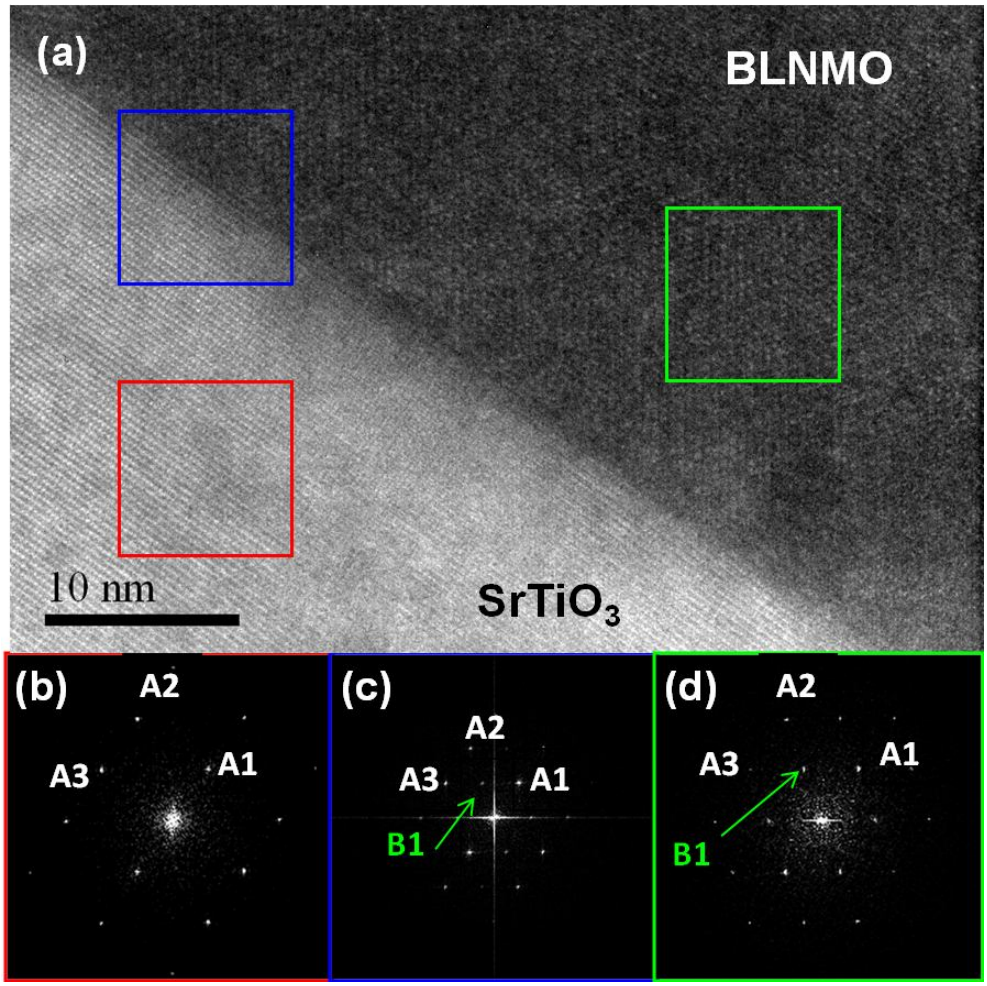

Fig. 5.19 – (a) *HRTEM image of cross-section prepared along the* $[1\bar{1}0]$ *zone axis of* $(Bi_{0.9}La_{0.1})_2NiMnO_6$ *(BLNMO) films on* $SrTiO_3$. **(b)** *FFT of the selected area* **(b)** *red square* **(c)** *blue square* **(d)** *green square taken from the HRTEM image. A1, A2 and A3 spots corresponds to (001), (111) and (110) crystallographic planes, respectively. The extra periodicity is signalled by B1.*

Fig. 5.19 (b) depicts the FFT of a selected area of pure $SrTiO_3$ [marked as a red square in HRTEM image, Fig. 5.19 (a)], which shows the spots A1, A2 and A3 corresponding to the (001), (111) and (110) planes, respectively. However, when FFT is are computed from selected areas in which $(Bi_{0.9}La_{0.1})_2NiMnO_6$ film is included [Fig. 5.19 (c) and (d), from the selected areas marked by a blue and green square, respectively, in HRTEM image Fig. 5.19 (a)], apart from the A spots which corresponds to the fundamental perovskite planes (corroborating the epitaxial growth of $(Bi_{0.9}La_{0.1})_2NiMnO_6$ film) additional weak spots are found along the [111] direction, marked as B1. These additional spots point out to an extra periodicity along the [111] direction, which is compatible with the aforementioned B-site order. Moreover, the fact that the additional spots appear as early as the first monolayers [Fig. 5.19 (c)] proves the existence of the superstructure in $(Bi_{0.9}La_{0.1})_2NiMnO_6$ films in the initial steps of the growth process.

To bear out the results of the computed FFT's of the HRTEM images, real diffraction is performed by selected area electron diffraction (SAED), equipped in TEM, on cross-sections prepared along the [1-10], enabling {111} planes to diffract. Nonetheless, due to the small thickness of $(Bi_{0.9}La_{0.1})_2NiMnO_6$ film (68 nm), SAED patterns of only $(Bi_{0.9}La_{0.1})_2NiMnO_6$ regions were no possible to be performed. Thus, in order to compare the electron diffraction patterns between $(Bi_{0.9}La_{0.1})_2NiMnO_6$ and $SrTiO_3$, SAED patterns were recorded in a region where only $SrTiO_3$ substrate is found and in a region where $(Bi_{0.9}La_{0.1})_2NiMnO_6$ film is included, with $SrTiO_3$ substrate contribution. Fig. 5.20 (a) and (b) shows SAED patterns of pure $SrTiO_3$ substrate, in which only the diffraction of the fundamental perovskite planes are found, identifying A1, A2 and A3 spots with the (001), (111) and (110) crystallographic planes, respectively, as found in the FFT's. In contrast, SAED patterns in which $(Bi_{0.9}La_{0.1})_2NiMnO_6$ film contribution is present [Fig. 5.20 (c) and (d)] an extra periodicity along the [111] direction is observed, marked with green circles, which we identify as the (1/2 1/2 1/2) superstructure diffraction peaks. Indeed, the value of the crystallographic interplanar distance of the planes corresponding to the extra periodicity (green circles) is about 0.45 nm (determined by the spot B1, see table 5.4), which is in close agreement with the expected interplanar distance of the (1/2 1/2 1/2) superstructure planes:

$$d_{hkl} = \sqrt{\frac{1}{\frac{h^2+k^2}{a}+\frac{l^2}{c^2}}} \Rightarrow d_{\frac{1}{2}\frac{1}{2}\frac{1}{2}} = 0.4496 \text{ nm} \qquad (5.2)$$

where a and c is the in-plane and the out-of-plane lattice parameter of $(Bi_{0.9}La_{0.1})_2NiMnO_6$ film.

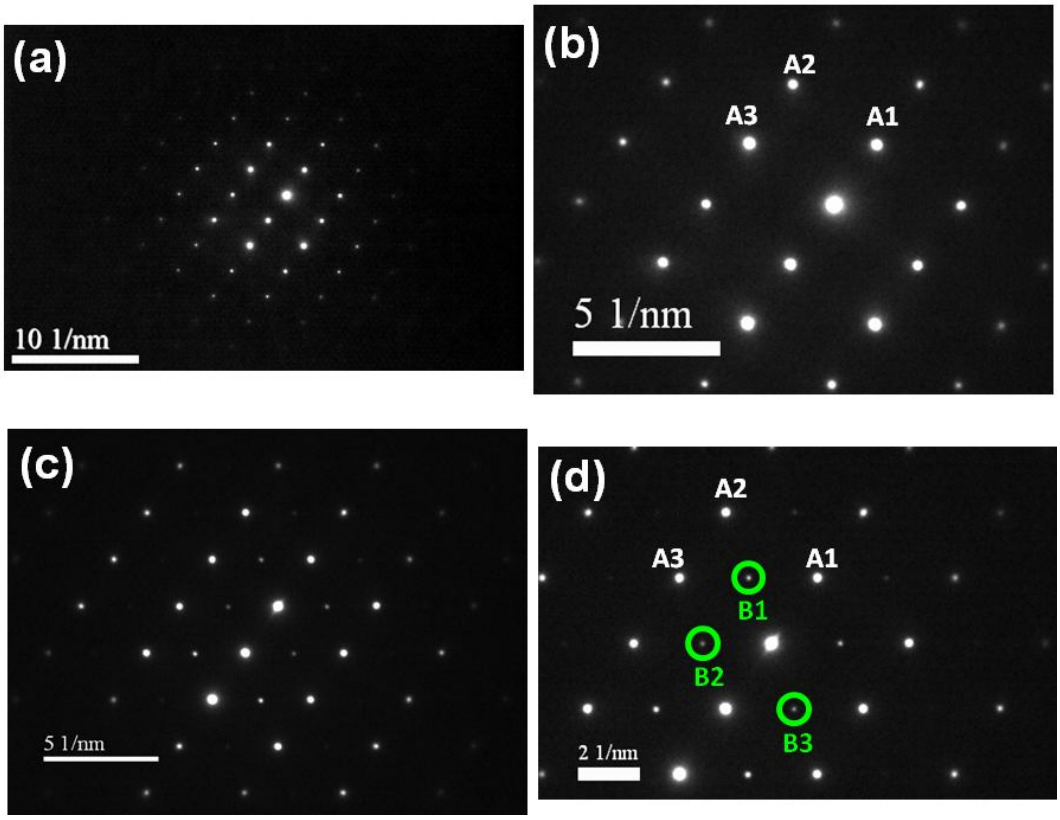

Fig. 5.20 – (a) *Selected area electron diffraction pattern of pure $SrTiO_3$ along the $[1\bar{1}0]$ zone axis.* **(b)** *Zoom of (a).* **(c)** *Selected area electron diffraction pattern of contribution of both $SrTiO_3$ and $(Bi_{0.9}La_{0.1})_2NiMnO_6$ film along the $[1\bar{1}0]$ zone axis.* **(d)** *Zoom of (c). A1, A2 and A3 spots correspond to the diffraction of (001), (111) and (110) crystallographic planes. Encircled spots correspond to the diffraction of superstructure planes.*

As a conclusion, despite the high temperature usually required for the formation of the rock-salt structure in double-perovskite thin films, like La_2CuSnO_6, Sr_2FeMoO_6, Sr_2CrReO_6 or La_2CoMnO_6 [10 – 12], experimental results evidence that long-range B-site order can be achieved in $(Bi_{0.9}La_{0.1})_2NiMnO_6$ films under relatively low deposition

temperatures of thin film growth (around 620ºC). On the other hand, the randomly distribution of Bi^{3+} and La^{3+} cations at the A-site in $(Bi_{0.9}La_{0.1})_2NiMnO_6$ films does not seem to affect the arrangement of the B cations.

Spot	Crystallographic plane	Distance (nm)
A1	(001)	0.39
A2	(111)	0.23
A3	(110)	0.28
B1	(1/2 1/2 1/2)	0.45

Table 5.4 – *Distance between the crystallographic planes of selected diffraction spots of Fig. 4.21.*

5.2.5 Surface topography

Most of the applications in which a multilayer structure of nanometric films is required (tunnel junctions, spin valves, etc) the surface morphology plays an essential role. In addition, studying the surface topography contributes to the understanding of the growth mechanism of $(Bi_{0.9}La_{0.1})_2NiMnO_6$ thin films on $SrTiO_3$, which may be extended to other similar substrates in perovskite structure with similar lattice parameters. AFM was used in the characterisation of surface topography, as explained in Sect. 2.3.2. In this study, only single-phase samples, *i.e.* those grown at 620ºC, were characterised.

$(Bi_{0.9}La_{0.1})_2NiMnO_6$ thin films grown on $SrTiO_3$ substrates exhibit a different morphology compared to their counterpart single-perovskite $BiMnO_3$ grown also on the same substrate (see Sect. 4.2.3). In the present case, the substrate steps and terraces are maintained when the film is grown, as shown in Fig. 5.21 (a). This is indicative of a 2D growth mode, which contrasts with the 3D growth mode found for $BiMnO_3$ thin films (Sect. 4.2.3). The height profile [Fig. 5.21 (c)] along the marked line in Fig. 5.21 (a) indicates steps of height between 1 and 2 $(Bi_{0.9}La_{0.1})_2NiMnO_6$ unit cells. Additionally, some 2D island can be found on the terraces, which might be pointing to a certain degree of a layer-by-layer growth mechanism, though with a likely coexistence of a step-flow growth mode. A systematic study of the surface morphology at the earlier

stages of the growth process was not carried out, which would contribute to discern whether the adatoms have a preferential diffusion toward the step edges (step-flow) or nucleate as 2D islands on the terraces (layer-by-layer). Step meandering can also be observed [Fig. 5.21 (a)]. Steps usually introduce Ehrlich–Schwoebel terrace potentials which oppose adatom to hop from the upper terrace to the bottom one, creating step bunching [13, 14]. However, these step mounds might not be uniform along the step edges due to the presence of kinks or irregularities. In a step-flow growth mode, this fact can cause different adatom diffusion rates over the edges, which may explain the observed meandering.

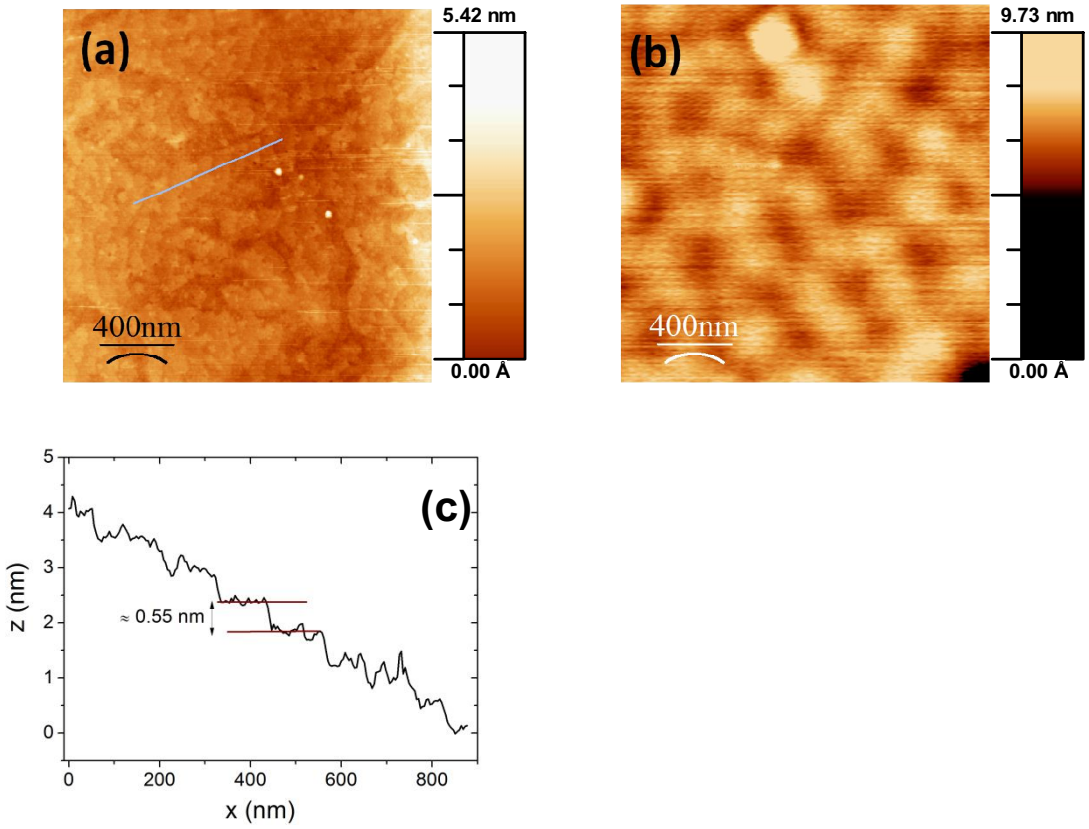

Fig. 5.21 – *AFM topographic images of $(Bi_{0.9}La_{0.1})_2NiMnO_6$ thin films grown on (001)-oriented $SrTiO_3$ substrates of thickness* **(a)** *68 nm (rsm = 0.35 nm)* **(b)** *125 nm (rsm = 0.6 nm).* **(c)** *Height profile corresponded to the marked line in AFM image of the 68-nm thick film (a). [Note the miscut angle was computed and subtracted from the height profile]*

For films thinner than 80 nm a 2D growth mode is found; however, for the thickest samples a 3D growth mode is observed [Fig. 5.21 (b)]], indicating that a transition from 2D to 3D is occurring at some critical thickness between 80 and 110 nm when the film continues growing.

Due to the fact that 2D growth mode is achieved in $(Bi_{0.9}La_{0.1})_2NiMnO_6$ thin films thinner than some critical thickness very flat surfaces are obtained, with root-mean-square (rsm) surface roughness of less than 0.5 nm. Yet for the thickest films in which a 3D growth mode is starting to dominate, the recorded rsm surface roughness values are still low, of less than 1 nm, which evidences the smooth surfaces obtained in $(Bi_{0.9}La_{0.1})_2NiMnO_6$ thin films grown on $SrTiO_3$ up to large values of thickness.

5.3 Chemical analysis

5.3.1 Composition analysis

The presence of highly volatile species, *i.e.* Bi, greatly hampers synthesising stoichiometric Bi-based multiferroic thin films, as observed in $BiMnO_3$ thin films (see Sect. 4.1). Although high substrate temperatures is required when it comes to forming single-phase and high-quality crystalline samples of Bi-based metastable multiferroics, it is not a free deposition parameter due to the fact that Bi-deficiency starts to be significant at temperatures as low as 640ºC, as found in $BiMnO_3$ (see Sect. 4.1.1). Here, a thorough study of the substrate temperature dependence of the Bi content in $(Bi_{0.9}La_{0.1})_2NiMnO_6$ thin films was not carried out, yet a similar behaviour with $BiMnO_3$ thin films is expected to be found as XRD results (Sect. 5.1) shows the presence of spurious phases above 640ºC of synthesising temperature, much likely related to the increasing Bi-deficiency. Single-phase samples, *i.e.* those grown at the intermediate temperatures around 620ºC (see sect. 5.1) were analysed by EELS, as explained in Sect. 2.4.3.

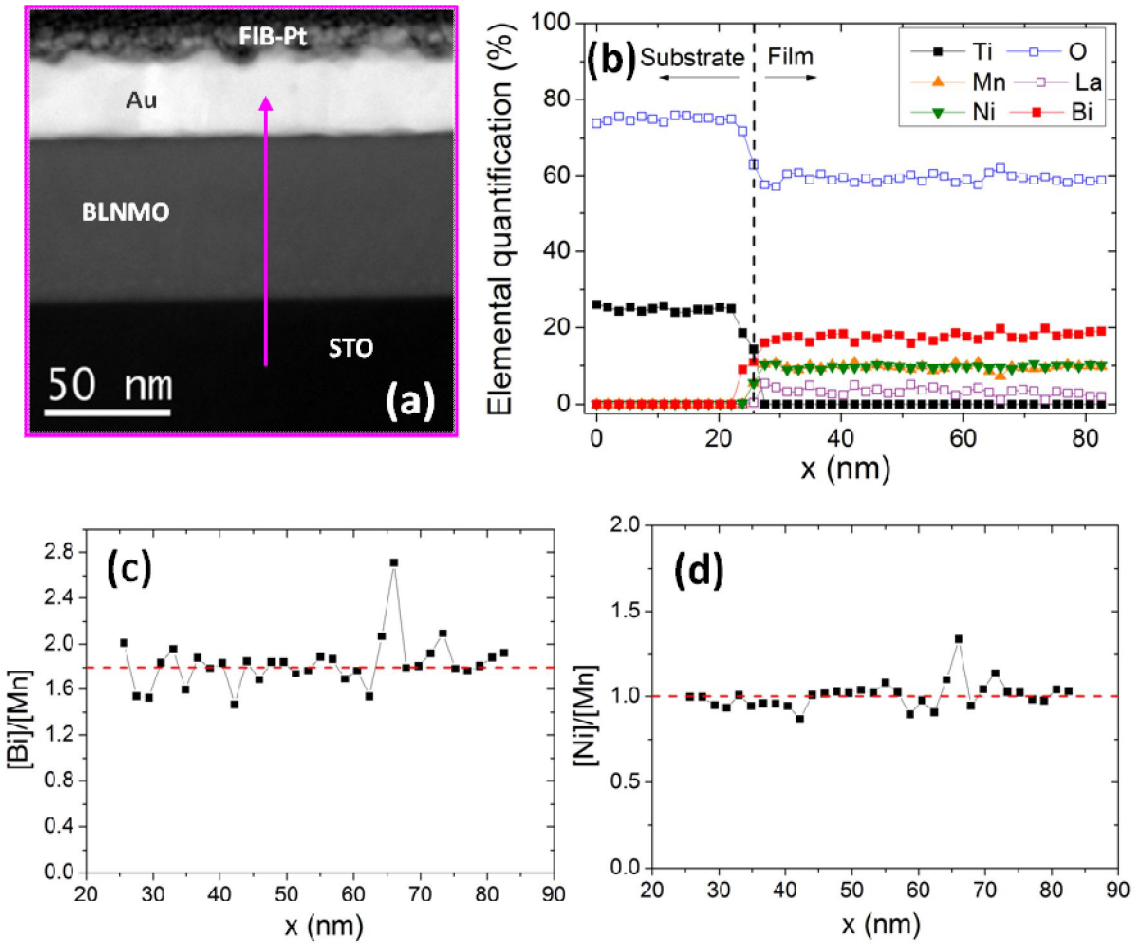

Fig. 5.22 – (a) *HAADF general image of a 68-nm $(Bi_{0.9}La_{0.1})_2NiMnO_6$ film on $SrTiO_3$ substrate. The purple line indicates the path on which EELS compositional profiles were taken.* **(b)** *Elemental quantification obtained by EELS along thickness (subjected to a relative error of 5 %). The dashed line indicates the interface between film and substrate.* **(c)** *Cationic composition ratio of [Bi]/[Mn] along the film thickness.* **(d)** *Cationic composition ratio of [Ni]/[Mn] along the film thickness.*

EELS compositional profiles obtained in [100] cross sectional TEM lamellas were acquired in perpendicular direction to $(Bi_{0.9}La_{0.1})_2NiMnO_6/SrTiO_3$ interface following the path marked in Fig. 5.22 (a). They have been determined from general spectra, in the low-loss (between 40 and 470 eV) and core-loss (between 420 eV and 930 eV) regions. The concentration of the different species is depicted in Fig. 5.23 (b), which, accordingly, no ionic interdiffusion across the interface is found. Neither does there seem to be noticeable cationic segregations along the film thickness, as it occurs with La also located at the A-site in $(La,Ca)MnO_3$ perovskite thin films grown on $SrTiO_3$ (001) [15]. Importantly enough, despite the high volatility of Bi, the film composition is

highly stoichiometric and homogeneous, bearing out 620ºC as an appropriate grown temperature, *i.e.* high enough to obtain single phase samples and low enough to prevent large Bi desorption during deposition. Thus, the Bi content normalized by Mn content is around the nominal value: 1.8, as shown in Fig. 5.22 (c). On the other hand, the compositional relationship between Ni and Mn is, as expected, 1:1 [Fig. 5.22 (d)].

5.3.2 Oxidation state of B-cations

As explained in the Ch.1, the oxidation state of Ni and Mn plays a crucial role in the magnetic properties as much as the long-range B-site order in a rock-salt configuration. In $(Bi,La)_2NiMnO_6$ two different configuration of the valence state of the B-cations are enabled, either Ni^{3+}/Mn^{3+} or Ni^{2+}/Mn^{4+}, being only the latter the appropriate for building up superexchange ferromagnetic paths, *i.e.* $Ni^{2+} – O – Mn^{4+}$ (see 1.2.5). Apart from the different possible configuration, the presence of oxygen vacancies may also alter the oxidation state of the B-cations, which, in turn, the magnetic properties of $(Bi,La)_2NiMnO_6$ thin films. The valence of the B-cations was studied by EELS and XPS (see Sect. 2.4.1 and 2.4.3) of single-phase samples grown at 620ºC.

EELS spectra in the 400 to 750 eV energy-loss range was recorded, where Mn $L_{2,3}$ edges take place. These peaks are known to be related to the formal valence of manganese ions [15, 16], as Mn L_2 and L_3 peak position are shifted to higher energies on decreasing the occupancy of *d* orbitals, whereas L_3/L_2 intensity ratio decreases when the orbital configuration varies from d^5 to d^0 or d^{10}. Thus, for Mn^{4+}, *i.e.* with an orbital configurations d^3, L_3 edge is expected to be shifted to higher energies than that of Mn^{3+} (d^4 of orbital configuration) and L_3/L_2 intensity ratio is to be found smaller for Mn^{4+} with regard to Mn^{3+}. The expected intensity ratios L_3/L_2 and energy positions of L_3 edges corresponding to the different oxidation states of Mn ions are depicted in dotted lines in Fig. 5.23 (a) and (b), respectively. The experimental collected data (solid square symbols in Fig. 5.23), determined by using a home-made software package MANGANITAS [15, 17, 18], are plotted in Fig. 5.23 (solid square symbols). Results evidence the homogeneity of Mn^{4+} within $(Bi_{0.9}La_{0.1})_2NiMnO_6$ thin films, without traces of Mn^{3+} or Mn^{2+} indicating that the films are fully oxidized. Likewise, the Ni oxidation state has been assessed by Ni L_2 and L_3 edges, which occur at 872 and 855 eV, respectively. The determined fine structure of these $L_{2,3}$ edges corresponds to the

divalent oxidation state [19], as expected taken into account that the valence of Mn is 4+.

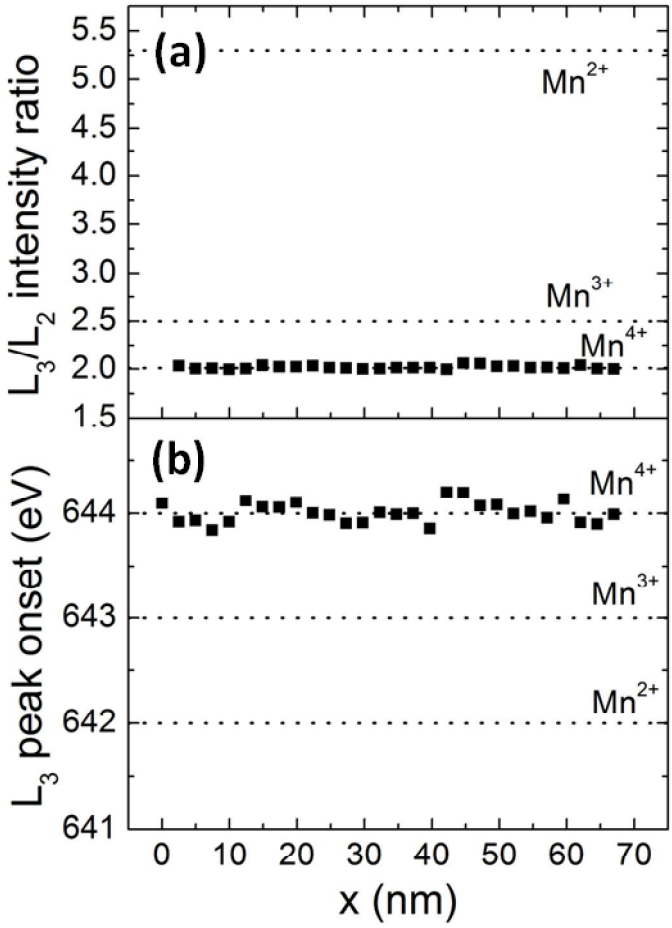

Fig. 5.23 – *Mn L_3/L_2 intensity ratio* **(a)** *and L_3 peak onset* **(b)** *obtained along thickness of a 68-nm $(Bi_{0.9}La_{0.1})_2NiMnO_6$ thin film [EELS profiles obtained along the marked line in Fig. 5.22 (a)]. L_3/L_2 intensity ratio is subjected to 5% of relative error. L_3 peak onset is subjected to a ± 0.4 eV error.*

On the other hand, as a complementary technique, XPS was also used to obtain the valence state of Mn of $(Bi_{0.9}La_{0.1})_2NiMnO_6$ thin films from the Mn 3*s* photelectron spectra, as explained in Sect. 2.4.1. Nonetheless, this technique is very surface sensitive, so that only the top ~2 nm of the film can be analysed. In order to perform XPS analysis along thickness, XPS is complemented by ion sputtering which allows obtaining XPS spectra at different depth by eroding the film. However, ion bombarding is a quite aggressive technique which may greatly alter the compositional ratios, but especially counter-productive is the fact that it modifies the chemical bonds completely giving rise

to misleading information about the oxidation state of the species. Therefore no ion bombarding was used to characterise the valence of the B cations.

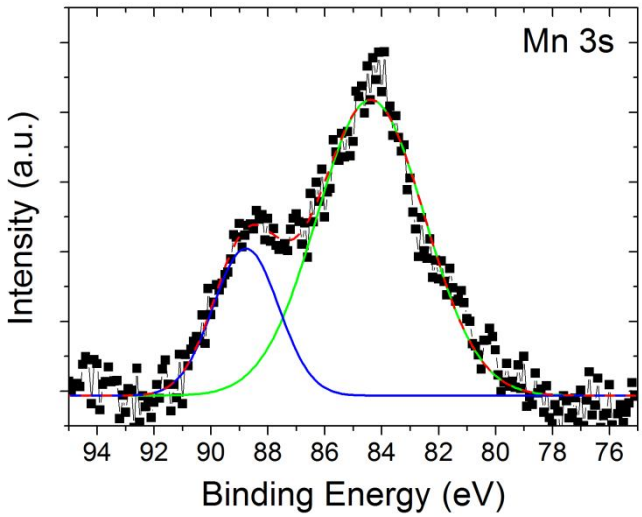

Fig. 5.24 – *Mn 3s photoemission spectra of 125-nm $(Bi_{0.9}La_{0.1})_2NiMnO_6$ thin film grown on $SrTiO_3$ (001).*

XPS measurements were performed on as-grown $(Bi_{0.9}La_{0.1})_2NiMnO_6$ thin films on $SrTiO_3$ substrates and recorded the Mn 3*s* photoelectron spectra, which takes place between 90 and 80 eV. The splitting of the Mn 3*s* into two peaks in the photoelectron spectra (see Fig. 5.24) is due to the exchange coupling between the 3*s* holes and 3*d* electrons and hence it is closely related to the valence of Mn (the 3*d* orbitals filling indicates the oxidation state of Mn) [20, 21]. Specifically, the difference in energy of the Mn 3*s* peaks monotonically decreases as the oxidation state of Mn increases from 2+ to 4+ (see Fig. 2.16, Sect. 2.4.1) [20]. The two peaks of Mn 3s photoelectron spectra were fitted by two Gaussian functions as plotted in Fig. 5.24, from which the splitting in energy ($\equiv\Delta E_{3s}$) was computed.

As the oxygen pressure during thin film growth is one of the main sources of the formation of oxygen vacancies in many oxide films [22 – 26], which would lead to lowering of the oxidation state of the cations, different $(Bi_{0.9}La_{0.1})_2NiMnO_6$ samples grown at different O_2 pressures were analysed by XPS. The computed ΔE_{3s} of Mn 3*s* spectra as a function of the oxygen pressure during growth is shown in Fig. 5.25. The expected ΔE_{3s} for Mn^{2+}, Mn^{3+} and Mn^{4+} is depicted as dashed lines. Accordingly, in the range of oxygen pressures used in this work (0.3 – 0.6 mbar) no variation in the

oxidation state of Mn is found, which remains 4+ irrespectively. On the other hand, Mn 3*s* spectra were also recorded for different thick films grown at 0.5 mbar of O_2 pressure, the computed ΔE_{3s} of which is plotted in Fig. 5.26. Likewise the previous case, at any thickness only the presence of Mn^{4+} is found.

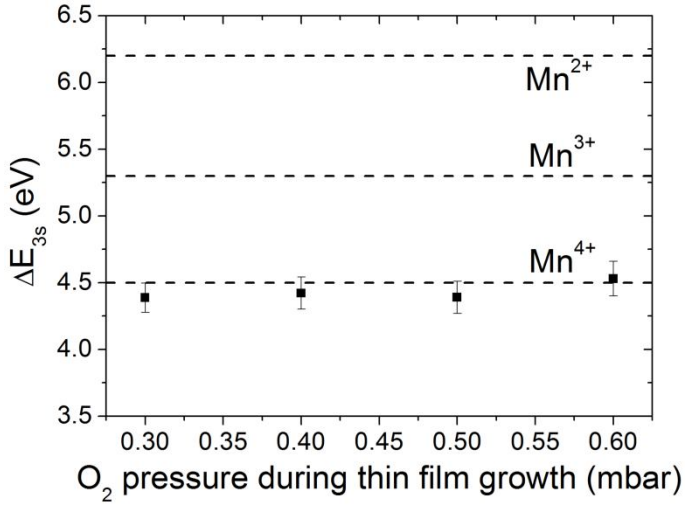

Fig. 5.25 – *Mn 3s energy splitting of 125-nm $(Bi_{0.9}La_{0.1})_2NiMnO_6$ thin films grown at 620°C at different O_2 pressures on $SrTiO_3$ (001). The dashed lines indicate the expected Mn 3s energy splitting of different oxidation states of Mn (extracted from Ref. 20).*

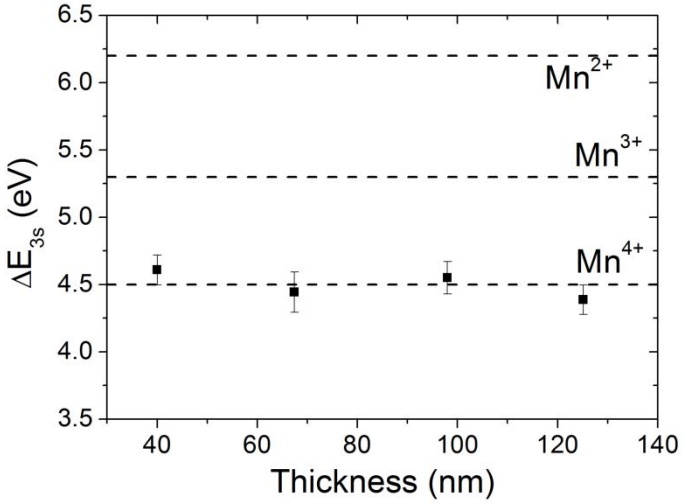

Fig. 5.26 – *Mn 3s energy splitting of $(Bi_{0.9}La_{0.1})_2NiMnO_6$ thin films of different thickness grown at 0.5 mbar of O_2 pressure on $SrTiO_3$ (001). The dashed lines indicate the expected Mn 3s energy splitting of different oxidation states of Mn (extracted from Ref. 20).*

To conclude, although XPS measurements are only sensitive to the top layers of the films, EELS has corroborated the homogeneity of the tetravalent state of Mn along thickness. Importantly enough, the oxygen pressure during thin film growth, which tends to be a crucial thin film deposition parameter in terms of oxygen vacancies formation, does not play a significant role in the oxidation state of Mn, which remains invariant 4+ (note that the valence state of Ni is never to be 1+ in order to compensate the electric equilibrium in presence of oxygen vacancies). Hence, $(Bi_{0.9}La_{0.1})_2NiMnO_6$ thin films are expected to be fully oxidised, within the sensitivity of EELS and XPS. It is to be remarked, though, that the films were always cooled down under 1000 mbar of O_2 pressure after deposition, resulting in both preventing the formation of oxygen vacancies during the cooling down process and oxygenating the film completely if it was not yet. On the other hand, no deviation of the tetravalent state of Mn is found when increasing the film thickness, pointing to an homogenous oxygenation along thickness.

Interesting enough, as only the divalent and trivalent sate of Ni cations are energetically favoured, the fact that only Mn^{4+} is found in $(Bi_{0.9}La_{0.1})_2NiMnO_6$ thin films rules out the presence of Ni^{3+}, evidencing the highly desirable configuration of Ni^{2+}/Mn^{4+} of the B-cations in $(Bi_{0.9}La_{0.1})_2NiMnO_6$ thin films, which favours the ferromagnetic interactions.

5.4 Magnetic properties

As explained in chapter 1, the magnetic order in $(Bi_{0.9}La_{0.1})_2NiMnO_6$ arises from the superexchange interaction of the magnetic ions, *i.e.* Ni and Mn, located at the B-site, mediated by the adjacent oxygen anions. Nonetheless, the sign of the magnetic superexchange interaction (whether it is ferromagnetic or antiferromagnetic) is strongly dependent on the electronic configuration of the magnetic ions and their order at the B-site. The results of previous sections (Sect. 5.3.2) give evidence for Ni and Mn cations being divalent and tetravalent, respectively. Moreover, crystal structure data (Sect. 5.2.4) proves that Ni and Mn orders alternatively along [100], [010], [001] pseudocubic directions in a rock-salt configuration (see Fig. 5.16), being Mn cations the first B-cation neighbours of each Ni cation and vice versa, separated just by the oxygen anions.

Hence, according to the Kanamori-Goodenough rules [27], ferromagnetic superexchange interaction is expected along the 180º-bond-angle $Ni^{2+}(t_{2g}^6 e_g^2$, half-filled e_g orbitals) – O – $Mn^{4+}(t_{2g}^6 e_g^0$, empty e_g orbitals). The long-range B-site order ensures a long-range ferromagnetic coupling of the spins of Ni^{2+} and Mn^{4+}, so that $(Bi_{0.9}La_{0.1})_2NiMnO_6$ thin films are expected to behave ferromagnetically.

Single-phase $(Bi_{0.9}La_{0.1})_2NiMnO_6$ thin film samples grown at 620ºC and 0.5 mbar of O_2 mbar were used for the magnetic characterisation. The applied magnetic field, H, has been applied along an in-plane direction. The large diamagnetic contribution of the substrate $SrTiO_3$ was removed from the raw data (see Appendix B). Magnetisation data versus applied magnetic field, $M(H)$, recorded at 10 K, is shown in Fig. 5.27, in which an hysteretic $M(H)$ behaviour can clearly be observed, proving the expected ferromagnetic character of $(Bi_{0.9}La_{0.1})_2NiMnO_6$ thin films. The magnetic remanence, which can be appreciated in the inset of Fig. 5.27, is rather low indicating a small magnetic anisotropy in the system.

The magnetisation measured at the highest applied magnetic field, 7 T, is around 3.5 μ_B/f.u. (Fig. 5.27), in close agreement with data reported for bulk $(Bi_{0.9}La_{0.1})_2NiMnO_6$ samples [M_S (7 T, 5 K) ~ 3.6 μ_B/f.u)] [7], although neither do bulk samples [7] nor do our thin films saturate at the highest magnetic field, but, instead, it shows a gradual increase. For an ideal ferromagnetic coupling of the spins of Ni^{2+} (S = 1) and Mn^{4+} (S = 3/2), a saturated magnetisation of M_S = 5 μ_B/f.u. is expected (see Sect. 1.2.5). Due to the lack of saturation of the $M(H)$ of our $(Bi_{0.9}La_{0.1})_2NiMnO_6$ thin films it is elusive to determine their M_S. Nonetheless, in the case of non-La-doped Bi_2NiMnO_6 samples, in which $M(H)$ saturates at 4 T, a reduced M_S is reported for both bulk samples (M_S ~ 4.1 μ_B/f.u) [5] and thin films (M_S ~ 4.5 μ_B/f.u) [8].

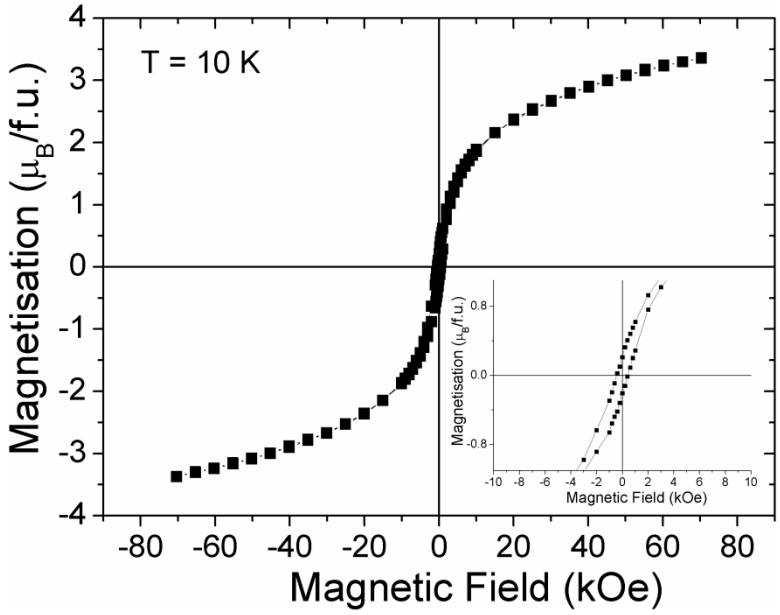

Fig. 5.27 – *Magnetic field dependence of the magnetization of a 100-nm-thick $(Bi_{0.9}La_{0.1})_2NiMnO_6$ thin film. Bottom inset: Zoom of the low field region. The coercive field is about 0.5 kOe.*

One possible explanation of the probable reduced magnetisation of our films could be the presence of some residual Mn^{3+} due to the formation of oxygen vacancies, as Ni^{2+} – O – Mn^{3+} can give rise to antiferromagnetic superexchange interaction. Note that Mn^{3+} contains one half-filled e_g orbital, z^2, in a Jahn-Teller distortion of the perovskite (chapter 1), which couples antiferromagnetically with the half-filled e_g orbitals of Ni^{2+} [27]. Still, this possibility is highly unlikely as Ni and Mn were proved to have an oxidation state of 2+ and 4+ irrespective of the partial oxygen pressure during thin film growth, indicating they were fully oxidised at any event (Sect. 5.3.2). Nonetheless, for the sake of completeness, a set of samples grown at 0.5 mbar of O_2 pressure were in-situ annealed at 450ºC under 1000 mbar of O_2 pressure after PLD deposition for different annealing time lengths in order to ensure full oxidation. Yet $M(H)$ data of the different annealed samples (Fig. 5.28) shows no significant different behaviour, recording almost the same saturated magnetisation, $M_S \sim 3.5$ μ_B/f.u, hence evidencing the presence of Ni^{2+} and Mn^{4+} solely.

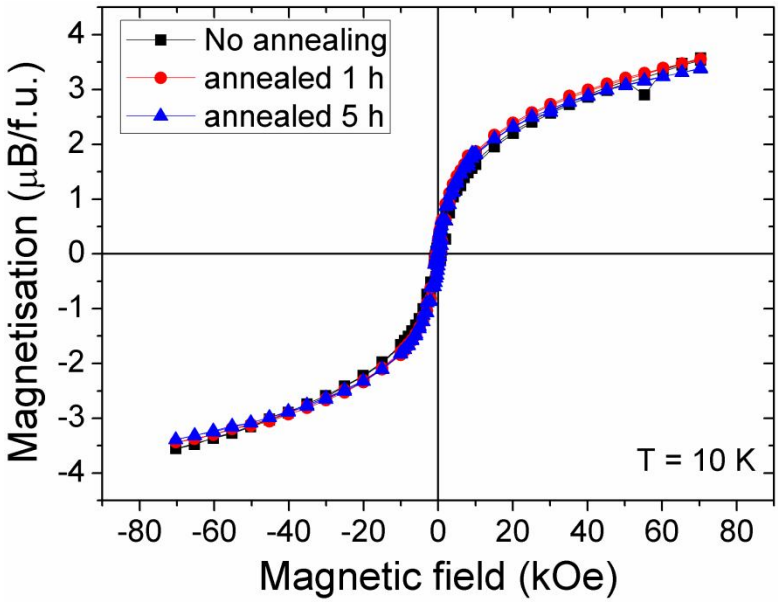

Fig. 5.28 – *Magnetic field dependence of the magnetization of 100-nm-thick $(Bi_{0.9}La_{0.1})_2NiMnO_6$ thin films in-situ annealed for different periods of time at 450ºC and 1000 mbar of O_2 pressure.*

Alternatively, the possible reduced magnetisation could be due to the presence of some antisite defects, *i.e.* the presence of either Ni – O – Ni or Mn – O – Mn, and antiphase boundaries, common defects in double perovskites structures [11, 28, 29], which may account for both the hardness to saturation and the accompanying reduced magnetization as found here. Yet it is worth remarking that $M(H)$ of bulk solid solution of $(Bi_{1-x}La_x)_2NiMnO_6$ samples, $0.1 \leq x \leq 0.4$ [7], unlike non-La-doped Bi_2NiMnO_6 samples [5, 8], saturates gradually in a wide range of La-doping, without reaching saturation at the highest applied magnetic fields (H = 7 T). Therefore, the distinct length and angles of Ni – O – Mn bonds around A-site when occupied either by La or Bi cations, absent in non-doped Bi_2NiMnO_6 samples, may also play a significant role in the ferromagnetic properties.

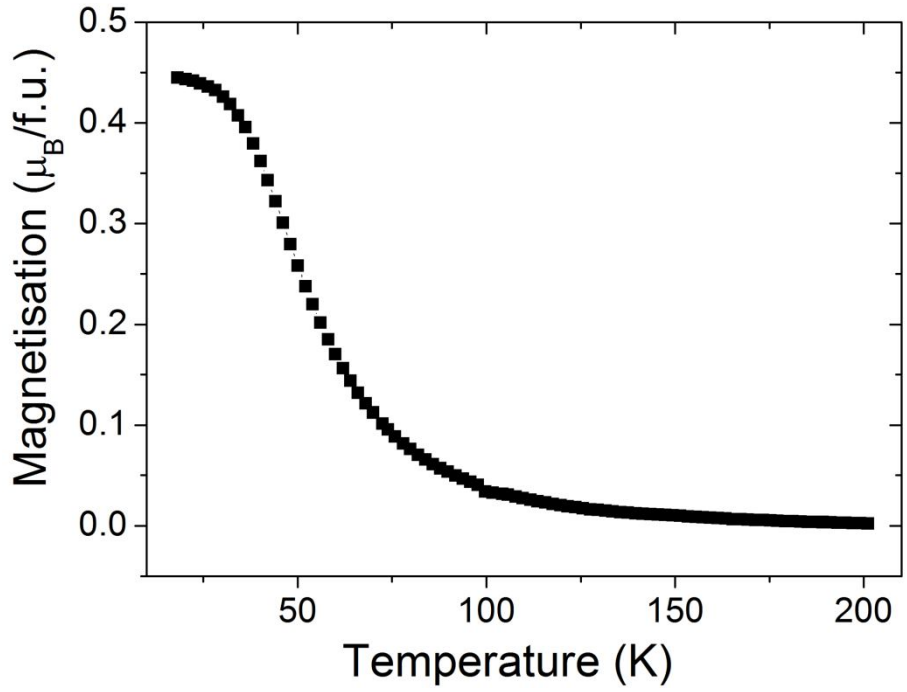

Fig. 5.29 – *Temperature dependence of the magnetization of 100-nm-thick $(Bi_{0.9}La_{0.1})_2NiMnO_6$ thin film under an in-plane applied magnetic field of 1000 Oe. Note that diamagnetic contribution was substracted from raw data (see Appendix B).*

The temperature dependence of the magnetisation, $M(T)$, of single-phase $(Bi_{0.9}La_{0.1})_2NiMnO_6$ thin films is exemplified in Fig. 5.29, in which the sample is cooled down under an applied in-plane magnetic field of 1000 Oe. The ferromagnetic transition temperature occurs at T_{FM} ~ 100 K. This value is significant lower than bulk $(Bi_{0.9}La_{0.1})_2NiMnO_6$ samples (T_{FM} ~ 150 K) [7]. Nonetheless, similarly, Bi_2NiMnO_6 thin films grown on (001)-oriented $SrTiO_3$ substrates show a significant reduced Curie temperature (T_{FM} ~ 100 K) [8, 30] with regard to bulk Bi_2NiMnO_6 samples (T_{FM} ~ 140 K) [5]. Hence, it seems reasonable to ascribe this reduced T_{FM} to the epitaxial strain exerted by the substrate, which imposed a different Ni – O – Mn bond length and angle (and consequently different intensity of the magnetic interaction) comparing to bulk samples with free-standing lattice parameters.

On the other hand, $M(T)$ curve shows a rather broad transition temperature (Fig. 5.29), which might point out to some distribution of magnetic superexchange interactions within the sample. This could be due to the presence of dissimilar cations at the A-site, as mentioned before, which no doubt results in distinct length and angles of

Ni – O – Mn bonds. However, very similar $M(T)$ curves, with very broad magnetic transitions temperatures, are reported for Bi_2NiMnO_6 thin films as well [8, 30], so that it might be an intrinsic magnetic behavior of these compounds when grown as thin films.

In summary, $(Bi_{0.9}La_{0.1})_2NiMnO_6$ thin films have been proved to be ferromagnetically ordered below 100 K, reaching a large magnetization value (compared to other multiferroics oxides, see table 1.5 in Ch. 1) of 3.5 μ_B/f.u at 7 T (at 10 K), in agreement with bulk magnetization values, but significantly smaller than expected (~ 5 μ_B/f.u.). Nonetheless, the Curie temperature is found to be smaller than bulk specimens likely driven by the epitaxial strain imposed by the substrate.

5.5 Ferroelectric properties

5.5.1 Background of the ferroelectric properties

As explained in chapter 1, the non-centrosymmetric distortion of Bi_2NiMnO_6 arises from the stereochemical activity of the lone-pare $6s^2$ electrons of Bi (see Fig. 1.5, Sect. 1.2.2), which shifts away from the centrosymmetric position generating an electric dipole. Polar structure is a required condition for ferroelectricity to be established but, yet, not a sufficient one. Ferroelectric order implies that spontaneous polarization appears which should be switchable by applying an electric field. Therefore, to definitive bear out the ferroelectric character it is necessary to measure either a ferroelectric hysteresis loop, *i.e.* polarisation versus electric field curves, $P(E)$, that is to measure the ferroelectric domain switching current when reverse the polarisation in the sample by applying an opposite electric field (see Sect. 3.3). Yet these experiments can be greatly hampered by the poor resistive character of multiferroic compounds, which can completely alter the measurement by the leakage current (see Sect. 3.3).

Temperature XRD data analysis of bulk Bi_2NiMnO_6 samples [5] showed that the crystal structure was not centrosymmetric (monoclinic C2) below 485 K (see Sect. 1.2.5). Above that temperature the structure was indexed as centrosymmetric monoclinic $P2_1/n$, which was accompanied with a large dielectric anomaly around the

transition temperature. These are the typical signatures of a ferroelectric phase transition, hence pointing to the highly likely possibility of this material to be ferroelectric below 485 K. On the other hand, La-doped Bi_2NiMnO_6 bulk samples were also proved to be equivalently non-centrosymmetric for lower values of La contents, *i.e.* less than 20% [7]. Yet neither ferroelectric hysteresis loop nor ferroelectric domain switching current was measured in either case, which might be due to the likely leaky character of $(Bi,La)_2NiMnO_6$ samples or the high voltages required for switching the ferroelectric domains in bulk samples. Note that the applied electric field, E, as a result of the applied voltage, V, in the common ferroelectric testing set-up parallel-plate capacitor (sect. 3.1) scales as the inverse of the electrodes separation, d, *i.e.* $E = V/d$. This distance is generally large in bulk specimens, hence giving rise to insufficient electric fields for switching the ferroelectric domains.

The first, and only, reported ferroelectric hysteresis loop was performed on Bi_2NiMnO_6 thin films at 7 K [8]. However, this hysteresis loop was far from being a robust ferroelectric proof as the reported $P(E)$ curve showed a negative slope at high positive E fields or a positive slope at high negative E fields, which would indicate an unphysical meaning negative dielectric permittivity, ε_r, as $\boldsymbol{P} = \varepsilon_0(\varepsilon_r - 1)\boldsymbol{E}$ (where bold notation of $\boldsymbol{P}$ and $\boldsymbol{E}$ denotes their vector character and ε_r is a tensor).

Therefore, although $(Bi_{1-x}La_x)_2NiMnO_6$, $x \leq 0.2$, compounds are promising candidates to be multiferroic, their ferroelectric character remained still to be unravelled.

5.5.2 Electric characterisation of the ferroelectric properties

For the electric characterisation of the ferroelectric properties of $(Bi_{0.9}La_{0.1})_2NiMnO_6$ thin films, the parallel-plate capacitor configuration (see Fig. 3.1 and 3.2, Ch. 3) was used, *i.e.* $Pt/(Bi_{0.9}La_{0.1})_2NiMnO_6/Nb:SrTiO_3$ sandwich-capacitors were fabricated (see Sect. 3.1). The thickness of the sample batch used was comprised between 100 and 110 nm. The deposition conditions of $(Bi_{0.9}La_{0.1})_2NiMnO_6$ thin films were the optimised ones for single-phase formation, *i.e.* at 620ºC and 0.5 mbar of O_2 pressure. The electric field was applied from top to top *Pt* electrodes (see Sect. 3.1),

which entails measuring two identical capacitors or equivalently a unique capacitor with $2t$ electrode-separation, where t is the film thickness. Hence, the applied electric field, E, on the sample was computed by $E = V/(2t)$, where V is the applied voltage. On the following, for the sake of simplicity, $\boldsymbol{P}$ and $\boldsymbol{E}$ are going to be considered one-dimensional, but actually what is measured in our experimental set-up (see Sect. 3.1) is the out-of-plane P_i component of $\boldsymbol{P}$ that has the same direction as the applied electric field $\boldsymbol{E}$.

As $(Bi_{0.9}La_{0.1})_2NiMnO_6$ thin films show a clear leaky behaviour, as it will be analysed in Sect. 5.6, the so-called Positive-Up-Negative-Down (PUND) technique (Fig. 3.16, Ch. 3) was used to measure the ferroelectric domain switching current (see Sect. 3.3). PUND measurements were performed at 5 K closely to the accessible lowest temperatures in the Physical Properties Measurement System (PPMS) (see Sect. 2.5.3) in order to reduce as much as possible the conductive current. Note that the resistivity of these compounds decreases exponentially on increasing temperature because of its semiconductor character (as be discussed in sect. 5.6).

Fig. 5.30 shows the current versus time (~voltage) recorded in each triangular voltage pulse (rise time of 25 μs, equivalent to 10 kHz) of the PUND measurement (inset of Fig. 5.30). Whereas the current resulting from P and N pulses (labelled with P and N in Fig. 5.30) contains the overall current (*i.e.* $I_{FE} + I_{\varepsilon} + I_{leakage}$, see Sect. 3.3), that resulting from U and D pulses (labelled with U and D in Fig. 5.30) only contains the non-ferroelectric part (*i.e.* $I_{\varepsilon} + I_{leakage}$, see Sect. 3.3) as the sample is already polarised. Thus, by subtracting the current from the U pulse from that of the P pulse (and similarly D from N) we only obtain the current related to the switch of the ferroelectric domains, I_{FE}. The two current peaks that appear in P and N curves, absent in U and D curves, unequivocally reveal the ferroelectric character of $(Bi_{0.9}La_{0.1})_2NiMnO_6$ films.

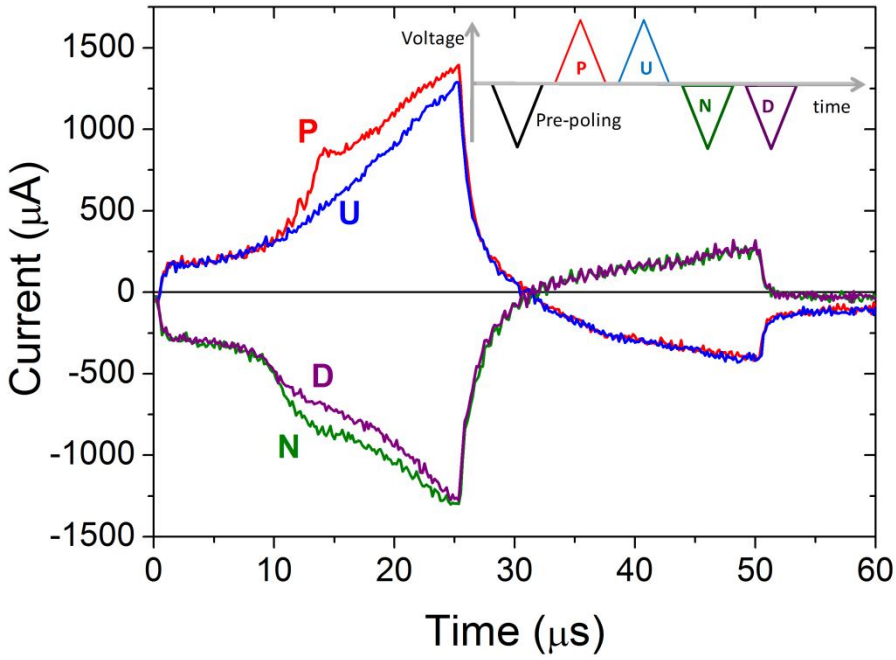

Fig. 5.30 – *PUND measurement performed on Pt/$(Bi_{0.9}La_{0.1})_2NiMnO_6$/Nb:$SrTiO_3$ capacitors at 5 K. Inset: Scheme of the PUND measurement.*

As the triangular voltage pulses are linearly related to the rise time of the pulse, current versus voltage, $I(V)$ curves, can be computed. Once subtracted the non-ferroelectric contributions, *i.e.* $I_\varepsilon + I_{leakage}$, $I_{FE}(V)$ curves (Fig. 5.31 left axis) is extracted, or equivalently, as a function of the applied electric field, E, as $E = V/(2t)$. As shown, the ferroelectric peaks can clearer be observed. The coercive field, E_c, lies at around E_c ~ 300 kV/cm for the frequency used (10 kHz). Note that E_c is frequency dependent in any ferroelectric material [31], which increases on increasing frequencies. Still, there is a little asymmetry likely related to little differences in the metal-insulator interfaces.

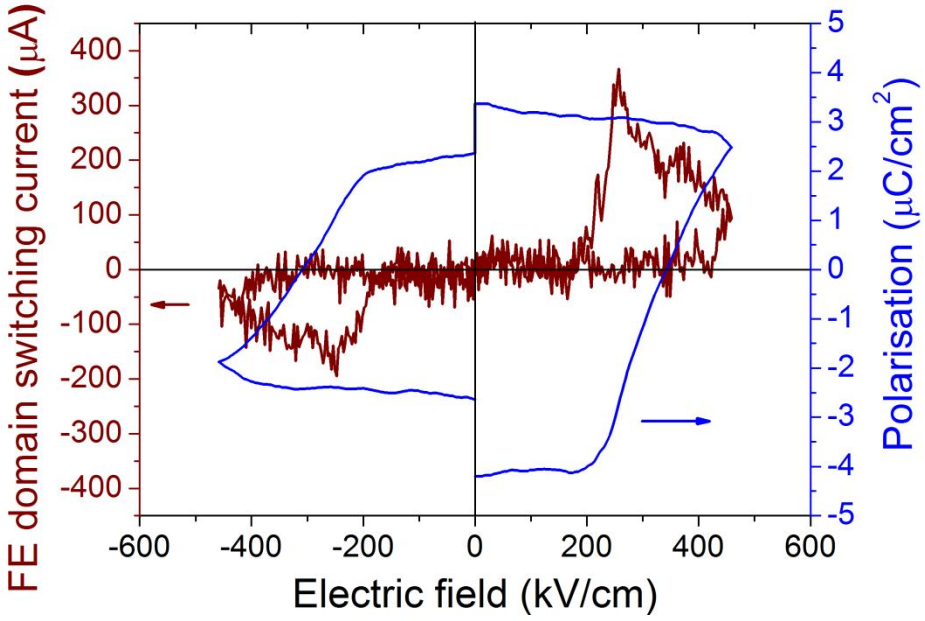

Fig. 5.31 – *Ferroelectric domain switching current once subtracted the non-ferroelectric contributions (left axis) and polarization (right axis) versus applied electric field of* $(Bi_{0.9}La_{0.1})_2NiMnO_6$ *thin films.*

The hysteresis loops of polarisation versus the applied electric field, $P(E)$, is computed by determining first the charge related to the ferroelectric domain switching current (see Sect. 3.3):

$$Q_{FE} = \int I_{FE}(t)dt \qquad (5.3)$$

integrated over the time of the cycle. Then the polarisation is extracted, $P = Q_{FE}/A$, where A is the area of the round-shaped electrodes (0.25 mm of radius). Note that as I_ε has been substracted in this measurement, the hysteresis loops $P(E)$ should be rectangular-shaped, *i.e.* without the positive slope at high electric fields, as corresponds to all dielectrics, $P = \varepsilon_0(\varepsilon_r - 1)E$. The results are shown in Fig. 5.31 (right axis). As observed, the hysteresis loop is quite asymmetric, giving rise to a not closed loop. This is due to the aforementioned little asymmetry in the $I_{FE}(E)$ curves [Fig. 5.31 (left axis)]. The remanent polarisation is found to be around ~3 μC/cm^2. Nonetheless, an exact value is quite difficult to be determined not only because of this asymmetry, but also because of the fact that the measured ferroelectric switching current is quite low with regard to that of the leakage.

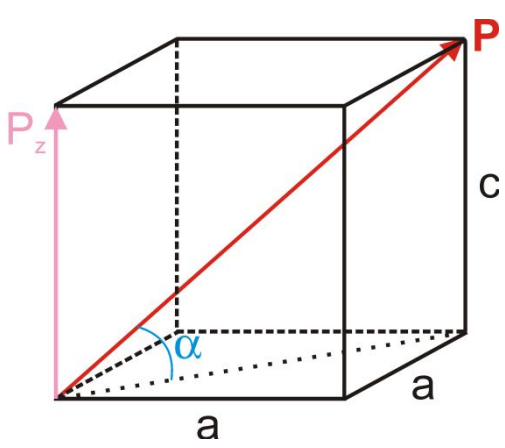

Fig. 5.32 – *Scheme of the out-of-plane projection of the polarisation, which is measured in our experimental set-up.*

Still, it is worth remarking that the measured remanent polarisation is a lower bound for the actual polarisation value since, as discussed in chapter 1, the polarisation axis is expected to lie along the [111] direction [8] and therefore, according to our experimental set-up (Sect. 3.1), on applying ***E*** from top to top electrode, it is the out-of-plane projection, P_z, of the polarisation vector ***P*** what is measured. Given the unit cell lattice parameters of $(Bi_{0.9}La_{0.1})_2NiMnO_6$ thin films grown on $SrTiO_3$ (determined in Sect. 5.2) the modulus of ***P*** is estimated (see Fig. 5.32) as follows:

$$\left|\vec{P}\right| = \frac{P_z}{\sin\alpha}; \qquad \tan\alpha = \frac{c}{a}\cdot\frac{1}{\sqrt{2}} \tag{5.4}$$

where a and c are the in-plane and out-of-plane lattice parameters of $(Bi_{0.9}La_{0.1})_2NiMnO_6$ thin films. The computed value of the polarisation modulus (~ 5.5 $\mu C/cm^2$ Eq. 5.4) is still lower than the predicted theoretical value for Bi_2NiMnO_6: ~18 $\mu C/cm^2$ or ~28 $\mu C/cm^2$, depending on the theoretic model that is used for estimating the polarisation (point-charge model or Berry-phase method, respectively) [32, 33]. Some reduction in the polarisation of $(Bi_{0.9}La_{0.1})_2NiMnO_6$ films is expected due to the 10% La doping (note that La is not a stereochemical active ion like Bi). Indeed, this reduction due to the La-doping may be quite severe, not only because it entails 10% less ferroelectric polarisable dipoles, but also because this doping may entail the disruption, at least locally, of the necessary cooperative phenomenon for the ferroelectric order of the electric dipoles formed by $6s^2$ lone-pairs of Bi^{3+}. Yet, it is worth noting that the constraints imposed by the substrate on a thin film were not taken into account in these predictions, which may significantly modify the polarisation values. Moreover, the large

discrepancy in polarisation values which both theoretic models give [32, 33] suggests a rough estimation of the prediction rather than closely exact values.

Finally, for the sake of comparison, it is worth mentioning that the remanent polarisation of $(Bi_{0.9}La_{0.1})_2NiMnO_6$ thin films, in the order of ~5.5 $\mu C/cm^2$, is much smaller than some ferroelectrics of huge polarisation like $PbZr_{0.2}Ti_{0.8}O_3$ (~70 $\mu C/cm^2$) [34] or multiferroic $BiFeO_3$ (~60 $\mu C/cm^2$) [35] and smaller than conventional ferroelectrics like $BaTiO_3$ (~20 $\mu C/cm^2$) [36]. Yet the recorded polarisation is larger than many multiferroic manganites, such as the rare-earth manganites, which possess polarisation values of the order of a few nC/cm^2 [37].

5.5.3 Ferroelectric phase transition

Once borne out the ferroelectric character of $(Bi_{0.9}La_{0.1})_2NiMnO_6$, and by extension Bi_2NiMnO_6, it remains to be deduced the ferroelectric Curie temperature of $(Bi_{0.9}La_{0.1})_2NiMnO_6$ thin films. Still, due to the increasing large leakage current when increasing temperature, it greatly hampers measuring the current related to the ferroelectric domain switching at higher temperatures. Thus, it makes unfeasible to determine the ferroelectric phase transition temperature by just electric measurements and therefore the use of indirect techniques becomes necessary. Here, Raman spectroscopy and temperature-dependent X-ray diffraction measurements were performed. Single-phase $(Bi_{0.9}La_{0.1})_2NiMnO_6$ thin films, of 70 nm thick, grown at 620ºC and 0.5 mbar of O_2 pressure on $SrTiO_3$ were used.

It is worth remarking that the ferroelectric phase transition of $(Bi_{0.9}La_{0.1})_2NiMnO_6$ thin films might be dramatically different from bulk Bi_2NiMnO_6 (T_{FE} ~ 485 K [5]), not only due to the presence of lanthanum, but also because of the fact that the epitaxial strain exerted by the substrate ($SrTiO_3$) may severely modify the critical temperatures, as it is the case in most ferroelectric thin films [34, 36, 38 – 41]. We recall here that $(Bi_{0.9}La_{0.1})_2NiMnO_6$ thin films coherently grown on $SrTiO_3$ are 0.72% tensile strained (Sect. 5.2.2).

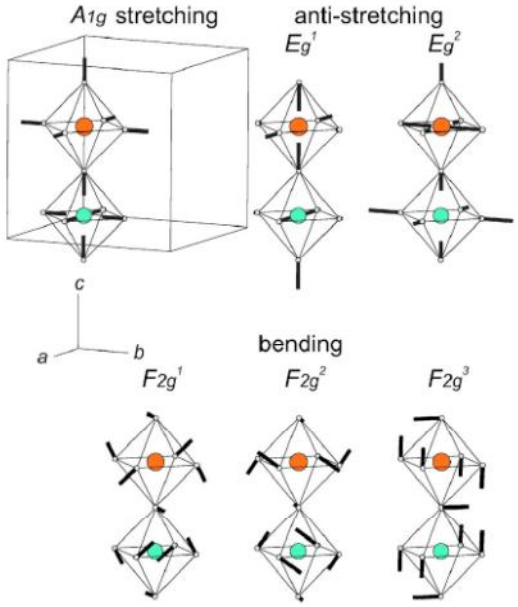

Fig. 5.33 – *High frequency phonon mode associated with stretching of $BO_6/B'O_6$ octahedrons and broad low frequency phonon mode associated with anti-stretching and bending vibrations of $BO_6/B'O_6$ octahedrons of Bi_2NiMnO_6, La_2NiMnO_6 and La_2CoMnO_6 double-perovskites [reproduced from Ref. 42].*

Raman spectroscopy is a well adapted technique to investigate phase transitions not only in pure Bi_2NiMnO_6 [43] but also lanthanide double-perovskites based on Ni – Mn and Co – Mn cations at the B-site [42 - 44]. Despite being different compounds, they show similar features in their Raman spectra. Characteristic to these double-perovskite structures is the presence of a pronounced phonon mode around 600 cm^{-1} and a broad phonon mode around 500 cm^{-1}, associated with stretching and antistretching/bending vibrations of $BO_6/B'O_6$ octahedrons, respectively (Fig. 5.33) [42 - 44]. Structural transitions in these double-perovskites were proved to have an impact in the temperature dependence of the phonon frequency of these modes, $\omega(T)$, shifting its frequency position around the transition temperature, $\Delta\omega_{lattice}$ [42 - 45]. Importantly enough for the purpose of determining the ferroelectric Curie temperature is the fact that the high frequency mode, *i.e.* the one corresponding to the stretching vibrations of MnO_6/NiO_6 octahedrons, was demonstrated to be very sensitive to these phase transitions [42 - 44], *i.e.* maximising $\Delta\omega_{lattice}$.

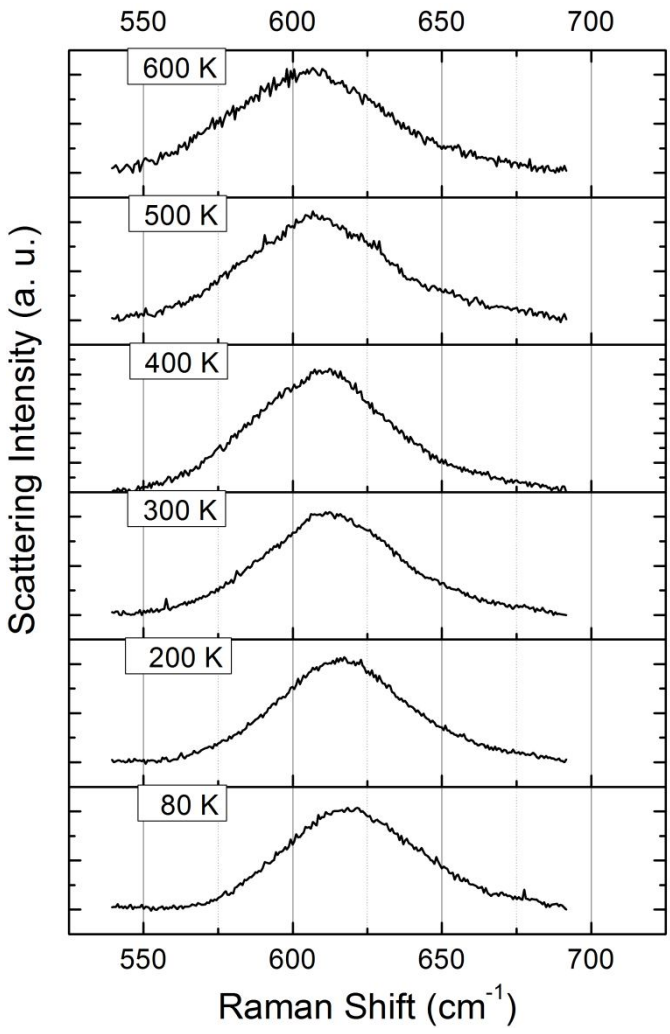

Fig. 5.34 – *Temperature dependence of the Raman spectra of the high frequency mode of $(Bi_{0.9}La_{0.1})_2NiMnO_6$ thin films.*

The Raman spectra of the high-frequency mode, $\omega(T)$, from $(Bi_{0.9}La_{0.1})_2NiMnO_6$ thin films obtained at different temperatures is depicted in Fig. 5.34. As observed, $\omega(T)$ shifts to low wavenumbers as temperature increase, consistent with the temperature evolution of Raman spectra of Bi_2NiMnO_6 and lanthanum double-perovskites [42 - 44]. The temperature dependence of $\omega(T)$ is plotted in Fig. 5.35 (left axis, solid symbols), which shows a change of slope around 430 K. Moreover, this signature is more pronounced in the temperature dependence of the corresponding linewidth, characterised by the FWHM [Fig. 5.35 (right axis, open symbols)]. These characteristic changes in $\omega(T)$ and FWHM(T) occur at temperatures remarkably close to T_{FE} of bulk Bi_2NiMnO_6 (~485 K [5]). Thus, it suggests that the structural transition observed in Fig. 5.35 occurring at around 430 K (with a rough error of ±20 K) should correspond to the ferroelectric phase transition of $(Bi_{0.9}La_{0.1})_2NiMnO_6$ thin films.

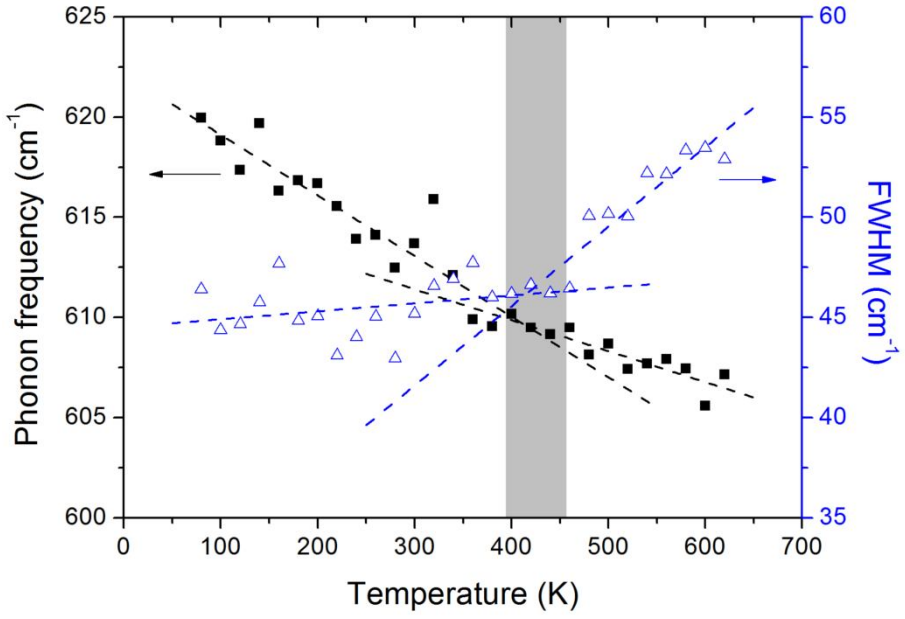

Fig. 5.35 – *Temperature dependence of the phonon frequency (solid square symbols, left axis) and linewidth (open triangular symbols, right axis). The dashed lines indicate the slope change of the temperature dependence of phonon frequency and linewidth around* T_{FE}.

To bring additional evidence for this transition, X-ray diffraction data (in particular symmetric $\theta/2\theta$ diffractograms, see Sect. 2.2.1) were recorded as a function of temperature (between 200 K and 470 K). We recall here that $(Bi_{0.9}La_{0.1})_2NiMnO_6$ thin films grow completely strained on $SrTiO_3$ (see Sect. 5.2.2). Therefore, as the film are in-plane clamped to the substrate all evidence related to structural changes lies in the out-of-plane lattice parameter, which was obtained from the corresponding angular position of the (003) Bragg reflexions of the θ/2θ diffractograms at each temperature (Appendix A).

Fig. 5.36 (left axis) shows the temperature dependence of the out-of-plane lattice parameter of both $(Bi_{0.9}La_{0.1})_2NiMnO_6$ film and $SrTiO_3$ substrate (corresponding to c_{BLNM} and c_{STO}, respectively). Due to thermal expansion, $c_{STO}(T)$ linearly increases over the full temperature range with a thermal expansion coefficient, $\alpha_{STO} \sim 4.2 \times 10^{-5}$ Å/K. In contrast, $c_{BLNM}(T)$ is non monotonic and clearly displays a kink at about 450 K pointing to a phase transition occurring at this temperature. A straight line is plotted to emphasis the fact that the film lattice parameter, below 450 K, gradually deviates from the normal linear behavior.

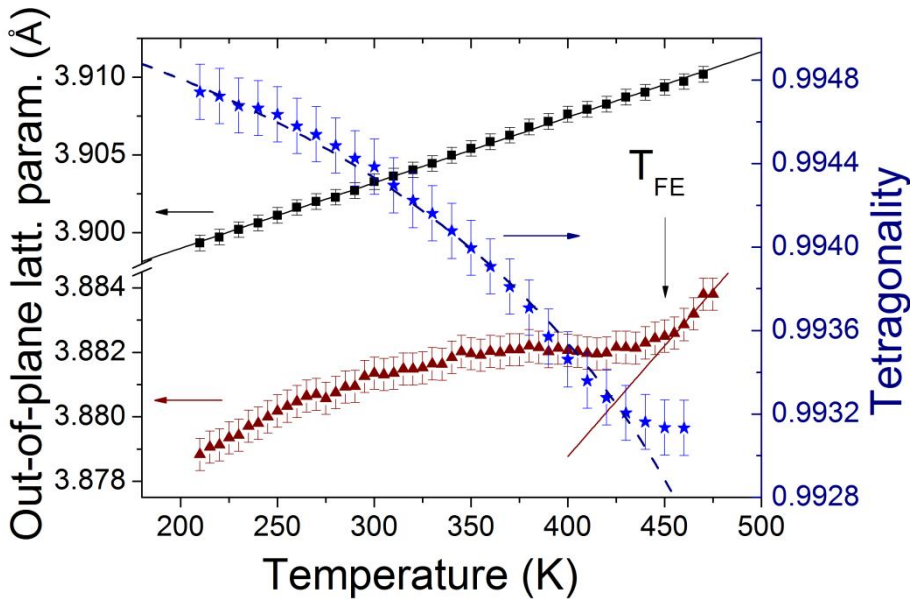

Fig. 5.36 – *(left axis) Temperature dependence of the out-of-plane lattice parameter of both substrate (solid square symbol) and $(Bi_{0.9}La_{0.1})_2NiMnO_6$ thin film (solid triangle symbol); (right axis) Temperature dependence of the tetragonality of $(Bi_{0.9}La_{0.1})_2NiMnO_6$ thin films (star symbols). The dashed line shows the fitting using Eq. 5.6.*

This transition can be even better appreciated in the tetragonality ratio $c_{BLNM}(T)/a_{BLNM}(T)$, where $a_{BLNM}(T)$ stands for the in-plane lattice parameter of $(Bi_{0.9}La_{0.1})_2NiMnO_6$ film. In computing this ratio it is assumed that $(Bi_{0.9}La_{0.1})_2NiMnO_6$ film remains coherent on the $SrTiO_3$ substrate and thus $a_{BLNM}(T) = a_{STO}(T)$, where $a_{STO}(T)$ denotes the in-plane lattice parameter of $SrTiO_3$; from the cubic structure of $SrTiO_3$ it follows that $a_{STO}(T) = c_{STO}(T)$ and thus $a_{BLNM}(T) = c_{STO}(T)$. These tetragonality values are depicted in Fig. 5.36 (right axis). The enhancement of the $(c/a)_{BLNM}(T)$ is very apparent at low temperatures and gradually reduced when approaching 450 K. This behaviour is obviously consistent with having a ferroelectric phase below this temperature, in which the spontaneous polarization induces an enlargement of the out-of-plane lattice parameter [34, 36, 40, 41, 46]. The tetragonality ratio $c_{BLNM}(T)/a_{BLNM}(T)$ data can be well fitted (dashed line through the data) by using:

$$\begin{cases} c_{BLNM}(T) = c^0_{BLNM} + \alpha_{BLNM} \times T + B \times \sqrt{T^* - T} \\ a_{BLNM}(T) = a_{STO}(T) = a^0_{STO} + \alpha_{STO} \times T \end{cases} \quad (5.5)$$

where $\alpha_{STO} \times T$ and $\alpha_{BLNM} \times T$ terms correspond to the thermal expansion and a^0_{STO} and c^0_{BLNM} the extrapolation at 0 K of the lattice parameter of $SrTiO_3$ and $(Bi_{0.9}La_{0.1})_2NiMnO_6$, respectively. The $B \times \sqrt{T^* - T}$ expansion term of the out-of-plane lattice parameter, where B and T^* are fitting constants, has been proved to be accomplished in ferroelectric perovskites driven by the stereochemical activity of the lone-pair of Bi, like $BiFeO_3$, when spontaneous polarisation develops at temperatures below T^* [40]. The excellent fitting of our data to this function, where T^* is found to be 450 K, gives an additional hint on the nature of the transition observed at T^*, which we, thus, identify with the ferroelectric transition temperature of $(Bi_{0.9}La_{0.1})_2NiMnO_6$ thin films.

Therefore, both x-ray diffraction and Raman spectroscopy data indicate that the ferroelectric phase transition in $(Bi_{0.9}La_{0.1})_2NiMnO_6$ thin films occurs around $T_{FE} \sim 450$ K (note that Raman technique does not allow determining the critical temperature value with a good accuracy), which is somewhat reduced compared to bulk Bi_2NiMnO_6 one (~ 485 K [5]). This reduction could just be due to the partial replacement of Bi by La; however, as a matter of fact, in Bi_2NiMnO_6 films on $NdGaO_3$, a similar T_{FE} has been reported thus suggesting that strain rather than Bi-La substitution is the dominant effect on the T_{FE} reduction. However, having said that, it is remarkable that the sensitivity of these double perovskites on strain is much more modest than typically found in other ferroelectric, such as $BaTiO_3$, whose Curie temperature is strongly dependent on strain [36]; indeed, in a 0.70 % of tensile strain, as found here, produces a change of T_{FE} by about 150 K [36]. Yet it may be enlightening to notice that in $BiFeO_3$ T_{FE} remains also roughly unchanged for 0.70% of tensile strain [40]. Thus, it seems to be reasonable to argue that the ferroelectric mechanism might play a role in the strain sensitivity of the ferroelectric properties. Note that the ferroelectric order in Bi-driven ferroelectric perovskites, like $BiFeO_3$ and Bi_2NiMnO_6, is of electronic nature (displacement of the lone-pair electrons away from the centrosymmetric positon), whereas conventional ferroelectrics, like $BaTiO_3$, consist of ionic displacements of d^0-cations, which are likely to be, the latter, much more sensitive to lattice distortions.

5.6 Electric and magnetoelectric properties

5.6.1 Background

One of the interesting features multiferroic materials may exhibit is the so-called magnetoelectric coupling (as explained in Sect. 1.1.3), which consists of the coupling between the ferroelectric and the magnetic order. Due to the poor insulating features of many multiferroics, an extensive route to investigate the magnetoelectric character consists of studying the effect on the dielectric permittivity, ε, of changes of the magnetic state of the magnetic layer, either by applying a magnetic field, the so-called magnetocapacitance (or magnetodielectric response), $\varepsilon(H)$, or by searching for variations of ε in the temperature dependence, $\varepsilon(T)$, in the vicinity of the magnetic transition temperature (see Sect. 1.1.3).

However, determining the intrinsic dielectric permittivity, and therefore the real dielectric response of multiferroics, can be, by itself, an arduous task, as explained in Sect. 3.2.3 and as noticed in $BiMnO_3$ thin films (Sect. 4.4.4). First, as observed in many dielectrics, extrinsic contributions, such as parasite capacitances formed at the interface between the dielectric film and the electrodes or at the grain boundaries in ceramic samples, very often account for the apparent colossal dielectric constants (see Sect. 3.2.3). Second, the leaky behavior of most multiferroic materials may give rise to apparent large magnetodielectric response, when in reality it might not be the permittivity but the resistivity of the dielectric material that is changing either on applying a magnetic field or with temperature (see Sect. 3.2.3 and 3.2.4). Moreover, the resistivity of $(Bi,La)_2NiMnO_6$ is still to be addressed, which is of the highest relevance in double-perovskites due to the multivalent configuration of the B-cations that may greatly enhance the conductivity of these materials.

These difficulties become apparent when comparing dielectric data reported for double-perovskite thin films. It has been reported that La_2NiMnO_6 films show temperature (T) dependence and frequency (ν) dependence of the dielectric permittivity $\varepsilon(T,\nu)$ [47], which was attributed to temperature-dependent electric dipole relaxation.

Yet the reported $\varepsilon(T,v)$ curves [Fig. 5.37 (a)] resemblances, to a large extent, to the simulations of a Maxwell-Wagner type of relaxation described in Sect. 3.2.3 (see Fig. 3.10 in Sect. 3.2.3), the behaviour of which was ascribed to the formation of a parasite capacitance at the interface electrode-dielectric and the temperature dependence of the resistivity of the dielectric film. On the other hand, the reported $\varepsilon(T)$ for Bi_2NiMnO_6 thin films at 100 kHz [30] shows a modest value ($\varepsilon \sim 50$) at low temperatures whilst an unexpected sharp increase takes place at 150 K ($\varepsilon \sim 450$) [Fig. 5.37 (b)], which was claimed to be due to the set of the magnetic order. Still, this $\varepsilon(T)$ could again be reproduced by a Maxwell-Wagner type of relaxation, as shown in our simulations in Fig. 3.10 (Sect. 3.2.3). Similar $\varepsilon(T)$ features were reported for Bi_2NiMnO_6/La_2NiMnO_6 multilayers [48]. Instead, a soft monotonous increase of ε along T was reported for Bi_2NiMnO_6 thin films at 1MHz [8], where ε varies from 145 to 155 in the range of temperatures comprised between 20 K to 200 K. Having said that, though, it is worth mentioning that the dielectric permittivity of bulk Bi_2NiMnO_6 greatly differs to what is reported in thin films, as found to be 200 around room temperature, with the sharp increase around 485 K corresponding to the ferroelectric transition temperature [5].

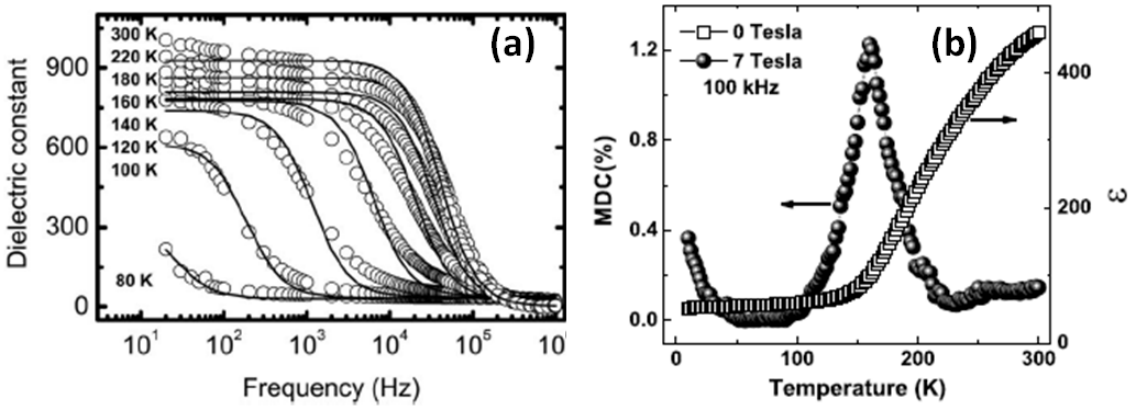

Fig. 5.37 – (a) *Frequency dependence of the dielectric permittivity of La_2NiMnO_6 thin films at different temperatures reproduced from Ref. 47;* **(b)** *Temperature dependence of the dielectric permittivity (right axis) and magnetocapacitance (left axis) of Bi_2NiMnO_6 thin films reproduced from Ref. 30.*

Regarding the magnetoelectric coupling, Bi_2NiMnO_6 thin films were reported to exhibit ~1% magnetocapacitance [(C(H)-C(0))/C(0)] [30]. Yet, as demonstrated in sect.

3.2.4, this magnetocapacitance effect may easily arise from magnetoresistance effect, which was neither elucidated in that report.

The lack of a thorough frequency and temperature dependent dielectric study in the literature, together with the absent deconvolution between contributions of the resistive part and the dielectric part, inhibits from discerning whether the reported dielectric and magnetoelectric properties of $(Bi,La)_2NiMnO_6$ thin films were intrinsic or extrinsic, thus claiming for a new regard on data and conclusions. Here in this section we performed an exhaustive study of the dielectric properties of $(Bi_{0.9}La_{0.1})_2NiMnO_6$ thin films, in which temperature dependent impedance spectroscopy (see Sect. 3.2) was used to disentangle extrinsic and intrinsic contributions to the measured permittivity. At the end of the section, the intrinsic magnetoelectric response of $(Bi_{0.9}La_{0.1})_2NiMnO_6$ thin films is obtained by deconvoluting magnetodielectric and magnetoresistive effect. To performed the dielectric measurements, Pt/$(Bi_{0.9}La_{0.1})_2NiMnO_6$/Nb:SrTiO3 capacitors were fabricated (see Sect. 3.1). $(Bi_{0.9}La_{0.1})_2NiMnO_6$ samples were grown at the optimised conditions for single-phase formation (*i.e.* at 620 ºC and 0.5 mbar of O_2 pressure). The thickness of the set of samples was comprised between 100 and 110 nm.

5.6.2 Complex dielectric constant and ac conductivity. Qualitative analysis

Fig. 5.38 depicts the temperature dependence of the dielectric permittivity at different frequencies, assuming that the measured capacitance is only due to the dielectric response of $(Bi_{0.9}La_{0.1})_2NiMnO_6$ film, *i.e.* $C = \varepsilon'\varepsilon_0 A/(2t)$ (see chapter 3). The dielectric permittivity ε' increases as temperature rises, with a well visible step-like behaviour. The step-like feature moves toward higher temperatures on increasing frequency, similar to what was reported for La_2NiMnO_6 thin films [47]. Moreover, the reported dielectric permittivity of Bi_2NiMnO_6 thin films measured at 100 kHz and at 1 MHz of Ref. 30 and Ref. 8 shows a clear resemblance to our data in Fig. 5.38 for 100 kHz and 1 MHz, respectively. Nonetheless, the fact that ε' at high temperatures is clearly frequency-dependent and it strongly reduces when frequency is increased, suggests that extrinsic effects are contributing to the dielectric response (see chapter 3).

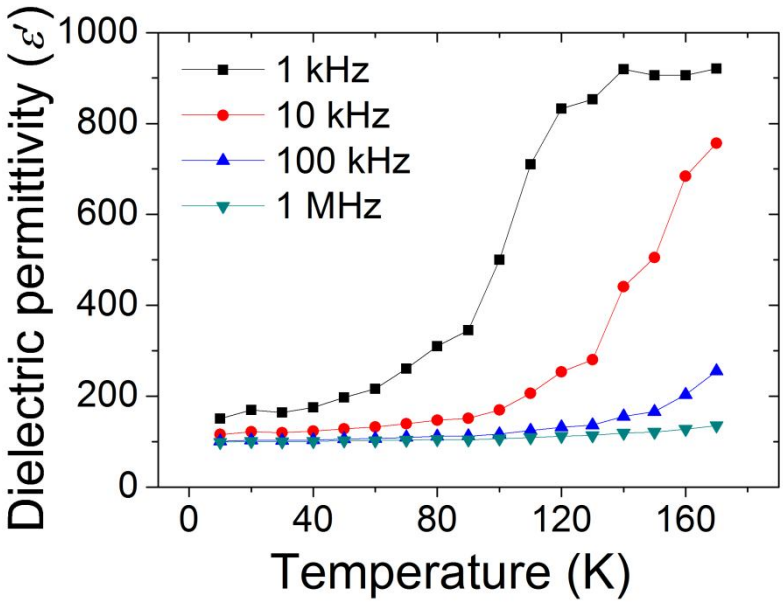

Fig. 5.38 – *Temperature dependence of the dielectric permittivity of* $Pt/(Bi_{0.9}La_{0.1})_2NiMnO_6/Nb:SrTiO_3$ *system measured at different frequencies.*

In order to assess the frequency response, the complex representation of the dielectric constant, $\varepsilon^* = \varepsilon' - i\varepsilon''$, will be used (see Sect. 3.2.2). Fig. 5.39 (a) and (b) depict the frequency dependence of the effective capacitance [$C = \varepsilon'\varepsilon_0 A/(2t)$] and the loss tangent ($\tan\delta = \varepsilon''/\varepsilon'$), respectively, of $Pt/(Bi_{0.9}La_{0.1})_2NiMnO_6/Nb:SrTiO_3$ capacitors at different temperatures. The measured capacitance [Fig. 5.39 (a)] shows the existence of two frequency regimes, where the $C(v)$ [and thus the permittivity $\varepsilon'(v)$] is rather constant, separated by a step-like region which is accompanied by a peak of $\tan\delta(v)$ and thus the imaginary part of the dielectric constant, ε'' [Fig. 5.39 (b)]. Both the step-like in $\varepsilon'(v) \sim C(v)$ and the peak of $\tan\delta(v)$ shift toward higher frequencies on increasing temperature. At first sight, this behaviour could be attributed to thermally activated Debye-like dielectric relaxation dominating the frequency dependence of $\varepsilon'(v)$ [49], with a thermal activation energy of $E_a \sim 75$ meV for temperatures higher than 100 K (Fig. 5.40) following:

$$\tau = 1/\omega_{max} = \tau_0 \exp\left[\frac{E_a}{k_B T}\right] \qquad (5.6)$$

where ω_{max} is the angular frequency ($2\pi v$) at which the peak of ε'' appears and k_B is the Botzman constant (Sect. 3.2). Nonetheless, it is demonstrated in chapter 3 that a

Maxwell-Wagner relaxation type may produce identical effects. The low-frequency dielectric permittivity, obtained assuming that the dielectric response is due to a unique capacitance, $\varepsilon' = C\cdot(2t/\varepsilon_0 A)$, is anomalous high ($\varepsilon' \sim 1000$) as shown in Fig. 5.39. In contrast, at higher frequency the capacitance is about one order of magnitude smaller, $\varepsilon' \sim 100$, which is indeed found to be in the range of that reported for Bi_2NiMnO_6 bulk materials, thus signalling a more plausible intrinsic character.

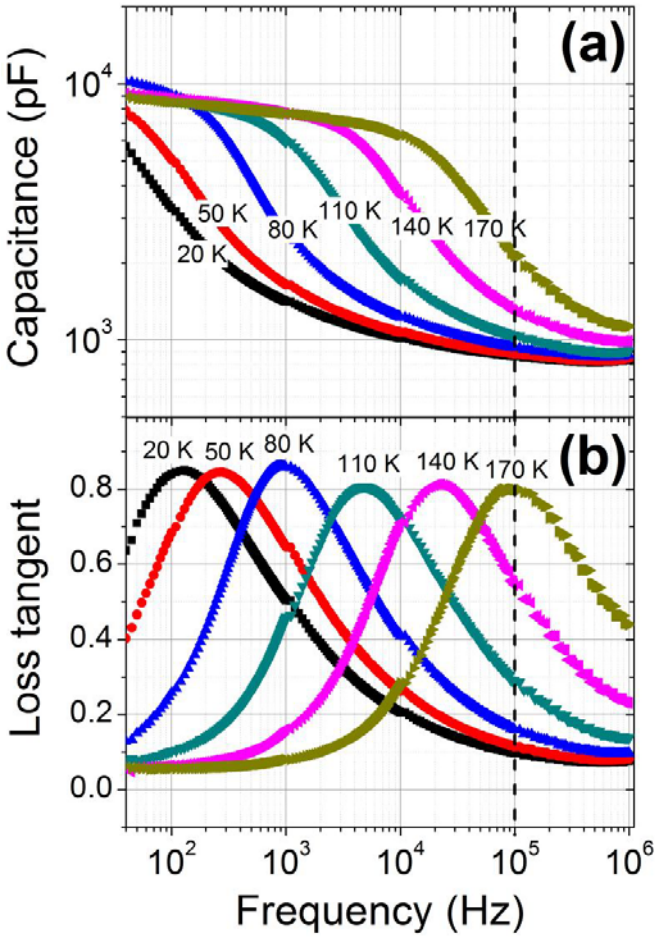

Fig. 5.39 – *Frequency dependence of the effective capacitance* **(a)** *and the loss tangent* **(b)** *of* $Pt/(Bi_{0.9}La_{0.1})_2NiMnO_6/Nb:SrTiO_3$ *capacitors measured at different temperatures. The dashed line signals the frequency at which magnetocapacitance measurements were performed (see Sect. 5.6.4)*

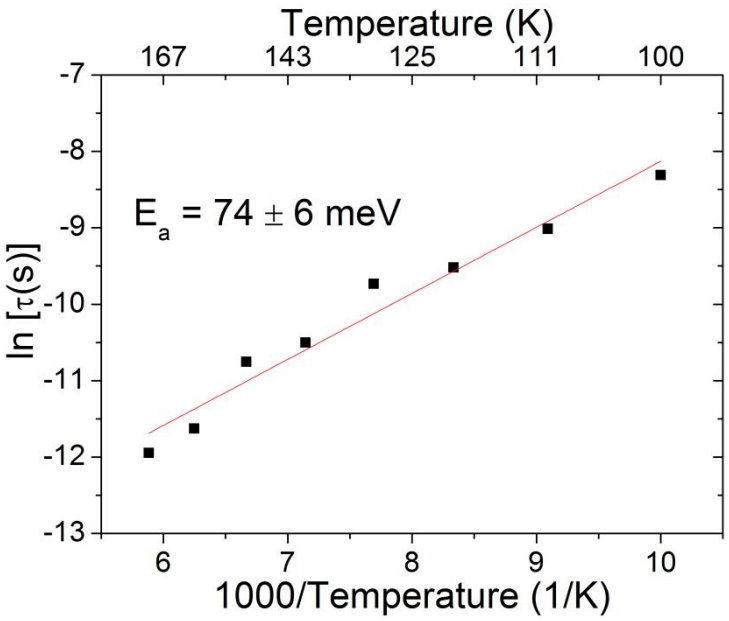

Fig. 5.40 – *Time constant, τ, in natural logarithm scale as a function of the inverse of temperature (correlated to the temperature in the upper scale).*

In the high frequency range, one can also observe [Fig. 5.39 (a)] a small but perceptible $\varepsilon'(\nu)$ dependence, which is at odds with the response of an ideal dielectric, but commonly observed in most of them and attributed to the non-ideality of the dielectric response, associated with the frequency dependent ac-conductivity σ_{ac} (see Sect. 3.2). This can be better seen in Fig. 5.41 where we plot the frequency dependence of the real part (σ') of the complex conductivity ($\sigma^* = i\omega\varepsilon_0\varepsilon^*$) at various illustrative temperatures (80 K, 110 K and 140 K). σ' should be the sum of the frequency-independent dc-conductivity (σ_{dc}), which is always present due to the leakage of the dielectric, and a frequency-dependent term σ_{ac}, that typically shows a power-law dependence on frequency $\sigma_{ac} = \sigma_0\omega^{\alpha}$, $\alpha \leq 1$ [49 – 51] (see Sect. 3.2.2). The $\sigma'(\nu)$ log-log data in Fig. 5.41 indeed shows that at high frequency there is a power-like $\sigma_{ac}(\nu)$ contribution superimposed to σ_{dc} term responsible for the flattening of $\sigma'(\nu)$ at intermediate frequencies. The extrapolation of $\sigma'(\nu)$ from the plateau towards zero frequency (dashed lines in Fig. 5.41) allows to estimate the σ_{dc} of the material or, equivalently, the resistivity at any temperature. Some illustrative values are shown in the inset of Fig. 5.41 (solid square symbols) where a rough exponential increase of resistance when lowering temperature can be appreciated. When further lowering ν,

conductivity is steeply reduced, deviating for the ideal behaviour marked in dashed lines. As shown by data in Fig. 5.41, this drop is also temperature dependent, and shifts toward higher frequencies as temperature rises. Not surprisingly, it coincides with the large enhancement of the dielectric constant shown in Fig. 5.39 (a) and the peak of ε'' [Fig 5.39 (b)].

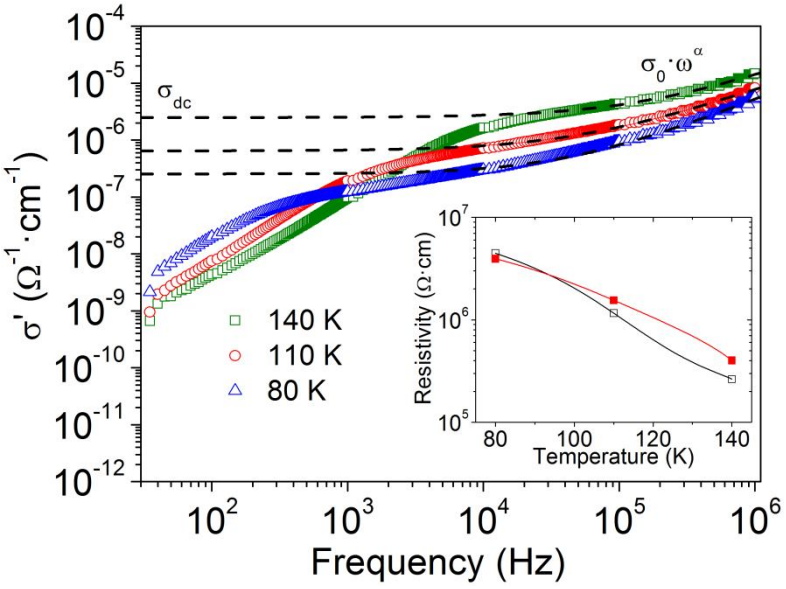

Fig. 5.41 – *Frequency dependence of σ' at different temperatures. The dashed line indicates the ideal behaviour, $\sigma' = \sigma'_{dc} + \sigma'_0\omega^{\alpha}$ (see text). The inset shows the temperature dependence of the resistivity obtained by extrapolation to zero frequency of σ' from the main panel (solid squares) and by impedance spectroscopy (open squares), the latter exposed in Sect. 5.6.3. Solid lines are visual guides.*

In the following it will be shown that both, the low-frequency region as well as the step-like region are not-intrinsic properties of $(Bi_{0.9}La_{0.1})_2NiMnO_6$ film but result from the contribution of interface effects.

5.6.3 Impedance spectroscopy. Quantitative analysis

To obtain a more quantitative insight into the dielectric response of the sample, to investigate the number of electrical responses present and to determine the intrinsic

properties of the film, complex impedance ($Z^* = Z' + iZ''$) spectroscopy was performed as described in Sect. 3.2.1.

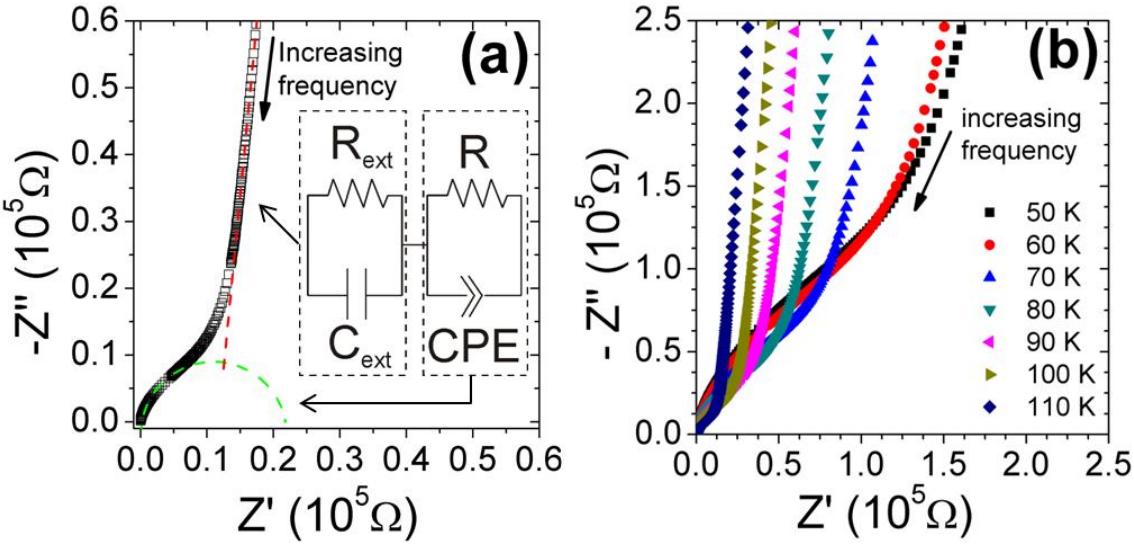

Fig. 5.42 – (a) *Impedance complex plane (–Z'' – Z' plots) from impedance data measured at 110 K. The visual guide of the dashed line indicates the two semicircles at high and low frequency. The inset sketch depicts the equivalent circuit, describing the different electrical responses present in Pt/$(Bi_{0.9}La_{0.1})_2NiMnO_6$/Nb:$SrTiO_3$ capacitors (see text for symbols).* **(b)** *–Z'' – Z' data plots measured at different temperatures.*

In Fig. 5.42 (a) illustrative *–Z''* - *Z'* plot of the impedance measured at 110 K is shown. Data signals the existence of two incomplete semicircles (marked with dashed lines as guide-to-eyes) at high and low frequency, respectively. The existence of these semicircles indicates that there are two electrical contributions to the frequency dependent impedance. Thus, as suspected, the dielectric response observed in Sect. 5.6.2 does not only come from the intrinsic dielectric properties of $(Bi_{0.9}La_{0.1})_2NiMnO_6$ film, which would produce a unique semicircle (Sect. 3.2.1). This behaviour is hence quite consistent with a Maxwell-Wagner relaxation, as explained in Sect. 3.2.3. On the other hand, it can be appreciated in Fig. 5.42 (a) that the radius of the low-frequency semicircle is much larger than the high-frequency one; this reflects that the low-frequency contribution is much more resistive than that of the high-frequency contribution. Additionally, inspection of the impedance data at different temperatures, shown in Fig. 5.42 (b), indicates that the high frequency semicircle significantly

decreases on increasing temperature, evidencing that the resistivity of the high frequency contribution decreases as temperature rises, according to data of the conductivity shown in Fig. 5.41.

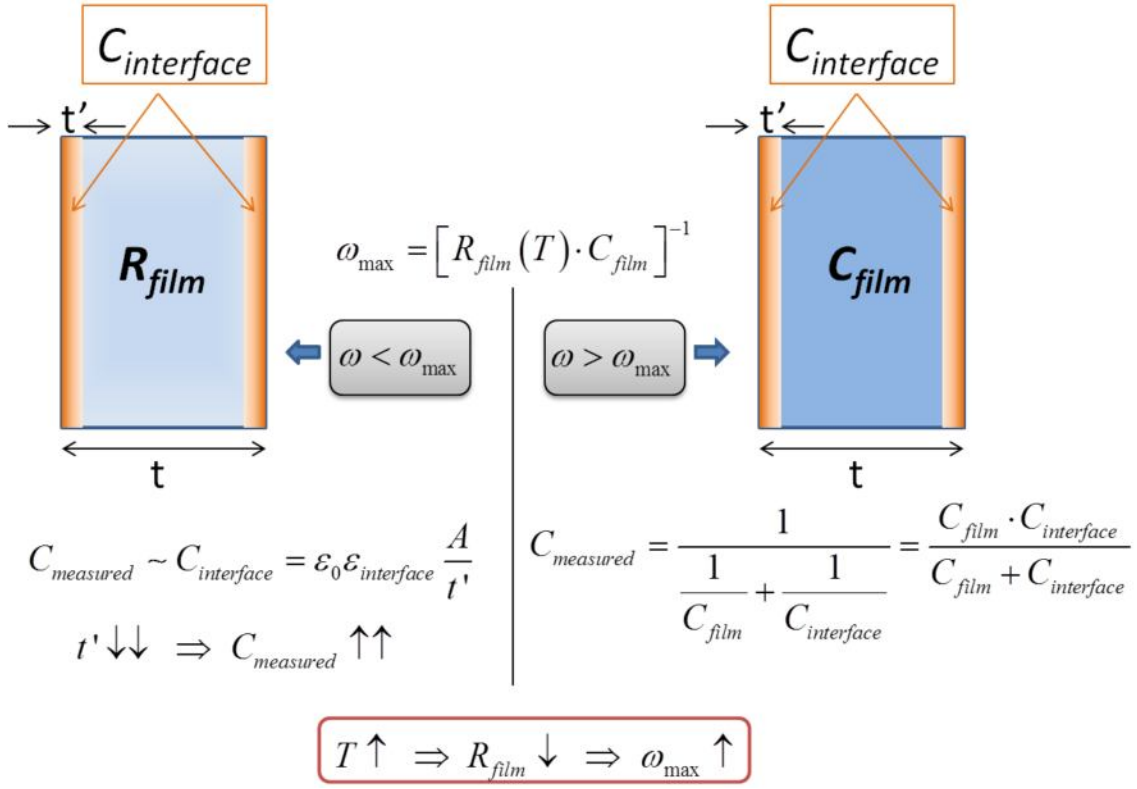

Fig. 5.43 – *Sketch of the dielectric behaviour of $(Bi_{0.9}La_{0.1})_2NiMnO_6$ thin films when the resistivity of the film and interface parasitic capacitance interferes.*

Thus, according to Fig. 5.42, the most natural explanation of the dielectric behaviour shown in section 5.6.2 comes from the formation of a capacitive layer at the interface and by the temperature dependence of the resistivity of the core of the film, as deduced in Sect. 3.2.3. The band bending caused by the difference between the work function of the metal and the electronic affinity of the dielectric gives rise to charge depletion/accumulation region at the interface [50, 52 – 54], which forms a relatively thin layer, behaving as a high resistive barrier, modelled as a capacitor, C_{ext}, and a low conductance, R_{ext}^{-1}, connected in parallel as illustrated by the circuit-model sketched in Fig. 5.42 (a). At high frequency, charge carriers have no time to follow the alternating electric field and the measured capacitance is the film and the interface capacitances in series (Fig. 5.43). However, at low frequencies, charge carriers do respond to the

electric field in the low resistive part, *i.e.* the core of the film [modelled as R inset Fig. 5.42 (a)], forming an electric current. This entails that the drop of the electric field is mostly taking place at the interface barrier, yielding the apparent high dielectric constant shown in Fig. 5.39 (a) because of the apparent reduction of the dielectric thickness (measured capacitance ~ $1/t'$) as shown in Fig. 5.43 [52]. On increasing temperature, the film resistivity decreases [so leakage, σ_{dc}, increases (Fig. 5.41)] and charge carriers can respond to faster alternation of the electric field. Thus, the apparent enhancement of the dielectric constant due to the apparent reduction of the dielectric thickness is shifting toward higher frequencies on increasing temperature, consistent with the observed temperature evolution of data of Fig. 5.39 (a). The cut-off frequency, ω_{max}, at which losses (~ε'') show a peak [Fig. 5. 39 (b)] is given by the condition $\omega_{max}(T) = [R(T)\cdot C]^{-1}$ [52] and is therefore temperature dependent. Hence, it is more reasonable to argue that the thermal activation of this apparent dielectric relaxation is driven by the temperature-dependence of the resistivity, instead of permanent dielectric dipoles suggested for La_2NiMnO_6 films [47]. Indeed, the dielectric relaxation of permanent dipole moments tends to occur at much higher frequencies, in the range of the microwaves [55], as indicated in Sect. 3.2.2.

Consequently, the impedance of $Pt/(Bi_{0.9}La_{0.1})_2NiMnO_6/Nb:SrTiO_3$ system (film + extrinsic contribution) is given by adapting of Eq. 3.10 in Sect. 3.2.3:

$$Z^*(R-CPE, R_{ext}-C_{ext}) = \frac{R}{1+R\cdot Q\cdot(i\omega)^{\alpha}} + \frac{R_{ext}}{1+i\omega\cdot R_{ext}\cdot C_{ext}} \qquad (5.7)$$

where the first and the second terms correspond to the film and the extrinsic contributions, respectively. A *CPE* element (see Sect. 3.2.1) is used for the film contribution accounting for the non-ideality of the dielectric behaviour shown in Sect. 5.6.2. Eq. 5.7 was used to fit impedance data in order to validate the proposed model. Fig. 5.44 shows some illustrative results of the fits to -Z''– Z' data at different temperatures. As observed, model (solid lines) and data match very reasonably, which is also extensive for the rest of temperatures up to 170 K. Above this temperature the low-frequency contribution dominates almost completely the experimentally available

frequency range (up to 1 MHz), and accurate extraction of the intrinsic properties (high-frequency contribution) was unfeasible.

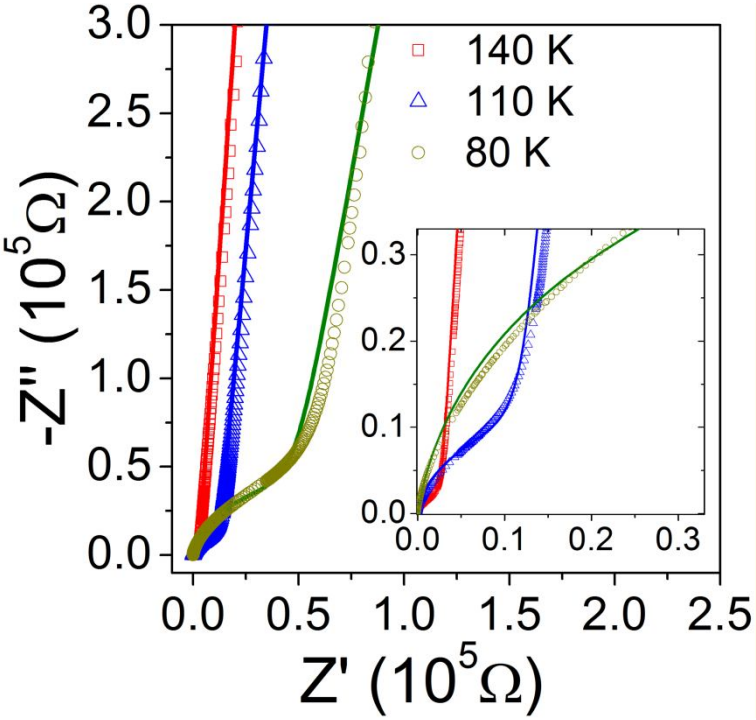

Fig. 5.44 – *Experimental data (open symbols) and fitting (solid line) using the model of Eq. 5.7 for some illustrative temperatures. The inset zooms the high-frequency region.*

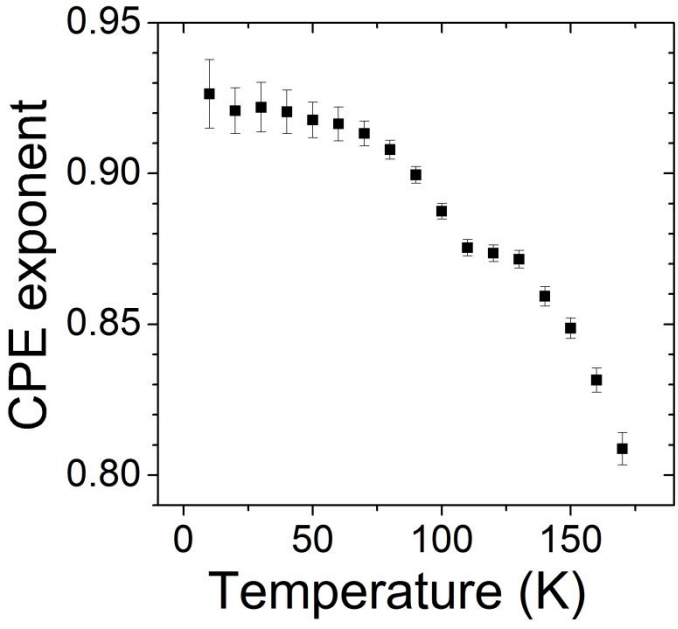

Fig. 5.45 – *Temperature dependence of the CPE exponent.*

Importantly enough, the fitting allows disentangling intrinsic and extrinsic contribution in the impedance data. The fitting values of the *R-CPE* element (*R*, *Q*, *α*), corresponding to the film contribution, are summarised in table 5.5. It is worth noticing that the CPE exponent, α, which decreases on increasing temperature (Fig. 5.45), pointing to an enhanced non-ideality of the dielectric behaviour of $(Bi_{0.9}La_{0.1})_2NiMnO_6$ films upon heating, displays a defined anomaly at about 100 K, closely coinciding with the ferromagnetic Curie temperature. From the *R*, *Q* and *α* values the intrinsic dielectric permittivity [$\varepsilon = C\cdot(2t/\varepsilon_0 A)$, where $C = (Q\cdot R)^{(1/\alpha)}/R$, see Appendix C] and resistivity [$\rho = A\cdot R/(2t)$] of $(Bi_{0.9}La_{0.1})_2NiMnO_6$ films can be computed at each temperature, as shown in Fig. 5.46 and 5.47, respectively. For the sake of clarity, in the following dielectric permittivity and resistivity are exclusively referring to the intrinsic properties of $(Bi_{0.9}La_{0.1})_2NiMnO_6$ films, obtained as aforementioned by impedance spectroscopy.

Temperature (K)	***Q*** **[$Fs^{\alpha-1}$]**	**error *Q* [%]**	***R*** **[Ω]**	**error *R* [%]**	***α***	**error *α* [%]**
10	$3.07\cdot10^{-9}$	5.0	$3.19\cdot10^{5}$	9.1	0.926	1.2
20	$3.46\cdot10^{-9}$	4.5	$1.61\cdot10^{5}$	5.7	0.921	0.8
30	$3.43\cdot10^{-9}$	4.7	$1.70\cdot10^{5}$	6.1	0.922	0.9
40	$3.52\cdot10^{-9}$	4.4	$1.41\cdot10^{5}$	5.3	0.920	0.8
50	$3.72\cdot10^{-9}$	4.1	$9.93\cdot10^{5}$	4.3	0.918	0.6
60	$3.81\cdot10^{-9}$	4.0	$8.99\cdot10^{5}$	4.0	0.916	0.6
70	$4.04\cdot10^{-9}$	3.5	$5.97\cdot10^{5}$	3.2	0.913	0.5
80	$4.31\cdot10^{-9}$	3.2	$4.35\cdot10^{5}$	2.5	0.908	0.3
90	$4.85\cdot10^{-9}$	3.2	$3.12\cdot10^{4}$	2.2	0.900	0.3
100	$5.77\cdot10^{-9}$	3.2	$2.13\cdot10^{4}$	1.8	0.888	0.3
110	$7.11\cdot10^{-9}$	3.5	$1.13\cdot10^{4}$	1.6	0.875	0.3
120	$7.51\cdot10^{-9}$	4.1	$6.98\cdot10^{4}$	1.5	0.874	0.3
130	$7.89\cdot10^{-9}$	4.5	$5.30\cdot10^{3}$	1.4	0.872	0.3
140	$1.01\cdot10^{-8}$	5.1	$2.58\cdot10^{3}$	1.3	0.859	0.4
150	$1.21\cdot10^{-8}$	5.4	$2.04\cdot10^{3}$	1.3	0.849	0.4
160	$1.67\cdot10^{-8}$	6.5	$1.15\cdot10^{3}$	1.4	0.832	0.5
170	$2.56\cdot10^{-8}$	11.6	$6.00\cdot10^{2}$	1.7	0.809	0.7

Table 5.5 – *Fitting results of the high-frequency R-CPE element, sketched in Fig. 5.43 (a).*

The dielectric permittivity of $(Bi_{0.9}La_{0.1})_2NiMnO_6$ films (Fig. 5.46) is found to be temperature independent, as expected for a ferroelectric material far below its ferroelectric transition temperature [~450 K (Sect. 5.5.3)]. It is rewarding to notice that

the value of permittivity (~ 220) is in close agreement with the reported bulk value (~200) [5]. It is also worth noting that around the magnetic ordering temperature T_{FM} (~100 K) there is no significant deviation of permittivity; however, its derivative $d\varepsilon/dT$ shown in Fig. 5.46 (right axis), seems to indicate a subtle variation at a temperature close to the magnetic transition temperature, much as the anomaly at 100 K of the exponent α (Fig. 5.45), suggesting a possible small influence of the magnetic order and thus magnetoelectric response.

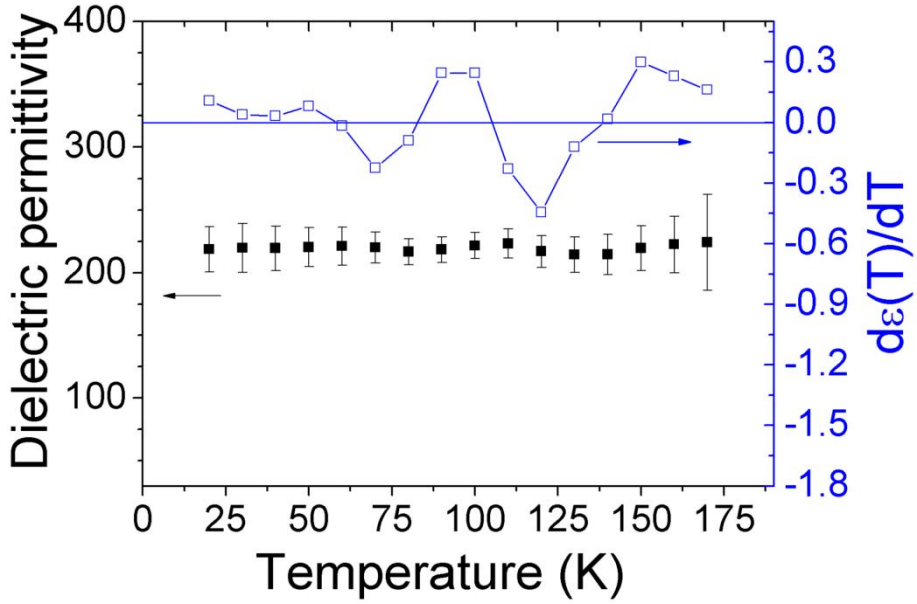

Fig. 5.46 – *Temperature dependence of the intrinsic dielectric permittivity of $(Bi_{0.9}La_{0.1})_2NiMnO_6$ films (left axis) and dielectric permittivity derivative (right axis).*

The temperature dependence of the resistivity, $\rho(T)$, (Fig. 5.47) shows a semiconductor-like behaviour, similar to what has been reported for other multiferroic perovskite oxides [53]. The resistivity decreases from ~10^8 Ω·cm at 20 K to ~10^4 Ω·cm at 170 K. The resistivity values obtained by impedance spectroscopy and σ_{dc} or, equivalently, the resistivity estimated by extrapolation of $\sigma'(\nu)$ from the plateau towards zero frequency (dashed lines in Fig. 5.41) are, as expected, in good agreement, as shown by some illustrative values in Fig. 5.41 (inset). At temperatures above 100 K, the resistivity seems to behave thermally activated, following an Arrhenius law, $\rho = \rho_0 \exp(E_a/k_BT)$, (dashed line in Fig. 5.47) with an activation energy (71 ± 5 meV). This value is remarkable close to the one obtained from Eq. 5.6, bearing out the claim stated

before that the thermal activation of the apparent dielectric relaxation observed in Sect. 5.6.2 is driven by the temperature dependence of the resistivity of $(Bi_{0.9}La_{0.1})_2NiMnO_6$ film.

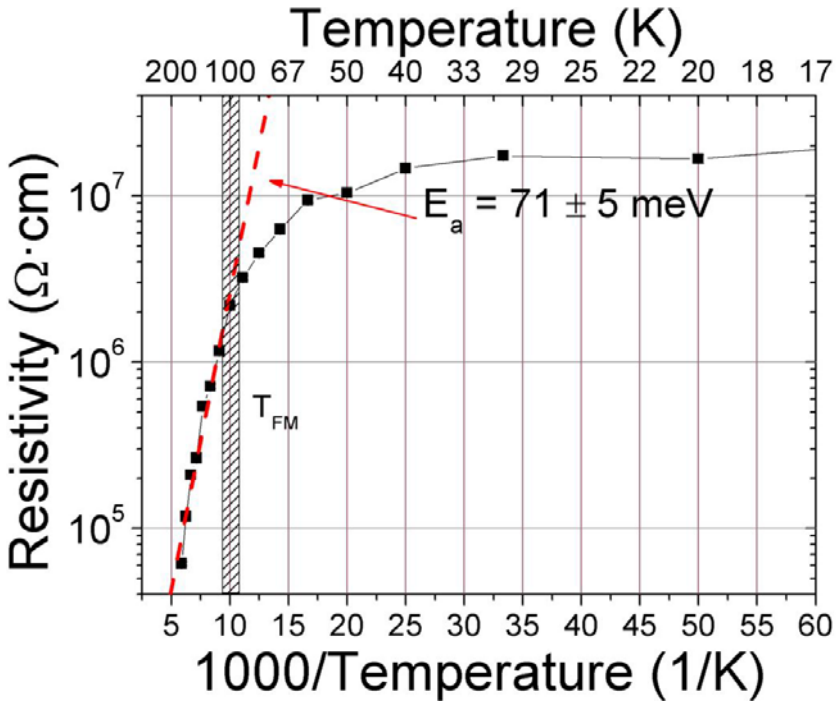

Fig. 5.47 – *Temperature dependence of the intrinsic resistivity of $(Bi_{0.9}La_{0.1})_2NiMnO_6$ films. The dashed line shows the Arrhenius fitting. Dashed region indicates the magnetic Curie temperature.*

Within the simplest picture, electron transport in $(Bi_{0.9}La_{0.1})_2NiMnO_6$ is related to electron hopping among dissimilar electronic configuration of the B-cations, *i.e.* Ni^{2+} and Mn^{4+}, which would entail a valence band formed by Ni^{2+} e_g spin up and the conduction band formed by Mn^{4+} e_g spin up (Fig. 5.48). The low activation energy found suggests that $(Bi_{0.9}La_{0.1})_2NiMnO_6$ films possess a small band gap, behaving more similar to a semiconductor material. Instead, for $BiMnO_3$ thin films (Sect. 4.4), a larger activation energy is found (E_a ~ 200 meV). Therefore, it might be possible that multiferroic double-perovskite materials may suffer from a poorer insulating character with regard to their counterpart single-perovskites, favoured by the dissimilar electronic configuration of the B-cations and their B-site order, which shrinks the gap. Not surprisingly, small activation energy was also reported for B-site ordered double-perovskite La_2NiMnO_6 thin films (E_a ~ 32 meV) [47]. However, it is worth mentioning

that the observed activation energy is noticeble much smaller than the predicted band gap in Bi_2NiMnO_6 (~200- 500 meV) [32, 33].

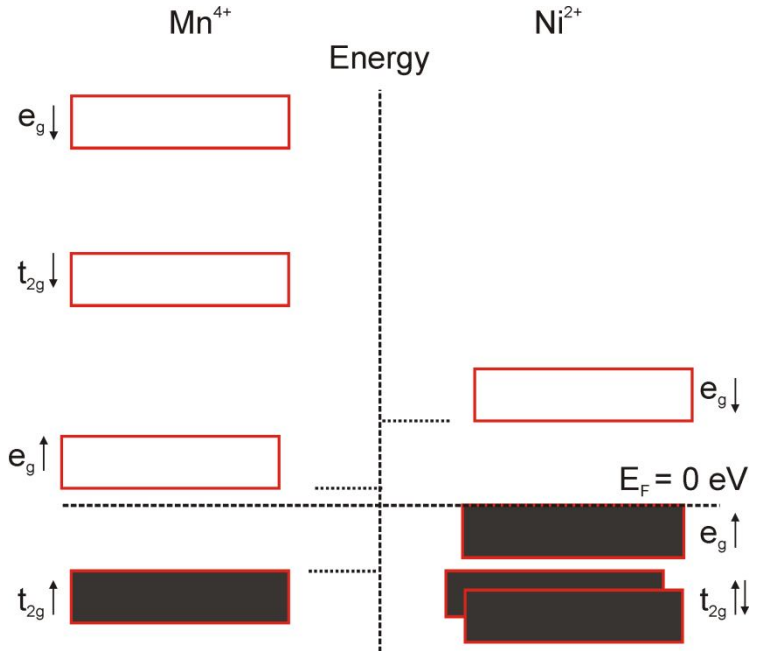

Fig. 5.48 – *Sketch of the band diagrams of Ni^{2+} and Mn^{4+} in Bi_2NiMnO_6, adapted from the density of states predicted for Bi_2NiMnO_6 in Ref. [5].*

A different behaviour is found, though, at lower temperature ($T < 100$ K). As shown in Fig. 5.47, in this temperature range the resistivity deviates from the Arrhenius law, reflecting a change in the predominant conduction mechanism. Alternative conduction mechanism, such Mott's Variable-Range-Hopping (VRH) or Efros and Shklovskii VRH conduction mechanisms [$\rho = \rho_0 \exp(T_0/T^{1/\gamma})$, $\gamma = 4$ or 2, respectively] have been considered [56 - 60], as shown in Fig. 5.49. It is found that none of these models allow describing satisfactorily the whole temperature range, either. Moreover, VRH model, in which electron hopping is not produced between first neighbour ions but there is an optimum hopping distance that maximise the hopping probability [60], is proposed for either disordered systems or with doping impurities, in which localised states are found. As this case is not expected in $(Bi,La)_2NiMnO_6$ films, the conduction mechanism shown in Fig. 5.47 has more physical meaning. In any event, data in Fig. 5.47 suggests either a change of the transport mechanism or the relevant energy for activated transport occurring at about 100 K. Interesting enough, at this temperature the film becomes

ferromagnetic. Thus, it might be quite plausible that the magnetic order may have some influence in the conduction mechanism, especially if the electron transport is expected to be driven by electron hopping between the *d*-orbitals of the magnetic ions, Ni^{2+} and Mn^{4+}.

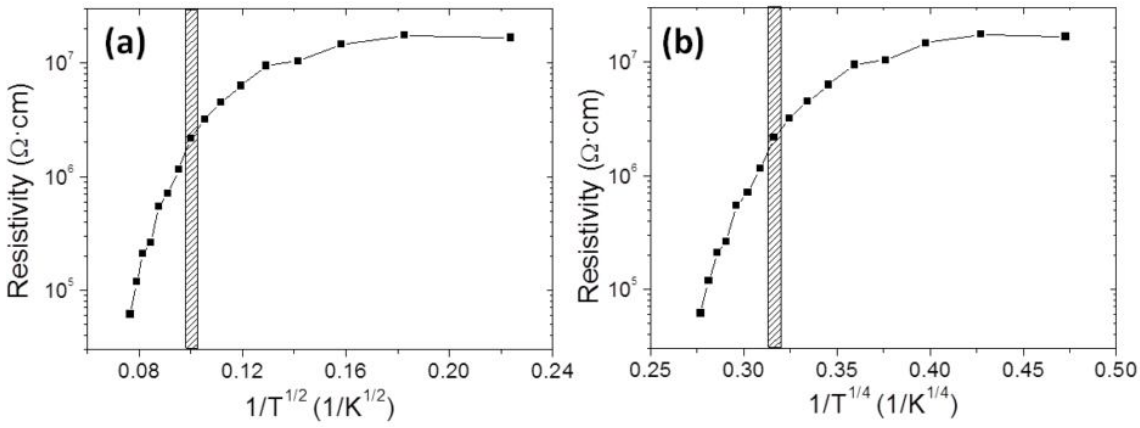

Fig. 5.49 – *Resistivity as a function of (1/Tempereture)$^{1/\gamma}$, being γ =2* **(a)** *and γ = 4* **(b)**. *The dashed region indicates the ferromagnetic Curie temperature.*

5.6.4 Magnetoelectric response

In order to detect any magnetoelectric effect in the dielectric properties of $(Bi_{0.9}La_{0.1})_2NiMnO_6$ films, dielectric measurements were performed under the presence of a magnetic field and without. The magnetic dependence of the effective capacitance, $C(H)$, of Pt/$(Bi_{0.9}La_{0.1})_2NiMnO_6$/Nb:$SrTiO_3$ system, assuming that the measured capacitance is only due to the dielectric response of $(Bi_{0.9}La_{0.1})_2NiMnO_6$ film as exposed in Sect. 5.6.2, $C = \varepsilon' \varepsilon_0 A/(2t)$, was obtained at 100 kHz for different temperatures. The magnetocapacitance, defined as MC = $[C(H)-C(0)]/C(0)$ as described in Sect. 3.2.4, is shown in Fig. 5.50 (a) for several temperatures. The MC curves are very much similar to the magnetocapacitance reported for Bi_2NiMnO_6 thin films [30]. It turns out that, at a given magnetic field, the temperature dependence of the magnetocapacitance, MC(T), displays a non-monotonic dependence on temperature, as shown in Fig. 5.50 (b), attaining a maximum (4.5 % at 8 T) around 140 K. Data shows a clear resemblance to the MC(T) reported for Bi_2NiMnO_6 films [30], shown in Fig. 5.37 (b) (left axis).

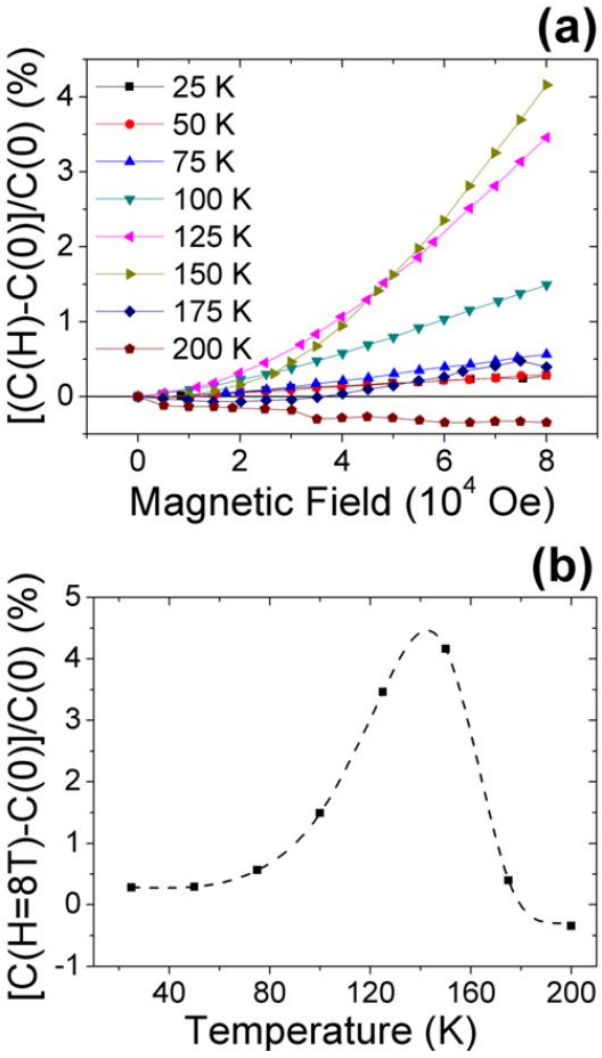

Fig. 5.50 – (a) *Magnetocapacitance of Pt/$(Bi_{0.9}La_{0.1})_2NiMnO_6$/Nb:STO system measured at 100 kHz at different temperatures.* **(b)** *Temperature dependence of the magnetocapacitance of Pt/$(Bi_{0.9}La_{0.1})_2NiMnO_6$/Nb:$SrTiO_3$ system at H = 8 T and 100 kHz. Dashed line are guide-to-eyes.*

Nonetheless, the maximum of the magnetocapacitance effect occurs at a temperature substantially above the ferromagnetic transition temperature (~100 K) where the largest magnetoelectric response due to the coupling between the ferroelectric and magnetic order is to be expected [61]. Moreover, at 100 kHz, the $\varepsilon'(\nu)$ and $\tan\delta(\nu)$ data in Fig. 5.39 indicate that the temperature range in which MC(T) shows the sharp increase coincides with the step-region in ε'(ν = 100 kHz) [marked with dashed line, Fig. 5.39 (a)] separating the two frequency regimes: the extrinsic low-frequency and the intrinsic high-frequency dielectric constant regimes. Indeed, at 100 kHz, for temperatures in which ε' is found either on the low-frequency plateau or the high-

frequency plateau [Fig. 5.39 (a), marked with the dashed line], MC(H) is almost inexistent (Fig. 5.50). This suggests that the observed large MC effect may occur due to the shift of the step-like dielectric response because of the magnetic-field inducing change in film resistivity. As demonstrated in Sect. 3.2.4, a Maxwell-type of relaxation, in which the film resistivity changes on applying a magnetic field, $\rho(H)$, would produce identical effects, without having a magnetoelectric coupling between the ferroelectric and magnetic order. In particular, if $\rho(H)$ decreases on increasing H, a positive MC peak is expected, as shown in the simulation of Fig. 3.13 (Sect. 3.2.4), reproducing data of Fig. 5.50 (b). As a matter of fact, $\rho(T)$ curve of $(Bi_{0.9}La_{0.1})_2NiMnO_6$ film shown in Fig. 5.47 show clear indications of the magnetic order having some influence.

Hence, as exposed in Sect. 5.6.3, magneto-impedance spectroscopy was performed in order to disentangle extrinsic and intrinsic effects, in particular, in order to deconvolue magnetoresistive effects from that coming from the genuine coupling of the two ferroic orders. Two set of impedance data were collected following the same procedure described in Sect. 5.6.3, one without applying a magnetic field and one with the presence of a magnetic field (H = 0 T and H = 9 T), in a temperature range close to the ferromagnetic transition temperature (80 K – 130 K). In both cases, as expected, two incomplete semicircles were observed in the $-Z''$-Z' plots as shown in Fig. 5.42 (a), and with the same temperature dependence as shown in Fig. 5.42 (b). Fitting both set of data with Eq. 5.7, *i.e.* using the same impedance circuit model of Sect. 5.6.3, the fitting values R, Q and α of the *R-CPE* element related to the intrinsic impedance response of $(Bi_{0.9}La_{0.1})_2NiMnO_6$ film can be obtained for each temperature, with and without an applied magnetic field. From these values it is computed the intrinsic dielectric permittivity, $\varepsilon(T, H)$, and resistivity, $\rho(T, H)$, of $(Bi_{0.9}La_{0.1})_2NiMnO_6$ film, as described in Sect. 5.6.3. In the following, for the sake of simplicity, dielectric permittivity and resistivity will exclusively refer to the intrinsic dielectric and resistive properties of $(Bi_{0.9}La_{0.1})_2NiMnO_6$ film.

Fig. 5.51 (a) shows the temperature dependence of the dielectric permittivity with and without an applied magnetic field, $\varepsilon(T, H = 0\ T)$ and $\varepsilon(T, H = 9\ T)$. Despite the large applied magnetic field, no significant change is observed within the experimental error. On the contrary, when plotting in Fig. 5.51 (b) the magnetoresistance of $(Bi_{0.9}La_{0.1})_2NiMnO_6$ film, *i.e.* $MR = [\rho(T, H = 9\ T) - \rho(T, H = 0\ T)]/\rho(T, H = 0\ T)$, the

resistivity is found to decrease noticeably when applying a large magnetic field. This fact provides support to the claim above mentioned that the magnetocapacitance shown in Fig. 5.50 arise from the magnetoresistive character of $(Bi_{0.9}La_{0.1})_2NiMnO_6$ film instead of a genuine coupling of the two ferroic orders. Hence, it is reasonable to extend this conclusion for the reported magnetocapacitance in (Bi,La)2NiMnO6 compounds. Taking into account that the coupling between the ferroelectric and ferromagnetic order would entail a change in the dielectric permittivity following $\Delta\varepsilon \sim \alpha_{ME}M^2$ (Sect. 1.1.3), the negligible $\varepsilon(H)$ perturbation points out to a weak coupling, if any, between the two ferroic orders, the causes of which are very likely related to the different mechanisms of the two ferroic orders (see Sect. 1.2) and their different energy scales ($T_{FM} \sim 100$ K, whereas $T_{FE} \sim 450$ K) in $(Bi,La)_2NiMnO_6$ compounds.

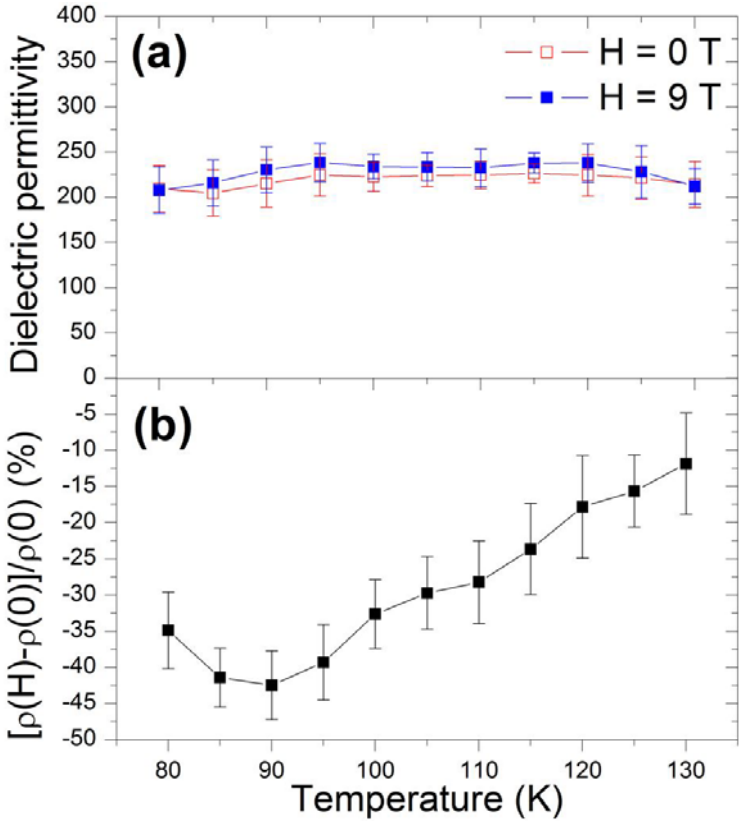

Fig. 5.51 – (a) *Temperature dependence of the intrinsic dielectric permittivity of $(Bi_{0.9}La_{0.1})_2NiMnO_6$ films obtained by magneto-impedance spectroscopy for H = 0 T (open symbols) and H = 9 T (solid symbols).* **(b)** *Magnetoresistance of $(Bi_{0.9}La_{0.1})_2NiMnO_6$ films obtained by magneto-impedance spectroscopy (for H = 0 T and H = 9 T).*

References

[1] A. F. Moreira dos Santos, A. K. Cheetham, W. Tian, X. Pan, Y. Jia, N. J. Murphy, J. Lettieri and D. G. Schlom, Appl. Phys. Lett. **84** 91 (2004).

[2] S. Fujino, M. Murakami, S. –H. Lim, L. G. Salamanca-Riba, M. Wuttig and I. Takeuchi, J. Appl. Phys. **101** 013903 (2007).

[3] M. Gajek, M. Bibes, F. Wyczisk, M. Varela, J. Fontcuberta and A. Barthélémy, Phys. Rev. B **75** 174417 (2007).

[4] S. Havelia, S. Wang, M. Skowronski and P. A. Salvador, J. Appl. Phys. **106** 123509 (2009).

[5] M. Azuma, K. Takata, T. Saito, S. Ishiwata, Y. Shimikawa and M. Takano, J. Am. Chem. Soc. **127** 8889 (2005).

[6] R. D. Shannon, Acta Cryst. **A32** 751 (1976).

[7] Y. Kobayashi, M. Shiozawa, K. Sato, K. Abe and K. Asai, J. Phys. Soc. Jpn **77** 084701 (2008).

[8] M. Sakai, A. Masuno, D. Kan, M. Hashisaka, K. Takata, M. Azuma, M. Takano and Y. Shimikawa, Appl. Phys. Lett. **90** 072903 (2007).

[9] M. Hashisaka, D. Kan, A. Masuno, M. Takano, Y. Shimakawa, T. Terashima, K. Mibu, Appl. Phys. Lett. **89** 032504 (2006).

[10] A. Masuno, M. Haruta, M. Azuma, H. Kurata, S. Isoda, M. Takano and Y. Shimakawa, Appl. Phys. Lett. **89** 211913 (2006).

[11] H. Asano, N. Koduka, K. Imaeda, M. Sugiyama and M. Matsui, IEEE Trans. Mag. **41** 2811 (2005).

[12] M. P. Singh, K. D. Truong, J. Lavardière, S. Charpentier, S. Jandl and P. Fournier, J. Appl. Phys. **103** 07E315 (2008).

[13] G. S. Bales and A. Zangwill, Phys. Rev. B **41** 5500 (1990).

[14] F. Sánchez, U. Lüders, G. Herranz, I. C. Infante, J. Fontcuberta, M. V. García-Cuenca, C. Ferrater and M. Varela, Nanotechnology **16** S190 (2005).

[15] S. Estradé, J. Arbiol, F. Peiró, I. C. Infante, F. Sánchez, J. Fontcuberta, F. de la Peña, M. Walls, C. Colliex, Appl. Phys. Lett. **93** 112505 (2008).

[16] H. Kurata and C. Colliex, Phys. Rev. B **48** 2102 (1993).

[17] S. Estradé, J. Arbiol, F. Peiró, Ll. Abad, V. Laukhin, Ll. Balcells and B. Martínez, Appl. Phys. Lett. **91** 252503 (2007).

[18] S. Estradé, J. M. Rebled, J. Arbiol, F. Peiró, I. C. Infante, G. Herranz, F. Sánchez, J. Fontcuberta, R. Córdoba, B. G. Mendis and A. L. Bleloch, Appl. Phys. Lett. **95** 072507 (2009).

[19] P. L. Potapov, S. E. Kulkova, D. Schryvers and J. Verbeeck, Phys. Rev. B **64** 184110 (2001).

[20] V. R. Galakhov, M. Demeter, S. Bartkowski, M. Neumann, N. A. Ovechkina, E. Z. Kurmaev, N. I. Lobachevskaya, Y. M. Mukovskii, J. Mitchell, D. L. Ederer, Phys. Rev. B **65** 113102 (2002).

[21] K. Kitamoto, Y. Taguchi, K. Mimura, K. Ichikawa, S. Kawamata, T. Ishida, O. Aita, J. Elect. Spect. Rel. Phenomena **137 – 140** 747 (2004).

[22] S. Madhukar, S. Aggarwal, A. M. Dhote , R. Ramesh, A. Krishnan, D. Keeble and E. Poindexter, J. Appl. Phys. **81** 3543 (1997).

[23] J. –M. Liu and C. K. Ong, Appl. Phys. Lett. **73** 1047 (1998).

[24] T. Zhao, F. Chen, H. Lu, G. Yang and Z. Chen, J. Appl. Phys. **87** 7442 (2000).

[25] W. J. Kim, W. Chang, S. B. Qadri, J. M. Pond, S. W. Kirchoefer, D. B. Chrisey and J. S. Horwitz, Appl. Phys. Lett. **76** 1185 (2000).

[26] K. Y. Yun, M. Noda, M. Okuyama, H. Saeki, H. Tabata and K. Saito, J. Appl. Phys. **96** 3399 (2004).

[27] J. B. Goodenough, *Magnetism and the Chemical Bond* (R. E. Krieger Pub. Co., Huntington, NY, 1976).

[28] J. Navarro, Ll. Balcells, F. Sandiumenge, M. Bibes, A. Roig, B. Martínez and J. Fontcuberta, J. Phys.: Condens. Matter **13** 8481 (2001).

[29] D. Serrate, J. M. de Teresa and M. R. Ibarra, J. Phys.: Condens. Matter **19** 023201 (2007).

[30] P. Padhan, P. LeClair, A. Gupta and G. Srinivasan, J. Phys.: Condens. Matter **20** 355003 (2008).

[31] M. E. Lines and A. M. Glass, *Principles and Applications of Ferroelectric and related materials*, Clarendon Press, Oxford, 1977.

[32] A. Ciucivara, B. Sahu and L. Kleinman, Phys. Rev. B **76** 064412 (2007).

[33] Y. Uratani, T. Shishidou, F. Ishii and T. Oguchi, Physica B **383** 9 (2006).

[34] A. Sambri, S. Gariglio, A. Torres Pardo, J. –M. Triscone, O. Stéphan, J. W. Reiner and C. H. Ahn, Appl. Phys. Lett. **98** 012903 (2011).

[35] J. Wang, J. B. Neaton, H. Zheng, V. Nagarajan, S. B. Ogale, B. Liu, D. Viehland, V. Vaithyanathan, D. G. Scholm, U. V. Waghmare, N. A. Spaldin, K. M. Rabe, M. Wuttig, R. Ramesh, Science **299** 1719 (2003).

[36] K. J. Choi, M. Biegalski, Y. L. Li, A. Sharan, J. Schubert, R. Uecker, P. Reiche, Y. B. Chen, X. Q. Pan, V. Gopalan, L. –Q. Chen, D. G. Schlom, C. B. Eom, Science **306** 1005 (2004).

[37] T. Kimura, G. Lawes, T. Goto, Y. Tokura, A. P. Ramírez, Phys. Rev. B **71** 224425 (2005).

[38] N. A. Perstev and B. Dkhil, Appl. Phys. Lett. **93** 122903 (2008).

[39] Z. Chen, Z. Luo, C. Huang, Y. Qi, P. Yang, L. You, C. Hu, T. Wu, J. Wang,C. Gao *et al.*, Adv. Funct. Mater. **21** 133 (2011).

[40] I. C. Infante, S.Lisenkov, B. Dupé, M. Bibes, S. Fusil, E. Jacquet, G. Geneste, S. Petit, A. Courtial, J.Juraszeck *et al.*, Phys. Rev. Lett. **105** 057601 (2010).

[41] D. G. Schlom, L. –Q. Chen, C. –B. Eom, K. M. Rabe, S. K. Streiffer and J. –M. Triscone, Annu. Rev. Mater. Res. **37** 589 (2007).

[42] M. N. Iliev, M. V. Abrashev, A. P. Litvinchuk, V. G. Hadjiev, H. Guo and A. Gupta, Phys. Rev. B **75** 104118 (2007).

[43] M. N. Iliev, P. Padhan and A. Gupta, Phys. Rev. B **77** 172303 (2008).

[44] M. N. Iliev, H. Guo and A. Gupta, Appl. Phys. Lett. **90** 151914 (2007).

[45] E. Granado, A. García, J. A. Sanjurjo, C. Rettori, I. Torriani, F. Prado, R. D. Sánchez, A. Caneiro and S. B. Oseroff, Phys. Rev. B **60** 11879 (1999).

[46] M. Dawber, N. Stucki, C. Lichtensteiger, S. Gariglio, P. Ghosez and J-M. Triscone, Adv. Mater. **19** 4153 (2007).

[47] P. Padhan, H. Z. Guo, P. LeClair and A. Gupta, Appl. Phys. Lett. **92** 022909 (2008).

[48] P. Padhan, P. LeClair, A. Gupta, M. A. Subramanian and G. Srinivasan, J. Condens. Matter **21** 306004 (2009).

[49] A. K. Jonscher, *Dielectric Relaxations in Solids*, Chelsea Dielectrics Press, London, 1983.

[50] P. Lunkenheimer, V. Bobnar, A. V. Pronin, A. I. Ritus, A. A. Volkov and A. Loidl, Phys. Rev. B **66** 052105 (2002).

[51] R. Schmidt and A. W. Brinkman, J. Appl. Phys. **103** 113710 (2008).

[52] G. Catalan, Appl. Phys. Lett. **88** 102902 (2006).

[53] R. Schmidt, W. Eerenstein, T. Winiecki, F. D. Morrison and P. A. Midgley, Phys. Rev. B **75** 245111 (2007).

[54] D. O'Neill, R. M. Bowman and J. M. Gregg, Appl. Phys. Lett. **77** 1520 (2004).

[55] T. Tsurumi, J. Li, T. Hoshima, H. Kakemoto, M. Nakada and J. Takedo, Appl. Phys. Lett. **91** 182905 (2007).

[56] A. Seeger, P. Lunkenheimer, J. Hemberger, A. A. Mukhin, V. Y. Ivanov, A. M. Balbashov and A. Loidl, J. Phys.: Condens. Matter **11** 3273 (1999).

[57] A. L. Efros and B. I. Shklovskii, J. Phys. C. Solid State Phys. **8** L49 (1975).

[58] J. M. D. Coey, M. Viret, L. Ranno and K. Ounadeja, Phys. Rev. Lett. **75** 3910 (1995).

[59] J. Fontcuberta, B. Martínez, A. Seffar, S. Piñol, J. L. García-Muñoz and X. Obradors, Phys. Rev. Lett. **76** 1122 (1996).

[60] D. Yu, C. Wang, B. L. Wehrenberg and P. Guyot-Sionnest, Phys. Rev. Lett. **92** 216802 (2004).

[61] T. Kimura, S. Kawamoto, I. Yamada, M. Azuma, M. Takano and Y. Tokura, Phys. Rev. B **67** 180401(R) (2003).

Appendix A: Lattice parameters from XRD data

A.1 Symmetric XRD scans

As described in Chapter 2, symmetric XRD scans allow the crystallographic planes that are parallel to the surface of the film to diffract (see Fig. 2.5, Ch. 2). From the Bragg's law (Eq. 2.1, Ch. 2), the interplanar distance of the (*hkl*) planes, d_{hkl}, planes can be computed from the $2\theta_{hkl}$ angle in which diffraction takes place. When (00*l*) crystallographic planes are the ones parallel to the surface, the out-of-plane lattice parameter, *c*, can trivially be related to the interplanar distance, d_{00l}, following Eq. 2.1:

$$d_{00l} = \frac{c}{l} = \frac{\lambda}{2\sin\left(\frac{2\theta_{00l}}{2}\right)} \tag{A.1}$$

where λ is the wavelength of the incoming X-ray radiation. Note that this is valid for orthogonal crystal structures, *i.e.* cubic, tetragonal and orthorhombic (a complete description of d_{hkl} of the different crystal structures is found in table A.1). Thus, by determining $2\theta_{00l}$ position of the (00*l*) XRD reflexion of the film, the out-of-plane lattice parameter of the film should be computed. Improvement of the accuracy can be achieved by Nelson-Riley extrapolation method [1], in which as many as possible of the (00*l*) XRD peaks, *i.e.* different *l*, is used.

Nonetheless, the diffractometer is not perfect aligned, which entails that the measured $2\theta_{00l}$ position is shifted from the correct position that should correspond to the diffraction (00*l*) planes. An easy way, and used in this work, to correct this shift and allow accurately estimating the lattice parameters consists of using the substrate lattice parameter, *a*, as a reference (considered a virtual perfect crystal), *i.e.* a_{STO} = 3.905 Å for $SrTiO_3$. From the $2\theta_{00l}$ positions of the XRD reflexions of the substrate, $2\theta_{s,00l}$, and considering a_{STO} = 3.905 Å, an effective wavelength, λ_{eff}, which contains the instrumental misalignment, can be defined as follows from Eq. A.1:

$$\lambda_{eff} = \frac{a_{STO}}{l} \cdot 2\sin\left(\frac{2\theta_{s,00l}}{2}\right) \tag{A.2}$$

From λ_{eff} the out-of-plane lattice parameter of the film is computed as follows:

$$c_{film} = \frac{l \cdot \lambda_{eff}}{2\sin\left(\frac{2\theta_{f,00l}}{2}\right)} \tag{A.3}$$

where $2\theta_{f,00l}$ is the measured 2θ position of the film (00l) XRD reflexion.

A.2 Reciprocal space maps

Similar to the lattice parameters extracted from the symmetric XRD scans, the substrate will be used to account for the instrumental misalignment. Given a (*hkl*) XRD reflexion of both substrate and film in the reciprocal space map (RSM), see Sect. 2.2.1, the film lattice parameters is evaluated by determining $\Delta\vec{q}_{hkl} \equiv \vec{q}_{f,hkl} - \vec{q}_{s,hkl}$, where subscript *f* and *s* stand for film and substrate XRD reflexion, respectively. The $\vec{q}_{s,hkl}$ position of the substrate ($SrTiO_3$), *i.e.* ($q_{s,parallel}$, $q_{s,perp}$) in the RSM, is used as a reference with lattice parameter a_{STO} = 3.905 Å.

In the following, a tetragonal structure is considered for the sake of simplicity (and due to the fact that it is actually the structure found in the films of this work), yet it is extensive for the rest of crystal structures, though with more complex expressions (table A.1). Thus, the out-of-plane lattice parameter of the film, c_f, is obtained from Δq_{perp} with regard to the q_{perp} component of the substrate, as follows:

$$\Delta q_{perp} \equiv q_{f,perp} - q_{s,perp} = \frac{l_f}{c_f} - \frac{l_s}{a_{STO}} \quad \Rightarrow \quad c_f = \frac{l_f}{\frac{l_s}{a_{STO}} + \Delta q_{perp}} \tag{A.4}$$

where l_f and l_s are the l Miller index of the (*hkl*) reflexion of the film and substrate, respectively. Similarly, the in-plane lattice parameter of the film, a_f, is assessed following:

$$\Delta q_{parallel} \equiv q_{f,parallel} - q_{s,parallel} = \frac{\sqrt{h_f^2 + k_f^2}}{a_f} - \frac{\sqrt{h_s^2 + k_s^2}}{a_{STO}} \quad \Rightarrow$$

$$\Rightarrow \quad a_f = \frac{\sqrt{h_f^2 + k_f^2}}{\frac{\sqrt{h_s^2 + k_s^2}}{a_{STO}} + \Delta q_{parallel}} \tag{A.5}$$

where h_f, k_f and h_s, k_s are the h, k index of the (hkl) XRD reflexion of the film and substrate, respectively.

The general algebraic expressions of $|\vec{q}_{hkl}|$ for the different crystal systems is shown in the following table, in which a, b, c, α, β and γ are the lattice parameters and the corresponding angles of the different unit cells (in the conventional notation [2]).

Crystal System	$\lvert\vec{q}_{hkl}\rvert^2 = \frac{1}{d_{hkl}^2}$
Cubic	$\frac{(h^2+k^2+l^2)}{a^2}$
Tetragonal	$\frac{(h^2+k^2)}{a^2} + \frac{l^2}{c^2}$
Orthorhombic	$\frac{h^2}{a^2} + \frac{k^2}{b^2} + \frac{l^2}{c^2}$
Hexagonal	$\frac{4}{3a^2} \cdot (h^2 + k^2 + hk) + \frac{l^2}{c^2}$
Trigonal	$\frac{1}{a^2} \cdot \left(\frac{(h^2+k^2+l^2) \cdot \sin^2\alpha + 2 \cdot (hk+hl+kl) \cdot (\cos^2\alpha - \cos\alpha)}{1 + 2\cos^3\alpha - 3\cos^2\alpha} \right)$
Monoclinic	$\frac{h^2}{a^2 \sin^2\beta} + \frac{k^2}{b^2} + \frac{l^2}{c^2 \sin^2\beta} - \frac{2hk\cos\beta}{ac\sin^2\beta}$
Triclinic	$\left(1 - \cos^2\alpha - \cos^2\beta - \cos^2\gamma + 2\cos\alpha\cos\beta\cos\gamma\right)^{-1} \cdot$ $\cdot \left(\frac{h}{a^2}\sin^2\alpha + \frac{k^2}{b^2}\sin^2\beta + \frac{l^2}{c^2}\sin^2\gamma + \frac{2kl}{bc}(\cos\beta\cos\gamma - \cos\alpha) + \right.$ $\left. + \frac{2lh}{ca}(\cos\gamma\cos\alpha - \cos\beta) + \frac{2hk}{ab}(\cos\alpha\cos\beta - \cos\gamma)\right)$

Table A.1 – *Distance between the crystallographic (hkl) planes for the different crystal structures.*

References

[1] H.P. Klug and L.E. Alexander, *X-ray Diffraction Procedures*, Wiley-Interscience Pub., 1974.

[2] C. Giacovazzo, H. L. Monaco, G. Arioli, D. Viterbo, G. Ferraris, G. Gilli, G. Zanotti, M. Catti, *Fundamentals of Crystallography*, Oxford University Press Inc., New York, 2002.

Appendix B: Diamagnetism of $SrTiO_3$ substrates

The diamagnetic contribution of $SrTiO_3$ substrates (provided by commercial company Crystec GmbH), used here for the growth of either $BiMnO_3$ or $(Bi,La)_2NiMnO_6$, was thoroughly studied in previous work in the group in the frame of the PhD thesis of Dr. X. Martí [1], onto which $YMnO_3$ thin films were grown using the same PLD facilities (Sect. 2.1). What is reproduced in this appendix is the procedures previously used [1] to determine the diamagnetic susceptibility of $SrTiO_3$ substrates, χ_{STO}, the value of which is the one used in this work.

First, in the aforementioned previous work [1], the magnetic field dependence of the magnetisation, $M(H)$, of a set of as-received bare $SrTiO_3$ susbtrates was measured at 35 K and 300 K. As $M = \chi_{STO} \cdot H$, the negative slope of $M(H)$ curves on increasing H allows obtaining the volume diamagnetic susceptibility of $SrTiO_3$, χ_{vSTO}, at both temperatures, which were remarkably close: $-1.13 \cdot 10^{-6}$ emu/[Oe·cm^3] and $-1.22 \cdot 10^{-6}$ emu/[Oe·cm^3] at 35 K and 300 K, respectively. Note that the volume susceptibility was computed using the dimensions of $SrTiO_3$ substrates: 5 x 5 x 0.5 mm^3.

Second, the diamagnetic susceptibility of $SrTiO_3$ substrates can also be determined by measuring $M(H)$ curves of different thick films already grown on $SrTiO_3$ substrates at temperatures belonging to the paramagnetic regime of the film. The $M(H)$ curves follows $M = (\chi_{vSTO} + \chi_{vfilm}) \cdot H$. The diamagnetic susceptibility will be independent of the film thickness, as all the substrates are identical in dimensions, but the paramagnetic susceptibility of the film will be proportional to the film thickness, *i.e.* $\chi_{vfilm} = K \cdot t$, where K and t are a constant and the film thickness, respectively. Thus, by differentiating $M(H)$ a linear dependence is found as a function of thickness: $dM/dH = \chi_{vSTO} + K \cdot t$. The interception at $t = 0$ of the linear fitting allows extracting the volume diamagnetic susceptibility of $SrTiO_3$, $\chi_{vSTO} = (-1.11 \pm 0.05) \cdot 10^{-6}$ emu/[Oe·cm^3], in close agreement with the one extracted from bare $SrTiO_3$ substrates. This latter value was used in this work to subtract the diamagnetic contribution of the substrate in the raw magnetic data.

References

[1] X. Martí, *Growth and characterization of magnetoelectric $YMnO_3$ epitaxial thin films*, PhD thesis, Universitat Autònoma de Barcelona, 2009. http://usuaris.tinet.cat/xmarti/talks/xmarti_phd.pdf

Appendix C: Capacitance values from the *R-CPE* element

As stated in chapter 3, the non-idealty of the dielectric behaviour is usually accounted by replacing the ideal capacitor, *C*, by a Constant Phase Element, *CPE*. Real dielectrics also display leakage, so that the simplest impedance representation of a non ideal real dielectric is by an *R-CPE* element (see Sect. 3.2.1), whose impedance response is given by the following expression:

$$Z^*_{R-CPE} = \frac{R}{1 + RQ(i\cdot\omega)^{\alpha}} \qquad \text{(C.1)}$$

where *Q* and α (α ≤ 1, being α = 1 the ideal dielectric behaviour) denote the amplitude and the phase of the *CPE*, respectively. Note that when α = 1, the impedance of the ideal *RC* element is obtained (see Eq. 3.2, Sect. 3.2.1) and, thus, *Q* can be identified as *C*. Yet, when α ≠ 1, *Q* does not have the dimension of capacitance, *i.e.* [F], but its units are given by [F·s$^{(\alpha-1)}$], so it turns out necessary to obtain the real capacitance values of the *R-CPE* element in order to correctly assess the dielectric properties.

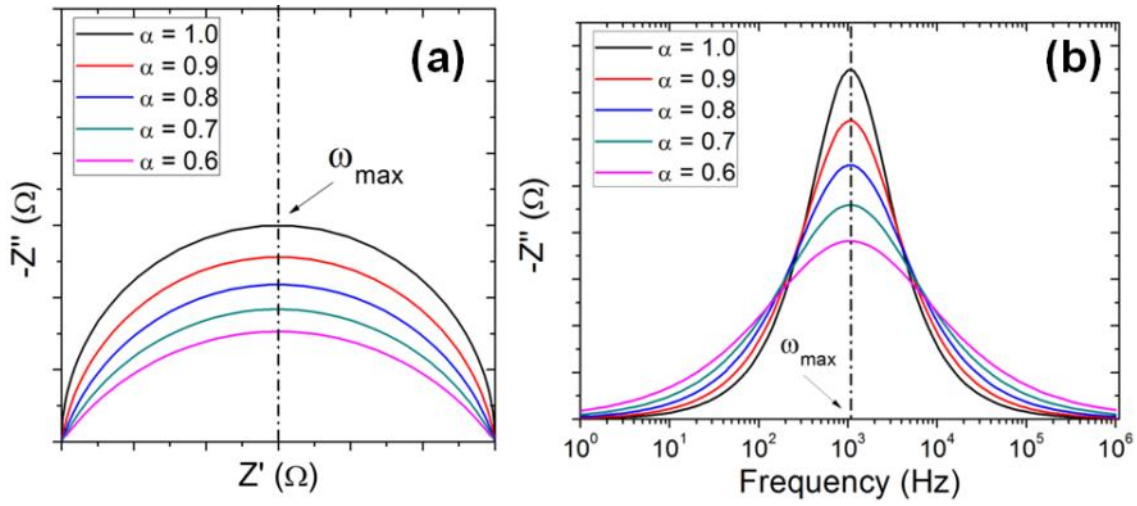

Fig. C.1 – *Simulated –Z''-Z' plots* **(a)** *and –Z'' vs frequency curves* **(b)** *for a R-CPE element using different values of CPE exponent, α. α = 1 denotes the ideal RC element. R and C values taken in the simulation were 1.5·10^3 Ω and 10^{-7} F, respectively.*

The ideal dielectric, modelled by a *RC* element, shows a semicircle in the *–Z''- Z'* plots [Fig. C.1 (a)], the maximum is found for the angular frequency $\omega_{max} = (R \cdot C)^{-1}$, which coincides with the peak in the imaginary part of the impedance, *Z''*, [Fig. C.1 (b)]. This frequency has a physical meaning and corresponds to the cut-off frequency at which higher frequencies the dielectric character prevails, whereas lower frequencies it is the leakage character that is predominant (See Sect. 3.2.1). The non-ideality, modelled by an *R-CPE* element, shows a depressed semicircle in the –Z''-Z' plots [Fig. C.1 (a)], but the cut-off frequency, ω_{max}, should coincide with that of an ideal *RC* element [Fig. C.1]. This is only reproduced when $C = Q \cdot (\omega_{max})^{\alpha-1}$ [1], which was the expression used in the simulations plotted in Fig. C.1. Note that in the simulations *R* was fixed at the same value for the different values of α.

Thus, by developing $C = Q \cdot (\omega_{max})^{\alpha-1}$ expression, taking into account that $\omega_{max} = (R \cdot C)^{-1}$, the capacitances values of the *R-CPE* element can be computed:

$$C = Q\left(\frac{1}{RC}\right)^{\alpha-1} \Rightarrow C^{\alpha} = \frac{Q}{R^{\alpha-1}} \Rightarrow C = Q^{1/\alpha} R^{\frac{1-\alpha}{\alpha}} = \frac{(Q \cdot R)^{1/\alpha}}{R} \qquad \text{(C.2)}$$

Note that this expression is only valid for *R-CPE* element, in which *R* and the *CPE* are connected in parallel. Yet this impedance circuit is the one containing *CPE*'s with dielectric physical meaning.

References

[1] For a deeper discussion see C. H. Hsu and F. Mansfeld, Corrosion **57** 747 (2001).

List of publications and other scientific contributions

1. List of primary publications

- *Thin films in ternary Bi - Mn - O system obtained by pulsed laser deposition*
  E. Langenberg, M. Varela, M. V. García-Cuenca, C. Ferrater, F. Sánchez, J. Fontcuberta
  Materials Science and Engineering B **144** 138 (2007)

- *Epitaxial thin films $(Bi_{0.9}La_{0.1})_2NiMnO_6$ obtained by pulsed laser deposition*
  E. Langenberg, M. Varela, M. V. García-Cuenca, C. Ferrater, M. C. Polo, I. Fina, L. Fàbrega, F. Sánchez, J. Fontcuberta
  Journal of Magnetism and Magnetic Materials **321** 1748 (2009)

- *Long-range order of Ni^{2+} and Mn^{4+} and ferromagnetism in multiferroic $(Bi_{0.9}La_{0.1})_2NiMnO_6$ thin films*
  E. Langenberg, J. Rebled, S. Estradé, C. J. M. Daumont, J. Ventura, L. E. Coy, M. C. Polo, M. V. García-Cuenca, C. Ferrater, B. Noheda, F. Peiró, M. Varela, J. Fontcuberta
  Journal of Applied Physics **108** 123907 (2010)

- *Ferroelectric phase transition in strained multiferroic $(Bi_{0.9}La_{0.1})_2NiMnO_6$ thin films*
  E. Langenberg, I. Fina, P. Gemeiner, B. Dkhil, L. Fàbrega, M. Varela, J. Fontcuberta
  Applied Physics Letters **100** 022902 (2012)

- *Dielectric properties of $(Bi_{0.9}La_{0.1})_2NiMnO_6$ thin films: Determining the intrinsic electric and magnetoelectric response*
  E. Langenberg, I. Fina, J. Ventura, B. Noheda, M. Varela, J. Fontcuberta
  Physical Review B **86** 085108 (2012)

2. Collaboration in publications

- *Synthesis and characterisation of platinum thin film as top electrodes for multifunctional layer devices by PLD*
  L. E. Coy, J. Ventura, C. Ferrater, E. Langenberg, M. C. Polo, M. V. García-Cuenca, M. Varela
  Thin solid films **518** 4705 (2010)

- *Structural and dielectric properties of (001) and (111)-oriented $BaZr_{0.2}Ti_{0.8}O_3$ epitaxial thin films*
  J. Ventura, I. Fina, C. Ferrater, E. Langenberg, L. E. Coy, M. C. Polo, M. V. García-Cuenca, L. Fàbrega, M. Varela
  Thin Solid Films **518** 4692 (2010)

- *Nonferroelectric contributions to the hysteresis cycles in manganite thin films: A comparative study of measurement techniques*
  I. Fina, L. Fàbrega, E. Langenberg, X. Martí, F. Sánchez, M. Varela, J. Fontcuberta
  Journal of Applied Physics **109** 074105 (2011)

- *Magnetoimpedance spectroscopy of epitaxial multiferroic thin films*
  R. Schmidt, J. Ventura, E. Langenberg, N. M. Nemes, C. Munuera, M. Varela, M. García-Hernandez, C. León, J. Santamaría
  Physical Review B **86** 035113 (2012)

3. Other scientific contributions

- *Bi-containing multiferroic perovskite oxide thin films*
  R. Schmidt, E. Langenberg, J. Ventura, M. Varela
  in "Perovskites - Crystallography, Chemistry and Catalytic Performance"
  Editors: J. Zhang, H. Li, Novascience Publishers
  Hauppauge, USA, 2013
  ISBN: 978-1-62417-800-9

List of oral presentations

- *Epitaxial $BiMnO_3$ thin films: optimisation of the deposition conditions*
  E. Langenberg, M. Varela, M. V. García-Cuenca, C. Ferrater, F. Sánchez, J. Fontcuberta
  Workshop Manipulating the Coupling in Multiferroic Films (MaCoMuFi)
  Bonn (Germany), 2007

- *Epitaxial thin films of multiferroic $(Bi_{0.9}La_{0.1})_2NiMnO_6$ obtained by pulsed laser deposition*
  E. Langenberg, M. Varela, M. V. García-Cuenca, C. Ferrater, M. C. Polo, I. Fina, L. Fàbrega, F. Sánchez, J. Fontcuberta
  European Materials Research Society (E-MRS, spring meeting)
  Strasbourg (France), 2008

- Growth of epitaxial *$(Bi_{0.9}La_{0.1})_2NiMnO_6$ thin films*
  E. Langenberg, M. Varela, C. Ferrater, M. C. Polo, M. V. García-Cuenca, J. Ventura, I. Fina, L. Fàbrega, F. Sánchez, J. Fontcuberta
  Workshop Manipulating the Coupling in Multiferroic Films (MaCoMuFi)
  Groningen (The Netherlands), 2008

- *$(Bi_{0.9}La_{0.1})_2NiMnO_6$ thin films: Impedance spectroscopy and ferroelectric characterisation*
  E. Langenberg, C. Daumont, I. Fina, J. Ventura, L. E. Coy, C. Ferrater, M. C. Polo, M. V. García-Cuenca, F. Sánchez, L. Fàbrega, B. Noheda, M. Varela, J. Fontcuberta
  International Symposium on Integrated Functionalities (ISIF)
  San Juan (Puerto Rico, USA), 2010

- *Ferroelectric phase transition of strained multiferroic $(Bi_{0.9}La_{0.1})_2NiMnO_6$ thin films*

  E. Langenberg, P. Gemeiner, I. Fina, J. Ventura, L. E. Coy, M. C. Polo, M. V. García-Cuenca, C. Ferrater, L. Fàbrega, M. Varela, B. Dkhil, J. Fontcuberta

  European Materials Research Society (E-MRS, fall meeting)

  Warsaw (Poland), 2011